Numerical investigation of compressible flow through a curtain of fixed particles with an immersed boundary method

Zur Erlangung des akademischen Grades eines

Doktors der Ingenieurwissenschaften (Dr. -Ing)

von der KIT-Fakultät für Bauingenieur-, Geo- und Umweltwissenschaften
des Karlsruher Instituts für Technologie (KIT)

genehmigte

Dissertation

von

M.Tech. Swagat Kumar Nayak

Tag der mündlichen Prüfung:	13. 12. 2024
Referent:	Prof. Dr. Markus Uhlmann
Korreferent:	Prof. Dr. Nikolaus Adams

Karlsruhe (2024)

Abstract

Compressible flows through particulate-flow systems are observed in many natural phenomena including volcanic eruptions, meteorite entry, and dust storms. In addition, they find relevance in industrial applications including flow through fluidized beds and in cold gas spray processes. In flows exhibiting significant compressibility effects, flow features like the presence of shock waves are typically observed, which are absent in incompressible flows. This can lead to complex flow mechanisms including shock-shock and shock-wake interactions in fluid-particle systems. The dispersed phase, in addition can experience increased drag forces through compressible flow mechanisms. Although, understanding of compressibility effects in such flow-systems in the past two decades has seen significant progress through experiments and numerical approaches, much remains to be answered, especially regarding the nature of heat transfer in particle clouds, and the flow dynamics in the wake of a finite-sized fixed particle array at a Reynolds number of $\mathcal{O}(100)$. Through the work presented in the thesis, such topic are explored and an attempt is made to progress the understanding of compressible particle-laden flows by performing particle-resolved Direct Numerical Simulations using a diffuse-interface immersed boundary procedure. Although, the current work is limited to fixed-particle arrangements, the introduced immersed boundary procedure can be extended to a computationally efficient numerical approach for studying flow near mobile particles in future.

In the thesis, first the numerical framework and the methodology was discussed. Following which, single and two-phase validations were performed at a range of Reynolds and Mach numbers. The two-phase validations with the available experimental or boundary-fitted reference data showed that the current immersed boundary approach performed well near the incompressibility limit, while also capturing the particle forces, heat transfer, and the wake regimes effectively for a range of Reynolds numbers and Mach numbers. A good agreement was also obtained for the drag forces and the variance of force fluctuations for flow through a homogeneous particle distribution, when comparing to the boundary-conforming data of Osnes et al. (2023).

Direct Numerical Simulations of shock-wave interacting with a fixed particle curtain with constant surface temperatures were performed for different shock-wave Mach numbers. The dynamics during the initial transient and in the established late-time flow-state were studied in detail. In addition, the local flow near the particles inside the curtain were studied using particle-conditioned averaging inside uniformly spaced slabs in the inhomogeneous direction. For the case with the lowest post shock Mach number, the late-time state was essentially incompressible, and the recirculation lengths were observed to peak near the downstream edge of the curtain. However, for the case with a supersonic post-shock Mach number, a decrease in the recirculation length was observed in the region. The particle-conditioned temperature fields showed strong temperature gradients near the particle surfaces, which were observed to be higher near the upstream stagnation point. The flow near the locality of particles may vary significantly in the streamwise direction. Hence, particle-conditioned averaging can be useful for studying streamwise variation of local-to-particle flow fields in similar non-homogeneous setups.

For the case with the highest post shock Mach number, alternating oblique wave structures were observed similar to shock cells in under-expanded jets. The signature of the shock cells were also seen in the profiles of mean flow, pseudo-turbulent kinetic energy, and the turbulent Reynolds number. The analysis of the curtain wake for the case also showed a strong correlation for cross-transverse velocity fluctuations due to these structures.

The drag coefficients showed a peak for the particles located near the downstream edge of the curtain in the two cases, for which the flow choked in the region. This feature was not observed for the case in which the post-shock conditions were essentially incompressible. In addition, the Nusselt number in general showed a decrease along the curtain for the two highest post shock Mach number cases.

The existing quasi-steady drag models by Osnes et al. (2023) for homogeneous particle distributions were compared with the current DNS result and their efficacy for inhomogeneous particle distribution used in the current work was tested. A one-dimensional model by Ling et al. (2012) was tested and compared with the current DNS results. The model could capture the general flow features at late times observed in the current DNS. Future efforts for numerical studies of compressible flow through particle clouds can benefit by performing preliminary tests with the model before setting up large scale simulations

Zusammenfassung

Partikel-beladene, kompressible Strömungen treten bei einer Vielzahl natürlicher Ereignisse wie Vulkanausbrüchen, Meteoriteneinschlägen oder Sandstürmen auf. Zudem sind Strömungen dieser Art von hoher Relevanz für industrielle Anwendungen wie beispielsweise Fließbettfilter sowie im Prozess des Kaltgasspritzens. Strömungen mit ausgeprägten Kompressibilitätseffekten weisen oftmals bestimmte Phänomene wie Schockwellen auf, die in inkompressiblen Strömungen nicht auftreten. Letztere können in Partikel-beladenen Strömungen zu komplexen Vorgängen wie der Interaktion mehrerer Schockwellen oder der Überlagerung der Schockwellen mit den Nachlaufzonen einzelner Partikel führen. Zusätzlich kann die partikuläre Phase durch die Kompressibilitätseffekte eine erhöhte Widerstandskraft erfahren. Obgleich die Auswirkungen solcher Kompressibilitätseffekte Dank intensiver Forschungsbemühungen in den vergangenen zwanzig Jahren nun deutlich verstanden werden, bleiben viele Fragen weiterhin ungeklärt. Dies gilt insbesondere für den Wärmetransport in Partikelwolken oder die Strömungsvorgänge in der Nachlaufzone derselben für Reynoldszahlen der Größenordnung $\mathcal{O}(100)$. In der vorliegenden Arbeit werden diese Themen eingehend untersucht mit dem Ziel, zu einem besseren Verständnis der physikalischen Prozesse in Partikel-beladenen, kompressiblen Strömungen beizutragen. Hierzu wurden partikelaufgelöste direkte numerische Simulationen (DNS) durchgeführt, in denen eine die Partikeldynamik mit Hilfe einer "diffuse-interface immersed boundary method" einbezogen wird. Auch wenn sich die vorliegende Arbeit ausschließlich auf Strömungen um unbewegliche Partikel fokussiert, kann die vorgestellt Methode in Zukunft so erweitert werden, dass sie dann auch eine effiziente Berechnung für Strömungen mit frei beweglichen Partikeln ermöglicht.

In der vorliegenden Arbeit wird die numerische Methodik zunächst vorgestellt und ihre Wirksamkeit anhand mehrerer ein- und zweiphasiger Validierungsfälle für verschiedene Reynolds- und Machzahlen unter Beweis gestellt. Ein Vergleich der Simulationsergebnisse für die zweiphasigen Testfälle mit Daten aus Experimenten und Simulationen (mit an die Körperform angepassten Simulationsgittern) unterstreicht die

Präzision der Simulationen: Für eine Reihe von Reynolds- und Machzahlen vom nahezu inkompressiblen Fall bis zu Strömungen mit deutlichen Kompressibilitätseffekten liefert die Methode gute Ergebnisse für verschiedene Referenzgrößen (die auf die Partikel wirkenden Kräfte, den Wärmeaustausch sowie die Abbeckung der verschiedenen Regime der Nachlaufzone). Im konkreten Fall einer Strömung durch eine Wolke gleichmäßig-verteiler, unbeweglicher Partikel zeigt sich eine gute Übereinstimmung mit den Simulationen von Osnes et al. (2023), in denen die Partikelkräfte und deren Varianz mit an die Körperform angepassten Simulationsgittern bestimmt wurden.

Im Anschluss wurde eine Reihe direkter mumerischer Simulationen durchgeführt, welche die Interaktion von Schockwellen mit einer unbeweglichen Partikelwolke für verschiedene Schock-Machzahlen und konstante Oberflächentemperaturen simuliert. Die Analyse der Simulationsergebnisse geht sowohl auf die Strömungsdynamik in der Anfangsphase als auch auf deren Langzeit-Entwicklung im Detail ein. Des Weiteren wurde die lokale Umströmung der einzelnen Partikel innerhalb der Partikelwolke mit Hilfe von Partikel-konditionierter Mittelung untersucht, wobei das Feld in der inhomogenen Raumrichtung gleichmäßig in einzelne Zellen unterteilt wurde. In der Simulation mit der geringsten Machzahl (gemessen nach Passieren der Schockwelle) ist der Langzeitzustand der Strömung annähernd inkompressibel und die Länge der Rezirkulationszonen ist am unterstromigen Ende der Partikelwolke am größten. In Fällen, in denen die Machzahl auch nach Passieren der Schockwelle supersonisch bleibt, wird stattdessen eine Abnahme der Länge der Rezirkulationszonen in dieser Region beobachtet. Die mittleren, partikelkonditionierten Temperaturfelder weisen starke Temperaturgradienten nahe der Partikeloberflächen auf, wobei diese am oberstromigen Stagnationspunkt am deutlichsten ausgeprägt sind. Hierbei kann die lokale Umströmung der Partikel stark entlang der Hauptströmungsrichtung variieren. Daher ist die Analyse basierend auf mittleren, partikelkonditionierten Feldern sehr hilfreich, um die Veränderung der lokalen Strömungsbedingungen in Partikelnähe in Hauptströmungsrichtung in vergleichbaren, inhomogenen Strömungen zu quantifizieren.

Für den Fall mit der höchsten Machzahl wird die Nachlaufzone der Partikelwolke zunehmend von einer Reihe wellenartiger Strukturen dominiert, die geneigt zur Hauptströmungsrichtung verlaufen und abwechselnd von hoher oder niedriger Intensität geprägt sind. In dieser Hinsicht gleichen diese Schockzellen unterexpandierten Strahlströmungen (“underexpanded jets”). Die Signatur der beobachteten Schockzellen ist auch in den Profilen der mittleren Geschwindigkeit, der pseudo-turbulenten kinetischen Energie sowie der turbulenten Reynoldszahl zu erkennen. Außerdem zeigt sich

ihre Dominanz in der Nachlaufzone der Partikelwolke in Form einer starken räumlichen Korrelation der Geschwindigkeitskomponenten quer zur Hauptströmungsrichtung.

In den beiden Fällen, in denen sich die Strömung zwischen den Partikeln verlangsamt, ist der Widerstandskoeffizient am unterstromigen Ende der Partikelwolke am höchsten. Im Fall mit der geringsten Machzahl, in welchem die Strömung nach Passieren der Schockwelle quasi inkompressibel ist, ist dieser Effekt dagegen nicht zu beobachten. Ebenfalls nur für die beiden Fällen mit höherer Machzahl wird beobachtet, dass die Nusseltzahl entlang der Hauptströmungsrichtung bei Durchströmung der Partikelwolke sukzessive abnimmt.

Schließlich wurde das quasi-statische Modell von Osnes et al. (2023) zur Abschätzung des Widerstandskoeffizienten für die Durchströmung einer Partikelwolke mit gleichmäßiger Partikelverteilung mit den DNS-Ergebnissen verglichen sowie dessen Anwendbarkeit unter den hier analysierten, inhomogenen Bedingungen untersucht. In diesem Zusammenhang wurde alternativ auch ein eindimensionales Modell von Ling et al. (2012) getestet und dessen Vorhersage mit den DNS-Ergebnissen verglichen. In der Tat war dieses Modell in der Lage, die Langzeitentwicklung der allgemeinen Strömungscharakteristika abzubilden. Modelle dieser Art könnten daher für zukünftige numerische Untersuchungen von kompressiblen Strömungen durch Partikelwolken von großem Vorteil sein, da sie eine erste Abschätzung der zu erwartenden Strömungsbedingungen bereits vor Durchführung aufwendigerer Simulationen erlauben.

Acknowledgements

This doctoral thesis represents a personal milestone marked by professional growth and the ability to conduct independent research. However, this journey has only been made possible through the support and encouragement of many individuals to whom I owe my deepest gratitude. I began this endeavor during the challenging times of the COVID-19 pandemic, which brought limitations on interactions and some uncertainties. I am immensely thankful for the continued support from my family, friends, and colleagues during these challenging times. This section is dedicated to the individuals and institutions who have made this journey possible.

First and foremost, I would like to extend my sincere gratitude to my supervisor, Prof. Markus Uhlmann, who has been instrumental in shaping my doctoral journey and whom I deeply admire as an exceptional researcher. A meticulous and thorough approach to problem-solving is a trait I have had the privilege of learning from him. Over the past four years, Markus has supported me professionally and has always been available to offer guidance, provide physical and mathematical insights, or engage in scientific discussions. I thoroughly enjoyed our meetings and greatly appreciate his invaluable suggestions, which have helped me immensely in my doctoral research. I truly feel privileged to have had him as my supervisor, and the work presented in this thesis would not be the same without his guidance.

I would also like to express my gratitude to the current and former members of the Institute of Water and Environment (IWU). The scientific and non-scientific discussions with my colleagues at the Institute have provided me with valuable research inspiration and opportunities to take a break from my work. I have greatly appreciated being part of an environment that embraced mutual respect and support, and I have been fortunate to form lasting friendships along the way. Some of my fondest memories include bouldering sessions and house parties with Manu, learning about the local German culture through interactions with Lina, Tiago, Markus S., and Michael, engaging in institute excursions, and sharing countless enjoyable lunch breaks with colleagues. I am particularly thankful to Markus Scherer for his insights on turbulent

channel flows, his assistance with teaching, and his kind words during challenging times. I would also like to share a special thanks to Manu, Michael, and Tiago for their scientific suggestions and help during my initial months at the institute. Additionally, I deeply appreciate the help and support of Angelika Fels, Helmut Oppmann, and Heidi Lauinger with IT, financial, and administrative matters, which ensured the smooth progression of my doctoral journey. To my friends and co-workers at the Institute over the years—Michele T., Tatia, Yulia, Michele P., Christof, Erni, Victor, and many others—thank you for your friendship, collaboration, and encouragement. While the limited space prevents me from giving proper credit to everyone who has contributed to my journey, please know that your support and kindness have been integral to my journey, and I am forever grateful.

I would like to extend my gratitude to Prof. Nikolaus Adams from TU Munich for reviewing my thesis and providing insightful feedback, particularly on the numerical aspects of my work. I am equally grateful to Prof. Bettina Frohnapfel for sharing her valuable perspectives and for being a part of my committee. My sincere thanks also go to Prof. Mario Franca for chairing my committee and for his interest in my research. I deeply appreciate the support of Prof. Olivier Eiff over the years at the institute and his willingness to share experimental perspectives regarding my research.

Throughout my doctoral journey, there were many moments when I felt low, facing both scientific and personal hurdles. During such times, I was fortunate to have the encouragement of my flatmates, friends, and family. I deeply value my Mom and Dad's kind words and support over the years. They have always put my happiness and well-being ahead of theirs. I can't thank them enough for their emotional support over the years. I would also like to thank my brother, who has been a constant source of support throughout this journey. Our shared stories and conversations about academic life have been a great source of motivation. A special thanks goes to Pallavi, who has been a pillar of support during my highs and lows. Her constant encouragement, lighthearted humor, and willingness to lend an ear whenever I needed to talk have been invaluable to me. I am also deeply thankful to Shobhna for the many moments we've shared—whether cooking Indian food, traveling, playing sports, or discussing our doctoral experiences. Finally, I want to express my gratitude to my flatmates for creating a warm and welcoming home environment. The board game nights, shared meals, and casual conversations brought much-needed joy and balance to my life during this journey.

I acknowledge the support of the German Research Foundation (DFG) for the scientific work presented in the thesis through the grant UH242/13-1. I want to thank the Steinbuch Centre for Computing (SCC) of the Karlsruhe Institute of Technology (KIT) for access to computational resources and storage solutions (BWUniCluster2.0, HoreKa, LSDF). Their technical support, expertise, and quick response to queries are highly appreciated.

Contents

Appendix

Notation

Acronyms

DNS	Direct Numerical Simulations
LES	Large Eddy Simulations
KIT	Karlsruhe Institute for Technology
LODI	Locally One-Dimensional Inviscid
ODE	Ordinary Differential Equation
PDE	Partial Differential Equation
WENO	Weighted Essentially Non Oscillatory
TENO	Targeted Essentially Non Oscillatory
PTKE	Pseudo Turbulent Kinetic Energy
PR-DNS	Particle resolved Direct Numerical Simulations

Mathematical operators and symbols

∇	Nabla operator, $\nabla = (\partial_x, \partial_y, \partial_z)^\mathsf{T}$
$\frac{\mathrm{d}}{\mathrm{d}t}$	Total derivative

Greek symbols

ρ	Density of fluid
τ	Total stress tensor
μ	First coefficient of viscosity
μ_b	Coefficient of bulk viscosity
γ	Ratio of the heat capacities C_p/C_v
κ	Thermal conductivity of the fluid
λ^{max}	Largest eigenvalue of the Jacobian matrix
δ_h	Discrete delta function
Λ	Compressibility of the medium
$p.d.f$	probability density function
$j.p.d.f$	joint probability density function
$\lambda_x, \lambda_y, \lambda_z$	Wavelengths along x, y, and z

Latin symbols

$\mathscr{V}(t)$	Arbitrary material volume whose surface moves with the local fluid velocity
$\mathscr{A}(t)$	Surface of the material volume $\mathscr{V}$
$\mathscr{T}(x, y, z, t)$	A tensor which varies smoothly in $\mathscr{V}$
$x_{i,j,k}$	Eulerian grid
$\mathbf{X}_l^{(m)}$	Lagrangian force point locations
$\mathbf{u}(x, y, z, t)$	The local velocity vector
$\mathbf{U}$	Vector of conservative variables
$\mathbf{Q}$	Vector of source terms
$\mathbf{F}^{(x)}, \mathbf{F}^{(y)}, \mathbf{F}^{(z)}$	Vectors of fluxes
$\mathscr{F}^{(x)}, \mathscr{F}^{(y)}, \mathscr{F}^{(z)}$	Numerical flux vectors
$\mathbf{K}, \mathbf{K}^{-1}$	Right and left eigenvector matrices
f_i	body force per unit mass along direction i

d_{ij}	Strain rate tensor given by $d_{ij} = \frac{1}{2}\left(\frac{\partial u_i}{\partial x_j} + \frac{\partial u_j}{\partial x_i}\right)$
C_p, C_v	Specific heats at constant pressure and volume
u, v, w	Velocity components
c	Speed of sound
p	Local thermodynamic pressure
e	internal energy per unit mass
T	Local temperature of the fluid
E	Total energy per unit volume
q_i	Heat flux density along the direction i
$\hbar$	Heat transfer coefficient
C_d, C_l	Drag and Lift coefficients
Re	Reynolds number
Pr	Prandtl number
Nu	Nusselt number
Kn	Knudsen number
Ma	Mach number
Ma_t	Turbulent Mach number
Ma_{crit}	Critical Mach number
Ma_s	Shock Mach number
St	Strouhal number
L_r	Recirculation length
$\mathcal{K}$	Pseudo turbulent kinetic energy
k_x, k_y, k_z	Wavenumbers along x, y, and z

1 Introduction

Fluid flows exhibiting substantial changes in density are observed in many naturally occurring events around us. From meteorites entering the earth's atmosphere (Silber et al. 2018), explosions of dusty matter (Johnston et al. 2016), and flows around high-speed particulate debris from volcanic eruptions (Chojnicki et al. 2006, Wohletz et al. 1984), many examples can be found in nature where the medium's compressibility is non-negligible. Gases, in general, exhibit much higher compressibility than liquids under similar conditions (about five orders of magnitude for air compared to water at one atm). Consequently, moderate to large pressure gradients can lead to significant density variation in gases. Owing to this property of gases, many interesting flow features like shock waves, expansion waves, and contact discontinuities can be observed in high-speed gas flows. Hence, in everyday practice, the study of gas dynamics is synonymous with the field of compressible flows. However, one must remember that, given sufficiently high-pressure gradients in the flow, even liquids can exhibit perceptible compressibility effects.

The earliest advances in compressible high-speed aerodynamics were made by Ernst Mach by distinguishing subsonic and supersonic flow behavior. His seminal work in the late 1800s laid the foundation for supersonic aerodynamics for the following decades. One of the earliest photographs of a bow shock in front of an airborne ballistic projectile traveling at a supersonic speed was captured by Mach and Salcher (Mach and Salcher 1887). Figure 1.1 shows one of the earliest Schlieren images of a bow shock upstream of a brass bullet in supersonic conditions taken by Ernst Mach in 1888.

Since then, significant advances have been made in the field of high-speed compressible flows, making its way into modern-day applications like cold gas spray process (Yin et al. 2016), syringe-free drug delivery systems (Kendall

2002, Liu and Kendall 2006), turbofans, and high-speed airplanes. In a cold gas spray process, metallic particles are accelerated to transonic velocities by feeding them into a supersonic flow. The high-speed metallic particles undergo plastic deformation and bonding with the substrate upon collision. Such a coating method experiences less thermal stress compared to traditional coating processes. Applications of syringe-free drug delivery systems involve accelerating pharmaceutical drugs in a shock tube for needle-less injection of drugs into the human skin.

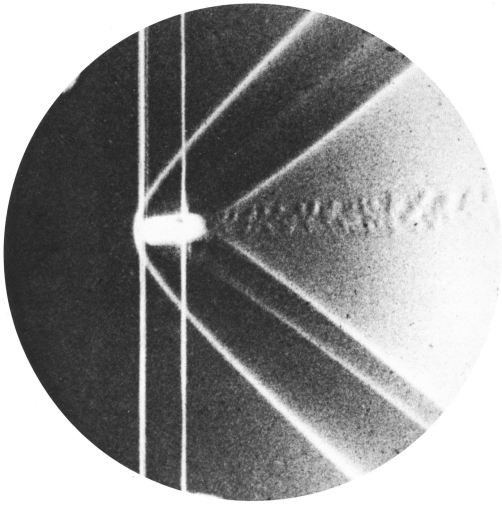

Figure 1.1: Schlieren photograph of shock waves in a supersonic flow by Ernst Mach in 1888, Prague near a 5 mm brass bullet. A standing bow shock upstream and a recovery shock downstream of the bullet can be seen. Taken from Wikimedia (2022)

The field of compressible flows is vast and exciting. Although significant progress has been made in high-speed single-phase aerodynamics over the last century, much remains to be explored, especially in the field of high-speed multiphase flows and induced pseudo-turbulence. The present work attempts to answer some of these knowledge gaps in compressible particulate flows using three-dimensional Direct Numerical Simulations (DNS) of flow around fully resolved spherical particles.

1.1 Motivation

Mach numbers of $\mathcal{O}(1)$ and Reynolds numbers of $\mathcal{O}(100)$ for air at normal temperatures represent compressible flows around particles with a diameter of the order of 10 microns. In nature, such flows are common in shock-wave particulate flow interactions during explosions of dusty matter (Houim and Oran 2015, Johnston et al. 2016), volcanic eruptions (Wohletz et al. 1984, Chojnicki et al. 2006), meteorite impacts (Silber et al. 2018), and lightning discharge (Jones et al. 1968). However, experiments for flow over particles of the mentioned sizes are difficult to perform and analyze carefully. Particle-resolved numerical simulations for compressible flows can help in studying compressible-particulate flows at low Reynolds numbers and Mach numbers of the order of unity.

Shock-wave interaction with isolated spherical particles and a curtain of particles of finite width have been studied extensively using particle-resolved and boundary-conforming numerical approaches in the last decade (Mehta et al. 2016b, Mehta et al. 2019, Osnes et al. 2019, Osnes et al. 2020, Khalloufi and Capecelatro 2023, Osnes et al. 2023). To the extent of the author's knowledge, no literature currently discusses the nature of fluid-solid heat exchange in detail inside the curtain through their particle-resolved numerical simulations. Although significant efforts have been made in the past decade to study flow with compressibility effects inside a finite-sized particle array, much remains to be explored. For example, the literature on the inter-phase heat transfer inside the curtain for a given thermal boundary condition is limited. Also, most of the previous works available at present for shock wave particle-curtain interaction focus on the transient flow as the incident shock wave sweeps the particle curtain. Previous studies have not fully explored the nature of the wake behind the particle curtain, the effect of the curtain width on the flow features, and the localized flow near the particles inside the curtain. The current work is motivated by the following objectives:

- To validate the developed compressible flow solver for single and multiple phases and establish its robustness for flows near the incompressibility limit. Since the immersed boundary procedure does not need continuous re-meshing at every timestep, the current flow solver can be extended to computationally efficient DNS of mobile particles.
- To perform DNS of shock wave interacting with a fixed particle curtain in a range of shock Mach numbers and study the flow in the transient and late times, both inside the curtain and in the wake of the curtain.
- To evaluate the Nusselt numbers for compressible flow through particle arrays of finite width. To compare its quasi-steady variation inside the curtains for a range of shock Mach numbers through particle-resolved DNS of shock-wave interaction with a finite-width particle curtain.
- To compare existing modeling efforts with the current DNS results in the context of flow through a fixed particle curtain.

1.2 Outline of the thesis

The thesis is organized as follows: In chapter 2, some historical remarks are provided, and the state of research in compressible single-phase and multi-phase flows involving spherical particles is discussed. The governing equations of the fluid phase are provided in chapter 3. In the subsequent chapter 4, the numerical schemes for advection, diffusion, and time integration are provided. In addition, a brief discussion of the characteristic inflow-outflow boundary conditions used in the present work and the diffuse-interface immersed boundary method in the context of compressible flows is discussed. In chapter 5, validation tests using Euler's equations or the complete Navier-Stokes equations are performed for compressible single-phase and multi-phase flows. Direct Numerical Simulations for shock interaction with an array of fixed particles of finite width at semi-dilute volume fractions are performed at different Mach numbers in chapter 6. The effect of the length of the curtain width and the volume fraction is analyzed, and the drag and heat transfer coefficients are computed. In addition, the local flow

around the particles is studied using particle-conditioned averaging. Finally, summary of the findings, concluding remarks, and outlook into future work are provided in chapter 7.

2 Literature Review

The fundamental theories of fluid statics and hydrodynamics were established through seminal works of intellectuals over the centuries. One of the earliest significant contributions to hydromechanics was Archimedes's study of floating bodies (285-212 BC). It led to the concept of buoyancy, which is used in modern day applications to evaluate drag on submerged bodies. Leonardo da Vinci's observations in the 15^{th} century on chaotic motion and the range of scales in air and water laid the foundation for modern-day turbulence. Over the past centuries, significant contributions were made by eminent academics like Sir Issac Newton, Daniel Bernoulli, Leonhard Euler, Jean d'Alembert, Joseph-Louis Lagrange, Pierre-Simon Laplace, Osborne Reynolds, Lord Rayleigh, Claude-Louis Navier, George Gabriel Stokes, and Ludwig Prandtl to the theoretical foundation of fluid mechanics.

The interest in compressible flow research grew from humanity's curiosity in aviation and ballistics. However, the applications have expanded to a range of modern-day applications. Starting with some basic definitions, the following sections summarize a brief overview of the past research in the field of compressible flows.

2.1 Compressible single phase flows

2.1.1 Definitions of compressibility and flow regimes

Before the early twentieth century, almost all practical engineering fluid flow problems involved the flow of low-speed gases or liquids. Hence, the incompressible flow theory could be used extensively to approach such problems.

Nevertheless, with the increasing importance of high-speed aviation and the invention of gas and steam turbines, it was obvious that the constant density assumption could not predict the presence of physical phenomena like shock waves in high-velocity gas flows. These shock waves arose from the finite acoustic speeds in a compressible medium, highlighting the limitations of incompressible theory in predicting high-speed physical flow phenomena. Following the classical textbook of Anderson (2003), a brief description of different compressible flow regimes is presented.

Compressibility (Λ) is a property of the medium defined as the fractional change of density per unit change in pressure and is defined in eq. (2.1). If the medium is compressed while keeping the temperature constant, the property is called isothermal compressibility (Λ_T). Meanwhile, if compression takes place adiabatically in the absence of any dissipative mechanisms, it is termed isentropic compressibility (Λ_s).

$$\Lambda = \frac{1}{\rho}\frac{\mathrm{d}\rho}{\mathrm{d}p} \tag{2.1}$$

Generally, the compressibility of gases is about four to five orders of magnitude higher than that of liquids at standard pressure. Higher flow velocities are associated with large pressure gradients. Hence, fluids with lower compressibilities can achieve high velocities without significant density variations for a given pressure change. Such fluid flow problems are considered incompressible. Conversely, gases can achieve substantial density changes under a similar influence of pressure and are classified as compressible flows. Typically, the density variations in incompressible flows are smaller than 5%. For ideal gases, fluid velocities less than 0.3 times the acoustic velocity in the medium are generally assumed incompressible.

$$Ma = \frac{|u|}{c} \tag{2.2}$$

The ratio of fluid and acoustic velocities is termed as Mach number (Ma) and is defined in eq. (2.2). Four different flow regimes can be defined based on the local Mach number of the flow. If the local Mach number of the flow is less

than unity everywhere, the flow is defined as a subsonic flow. In such flows, the flow velocity is less than the acoustic velocity everywhere and consists of smoothly varying properties. Meanwhile, if the local flow velocity exceeds the local speed of sound everywhere in the region of interest, it is considered a supersonic flow. A supersonic flow is characterized by shock waves across which there is an instantaneous change of properties. At very high Mach numbers, the shock wave strengths are so high, that there is an almost explosive change of flow properties across it. The standing shocks in such cases lie much closer to the existing solid obstacles, and the region between the shock and the solid boundary (shock layer) may become very hot. Consequently, features like chemical reactions and ionization inside the shock-layer may become important. Such flows at very high Mach numbers are classified into hypersonic flows. There, is no general criteria on the Mach number to separate hypersonic flows from supersonic flows. However, the general class of problems with very thin shock-layers, where the thermal effects become important are termed as hypersonic flow problems. Sometimes, expansion near solid boundaries can lead to a mixed flow, where the fluid velocity can locally exceed the acoustic velocity. Such a flow with mixed pockets of locally subsonic and supersonic flows is known as a transonic flow.

2.1.2 One-dimensional conservation equations and normal shock relations

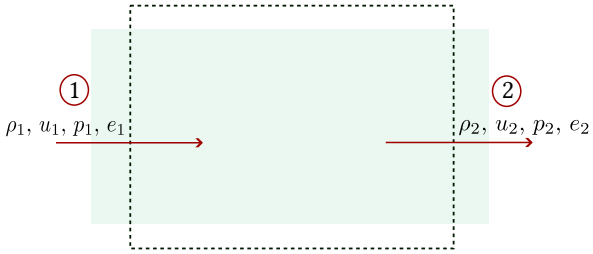

Figure 2.1: Variation of flow properties across the rectangular control volume from state 1 to state 2 for an inviscid flow.

Control volume analysis under steady-state conditions can simplify the governing equations for a one-dimensional inviscid flow. The equations are taken from Anderson (2003) and repeated here for completeness. Assuming that the flow properties like density (ρ), velocity (u), pressure (p), and specific internal energy (e) vary from "state 1" to "state 2" as the fluid flows through the control volume boundaries, the eq. (2.3) can be obtained.

$$\begin{aligned} \rho_1 u_1 &= \rho_2 u_2 \\ p_1 + \rho_1 u_1^2 &= p_2 + \rho_2 u_2^2 \\ h_1 + \frac{u_1^2}{2} + q &= h_2 + \frac{u_2^2}{2} \end{aligned} \tag{2.3}$$

In eq. (2.3), q is the heat added per unit mass to the control volume, and h is the specific enthalpy given by $h = e + p/\rho$. Shock waves can physically appear as thin fluid layers in supersonic flows, through which flow quantities vary rapidly. Mathematically, a discontinuous flow assumption is usually adopted to represent changes in flow properties across the shock wave. In nature, shock waves can exist in different shapes influenced by the geometry and flow conditions. For example, detached bow shocks can be observed upstream of a blunt body, spherical shocks can emerge from the explosion of point sources, and conical shock waves can form upstream of pointed solid geometries in supersonic flows. The current section considers the simplest case of planar shock waves, for which normal shock relations can be obtained by applying Rankine-Hugoniot conditions (Rankine 1870, Hugoniot 1887).

Let L and R represent the left and right states for a planar shock wave traveling with a shock speed S to the right as shown in fig. 2.2. Then the shock Mach number (M_s) is defined as $M_s = S/a_R$, where a_R is the acoustic velocity based on the right state. Assuming that no heat is added as the fluid traverses across the shock wave, the equations relating the pressure, density, and internal energy between the left (post-shock conditions) and the right (pre-shock conditions) states are taken from Toro (2013) and shown in eq. (2.4).

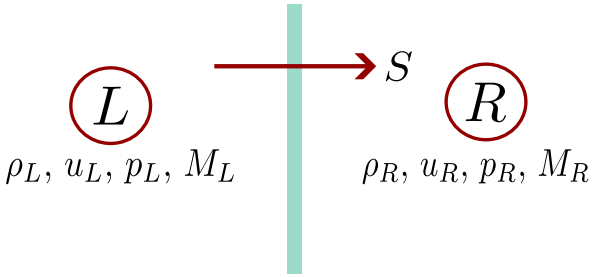

Figure 2.2: Representation of the flow states to the left and right of normal shock wave traveling to the right with a shock speed S. $M_L = u_L/a_L$ and $M_R = u_R/a_R$ represent the Mach number of the left and right states, where the corresponding acoustic velocities are a_L and a_R.

$$\begin{aligned}
\frac{\rho_L}{\rho_R} &= \frac{(\gamma+1)(M_R - M_S)^2}{(\gamma-1)(M_R - M_S)^2 + 2} \\
\frac{p_L}{p_R} &= \frac{2\gamma(M_R - M_S)^2 - (\gamma-1)}{\gamma+1} \\
\frac{e_L}{e_R} &= \left(\frac{p_L}{p_R}\right)\left(\frac{\rho_R}{\rho_L}\right)
\end{aligned} \tag{2.4}$$

The shock speed S is a function of the pressure ratio across the shock wave and is given by eq. (2.5)

$$S = u_R + a_R\sqrt{\left(\frac{\gamma+1}{2\gamma}\right)\left(\frac{p_L}{p_R}\right) + \left(\frac{\gamma-1}{2\gamma}\right)} \tag{2.5}$$

The velocity (u_L) and the Mach number (M_L) to the left of the shock wave can be found as in eq. (2.6).

$$\begin{aligned}
u_L &= \left(1 - \frac{\rho_R}{\rho_L}\right)S + \frac{u_R\rho_R}{\rho_L} \\
M_L &= \frac{u_L}{a_L}
\end{aligned} \tag{2.6}$$

In eq. (2.6) and eq. (2.5), a_L and a_R represent the speed of sound for the left and right states respectively.

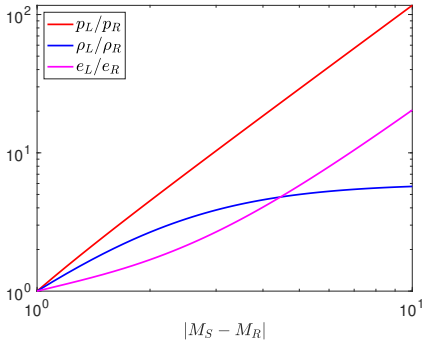

Figure 2.3: Ratio of flow quantities between left and right states for a right traveling planar shock wave as a function of the magnitude of relative mach number $|M_S - M_R|$.

2.1.3 Supersonic compressible turbulent channel flow

Coleman et al. (1995) performed Direct Numerical Simulations for compressible turbulent supersonic channel flows at Mach numbers of ($Ma = 1.5, 3$) based on the bulk velocity and speed of sound near the walls, a Reynolds number ($Re_b = 3000$) based on bulk flow quantities and wall viscosity, ratio specific heats ($\gamma = 1.4$), and a Prandtl number ($Pr = 0.7$). In their study, they used a power-law for the temperature-dependent dynamic viscosity. The flow was driven by a body force such that the total mass across the channel was conserved. They found that the flow near the walls had strong temperature and density gradients. In addition, strong fluctuations were observed in the buffer region, which were attributed to the turbulent mixing driven by the sharp near-wall gradients. Compressibility effects were observed in the enhanced coherence of near-wall streaks with increased Mach number.

Lechner et al. (2001) tested their pressure-velocity-entropy formulation of the Navier-Stokes equations for supersonic turbulent channel flows at a Mach number ($Ma = 1.5$), while keeping the other parameters the same as Coleman et al. (1995). They confirmed that, at their choice of Mach number, the effects of compressibility were observable only in the near-wall region. Increased compressibility effects enhanced the axial component of the Reynolds stress while suppressing the shear stress components. Foysi et al. (2004) used

the Navier-Stokes formulation of Lechner et al. (2001) to study turbulent scaling in isothermal supersonic channel flows at a range of Mach numbers and identified the changes in the Reynolds stress components to the reduction of near-wall pressure strain. Direct Numerical Simulations for turbulent supersonic channel flow between isothermal and adiabatic walls were performed by Morinishi et al. (2004) and were used to compare the near-wall mean flow and turbulence structures. Analysis of the flow field fluctuations, scaling with Reynolds and Mach numbers, and transport equations of variances and fluxes of flow quantities were performed by Gerolymos and Vallet (2014). Further research in the field of compressible plane channel flows was performed by Sciacovelli et al. (2017), Yu et al. (2019), Yao and Hussain (2020), and Baranwal et al. (2023).

The choice of parameters used by Lechner et al. (2001) and Coleman et al. (1995) were used to perform Direct Numerical Simulations for comparison in the current work in section 5.2.4.

2.2 Flow through grids and porous media

Compressible flow through porous media of finite thickness and the turbulence generated by the grids can provide an idea about the flow through a particle array of finite thickness investigated in the current work. Zwart et al. (1997) performed an experimental study of grid turbulence for subsonic flow in the Mach number range of 0.15 to 0.7 and a Grid Reynolds number (Re_m) between $\mathcal{O}(10^4)$ and $\mathcal{O}(10^5)$ using laser Doppler velocimetry. In their work, Re_m was based on the effective grid spacing and the mean streamwise flow velocities. Their experiments found that the turbulence generated through the grid was approximately homogenous and isotropic. The low subsonic regime's ($Ma < 0.7$) turbulent intensity was fairly constant. However, in the high subsonic regime ($0.7 < Ma < 1$), the presence of quasi-normal shocks led to a jump in the measured turbulent intensity and flow unsteadiness. Under supersonic conditions, however, the turbulent intensity was lower than the high subsonic regime. The exponent for the decay rate was observed to be much lower in the high subsonic regime compared to the low subsonic

regime. In the low subsonic regime, the decay exponent seemed to reduce with increasing Mach number until $Ma = 0.3$, where it achieved a minimum and then increased afterward until $Ma = 0.7$. The observed trend in the decay exponent was attributed to the changes in the flow characteristics near the grid with changing Mach numbers. However, the reasoning behind the obtained minima near $Ma = 0.3$ was not specified by Zwart et al. (1997).

The effects of compressibility in a weakly compressible flow ($Ma = 0.3 - 0.6$) on grid-generated turbulence were investigated by Briassulis et al. (2001) through experiments in a large-scale shock tube facility. The Mach number of the flow was small enough to avoid any shock waves or shocklets, but large enough to have finite compressibility effects. The grids used in their experiments provided a range of turbulent Reynolds numbers (Re_λ) based on the Taylor's micro-scale (λ) and the grid solidity (σ) up to 700. In their experiments, as the incident shock wave generated in the shock tube interacted with the grid, a reflected shock wave originated and traveled upstream in the opposite direction. It was observed that the reflected shock wave reduced the velocity and increased the temperature of the incoming flow by small amounts. In addition, it was observed that the strength of the reflected shock wave increased with higher values of projected solid area per unit total area of the grid. Long after the incident shock wave had passed through the grid, a nearly homogenous and isotropic flow was observed behind the grid, generated by the modified incoming flow. In addition, the decay of the Mach number fluctuations behind the grid followed a power law similar to the decay of incompressible isotropic turbulence, where the exponent depended on the flow Mach number as well as the Mesh Reynolds number. However, the growth rate of the shear layers behind the grid was reduced due to compressibility effects.

One of the earliest works in flow through porous media was from Muskat (1934), who used the generalized Darcy's law to obtain simplified partial differential equations for compressible liquids and gases. Later, Emanuel and Jones (1968) derived a one-dimensional set of equations under the assumption of steady, frictionless, adiabatic flow. Contrary to incompressible flows, where the volumetric flow rate is assumed constant across the porous media,

they used an isentropic assumption that allowed the flow exiting the porous media to adjust to the downstream pressure with changes in Mach number, even when the flow was choked. Darcy's equations were also used in a modified form that considered the compressibility effects. They summarised their results in a plot between the upstream Mach number and the pressure ratio across the porous plate, comparing their results to the incompressible flow results. Using the Finite-Element method, a simplified numerical analysis of fluid flow through a porous elastic media was performed by Ghaboussi and Wilson (1973). Direct numerical studies of compressible flow through finite-sized particle arrays can provide more information on the effects of compressibility and porosity on the flow dynamics and can be used to improve available simplified models.

2.3 Compressible flow with particles

The flow of compressible flow over bluff bodies and the effect of the flow Mach number on the drag and lift forces has been extensively studied in the last century because of its applications in the design of aircraft, projectiles, fluidized beds, sports equipment, drug, and aerosol delivery systems to name a few. In the current section, some of the notable research in the field of compressible flow through particles is discussed.

2.3.1 Compressible flow over isolated particle

One of the earliest works for the evaluation of drag coefficient over a sphere as a function of Mach number was from Naumann (1953). From their measurements at high Reynolds numbers ($Re = \mathcal{O}(10^5)$), they realized that the drag coefficient increased with the Mach number of the flow, and the dependence on Reynolds numbers became less significant at higher Mach numbers. It was suggested by Schlichting and Kestin (1961) that the reason was the stronger influence of forces due to the pressure differential across the sphere compared to the frictional forces.

Kassoy et al. (1966) studied the low Reynolds number compressible flow around a sphere with a significant temperature difference between the particle and the freestream. They specified that the impressed temperature difference is vital in studying viscous compressible flows in addition to the Reynolds and Mach numbers. They derived the Drag coefficient and Nusselt number considering the effect of the temperature difference (τ). Their work predicted an increase in the Drag coefficient and a decrease in the Nusselt number with a higher impressed temperature difference for a heated particle when $\tau = \mathcal{O}(1)$.

Bailey and Hiatt (1972) made experimental measurements of the drag coefficient of a sphere in a range of freestream Mach numbers ($0.1 < Ma_\infty < 6$) and ($20 < Re < 10^5$) for a temperature ratio ($T_w/T_\infty \approx 1.0$). Here, T_w represents the temperature on the sphere-surface and T_∞ is the freestream temperature. In addition, they summarized the results of the drag coefficient as a function of the Temperature ratio for a freestream Mach number ($Ma_\infty = 2$) from existing data where ($T_w/T_\infty \neq 1.0$). They observed that higher Temperature Ratios on the sphere at the chosen freestream Mach number ($Ma_\infty = 2$) increased the drag coefficient at a fixed Reynolds number. The results for drag coefficients in the transonic regime were further improved in a later article (Bailey and Starr 1976).

Cebeci and Bradshaw (1977) used the triple-deck model of Lighthill and Newman (1953) to mention that at high Mach number flows, the effect of viscosity inside the boundary layer is only close to the surface, where the flow is viscous and rotational. Far from the surface, the flow could be assumed irrotational and inviscid. Chang and Lei (1996) studied the different sources of aerodynamic forces for a steady flow around spheres and cylinders. They stated that the freestream Mach number directly contributed to the drag of the bluff body when it was sufficiently close to the upstream stagnation point by compression of the fluid. The drag coefficient did not increase indefinitely with the upstream Mach number owing to the presence of the front boundary layer.

Unsteady forces on a sphere in the presence of a shock wave have been studied through multiple experiments and particle-resolved numerical simulations. Detailed quantitative measurements of the transient total drag coefficient on

a sphere for a shock-particle interaction were performed by Tanno et al. (2003) for shock Mach number ($Ma_s = 1.22$) and a Reynolds number ($Re = 3 \times 10^5$). They observed a peak in the drag coefficient shortly before the arrival of the shock wave at the equator and a negative drag coefficient due to the shock wave focusing near the sphere's rear part. Sun et al. (2005) also performed experiments and axisymmetric boundary-conforming numerical simulations for $Ma_s = 1.22$ and Reynolds number (Re) in the range $50 - 5 \times 10^5$. They observed that the peak in the drag coefficient as the incident shock wave swept the particle could be an order of magnitude higher than the steady-state value. During this time, the effects of viscosity on the total drag were negligible, and pressure contributions dominated the total drag. Similar transient behavior in the drag coefficient over spheres was also observed by Skews et al. (2007).

Studies of trajectory, velocity, and acceleration for isolated mobile particles swept by an incident shock wave have been studied by Britan et al. (1995) at shock Mach numbers ($Ma_s = 1.5$ and 1.25) in a shock tube. Experiments of shock particle interaction for mobile isolated particles by Jourdan et al. (2007) and Wagner et al. (2012a) further confirmed that compressibility indeed increased the drag coefficient on the sphere in the high subsonic regime. Wagner et al. (2012a) also showed that the existing drag model by Parmar et al. (2010) showed a good agreement with their experiments for post-shock Mach numbers between 0.7 and 1.

More recently, boundary-conforming and particle-resolved numerical simulations for shock-particle interactions have provided a robust database for improving existing drag and heat-transfer correlations. Mehta et al. (2016a) performed boundary conforming inviscid simulations for shock wave interacting with an isolated fixed sphere in a range of Mach numbers. Nagata et al. (2016) performed Direct Numerical Simulations for subsonic and supersonic flows for Mach numbers between 0.3 and 2 and Reynolds numbers between 50 and 300. An adiabatic wall boundary condition was imposed on the surface of the sphere. They observed an increase in the quasi-steady drag with Mach number. Moreover, the total drag coefficient at supersonic values was much higher than the incompressible values at the same Reynolds number.

The unsteady fluctuation in the wake of the particle also became weak as the separation point moved further downstream.

In an extension of their previous study, Nagata et al. (2018) performed Direct Numerical simulations for viscous flow around a particle in a similar range of Reynolds and Mach numbers but with the particle temperature fixed. In their work, they studied the effect of Reynolds number, Mach number, and the imposed Temperature Ratio on the wake stability, drag, and heat transfer. Their study suggested that higher temperature ratios stabilized the wake and increased the drag coefficient. The behavior of Nusselt numbers depended heavily on the local flow conditions based on the imposed non-dimensional parameters and showed a more complex trend. More recently, Osnes and Vartdal (2022) performed particle-resolved large eddy simulations in a boundary-fitted grid for shock-wave interacting with a fixed particle for Reynolds numbers between 100 to 1000 and shock Mach numbers between 1.22 and 2.51. They concluded that the existing inviscid unsteady force models produced significant errors in supercritical flow conditions and emphasized the need for improvement in the models.

2.3.2 Compressible flow around multiple particles

Experimental efforts

Multiple experiments have been performed for shock-wave interaction with a multi-particle system. For a shock wave interacting with a fixed particle array, it was shown experimentally by Sommerfeld (1985) that the incident shock wave attenuates as it passes through a particle array by energy and momentum exchange with the solid phase. The attenuation was observed to be stronger at higher particle mass loading. Later, Wagner et al. (2012b) performed experiments for shock wave interaction with a dense particle array in a shock tube at a range of shock Mach numbers. Using a high-speed Schlieren imaging system, they visualized the transmitted and reflected shock waves along with a spread of the curtain by shock-wave impingement. They attributed the spread of the curtain to the streamwise variation of the total drag force experienced by the particles. Theofanous et al. (2016) also performed a

similar experiment, studied the particle clouds' dispersal characteristics, and provided scaling laws for the positions of the upstream and downstream front of the particle curtain. The scaling laws were further improved using volume fraction corrections in DeMauro et al. (2019). More recently, Daniel and Wagner (2022) provided a new scaling method based on force balance and experimentally measured pressure differentials inside the curtain, which provided the closest fit compared to the existing scaling laws. The mentioned experiments have observed that the curtain width spread faster at higher shock Mach numbers and lower particle-to-fluid density ratios. From the experiments of Theofanous et al. (2016), it is observed that an increase in initial curtain width reduced the rate of curtain spread. Through a pulse-burst PIV method, jetting structures downstream of the dispersing particle curtain were observed by DeMauro et al. (2017). These jetting structures were attributed to the favorable pressure gradient across the curtain. They also observed unsteadiness in the mean drag, which could be explained by the decrease in the magnitude of the pressure gradient with time as the curtain width expanded. Theofanous et al. (2018) in their experiments, observed the choking behavior downstream of particle-curtain followed by flow-expansion.

Dusty-gas approaches

The attenuation of the incident shock is also predicted by dusty gas approaches Marble (1970), in which the entire mixture is considered a single phase with modified properties. Through their approach, Miura et al. (1982) predicted that if the particle mass loading was sufficiently high, the incident shock wave could decay to a Mach wave and become fully dispersed. Further studies in shock wave attenuation using this approach were performed by Olim et al. (1990) and Aizik et al. (1995). The dusty gas approaches are closed using models for drag and heat transfer coefficients, which can be provided by accurate particle-resolved and boundary-conforming numerical simulations.

Numerical simulations

Inviscid numerical simulations have been performed previously to study the effect of indirect particle-particle interactions in an assembly of spheres (Sridharan et al. 2015, Mehta et al. 2016a, Mehta et al. 2016b). Recently, particle

resolved Direct Numerical Simulations (PR-DNS) for shock-particle array interactions have provided deeper insight into the flow dynamics and nature of particle forces and heat transfer. Mehta et al. (2019) performed boundary conforming inviscid numerical simulations for shock waves at $Ma_s = 1.22$, 1.66, and 3 interacting with a random array of fixed particles. The attenuation of the peak drag force was observed at all shock Mach numbers along the streamwise direction. This effect was more pronounced at higher shock Mach numbers and higher volume fractions. A large variance in particle drag and lift forces was also observed, which seemed to increase with solid volume fraction. Vartdal and Osnes (2018) also performed particle-resolved large eddy simulations at different Mach numbers, Reynolds number of $\mathcal{O}(10^3)$ and solid volume fractions for a shock wave traversing a random array of particles and observed that the fluctuating kinetic energy could be as high as two-thirds of the mean value inside the curtain. In addition, they compared a simplified 1D model for the shock wave interacting with the particle array, where they used the particle forces from their actual three-dimensional computations. In their later work (Osnes et al. 2019), they provided a model for Pseudo-turbulent Reynolds stresses. The Reynolds stresses were defined as the single-point, Favre-averaged velocity fluctuation correlations and given by $R_{ij} = \widetilde{u_i'' u_j''}$, where $\widetilde{(\cdot)}$ represents the Favre-average evaluated in streamwise x-slabs of specified bin-width and u_i'' and u_j'' are the spatial fluctuations of the velocity components with respect to the Favre-average. They concluded that the Reynolds stresses computed in their viscous simulations were much higher than the inviscid simulations, and their gradients were substantial at the edges of the particle curtain. They also observed that the shock wave attenuation and the strength of the reflected shock wave increased with decreasing Reynolds number (Osnes et al. 2020). Initial data for compressible flow over a homogenous array of randomly distributed particles were provided by Khalloufi and Capecelatro (2023), and the data set was later expanded by Osnes et al. (2023). Their work concluded that the drag coefficient increased, and the critical Mach number for achieving sonic conditions decreased with solid volume fraction.

2.4 Modeling efforts

The hydrodynamic force experienced by a particle in a flow can be split into the quasi-steady drag force, force due to the existing stress-gradients, added mass force, and the viscous unsteady force (or the history force). The contributions of each of these terms in the context of compressible flows were provided by Parmar et al. (2011) and Parmar et al. (2012) and are summarized in eq. (6.25). The physical significance of the different force contributions for a single particle in an inviscid setup for an isolated particle were discussed by Behrendt et al. (2022) and are discussed briefly. The quasi-steady force contribution for an isolated particle in inviscid flows depends on the relevant flow-structures at late times. Hence, it will drop to zero for subcritical flows (post shock Mach number less than 0.6), but will remain non-zero for supercritical flows due to the presence of bow-shocks. In viscous flows, the quasi-steady force on a particle will additionally have a Reynolds number dependence, or in multi-particle setups, an additional volume fraction dependence. The stress-gradient force contribution depends on the local pressure and viscous-stress gradients in the flow. The added-mass contribution for a particle depends on the acceleration of the undisturbed ambient flow, which results in virtual enhancement of the particle inertia. In inhomogeneous multi-fixed-particle setups, as will be later observed in chapter 6, the added-mass contribution remains non-zero at late times due to the non-zero velocity/pressure-gradients inside the particle cloud. The viscous unsteady contributions or the history forces depend on the time history of volume-averaged or surface-averaged quantities.

The quasi-steady drag models for incompressible flows have been provided by Schiller and Naumann (1933) and Clift and Gauvin (1971a). The drag coefficient on the particle in a compressible flow is more complicated, as it is affected by the Reynolds number, Mach number, and the temperature boundary conditions on the sphere's surface. The compressibility effect on the drag coefficient of an isolated sphere can be explained as follows. As the Mach number increases from 0.3 to a critical value of 0.6, a weak dependence of the quasi-steady drag coefficient on the Mach number is observed, increasing slowly

with the Mach number. For supercritical but subsonic flows ($0.6 < Ma < 1$), the drag coefficient increases rapidly with Mach number due to the presence of shocklets, which enhances the inviscid contribution to the quasi-steady drag. A standing bow shock is formed upstream of the particle for supersonic flows, resulting in a non-zero contribution to the sphere's drag coefficient by inviscid mechanisms at late times.

Efforts have been made previously to include the compressibility effects in drag models. Henderson (1976) provided drag correlations for subsonic and supersonic flows (at $Ma > 1.75$), including rarefied flows, and interpolated the data between $1 < Ma < 1.75$. Loth (2008) later provided drag correlations for compression-dominated ($Re > 45$) and rarefaction-dominated ($Re < 45$) flows. Although they considered the temperature ratio effects in the rarefaction-dominated region, they neglected it for the compression-dominated region. However, it is known from the particle-resolved DNS of Nagata et al. (2018) that the temperature ratio can play a major role even in the compression-dominated flow regime ($Re > 45$). Parmar et al. (2010) assessed the existing drag models of Henderson (1976) and Loth (2008) and concluded that the models did not yield accurate results in the transonic regime. They also provided improved drag correlations by dividing the Mach number range into subcritical ($Ma < 0.6$), intermediate, and supersonic regimes. Their correlations were based on the experiments of Bailey and Starr (1976) and existing incompressible drag models of Clift and Gauvin (1971b). Loth et al. (2021) developed updated drag correlations using available particle-resolved DNS and experimental data. However, adiabatic boundary conditions were assumed in their correlations. A more generalized drag correlation for spheres valid for a range of Reynolds numbers, Mach numbers, Knudsen numbers, and Temperature Ratios was provided by Singh et al. (2022).

The model for the drag coefficient for an isolated particle given by Loth et al. (2021) is briefly discussed here. Their correlations were a function of the Reynolds number (Re) and the Mach number (Ma) and were obtained by separating the flow into compression ($Re > 45$) and rarefaction ($Re < 45$) dominated regimes. At $Re = 45$, their suggested drag coefficient was independent of the Ma. In the compression, dominated regime, the drag was observed

to increase with the Mach numbers. Consequently, the compressibility effects in the compression-dominated region was incorporated in their work in a modified Clift-Gauvin drag expression as shown in eq. (2.7).

$$
\begin{aligned}
C_D &= \frac{24}{Re}(1+0.15Re^{0.687})H_M \\
&\quad + \frac{0.42C_M}{1+(42500/Re^{1.16C_M})+(G_M/Re^{0.5})} && \text{for} \quad 45 < Re < Re_{crit} \\
G_M &= 166Ma^3 + 3.29Ma^2 - 10.9Ma + 20 && \text{for} \quad Ma < 0.8 \\
&= 5 + 40Ma^{-3} && \text{for} \quad Ma < 0.8 \\
H_M &= 0.0239Ma^3 + 0.212Ma^2 - 0.074Ma + 1 && \text{for} \quad Ma < 1 \\
&= 0.93 + \frac{1}{3.5 + Ma^5} && \text{for} \quad Ma > 0.8
\end{aligned}
\tag{2.7}
$$

$$
\begin{aligned}
C_D &= \frac{C_{D,Kn,Re}}{1+Ma^4} + \frac{Ma^4 C_{D,fm,Re}}{1+Ma^4} && \text{for} \quad Re \leq 45 \\
J_M &= 2.26 - \frac{0.1}{Ma} + \frac{0.14}{Ma^3} && \text{for} \quad Ma \leq 1 \\
&= 1.6 + \frac{0.25}{Ma} + \frac{0.11}{Ma^2} + \frac{0.44}{Ma^3} && \text{for} \quad Ma > 1 \\
C_{D,fm,Re} &= \frac{C_{D,fm}}{1+[(C_{D,fm}/J_M)-1]\sqrt{Re/45}} \\
C_{D,fm} &= \frac{(1+2s^2)\exp(-s^2)}{s^3\sqrt{\pi}} \\
&\quad + \frac{(4s^4+4s^2-1)\mathrm{erf}(s)}{2s^4} + \frac{2}{3s}\sqrt{\pi} \\
s &= Ma\sqrt{\gamma/2} \\
C_{D,Kn,Re} &= \frac{24}{Re}(1+0.15Re^{0.687})f_{Kn} \\
f_{Kn} &= \frac{1}{1+Kn[2.514+0.8\exp(-0.55/Kn)]}
\end{aligned}
\tag{2.8}
$$

In the rarefaction dominated region, the Knudsen number effects (defined in eq. (2.9)) were observed as important in the evaluation of the drag coefficient. The increasing rarefaction effects in general resulted in a decreasing drag by the sphere. This was incorporated in the correlation for $Re < 45$ range as shown in eq. (2.8). In the equations, $C_{D,fm,Re}$ and J_M expressions are based on the assumption that the gas and the particle temperatures are equal.

Although the existing drag models considered the steady state forces, the unsteady forces on the particle due to the local flow acceleration had not been considered. It is known from the experiments of Sun et al. (2005) that the unsteady drag on a sphere due to shock-wave impingement could be an order of magnitude higher than the steady-state values. Hence, newer models were needed to capture the unsteady forces on the particles. Eames et al. (2008) provided an expression for the inviscid unsteady force on spheres in the subcritical limit ($Ma < 0.6$). They found that the added mass coefficient scaled as $C_M \propto 1 + Ma^2 + \mathcal{O}(Ma^4)$. In their later work (Parmar et al. 2009), they extended their work to a simple model for shock-wave interacting with a fixed sphere. In their model, they considered the quasi-steady, pressure-gradient, and added mass contributions while neglecting the unsteady viscous contributions. In their later works (Parmar et al. 2011, Parmar et al. 2012), the viscous unsteady effects were also considered, and complete force models for compressible flows were provided. Later, Annamalai and Balachandar (2017) provided a time-dependent Faxén form of forces on the particles for inhomogeneous, viscous, compressible flows in the limit of zero Reynolds and Mach numbers.

It has been observed experimentally and numerically that the forces experienced by a particle in the presence of other neighboring particles can significantly vary compared to when it is isolated (Akiki et al. 2017). Based on the force and heat transfer models of Ling et al. (2011), Parmar et al. (2011), and Parmar et al. (2012), Ling et al. (2012) suggested a simplified eulerian-lagrangian one-dimensional model for shock-wave interaction with a particle array. Quasi-steady drag correlations for compressible flow through an array of fixed particles have only started to come up recently for quasi-steady forces in streamwise and transverse directions (Osnes et al. 2023). The model

(Osnes et al. 2023) is based on the particle-resolved DNS data and depends on the flow's Reynolds number, Mach number, and volume fraction. It should be noted that their drag model at a zero volume fraction corresponds to the isolated particle drag data of Loth et al. (2021) and to the incompressible finite volume fraction expression of Tenneti et al. (2011) as the Mach number tends to zero. Since the drag model of Loth et al. (2021) assumes that the flow is in thermal equilibrium with its surroundings, their force correlations are expected to provide significant errors when the temperature ratio between the particle and freestream conditions is not equal to unity. In addition to the models for force coefficients, correlations have also been provided by Osnes et al. (2023) for streamwise force fluctuations by providing Mach corrections to the incompressible correlation of Lattanzi et al. (2022).

The literature on compressibility effects on heat transfer between spheres and surrounding fluid is more limited. Sauer (1951) provided a Nusselt number correlation for spheres in rarefied flows using kinetic theory in monoatomic and diatomic fluids. Fox et al. (1978) provided Nusselt number correlation through their experiments involving the ignition of magnesium powders using shock waves. Unsteady heat transfer models for a sphere were provided by Ling et al. (2011). They used the available force models from Parmar et al. (2012), quasi-steady Nusselt correlations of Fox et al. (1978), and their provided unsteady heat transfer model to analyze shock-wave interaction with an isolated particle. More recently, Ling et al. (2016) used a scaling analysis to understand the relative importance of unsteady heat-transfer terms.

2.5 Knowledge gaps

In the previous sections, the historical development in compressible flows was reviewed, and the current state of research in compressible single and particulate flows was discussed. Experiments for detailed study of compressible particulate flows are difficult owing to the sensitivity of the experimental conditions and the small timescales associated with the propagation of acoustic waves in the flow. Hence, the complex interactions between the solid and the

fluid phase are currently difficult to analyze experimentally. The available experimental studies have not characterized the combined effects of Reynolds numbers (Re), Mach numbers (Ma), particle-to-fluid Temperature ratios (TR), and Knudsen numbers (Kn) on the momentum and heat exchange between the solid and fluid phases in detail. The Knudsen number is the ratio of the mean free path of molecular collisions to the particle diameter and proportional to Ma/Re (Loth et al. 2021). Kn is defined in eq. (2.9).

$$Kn = \sqrt{\frac{\pi\gamma}{2}}\frac{Ma}{Re} \tag{2.9}$$

Recently, particle-resolved Direct Numerical Simulations have aided in developing drag and heat transfer coefficients for spheres in compressible flows. It was realized that although significant improvement in drag correlations for compressible flow over isolated spherical particles has been made at a range of Reynolds numbers, Mach numbers, and Temperature ratios, quasi-steady drag correlations considering the effects of local temperature gradients in multi-particle systems are not available.

The correlations for quasi-steady Nusselt numbers are more limited. As seen from the particle-resolved DNS of Nagata et al. (2018), the Nusselt number in the presence of compressibility effects can be strongly influenced by the local temperature gradients between the sphere and the surrounding medium. To the extent of the author's knowledge, no available Nusselt number correlations currently exist that consider the combined effect of the Mach number, Reynolds number, and the temperature ratio between the particle and the freestream conditions on the heat transfer behavior. In addition, no Nusselt number correlations are available with compressibility effects in particle clouds.

Although shock-wave interaction with a particle array of finite width has been studied extensively in the past decade through boundary-conforming and particle-resolved numerical simulations, most of the studies focus on the transient on a time scale of the order of shock-particle array interaction. Moreover, the nature of the flow in the wake of the particle curtain has not

been thoroughly investigated. In addition, the available particle-resolved numerical simulations do not comment on the nature of heat exchange between the solid and fluid phases in multi-particle systems in non-adiabatic conditions.

2.6 Objectives and scope of research

In the current work, the newly developed compressible DNS multiphase flow solver with diffuse-interface immersed boundary method is validated for single-phase and multi-phase tests based on available analytical data or reference solutions. Particle-resolved Direct Numerical Simulations for compressible flow around an isolated particle and through an array of homogenously distributed or finite array of fixed particles are performed in a limited range of Reynolds numbers, Mach numbers, volume fractions, and Temperature Ratios. The mean drag coefficients and force fluctuations are computed and compared to the available models or particle-resolved DNS data for flow through a homogenously distributed or finite-width array of particles. The local Nusselt numbers are computed for the particles inside the array for multi-particle systems, and their variation with Mach numbers is analyzed. The wake region behind a particle array of finite width in viscous compressible flow is studied at late times for a range of Mach numbers at a fixed Reynolds number. In addition, the localized flow near the particles inside the particle array is analyzed using particle-conditioned or localized flow averaging.

3 Mathematical Framework

3.1 Governing equations of the fluid phase

In this section, the compressible Navier-Stokes equations are derived from the fundamental equations of mass, momentum, and energy conservation. These equations are stated in the integral and differential forms. The differential and integral forms of the equations are valid for fluid as a continuum. The integral form also applies to a control volume (a fixed region in space) or a material volume (whose boundary moves with the fluid, resulting in fixed mass). The fluid is assumed to be Newtonian and isotropic and to satisfy Stokes' hypothesis.

Reynolds Transport Theorem

Consider a material volume $\mathscr{V}(t)$ in a region that moves with the local fluid velocity. Given the local fluid velocity $\mathbf{u}$, the Reynolds Transport Theorem for a tensor $\mathscr{T}(x, y, z, t)$ defined in that region is given by eq. (3.1). Derivation of the Reynolds Transport Theorem is given in (Kundu et al. 2015).

$$\frac{\mathrm{d}}{\mathrm{d}t}\int_{\mathscr{V}(t)} \mathscr{T}(x, y, z, t)\ \mathrm{d}\mathscr{V} = \int_{\mathscr{V}(t)} \frac{\partial \mathscr{T}}{\partial t}\ \mathrm{d}\mathscr{V} + \int_{\mathscr{A}(t)} \mathrm{d}\mathscr{A} \cdot \mathbf{u}\,\mathscr{T} \tag{3.1}$$

Conservation of mass

Using the Reynolds Transport Theorem in section 3.1, and replacing the tensor $\mathscr{T}$ with the density of the fluid $\rho(x, y, z, t)$, we obtain

$$\frac{\mathrm{d}}{\mathrm{d}t}\int_{\mathscr{V}(t)} \rho(x,y,z,t)\,\mathrm{d}\mathscr{V} \;=\; \int_{\mathscr{V}(t)} \frac{\partial \rho}{\partial t}\,\mathrm{d}\mathscr{V} + \int_{\mathscr{A}(t)} \mathrm{d}\mathscr{A}\cdot\mathbf{u}\,\rho \tag{3.2}$$

Now, using the Gauss divergence theorem for the last term in eq. (3.2) and simplifying, we obtain the mass conservation equation in the integral form as follows

$$\int_{\mathscr{V}(t)} \left(\frac{\partial \rho}{\partial t} + \nabla\cdot\rho\,\mathbf{u} \right) \mathrm{d}\mathscr{V} = 0 \tag{3.3}$$

Since the integral in eq. (3.3) should vanish for any arbitrary volume, it must also vanish at a point in the limit of an infinitesimally small volume. Using this information, the mass conservation equation in the differential form can be obtained and is given in eq. (3.4).

$$\frac{\partial \rho}{\partial t} + \nabla\cdot\rho\mathbf{u} = 0 \tag{3.4}$$

Conservation of momentum

Consider the Cauchy-momentum equation eq. (3.5). This equation can be derived from the concepts of force balance and stresses at a point or by using the Reynolds' Transport Theorem. A detailed derivation can be obtained from (Kundu et al. 2015).

$$\rho\frac{\mathrm{d}u_i}{\mathrm{d}t} = \rho f_i \;+\; \frac{\partial \tau_{ji}}{\partial x_j} \tag{3.5}$$

In eq. (3.5), τ_{ji} is the total stress tensor, and f_i is the body force per unit volume. Based on the rotational equilibrium of the fluid element under consideration, $\tau_{ij} \;=\; \tau_{ji}$ can be assumed. In addition, a constitutive relation between the stress tensor and the fluid element deformation reads

$$\tau_{ij} \;=\; -p\delta_{ij} \;+\; 2\mu d_{ij} \;+\; \lambda\delta_{ij}\frac{\partial u_k}{\partial x_k} \tag{3.6}$$

The eq. (3.6) is based on the assumption that the fluid is isotropic and Newtonian. $d_{ij} = \frac{1}{2}\left(\frac{\partial u_i}{\partial x_j} + \frac{\partial u_j}{\partial x_i}\right)$ is the strain rate tensor, μ is the first coefficient of viscosity, μ_b is the coefficient of bulk viscosity, and $\lambda = \mu_b - 2\mu/3$. Using the Stokes' hypothesis (setting μ_b to zero), the constitutive equation simplifies to

$$\tau_{ij} = -p\delta_{ij} + 2\mu d_{ij} - \frac{2\mu}{3}\delta_{ij}\frac{\partial u_k}{\partial x_k} \tag{3.7}$$

Substituting the eq. (3.7) in the eq. (3.5) and simplifying along with the mass conservation equation, we obtain the momentum equations for the compressible flow

$$\frac{\partial}{\partial t}(\rho u_i) + \frac{\partial}{\partial x_j}(\rho u_i u_j) + \frac{\partial p}{\partial x_i} = \frac{\partial \sigma_{ji}}{\partial x_j} + \rho f_i \tag{3.8}$$

Where $\sigma_{i,j}$ is the deviatoric stress tensor arising from the non-isotropic component of the total stress based on the fluid motion and is defined in eq. (3.9). The eq. (3.8) does not assume a constant viscosity and hence allows for the inclusion of different temperature-dependent viscosity laws.

$$\sigma_{ij} = 2\mu d_{ij} - \frac{2\mu}{3}\delta_{ij}\frac{\partial u_k}{\partial x_k} \tag{3.9}$$

Conservation of energy

The equation for energy conservation can be derived from the direct application of the first law of thermodynamics, which states that the rate of change of the total energy is the sum of the rate of the heat addition and the work done on a material volume. Let e represent the internal energy per unit mass. Then, the total energy per unit volume reads

$$E = \rho\left(e + \frac{1}{2}|\mathbf{u}|^2\right) \tag{3.10}$$

Then, using the first law of thermodynamics in the integral form can be stated as follows

$$\frac{\mathrm{d}}{\mathrm{d}t}\int_{\mathscr{V}} \rho\left(e + \frac{1}{2}u_i^2\right)\mathrm{d}\mathscr{V} = \int_{\mathscr{V}} \rho f_i u_i \,\mathrm{d}\mathscr{V} + \int_{\mathscr{A}} \tau_{ji} u_i \,\mathrm{d}\mathscr{A}_j - \int_{\mathscr{A}} q_i \,\mathrm{d}\mathscr{A}_i \quad (3.11)$$

q_i is the heat flux through the control surface. Using the Gauss divergence theorem to convert the surface integrals to volume integrals and assuming that the fluid medium is a continuum, the eq. (3.11) can be written in differential form

$$\rho\frac{\mathrm{d}}{\mathrm{d}t}\left(e + \frac{1}{2}u_i^2\right) = \rho f_i u_i + \frac{\partial}{\partial x_j}(\tau_{ji}u_i) - \frac{\partial q_i}{\partial x_i} \quad (3.12)$$

By using the concept of material derivatives and the eq. (3.10) along with the mass conservation equation given by eq. (3.4), we obtain the equation for the conservation of energy in differential form

$$\frac{\partial E}{\partial t} + \frac{\partial}{\partial x_j}\left[\, u_j(E+p)\,\right] = \rho f_i u_i + \frac{\partial}{\partial x_j}(\sigma_{ji}u_i) - \frac{\partial q_i}{\partial x_i} \quad (3.13)$$

where σ_{ji} is given by eq. (3.9) and q_i is the local heatflux density along the i_{th} direction. Finally, the equations of the state and heat transfer are used to close the system

Equation of state

The equation of state relates the internal energy of the fluid to the pressure and density. For a calorically ideal gas, it reads as

$$e = \frac{p}{(\gamma-1)\rho} \quad (3.14)$$

Equation of heat transfer

In the present work, it is assumed that the fluid obeys Fourier's law of heat conduction given by

$$q_i = -\kappa \frac{\partial T}{\partial x_i} \tag{3.15}$$

In eq. (3.15), κ is the thermal conductivity of the fluid. The thermal conductivity κ and the dynamic viscosity μ are related as

$$\kappa = \frac{\mu C_p}{Pr} \tag{3.16}$$

Pr is the Prandtl number, and C_p is the heat capacity at constant pressure. The Prandtl number is the ratio of momentum and thermal diffusivities and is a relative measure of momentum and thermal boundary layer thicknesses. The equations of conservation of mass, momentum, and energy, along with the equations of state and heat transfer, close the governing equations for fluid.

4 Numerical Framework

The compressible Navier Stokes equations described in chapter 3 do not have an analytical solution. These equations can be solved analytically only for certain flow problems and with added assumptions and simplifications. Hence, the governing equations need to be computed on a machine with numerical approximations of the different terms to obtain the relevant flow information. A numerical technique must be chosen with approximations to the advection, diffusion, and time integration terms based on the different spatial and temporal scales of the flow problem. The current work uses a Direct Numerical Simulation (DNS) approach for solving the compressible Navier Stokes equations, i.e., all relevant spatial and temporal scales are handled directly by the discretization procedure, and no additional models or assumptions are introduced.

4.1 Single phase simulations

Let the compressible Navier-Stokes equations described in chapter 3 in differential form be written as follows

$$\mathbf{U}_t + \mathbf{F}^{(x)}(\mathbf{U})_x + \mathbf{F}^{(y)}(\mathbf{U})_y + \mathbf{F}^{(z)}(\mathbf{U})_z = \mathbf{Q} \tag{4.1}$$

In the eq. (4.1), $\mathbf{F}^{(x)}, \mathbf{F}^{(y)}, \mathbf{F}^{(z)}$ are the fluxes along x, y, z directions respectively on a 3D cartesian grid, $\mathbf{U}$ is the vector of conserved variables, and $\mathbf{Q}$ is the vector of source terms. The numerical fluxes, in turn, are the sum of contributions from convective and viscous effects

$$\mathbf{F}^{(x)} = \begin{pmatrix} \rho u \\ \rho u^2 + p - \sigma_{11} \\ \rho uv - \sigma_{21} \\ \rho uw - \sigma_{31} \\ u(E+p) - (\sigma_{11}u + \sigma_{12}v + \sigma_{13}w) + q_1 \end{pmatrix} \tag{4.2}$$

$$\mathbf{F}^{(y)} = \begin{pmatrix} \rho v \\ \rho vu - \sigma_{12} \\ \rho v^2 + p - \sigma_{22} \\ \rho vw - \sigma_{32} \\ v(E+p) - (\sigma_{21}u + \sigma_{22}v + \sigma_{23}w) + q_2 \end{pmatrix} \tag{4.3}$$

$$\mathbf{F}^{(z)} = \begin{pmatrix} \rho w \\ \rho wu - \sigma_{13} \\ \rho wv - \sigma_{23} \\ \rho w^2 + p - \sigma_{33} \\ w(E+p) - (\sigma_{31}u + \sigma_{32}v + \sigma_{33}w) + q_3 \end{pmatrix} \tag{4.4}$$

Furthermore, the vector of conservative variables $\mathbf{U}$ and the vector of source terms $\mathbf{Q}$ are written as

$$\mathbf{U} = \begin{pmatrix} \rho \\ \rho u \\ \rho v \\ \rho w \\ E \end{pmatrix}, \qquad \mathbf{Q} = \begin{pmatrix} 0 \\ \rho f_1 \\ \rho f_2 \\ \rho f_3 \\ \rho f_4 \end{pmatrix} \tag{4.5}$$

$\rho f_1, \rho f_2, \rho f_3, \rho f_4$ are the source terms for the x, y, z momentum equations and the total energy equation respectively. The source terms arise from the presence of the dispersed phase and are described in detail in section 4.3.

4.1.1 Time integration

The current work uses the 3^{rd} order low-storage Runge Kutta method, which has previously been used by Rai and Moin (1991), Spalart et al. (1991), and Verzicco and Orlandi (1996) for time stepping. The convective and diffusive terms in the governing equations are handled explicitly. The time discrete form of the governing equations is written as

$$\begin{aligned} \mathbf{U}^{(k)} \;=\; \mathbf{U}^{(k-1)} \;&-\; \gamma_k \,\Delta t\, \mathscr{L}_\Delta(\,\mathbf{U}^{(k-1)}\,) \\ &-\; \zeta_k \,\Delta t\, \mathscr{L}_\Delta(\,\mathbf{U}^{(k-2)}\,) \;+ \Delta t\, \mathbf{Q}, \qquad \forall k \in 1,2,3 \end{aligned} \tag{4.6}$$

where $\mathscr{L}_\Delta(\,\mathbf{U}\,)$ is the discrete spatial operator is approximated as

$$\begin{aligned} \mathscr{L}_\Delta(\,\mathbf{U}\,)_{i,j,k} \;\approx\; &\frac{1}{\Delta x}\left(\,\mathscr{F}^{(x)}_{i+1/2,\,j,\,k} \;-\; \mathscr{F}^{(x)}_{i-1/2,\,j,\,k}\,\right) \\ &+ \frac{1}{\Delta y}\left(\,\mathscr{F}^{(y)}_{i,\,j+1/2,\,k} \;-\; \mathscr{F}^{(y)}_{i,\,j-1/2,\,k}\,\right) \\ &+ \frac{1}{\Delta z}\left(\,\mathscr{F}^{(z)}_{i,\,j,\,k+1/2} \;-\; \mathscr{F}^{(z)}_{i,\,j,\,k-1/2}\,\right) \end{aligned} \tag{4.7}$$

In the eq. (4.7), $\mathscr{F}$ is the numerical flux function approximated from the physical flux function $\mathbf{F}$ and is described in section 4.1.2. During the time stepping procedure between t^n and t^{n+1}, the Runge Kutta procedure is initialized and terminated with the following equations

$$\mathbf{U}^{(0)} \;=\; \mathbf{U}(t^n), \qquad \mathbf{U}(t^{n+1}) \;=\; \mathbf{U}^{(3)} \tag{4.8}$$

It ensures that one needs to store the flow fields only at a single time level to restart the simulation. γ_k and ζ_k are the Runge Kutta coefficients and are chosen to ensure third-order temporal accuracy for smooth flows

$$\gamma_k = \left[\frac{8}{15}, \frac{5}{12}, \frac{3}{4}\right], \qquad \zeta_k = \left[0, \frac{-17}{60}, \frac{-5}{12}\right] \tag{4.9}$$

4.1.2 Advection scheme

Many compressible flow problems involve solving the hyperbolic conservation laws like the inviscid Euler's equations or the compressible Navier Stokes equations at high Reynolds and Mach numbers. In such cases, discontinuities, shock waves, or regions of high gradients can exist in the solutions. In addition, such flows may involve a wide range of time and length scales. Hence, it is crucial to resolve the range of length scales stably and capture the sharp gradients or shock waves present in the flow by reducing the amount of numerical dissipation. Considerable efforts have been made in the past to develop numerical methods suitable for such a category of fluid flow problems. Some of the popular methods include essentially non-oscillatory (ENO) schemes (Harten et al. 1997), artificial viscosity methods (VonNeumann and Richtmyer 1950), weighted essentially non-oscillatory (WENO) methods (Jiang and Shu 1996, Shu 2016, Borges et al. 2008), and more recently the targeted essentially non-oscillatory (TENO) based schemes (Fu et al. 2016, Takagi et al. 2022, Liang et al. 2022).

The current work uses a 5^{th} order finite-difference WENO scheme (Shu 2016) abbreviated as WENO-JS, a 5^{th} order TENO scheme (Liang et al. 2022), or a finite difference scheme on the entire large stencil based on the union of the smaller stencils used in WENO-JS or TENO for numerical discretization of the advection term. The choice of the advection scheme is specified individually in the sections corresponding to the flow problem to be studied. The WENO-JS scheme uses a weighted average of the flow stencils based on smoothness indicators to achieve the shock-capturing properties of the ENO schemes. However, previously, it has been observed that it introduces excessive numerical dissipation (Zhao et al. 2014, Martin 2000) and may perform unsatisfactorily in the presence of multiple shocks adjacent to each other (Titarev and Toro 2004). The TENO schemes approach these problems by following an ENO-like

stencil selection. A candidate stencil is either selected with optimal weight in the smooth regions of the flow or entirely disregarded in the presence of discontinuities, leading to suppressed numerical dissipation while providing robust shock-capturing properties (Fu et al. 2016).

The steps for numerical discretization of the advection terms can be summarized as follows.

- First, the primitive variables at the interfaces are evaluated using an arithmetic average of the values at the adjacent grid points.
- The averaged quantities are then used to evaluate the left and right eigenvectors ($\mathbf{K}^{-1}, \mathbf{K}$) of the Jacobian matrix $\partial\mathbf{F}/\partial\mathbf{U}$ at the interface.
- The physical flux ($\mathbf{F}$) and the vector of conservative variables ($\mathbf{U}$) are recast into the characteristic space by premultiplying it with the left eigenvector matrix.

$$\begin{aligned} \mathbf{U}_{char} &= \mathbf{K}^{-1}\mathbf{U} \\ \mathbf{F}_{char} &= \mathbf{K}^{-1}\mathbf{F} \end{aligned} \tag{4.10}$$

- The positive and negative fluxes at each cell interface are obtained by a local Lax-Friedrichs flux splitting.

$$\begin{aligned} \mathbf{F}^{+}(\mathbf{U}) &= \mathbf{F}_{char} + \lambda_{max}\mathbf{U}_{char} \\ \mathbf{F}^{-}(\mathbf{U}) &= \mathbf{F}_{char} - \lambda_{max}\mathbf{U}_{char} \end{aligned} \tag{4.11}$$

  In the eq. (4.11), λ_{max} is the eigenvalue corresponding to the fastest characteristic wave associated with the states on both sides of the interface.
- The positive and the negative fluxes are then reconstructed at the cell interface using the appropriate numerical procedure (WENO-JS, TENO, or a Finite Difference approximation on the entire union of WENO/TENO sub-stencils).

$$\begin{aligned} \mathbf{F}^{+} &\rightarrow \mathbf{F}^{+}_{reconstructed} \\ \mathbf{F}^{-} &\rightarrow \mathbf{F}^{-}_{reconstructed} \end{aligned} \tag{4.12}$$

- Next, the numerical flux $\mathscr{F}$ at the interface is evaluated by recasting the flux terms into the physical space and averaging the positive and numerical fluxes at the interface.

$$\begin{aligned} \mathbf{F}^{+}_{phy} &= \mathbf{K}\mathbf{F}^{+}_{reconstructed} \\ \mathbf{F}^{-}_{phy} &= \mathbf{K}\mathbf{F}^{-}_{reconstructed} \\ \mathscr{F}(\mathbf{U}) &= \frac{1}{2}\left(\mathbf{F}^{+}_{phy} + \mathbf{F}^{-}_{phy}\right) \end{aligned} \tag{4.13}$$

- The expression for $\mathscr{F}$ in eq. (4.13) is further used to evaluate the discrete spatial operator as follows

$$\mathscr{L}_{\Delta}(\,\mathbf{U}\,) \approx \frac{\Delta\mathscr{F}^{(x)}}{\Delta x} + \frac{\Delta\mathscr{F}^{(y)}}{\Delta y} + \frac{\Delta\mathscr{F}^{(z)}}{\Delta z} \tag{4.14}$$

  Here, $\mathscr{F}^{(x)}$, $\mathscr{F}^{(y)}$, and $\mathscr{F}^{(z)}$ represent the numerical numerical fluxes corresponding to the physical fluxed given in eq. (4.1).

- Finally, $\mathscr{L}_{\Delta}(\,\mathbf{U}\,)$ is coupled with the time-stepping procedure to give the discrete form of governing equations as follows

$$\begin{aligned} \mathbf{U}^{(k)} = \mathbf{U}^{(k-1)} &- \gamma_k\,\Delta t\,\mathscr{L}_{\Delta}(\,\mathbf{U}^{(k-1)}\,) \\ &- \zeta_k\,\Delta t\,\mathscr{L}_{\Delta}(\,\mathbf{U}^{(k-2)}\,) + \Delta t\,\mathbf{Q}, \qquad \forall k \in 1,2,3 \end{aligned} \tag{4.15}$$

  Here, k represents the Runge-Kutta coefficients given in eq. (4.9)

4.1.3 Diffusion scheme

The current work uses a 2^{nd} order central difference scheme for numerical discretization of the viscous terms. The discretization of the viscous terms on

a 2D collocated grid is described in appendix B. The extension of the procedure to a 3D collocated grid is straightforward.

4.2 Boundary conditions

Characteristic wave analysis for imposing inflow-outflow boundary conditions is typical in compressible flow problems (Chan et al. 2024, Cogo et al. 2023, Baumgart and Blanquart 2023) in which the acoustic-wave reflections from the boundaries need to be minimized. It becomes essential when transient flow features occurring on a time scale comparable to the acoustic-wave reflections from the boundaries need to be studied. Some examples include the growth of shear layers (Bechert and Stahl 1988) and instabilities in turbulent combustion (Poinsot et al. 1987).

The current work chooses non-reflecting boundary conditions for inflow and outflow boundaries from Poinsot and Lele (1992). The idea is to impose the number of physical boundary conditions equivalent to the number of characteristic waves entering the system (Thompson 1987). At the same time, information within the domain is used to evaluate the remaining numerical (soft) boundary conditions. These boundary conditions are required in addition to physical boundary conditions to solve the system of equations numerically (Yee 1981). However, they are not necessarily given by the physical behavior at the boundaries. The sufficient and necessary number of physical boundary conditions that should be specified for Euler's equations has been previously studied by Oliger and Sundström (1978) and Dutt (1988) and summarised in table 4.1.

Table 4.1: Physical boundary conditions required for well-posedness of Euler's equations

Boundary type	**1D**	**2D**	**3D**
Subsonic inflow	2	3	4
Subsonic outflow	1	1	1
Supersonic inflow	3	4	5
Supersonic outflow	0	0	0

Several approaches have been adopted previously regarding the specification of numerical boundary conditions. Some of the common approaches include extrapolation (Grinstein et al. 1987), compatibility equations based on the conservation equations (Poinsot and Lele 1992), and inverse Lax-wendroff schemes (Tan and Shu 2010).

Unless specified otherwise, the number of physical boundary conditions are imposed in the current work based on characteristic wave analysis by Thompson (1987). The non-reflection property at the subsonic inflow-outflow boundaries is based on the works of Poinsot and Lele (1992). The remaining soft boundary conditions are implemented using extrapolation similar to the works of Grinstein et al. (1987) and Yee (1981). Since the current work uses ghost cells at the boundary, the Mach number at the inflow or outflow plane is checked locally, and subsequently, an appropriate boundary condition is implemented to fill up the ghost cells. The following sections briefly explain the implementation of the inflow/outflow boundary conditions used in the present work.

4.2.1 Supersonic inflow

If the local Mach number exceeds one ($Ma > 1$), a supersonic inflow boundary condition is chosen at the inflow plane, and all the primitive variables are imposed.

$$\rho = \rho_{\text{imposed}} \qquad w = w_{\text{imposed}}$$
$$u = u_{\text{imposed}} \qquad p = p_{\text{imposed}}$$
$$v = v_{\text{imposed}}$$

4.2.2 Supersonic outflow

If the local Mach number at the outflow plane exceeds one ($Ma > 1$), then all the primitive variables at the ghost cells are filled up by nearest neighbor extrapolation (zeroth order).

$$\rho = \rho_{\text{extrapolated}} \qquad w = w_{\text{extrapolated}}$$
$$u = u_{\text{extrapolated}} \qquad p = p_{\text{extrapolated}}$$
$$v = v_{\text{extrapolated}}$$

4.2.3 Subsonic inflow

The approach of Poinsot and Lele (1992) is used for implementing a non-reflecting subsonic boundary condition at the inflow. The idea is to assume a locally one-dimensional inviscid (LODI) flow at the inflow boundary by neglecting the transverse and viscous terms. The governing equations are then recast in terms of the amplitude variation of characteristic waves crossing the boundaries. Finally, the amplitude variations corresponding to the characteristic waves entering the flow domain through the inflow boundary are set to zero to enforce a non-reflecting inflow boundary condition. Following the number of physical boundary conditions in table 4.1 and the LODI relations (Poinsot and Lele 1992), the boundary conditions for pressure and density are imposed using the ordinary differential equations, while those for transverse velocity components (v, w) are directly specified. The longitudinal flow component (u) is extrapolated using the nearest-neighbor extrapolation.

$$\frac{\partial \rho}{\partial t} + \frac{\rho}{c}\left(\frac{\partial u}{\partial t}\right) = 0 \qquad w = w_{\text{imposed}}$$
$$u = u_{\text{extrapolated}} \qquad \frac{\partial p}{\partial t} + \rho c\left(\frac{\partial u}{\partial t}\right) = 0$$
$$v = v_{\text{imposed}}$$

The time-discrete form of the ODEs for pressure and density can be written by using the third-order Runge Kutta scheme from Rai and Moin (1991) as follows

$$\rho^k = \rho^{k-1} - \Delta t\left[\gamma_k\left(\frac{\rho}{c}\frac{\mathrm{d}u}{\mathrm{d}t}\right)^{k-1} + \zeta_k\left(\frac{\rho}{c}\frac{\mathrm{d}u}{\mathrm{d}t}\right)^{k-2}\right] \tag{4.16}$$

$$p^k = p^{k-1} - \Delta t \left[\gamma_k \left(\rho c \frac{\mathrm{d}u}{\mathrm{d}t} \right)^{k-1} + \zeta_k \left(\rho c \frac{\mathrm{d}u}{\mathrm{d}t} \right)^{k-2} \right] \tag{4.17}$$

4.2.4 Subsonic outflow

The approach for setting the non-reflecting boundary conditions is similar to section 4.2.3. However, only the amplitude variation of a single characteristic wave entering the domain at the outflow is set to zero. Using the LODI relations, we extrapolate the values of (ρ, u, v, w) using nearest-neighbor extrapolation while solving an ordinary differential equation for pressure (p) at the subsonic outflow boundary. The implementation can be summarised as follows

$$\rho = \rho_{\text{extrapolated}} \qquad w = w_{\text{extrapolated}}$$

$$u = u_{\text{extrapolated}} \qquad \frac{\partial p}{\partial t} - \rho c \left(\frac{\partial u}{\partial t} \right) = 0$$

$$v = v_{\text{extrapolated}}$$

The time-discrete form for the pressure ODE for the subsonic outflow boundary condition is given as follows

$$p^k = p^{k-1} + \Delta t \left[\gamma_k \left(\rho c \frac{\mathrm{d}u}{\mathrm{d}t} \right)^{k-1} + \zeta_k \left(\rho c \frac{\mathrm{d}u}{\mathrm{d}t} \right)^{k-2} \right] \tag{4.18}$$

In the eqs. (4.16) to (4.18), γ_k and ζ_k are the Runge Kutta coefficients at k^{th} Runge Kutta step. The time integration scheme details are explained in section 4.1.1.

It is to be noted that the boundary conditions described in the previous sections only consider the characteristic waves associated with the hyperbolic part of the governing equations. However, the viscous terms introduce additional waves that can travel into the flow domain from the boundaries. Consequently, additional physical boundary conditions are needed for the complete

Navier Stokes equations to account for the characteristic waves associated with the diffusion processes (Poinsot and Lele 1992). However, in cases where the final steady state is the focus or the transient flow before the wave reflections from the boundary polluting the flow need to be studied, the considered approximations serve as a good solution. Naturally, the boundary conditions also approximate flows at high Reynolds numbers well.

4.3 Multi phase simulations

Particle-resolved numerical simulations of compressible flows in two spatial dimensions have been carried out in the past (Regele et al. 2014, Xu et al. 2013). However, 2D simulations do not entirely capture the physics of the flow, such as vortex dynamics and complex wake structures. Three-dimensional boundary-conforming numerical studies are commonly performed for fluid flow problems involving fixed particles. Examples include flow around isolated fixed particles (Sun et al. 2005, Nagata et al. 2016, Nagata et al. 2018) and around fixed-particle arrays (Mehta et al. 2016b, Vartdal and Osnes 2018, Osnes et al. 2023). However, boundary-fitted simulations around mobile particles are rarely performed, especially for a large array of particles, because of the large computational overhead arising from the need for continuous remeshing. Exception to the remark is the recent work by Behrendt et al. (2022), who studied shock wave with ($Ma_s = 1.22$) interacting with an isolated mobile particle under inviscid conditions at particle-to fluid density ratios of 2 and 20 using a boundary-fitted approach. Immersed boundary methods are optimal for solving such a class of problems. The need for the computational grid to conform to the complex geometries and the requirement for continuous remeshing in mobile particle simulations is eliminated. The current work uses a diffuse interface immersed boundary method, which is an extension of the incompressible flow counterpart (Uhlmann 2005) and is described in the following section.

4.3.1 Immersed boundary method

The dispersed phase in the flow domain is represented as a solid/fluid coupling force and energy source terms, $\mathbf{Q}$ in the eq. (4.1). The source terms enforce a desired boundary condition for temperature or momentum at the solid-fluid interface.

First, a pure fluid problem is solved by neglecting the source terms in the governing equations eq. (4.1).

$$\widetilde{\mathbf{U}}^{(k)} \;=\; \mathbf{U}^{(k-1)} \;+\; f(\mathbf{U}^{(k-1)},\mathbf{U}^{(k-2)}) \tag{4.19}$$

$\widetilde{\mathbf{U}}^{(k)}$ is the preliminary conservative flow field obtained by disregarding the presence of the dispersed phase at the k^{th} Runge Kutta step. The preliminary field does not satisfy the constraints of the solid-fluid interface. f is the time-discrete form of the pure fluid problem given by

$$f(\mathbf{U}^{(k-1)},\mathbf{U}^{(k-2)}) \;=\; -\gamma_k\,\Delta t\,\mathscr{L}_\Delta(\,\mathbf{U}^{(k-1)}\,) \;-\; \zeta_k\,\Delta t\,\mathscr{L}_\Delta(\,\mathbf{U}^{(k-2)}\,) \tag{4.20}$$

Where $\mathscr{L}_\Delta$ is the discrete spatial operator given in eq. (4.7). A primitive preliminary field is calculated from the preliminary conservative field comprised of the fluid density, velocities, and internal energy

$$\widetilde{\mathbf{V}} \;=\; (\,\tilde{\rho},\tilde{u},\tilde{v},\tilde{w},\tilde{e}\,) \tag{4.21}$$

First, the spherical particles constituting the dispersed phase are resolved uniformly using lagrangian force point locations throughout the volume. Then, the flow field at the lagrangian marker positions is forced appropriately to calculate the source terms. Finally, the preliminary flow field $\widetilde{\mathbf{V}}$ is updated by adding these source terms.

The discretization details for the outermost shell of a spherical particle are explained in (Uhlmann 2005). The current procedure, however, considers multiple shells extending from the boundary to the sphere center for discretization of the lagrangian markers. An approach for distributing

lagrangian force points inside the interior was also adapted by Moriche et al. (2021) for spheroids. The reason for the modification is that in the current compressible setting, allowing the flow to develop inside the particle volume freely leads to strong pressure waves that might pollute the exterior flow. Hence, the spheres constituting the dispersed phase should be considered rigid in the current work. The details of the sphere volume discretization are explained again in appendix D for completeness.

After discretizing the dispersed phase, the preliminary primitive field is interpolated from the Eulerian grid ($x_{i,j,k}$) to the lagrangian force point locations ($\mathbf{X}_l^{(m)}$), using a discrete delta function δ_h (Roma et al. 1999).

$$\widetilde{\mathbf{V}}(\,\mathbf{X}_l^{(m)}\,) \;=\; \sum_{i,j,k} \widetilde{\mathbf{V}}(\,x_{i,j,k}\,)\,\delta_h(\,x_{i,j,k} \;-\; \mathbf{X}_l^{(m)}\,)\Delta x^3 \qquad \forall\, l, m \quad (4.22)$$

In the eq. (4.22), $m \;=\; 1 \ldots N_p$ is the solid particle index, and $l \;=\; 1 \ldots N_l$ is the index of the lagrangian force point location on the m^{th} particle.

4.3.1.1 IBM for compressible viscous flows

A solid-fluid coupling force is evaluated to implement a no-slip, no-penetration boundary condition in case of a viscous flow as in eq. (4.23).

$$q_{\mathbf{u}}(\mathbf{X}_l^{(m)}) \;=\; \tilde{\rho}\,\frac{\mathbf{u}^{(d)} - \tilde{\mathbf{u}}_l^{(m)}}{\Delta t} \quad (4.23)$$

$\tilde{\mathbf{u}}$ is the preliminary velocity field given by the corresponding elements in $\widetilde{\mathbf{V}}$, i.e., $\tilde{\mathbf{u}} \;=\; (\,\tilde{u},\,\tilde{v},\,\tilde{w}\,)$ and $\mathbf{u}^{(d)}$ is the desired velocity field at the lagrangian marker positions obtained from the linear (u_c) and angular (ω_c) velocity of the m^{th} solid object located at x_c.

$$\mathbf{u}^{(d)}(\mathbf{X}_l^{(m)}) \;=\; u_c^{(m)} \;+\; \omega_c^{(m)} \times (\,\mathbf{X}_l^{(m)} \;-\; x_c^{(m)}\,) \quad (4.24)$$

Similarly, the fixed temperature boundary condition is enforced on the lagrangian markers of the m^{th} particle and reads

$$q_e(\mathbf{X}_l^{(m)}) \;=\; \tilde{\rho}\,\frac{e^{(d)} - \tilde{e}_l^{(m)}}{\Delta t} \tag{4.25}$$

In eq. (4.25), $e^{(d)}$ is the desired internal energy on the surface of the sphere and $\tilde{e}_l^{(m)}$ is the preliminary internal energy field evaluated at the lagrangian marker locations. After evaluation, the forcing terms must be interpolated back to the Eulerian grid using the same discrete delta function (Roma et al. 1999).

$$q_{\mathbf{u}}^{(ibm)}(\,x_{i,j,k}\,) \;=\; \sum_{m=1}^{N_p}\sum_{l=1}^{N_l} q(\mathbf{X}_l^{(m)})\,\delta_h(x_{i,j,k} \;-\; \mathbf{X}_l^{(m)})\,\Delta V_l^{(m)} \tag{4.26}$$

$q_{\mathbf{u}}^{(ibm)}$ is the vector composed of the immersed boundary forcing terms for velocity ($q_{\mathbf{u}}$) and energy (q_e) on the Eulerian grid. $\Delta V_l^{(m)}$ is the volume associated with the l^{th} lagrangian marker for the m^{th} particle and is defined in appendix D. Finally, the source term vector $\mathbf{Q}$ on the Eulerian grid is given by

$$\mathbf{Q} \;=\; \begin{pmatrix} 0 \\ q_u^{(ibm)} \\ q_v^{(ibm)} \\ q_w^{(ibm)} \\ q_e^{(ibm)} + u\,q_u^{(ibm)} + v\,q_v^{(ibm)} + w\,q_w^{(ibm)} \end{pmatrix} \tag{4.27}$$

4.3.1.2 IBM for compressible inviscid flows

Additional simplifications in the immersed boundary source terms can be obtained by considering inviscid flows. Let us first consider a unit normal vector ($\hat{n}_l^{(m)}$) to the lagrangian force point location ($\mathbf{X}_l^{(m)}$) given by eq. (4.28).

$$\hat{n}_l^{(m)} = \frac{\mathbf{X}_l^{(m)} - x_c^{(m)}}{|\,\mathbf{X}_l^{(m)} - x_c^{(m)}\,|} \tag{4.28}$$

The no-penetration boundary condition on the lagrangian force-point location ($\mathbf{X}_l^{(m)}$) in the immersed boundary sense is implemented with a source term that attempts to bring the normal flow velocity ($\tilde{\mathbf{u}}_l^{(m)} \cdot \hat{n}_l^{(m)}$) to the desired normal particle velocity ($\mathbf{u}^{(d)} \cdot \hat{n}_l^{(m)}$) as given in eq. (4.29).

$$q_{\mathbf{u},i}(\mathbf{X}_l^{(m)}) = \tilde{\rho}\,\frac{\mathbf{u}^{(d)} \cdot \hat{n}_l^{(m)} - \tilde{\mathbf{u}}_l^{(m)} \cdot \hat{n}_l^{(m)}}{\Delta t} \tag{4.29}$$

In eq. (4.29), $\tilde{\mathbf{u}}$ is the preliminary velocity field given by the corresponding elements in $\widetilde{\mathbf{V}}$, i.e., $\tilde{\mathbf{u}} = (\,\tilde{u},\,\tilde{v},\,\tilde{w}\,)$ and $\mathbf{u}^{(d)}$ is the velocity field at the lagrangian marker positions given by eq. (4.24).

Similar to the approach in viscous-compressible flows given in eq. (4.30), the velocity forcing term is interpolated back to the Eulerian grid as follows

$$q_{\mathbf{u},i}^{(ibm)}(\,x_{i,j,k}\,) = \sum_{m=1}^{N_p}\sum_{l=1}^{N_l} q_{\mathbf{u},i}(\mathbf{X}_l^{(m)})\,\delta_h(x_{i,j,k} - \mathbf{X}_l^{(m)})\,\Delta V_l^{(m)} \tag{4.30}$$

The immersed boundary source vector ($\mathbf{Q}$) on the Eulerian grid is given as

$$\mathbf{Q} = \begin{pmatrix} 0 \\ q_{u,i}^{(ibm)} \\ q_{v,i}^{(ibm)} \\ q_{w,i}^{(ibm)} \\ u q_{u,i}^{(ibm)} + v\, q_{v,i}^{(ibm)} + w\, q_{w,i}^{(ibm)} \end{pmatrix} \tag{4.31}$$

4.3.1.3 Final evaluation of the conservative force field

The vector $\mathbf{Q}$ evaluated for inviscid or viscous flows is finally added to the preliminary conservative field $\widetilde{\mathbf{U}}$ to obtain the conservative force field at the k^{th} Runge Kutta step.

$$\widetilde{\mathbf{U}}^{(k)} = \widetilde{\mathbf{U}} + \Delta t\, \mathbf{Q} \tag{4.32}$$

5 Validation

The current chapter summarises the validation tests for the compressible DNS flow solver used in the present work. The first two sections focus on the validation tests for the single-phase inviscid and viscous flows. Following this, the last two sections focus on validating the diffuse interface immersed boundary method used in the context of compressible flows. The following definitions in eq. (5.1) and eq. (5.2) for the L_1 and L_2 errors are used for convergence tests.

$$\mathscr{E}^{l}_{L1}(\psi) \;=\; \frac{1}{N^{(l)}} \sum_{i=1}^{N^{(l)}} \left| \psi_i - \widehat{\psi}_i \right| \tag{5.1}$$

$$\mathscr{E}^{l}_{L2}(\psi) \;=\; \sqrt{\frac{1}{N^{(l)}} \sum_{i=1}^{N^{(l)}} \left(\psi_i - \widehat{\psi}_i \right)^2} \tag{5.2}$$

$N^{(l)}$ represents the number of grid points considered in a grid convergence study ($N^{(l)} = N_x$ for a 1D study, $N^{(l)} = N_x N_y$ for a 2D study, and $N^{(l)} = N_x N_y N_z$ for a grid convergence study in three spatial dimensions). ψ_i is the numerical approximation at cell i and $\widehat{\psi}_i$ is the analytical solution at the same position. A convergence rate can further be defined in eq. (5.3).

$$R_{LX} \;=\; \frac{\log\left(\mathscr{E}^{(l)}_{LX}(\psi) \;-\; \mathscr{E}^{(l-1)}_{LX}(\psi) \right)}{\log\left(N^{(l-1)}_{LX} \;-\; N^{(l)}_{LX} \right)} \tag{5.3}$$

The superscript l represents the index of the grid representing $N^{(l)}$ discrete grid points.

5.1 Inviscid single phase validation

5.1.1 Smooth flow test cases

5.1.1.1 1D Advection of a smooth flow perturbation

In this section, two tests for advection of smooth flow fields in a one-dimensional domain are provided to evaluate the efficacy of the compressible DNS solver with an underlying 5^{th} order advection scheme to capture the expected grid convergence rate. The first test is the advection of a linear density perturbation in a periodic domain, and the other test is the advection of a smooth gaussian pulse.

Advection of a linear density perturbation

The test corresponds to a linear one-dimensional test for inviscid Euler equations. A sinusoidal perturbation is initially added to the density field, which is advected at a constant velocity while the pressure field remains constant. It is the consequence of the solution of the Euler equations remaining uncoupled. Similar tests have been performed in two dimensions by Zhang et al. (2011) and Buchmüller and Helzel (2014).

The test is performed on a periodic computational domain with a fundamental period of L. The inviscid equations are computed using a 5^{th} order Finite-Difference WENO-JS scheme (Shu 2016) for advection terms and a 3^{rd} order Runge Kutta scheme for time stepping and the primitive variables density, velocity, and pressure are initialized as in eq. (5.4).

$$\begin{pmatrix} \rho \\ u \\ p \end{pmatrix}_{t=0} = \begin{pmatrix} \rho_\infty + \delta\rho \, \sin(2\pi x/L) \\ u_\infty \\ p_\infty \end{pmatrix} \tag{5.4}$$

In the eq. (5.4), $u_\infty, \rho_\infty, p_\infty$ and the fundamental period L are set to unity and a fixed time step of $dt = 10^{-4}$ is chosen. $\delta\rho/\rho_\infty$ is set to 0.5. Hence, the reference Mach number is given by $Ma_\infty = u_\infty/\sqrt{\gamma p_\infty/\rho_\infty} = 1/\sqrt{\gamma}$. The

value of γ is taken as 1.4. The simulation is run until $t = 1.5L/u_\infty$. The exact solution at time t is given in eq. (5.5)

$$\begin{pmatrix} \rho \\ u \\ p \end{pmatrix}_t = \begin{pmatrix} \rho_\infty + \delta\rho \sin(2\pi(x - u_\infty t)/L) \\ u_\infty \\ p_\infty \end{pmatrix} \tag{5.5}$$

Table 5.1: Convergence of one-dimensional test for advection of linear density perturbation

N	dt	$\mathscr{E}_{L1}(\rho)$	rate $R_{L1}(\rho)$	$\mathscr{E}_{L2}(\rho)$	rate $R_{L2}(\rho)$
16	10^{-4}	8.98×10^{-3}	-	9.78×10^{-3}	-
32	10^{-4}	3.14×10^{-4}	4.84	3.51×10^{-4}	4.80
64	10^{-4}	9.10×10^{-6}	5.11	1.03×10^{-5}	5.08
128	10^{-4}	2.75×10^{-7}	5.05	3.09×10^{-7}	5.06
256	10^{-4}	8.49×10^{-9}	5.02	9.50×10^{-9}	5.03

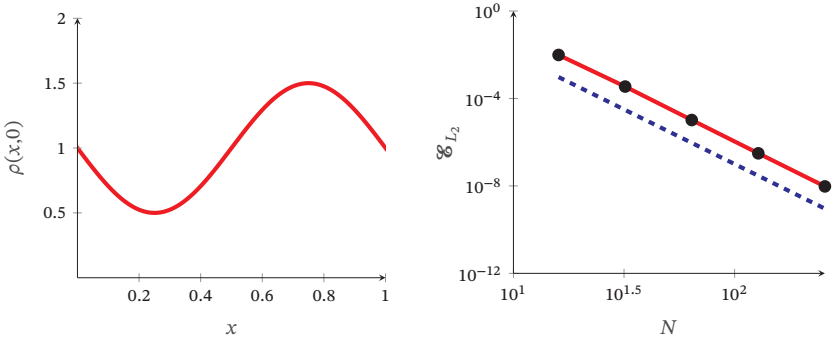

(a) **(b)**

Figure 5.1: Initial density distribution and grid convergence results for the advection of linear density perturbation. (a) Initial sinusoidal distribution of density (b) Grid convergence plot in terms of the errors obtained by L_2-norm compared to the analytical solution. The dashed line represents the N^{-5} power law.

As expected, a 5^{th} order convergence is obtained for the one-dimensional test for Euler equations.

Advection of a gaussian pulse

This test involves the advection of a smooth Gaussian pulse along the x-direction and is similar to the test of Yamaleev and Carpenter (2009), but with a perturbation in the density field. The idea is to test the performance of TENO scheme given by Liang et al. (2022) to capture the accuracy of background 5^{th} order linear scheme obtained by considering the entire 5-point stencil in smooth problems for evaluating numerical fluxes. The flow is initialized as in eq. (5.6).

$$\begin{pmatrix} \rho \\ u \\ p \end{pmatrix}_{t=0} = \begin{pmatrix} \rho_\infty(1 + e^{-300(x-x_c^2)}) \\ u_\infty \\ p_\infty \end{pmatrix} \tag{5.6}$$

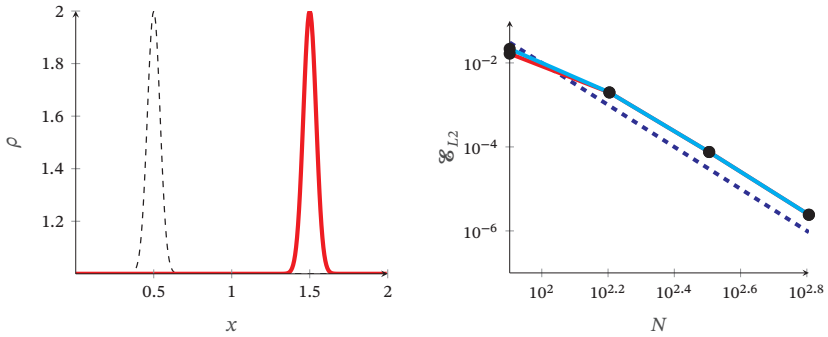

(a) **(b)**

Figure 5.2: (a) The initial (_ _ _) and final (▬) positions of the Gaussian pulse at the initial and final state (b) Grid convergence plot in terms of the errors obtained by L_2-norm compared to the analytical solution for TENO (▬) and background linear scheme (▬). The dashed line (▪ ▪ ▪) represents the N^{-5} power law.

The Gaussian pulse is initially centered at $x_c = 0.5$ and the reference Mach number (Ma_∞) is chosen as 0.5. ρ_∞ and u_∞ are set to unity and p_∞ is evaluated as $p_\infty = \rho_\infty u_\infty^2/\gamma Ma_\infty^2$. A 5^{th} order TENO and the corresponding 5^{th} order large stencil schemes are chosen to evaluate the numerical fluxes. A fixed time-step of $dt = 10^{-5}$ is chosen, and the solution is advanced in time until $t = 1$ in a domain of length $L_x = 2$. The exact solution at time t for density is given by $\rho_t = \rho_\infty(1 + e^{-300(x-x_c-u_\infty t)^2})$.

A 5^{th} order convergence is observed with TENO and the corresponding linear scheme with the large stencil as seen in fig. 5.2. Moreover, the TENO scheme captures the accuracy of the optimal background linear scheme at higher resolutions for this smooth flow problem.

5.1.1.2 Advection of isentropic vortex

The present test case for smooth flows involves the advection of an isentropic vortex field by a mean flow in two dimensions, which tests the ability of the spatial scheme to preserve the smooth flow features of the vortex field. This test has been previously performed by Yee et al. (1999), Zhang et al. (2011), Buchmüller and Helzel (2014), and Al Jahdali et al. (2022). The initial flow field can be represented in terms of the primitive variables as in eq. (5.7).

$$
\begin{aligned}
u(x,y,0) &= u_\infty + \frac{\beta}{2\pi} e^{\frac{1-r^2}{2}}(-\overline{y}) \\
v(x,y,0) &= v_\infty + \frac{\beta}{2\pi} e^{\frac{1-r^2}{2}}(\overline{x}) \\
T(x,y,0) &= \frac{p_\infty}{\rho_\infty} - \frac{(\gamma-1)\beta^2}{8\pi^2\gamma} e^{1-r^2} \\
S(x,y,0) &= \frac{p_\infty}{\rho_\infty^\gamma} \\
\rho(x,y,0) &= \left(\frac{T(x,y,0)}{S(x,y,0)}\right)^{1/(\gamma-1)} \\
p(x,y,0) &= \rho(x,y,0) T(x,y,0)
\end{aligned}
\tag{5.7}
$$

$\rho_\infty, u_\infty, v_\infty$ and p_∞ represent the base flow field, and $\overline{x}$ and $\overline{y}$ are defined as $\overline{x} = x - x_0$ and $\overline{y} = y - y_0$, where (x_0, y_0) are the coordinates of the initial position of the vortex center. $r = \sqrt{\overline{x}^2 + \overline{y}^2}$ and β represents the vortex strength. The entropy represented by $S = p/\rho^\gamma$ is kept constant. The perturbations to the background flow satisfy the radial momentum equations for a constant entropy inviscid ideal gas. Hence, the perturbations representing the vortex are convected at the background flow velocity. The exact solution at time t is represented by $U_{prim}(x,y,t) = U_{prim}(x - u_\infty t, y - v_\infty t, 0)$, where U_{prim} represents a primitive flow field.

Table 5.2: Convergence of two-dimensional test for advection of an isentropic vortex

N	dt	$\mathscr{E}_{L2}(\rho)$	rate $R_{L2}(\rho)$
32	$0.001/\sqrt{2}$	7.42×10^{-3}	-
64	$0.001/\sqrt{2}$	1.01×10^{-3}	2.87
128	$0.001/\sqrt{2}$	1.00×10^{-4}	3.34
256	$0.001/\sqrt{2}$	3.84×10^{-6}	4.70
512	$0.001/\sqrt{2}$	6.82×10^{-8}	5.81

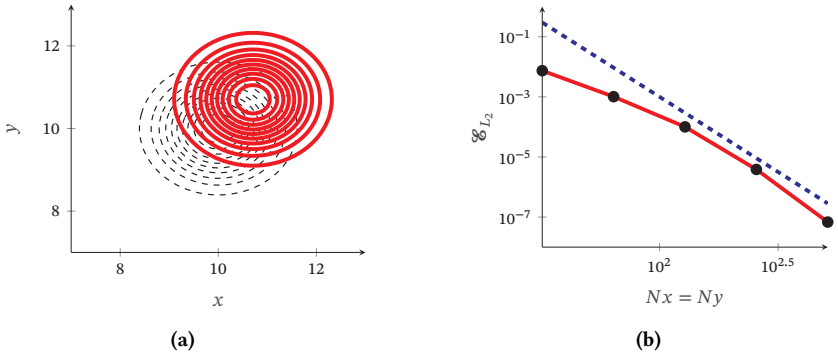

Figure 5.3: (a) The initial (dashed line) and final (solid line) positions of the isentropic vortex represented as the density contours (b) Grid convergence plot in terms of the errors obtained by L_2-norm compared to the analytical solution. The dashed line represents the N^{-5} power law.

The background primitive fields are chosen as $[\rho_\infty, u_\infty, v_\infty, p_\infty] = [1,1,1,1]$ respectively leading to an oblique flow at 45 in the xy plane and the vortex center is initially placed at $[x_0, y_0] = [10,10]$. The reference Mach number (M_∞) is then evaluated as $M_\infty = \sqrt{u_\infty^2 + v_\infty^2}/\sqrt{\gamma p_\infty/\rho_\infty} = 2/\sqrt{\gamma}$. The vortex strength $\beta = 5$ and the domain is chosen such that $L_x = L_y = 20$ and is periodic. The solution is advanced until $t = 0.05L_x/\sqrt{u_\infty^2 + v_\infty^2}$ using a 3^{rd} order low-storage Runge-Kutta method of Rai and Moin (1991) and a 5^{th} order WENO-JS scheme for advection term. A fixed time step size of $0.001/\sqrt{2}$ is chosen for the simulations. A close to 5^{th} order convergence is obtained as seen from fig. 5.3.

5.1.2 Tests with flow discontinuity

5.1.2.1 Linear advection of multiple waves

The current test involves the one-dimensional advection of a Gaussian pulse, a square wave, a sharp triangle, and a half-ellipse in a periodic computational domain with $x \in [0,2]$. This test has previously been performed by Takagi et al. (2022) and Jiang and Shu (1996). The flow is initialized as in eq. (5.8).

$$u(x,0) = \begin{cases} \frac{1}{6}\begin{bmatrix} G(x-1,\beta,z-\theta) + G(x-1,\beta,z+\theta) \\ +4G(x-1,\beta,z) \end{bmatrix}, & 0.2 \le x \le 0.4 \\ 1, & 0.6 \le x \le 0.8 \\ 1 - |10(x-1.1)|, & 1.0 \le x \le 1.2 \\ \frac{1}{6}\begin{bmatrix} F(x-1,\alpha,a-\theta) + F(x-1,\alpha,a+\theta) \\ +4F(x-1,\alpha,a) \end{bmatrix}, & 1.4 \le x \le 1.6 \\ 0, & \text{otherwise} \end{cases} \tag{5.8}$$

where $G(x,\beta,z) = e^{-\beta(x-z)^2}$ and $F(x,\alpha,a) = \sqrt{max(1-\alpha^2(x-a)^2,0)}$ with $\alpha = 0.5$, $z = -0.7$, $\alpha = 10$, $\beta = \frac{\log 2}{36\theta^2}$. A fixed time step with $dt = 10^{-3}$ and $N = 160$ grid points are chosen. The final simulation time is $t = 10$. The performance of WENO-JS is compared to TENO in capturing the discontinuous solutions at the final time. A third-order Runge-Kutta method is used for time-stepping. The results are shown in fig. 5.4. It is seen that TENO5 is

better at capturing the solutions with large gradients at the same grid resolutions. The L_2 errors ($\mathscr{E}_{L2}$) at $N = 160$ was observed to be 0.0902 with the 5^{th} order TENO scheme and 0.1152 with the 5^{th} order WENO-JS scheme.

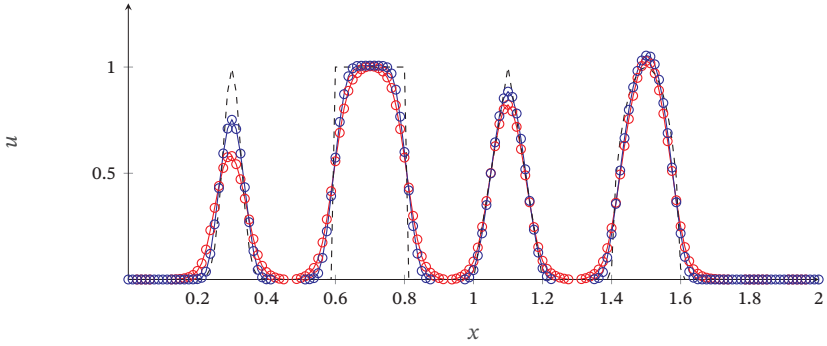

Figure 5.4: Comparison of the performance of 5^{th} order TENO and WENO-JS schemes to capture discontinuities at a given spatial discretization step size. (——) represents the numerical solution obtained by WENO-JS, (——) represents the solution approximated by TENO, and (_ _ _) represents the analytical solution at the final time.

5.1.2.2 Sod shock tube problem

The sod shock tube problem is a classical one-dimensional Riemann problem leading to the generation of a rarefaction wave, a contact discontinuity, and a shock wave. The initial flow field consists of a flow discontinuity with a sharp variation of flow-field quantities.

$$\begin{pmatrix} \rho_L \\ u_L \\ p_L \end{pmatrix} = \begin{pmatrix} 1 \\ 0 \\ 1 \end{pmatrix} \quad \begin{pmatrix} \rho_R \\ u_R \\ p_R \end{pmatrix} = \begin{pmatrix} 0.125 \\ 0 \\ 0.1 \end{pmatrix} \tag{5.9}$$

The flow field is initialized with left and right states as in eq. (5.9) in a domain of length L and with the discontinuity at $x = L/2$. WENO-JS and TENO schemes are used, and a 3^{rd} order Runge-Kutta scheme is used for time-stepping. The solution is advanced in time until $t = 0.2$.

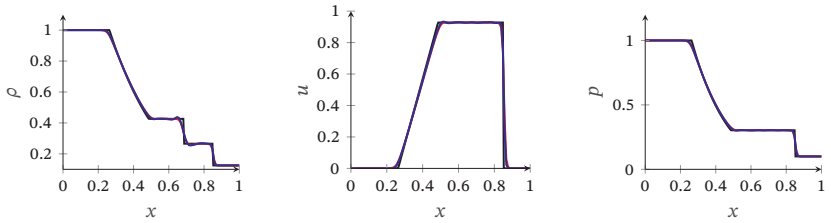

Figure 5.5: Sod's shock tube problem at $N = 100$ and simulation time $t = 0.2$ with TENO (——) and WENO-JS (——) schemes compared to analytical solution (——). (a) Spatial density variation (b) Velocity variation (c) Pressure variation.

The TENO and WENO-JS schemes capture the different characteristic waves (shock wave, rarefaction wave, and contact discontinuity) in the problem. The TENO scheme resolves the flow features near the discontinuities better than the WENO-JS scheme at the same grid resolutions. At higher resolutions, the numerical approximation converges towards the analytical solution. The L_2 errors for the density fields compared to the analytical solution for the 5^{th} order WENO-JS and TENO schemes are shown in fig. 5.6. It is observed that the L_2 errors in density are smaller with the TENO scheme compared to the WENO-JS schemes at the chosen grid-resolutions.

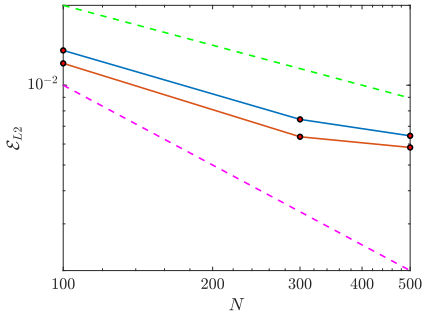

Figure 5.6: Comparison of the L_2 errors of density fields ($\mathcal{E}_{L2}$) for the Sod-shock-tube problem compared to the exact solution evaluated with (——) 5^{th} order WENO-JS and (——) 5^{th} order TENO. (- - -) represents the $N^{-0.5}$ power law and (- - -) represents the N^{-1} power law.

5.1.2.3 Lax problem

The Lax problem is another Riemann problem where the initial flow field is initialized as in eq. (5.10). A 5^{th} order WENO-JS and TENO schemes are used for the advection scheme, and a 3^{rd} order Runge Kutta scheme is used for temporal discretization.

$$\begin{pmatrix} \rho_L \\ u_L \\ p_L \end{pmatrix} = \begin{pmatrix} 0.445 \\ 0.698 \\ 3.528 \end{pmatrix} \qquad \begin{pmatrix} \rho_R \\ u_R \\ p_R \end{pmatrix} = \begin{pmatrix} 0.5 \\ 0 \\ 0.571 \end{pmatrix} \tag{5.10}$$

The solution is advanced in time until $t = 0.14$, and a grid size of $N = 500$ is used. The results are shown in fig. 5.7. It is observed that although the TENO scheme is sharper near the discontinuities, it also introduces slightly more numerical dispersion with the current choice of schemes.

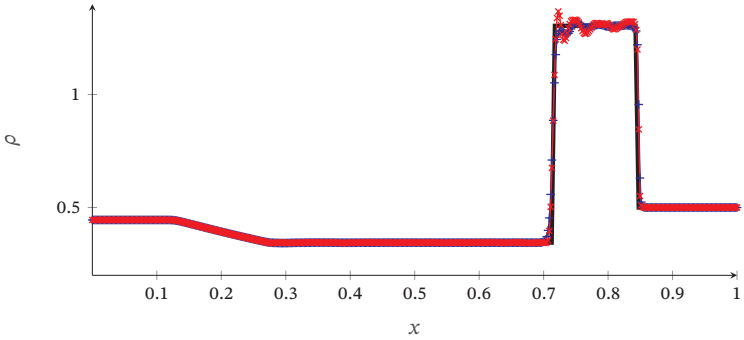

Figure 5.7: Density variation as a function of x for Lax problem at $t = 0.14$ with the WENO-JS and TENO schemes. (▬) represents the analytical solution, (+) represents the numerical solution at $N = 500$ with WENO-JS scheme, and (×) represents the numerical solution at the final time with the TENO scheme at the same grid resolution.

The L_2 errors ($\mathcal{E}_{L2}$) of the density fields with respect to the exact solutions at $N = 500$ (evaluated through the exact Riemann solver) are evaluated for the WENO-JS and TENO schemes. $\mathcal{E}_{L2}$ with the WENO-JS scheme was 0.0403 and

with TENO scheme, $\mathcal{E}_{L2}$ was 0.0320. Although higher numerical dispersion is observed near the discontinuities with the TENO scheme, the L_2 errors for the density fields at $N = 500$ was lower than the WENO-JS scheme.

5.1.2.4 Shock density wave interaction

The test case has previously been performed by Shu and Osher (1988) and Takagi et al. (2022). It involves a shock wave of Mach 3 interacting with a sinusoidal density wave. The initial flow field distribution in the domain $x \in [-5,5]$ is given by eq. (5.11). A fixed time-step of $dt = 10^{-4}$ is chosen, and the solution is advanced in time until $t = 2$. The reference solution is obtained with the WENO-JS scheme with 5000 grid points ($N = 5000$).

$$(\rho, u, p) = \begin{cases} (3.857, 2.629, 10.33), & x \in [-5, -4) \\ (1 + 0.2\sin(5x), 0, 1). & x \in [-4, 5] \end{cases} \tag{5.11}$$

The numerical solution with WENO-JS and TENO schemes with $N = 300$ is compared to the reference solution. The results with the two spatial discretization schemes are shown in fig. 5.8

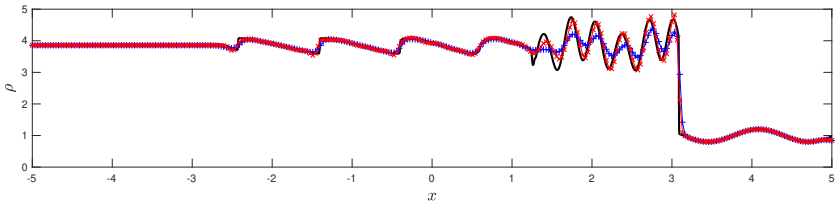

Figure 5.8: Density variation as a function of x for the interaction of a shock wave with Mach 3 interacting with a density wave at $t = 2$ with the WENO-JS and TENO schemes. (▬) represents the reference solution computed with the WENO-JS scheme with 5000 grid points. (+) represents the numerical solution obtained with the WENO-JS scheme at $N = 300$ and (×) represents the numerical solution with the TENO scheme at the same grid resolution.

It is observed that the TENO scheme is better at resolving large gradients than the WENO-JS scheme at equal resolutions. The L_2 errors ($\mathcal{E}_{L2}$) in the density field at $N = 300$ was evaluated with respect to the corresponding reference

solution obtained by linearly interpolating the WENO-JS numerical solution at $N = 5000$ to $N = 300$. It was observed that $\mathcal{E}_{L2}$ at N = 300 for the WENO-JS scheme was 0.1911 and with the TENO scheme, $\mathcal{E}_{L2}$ was 0.1176.

5.1.2.5 Explosion test in two dimensions

The current validation test is for Euler's equations in two spatial dimensions taken from Toro (2013). The flow is initialized with a circular discontinuity centered at (1,1) with a radius of $R = 0.4$ on a square domain 2.0×2.0 in the $x - y$ plane. Flow properties vary sharply from the inside of the circular region to the outside. The initial flow distribution is given by eq. (5.12).

$$\begin{pmatrix} \rho_{in} \\ u_{in} \\ v_{in} \\ p_{in} \end{pmatrix} = \begin{pmatrix} 1.0 \\ 0.0 \\ 0.0 \\ 1.0 \end{pmatrix} \quad \begin{pmatrix} \rho_{out} \\ u_{out} \\ v_{out} \\ p_{out} \end{pmatrix} = \begin{pmatrix} 0.125 \\ 0.0 \\ 0.0 \\ 0.1 \end{pmatrix} \tag{5.12}$$

The subscript "in" represents the primitive flow variables inside the circular region, and "out" represents the flow quantities outside.

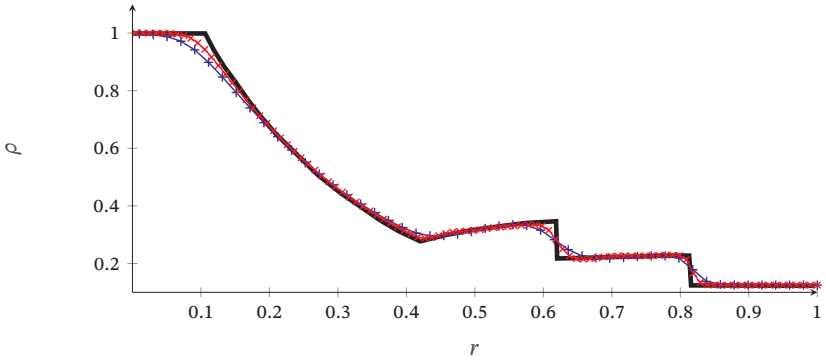

Figure 5.9: Density variation as a function of radial position r for explosion test in two spatial dimensions at $t = 0.25$ with the WENO-JS scheme. (▬) represents the reference solution from Toro (2013), (+) represents the numerical solution at $N_x = 100, N_y = 100$, and (×) represents the numerical solution with $N_x = 200, N_y = 200$.

The solution is an outward traveling shock wave, a circular rarefaction wave traveling inwards, and a contact discontinuity traveling away from the center. A WENO-JS scheme is used to advance the solution until a final time of $t = 0.25$ in a uniform grid with $[N_x,N_y] = [100,100]$ and $[N_x,N_y] = [200,200]$. The numerical approximation of density at the two grid resolutions is given in fig. 5.9. As expected, at higher grid resolutions, the numerical solution converges towards the reference solution.

5.1.2.6 2D Riemann problem of Lax

In this section, a two-dimensional Riemann problem from configuration 3 of Lax and Liu (1998) is chosen. The two-dimensional square domain $L_x = L_y = 1$ is distributed in four equiareal quadrants. The initial flow field consists of the primitive variables distributed in a way such that they are constant in each quadrant. The initial distribution of the density, velocity, and pressure in the $x - y$ plane is given in eq. (5.13).

$$(\rho, u\, v, p) = \begin{cases} (1.5, 0, 0, 1.5) & x > 0.5, y > 0.5 \\ (0.5323, 1.206, 0, 0.3) & x < 0.5, y > 0.5 \\ (0.138, 1.206, 1.206, 0.029) & x < 0.5, y < 0.5 \\ (0.5323, 0, 1.206, 0.3) & x > 0.5, y < 0.5 \end{cases} \tag{5.13}$$

A mesh resolution of 400×400 (similar to Lax and Liu (1998)) is chosen. The WENO-JS scheme is used, and the solution is advanced in time until $t = 0.3$ using the 3^{rd} order Runge Kutta procedure with a CFL of 0.5. The density contour plot at the final computational time is shown in fig. 5.10.

The exact solution consists of four shock waves emanating from the initial flow discontinuities at the quadrant boundaries and a complex intermediate flow pattern. As seen in fig. 5.10, the complex flow patterns and the shock waves were captured stably.

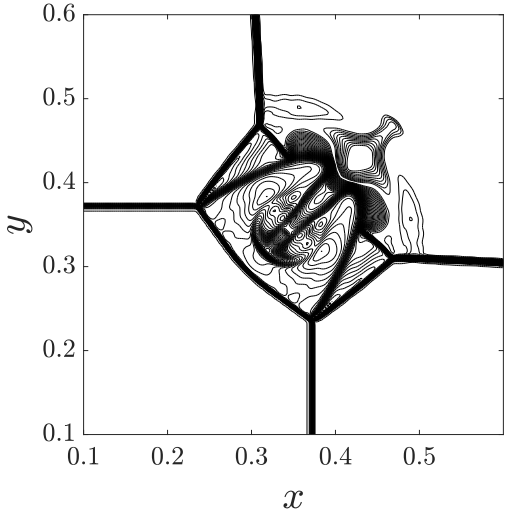

Figure 5.10: Zoomed in view of the density contours for the 2D Riemann problem from configuration 3 of Lax and Liu (1998) at the final computational time of $t = 0.3$ using WENO-JS advection scheme. The shock waves and flow patterns are captured, and the symmetry is preserved.

5.2 Viscous single phase validation

A series of viscous single-phase validations are performed in the present section. The inviscid Euler momentum and total energy equations are augmented with additional viscous terms as shown in section 3.1. The dissipative terms introduce two new non-dimensional parameters: the Reynolds number (Re) and the Prandtl number (Pr). The Reynolds number is the ratio between inertial and viscous forces, whereas the Prandtl number is defined as the ratio between momentum and thermal diffusivities. Unless stated otherwise, the value of the Prandtl number is fixed at ($Pr = 0.7$), and the ratio of specific heat capacities is set to ($\gamma = 1.4$) for the validation tests.

First, the Taylor Green Vortex (TGV) test case is validated with the known exact solutions for incompressible flows at low Mach numbers. Next, a simple test case for Couette flow presented by Jain (1973) is tested for equal and

non-equal wall temperatures, also at low Mach numbers. Their hypothetical viscous law makes the system of equations solvable to obtain an analytical solution that can be used for validation. Next, a more general compressible flow test case for simple shearing motion, given by Illingworth (1950), is used to test the viscous law implementation at higher Mach numbers. Their viscous law simplifies the compressible Navier Stokes equations into a series of ordinary differential equations that can be solved numerically. Finally, the compressible turbulent plane channel flow with isothermal walls by Coleman et al. (1995) is run and compared with available reference data.

5.2.1 Taylor Green Vortices

The test case of the Taylor-Green vortex is a simple, unsteady solution of the incompressible Navier-Stokes equations for a decaying vortex in a periodic two-dimensional domain. In the DNS runs, The flow fields remain unchanged along the third direction in a three-dimensional domain; hence, there is no spatial dependence of the computed solution along the third direction. The DNS results are compared with the analytical solution at a low Mach number. The time-dependent exact solution of the Taylor Green Vortices solved on a square domain for incompressible flows is given in eq. (5.14).

$$\begin{aligned} u(x,t) &= u_o sin(kx)cos(ky)e^{-2k^2\nu t} \\ v(x,t) &= -u_o cos(kx)sin(ky)e^{-2k^2\nu t} \\ p(x,t) &= p_o + \frac{\rho_o {u_o}^2}{4}[cos(2kx) + cos(2ky)]e^{-4k^2\nu t} \end{aligned} \tag{5.14}$$

In the eq. (5.14), u and v are the velocities, p is the pressure, and ν is the constant kinematic viscosity. p_o is the background pressure, ρ_o is the initial constant density of the flow field, and u_o is the amplitude of the velocity field. The wave number k is defined as $k = 2\pi/L$, where the periodic domain is $\Omega = [0 \leq x,y \leq L]$.

For the current problem, $\rho_o = 1$ and $p_o = 7.9365$ is chosen such that the reference Mach number ($Ma = \sqrt{\gamma p_o/\rho_o}$) is 0.3. At this low Mach number, the compressibility effects are negligible, and an incompressible flow can be

assumed. Hence, the variation in density remains small, and the DNS results can be compared against the analytical incompressible Taylor Green Vortex solutions. The flow is initialized on a cubical domain of $[L \times L \times L]$ with $L = 1$, and the dynamic viscosity μ is obtained from the kinematic viscosity as $\mu = \nu\rho$. The Reynolds number (Re) based on L, u_o and ν is fixed at 100. The physical parameters are summarised in table 5.3.

Table 5.3: Physical parameters used for the DNS runs of Taylor Green Vortices

Pr	Ma	Re
0.7	0.3	100

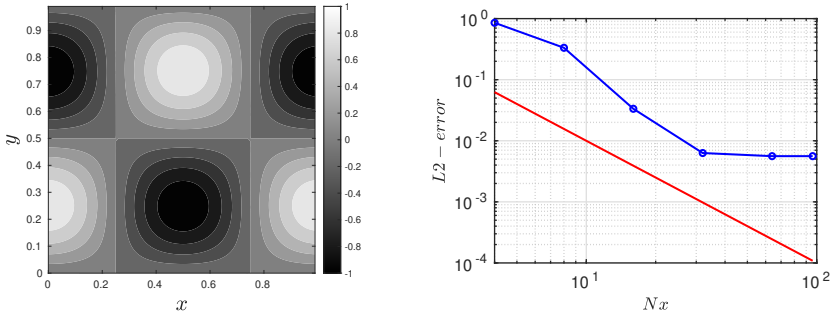

(a) **(b)**

Figure 5.11: Taylor Green Vortices: (a) Contour of initial x-velocity field (b) Grid convergence plot in terms of the errors obtained by L_2-norm (——) compared to the analytical solution. (——) represents the N^{-2} power law.

The flow is initialized with the exact solution at $t = 0$, and the test is run for 10^5 time-steps at a fixed time-step of 5×10^{-5} at different resolutions along the length (L) in $x - y$ directions. The convergence of the x-velocity to the analytical incompressible solution is shown in fig. 5.11b. A second-order convergence is observed with grid refinement. At higher resolutions, the effect of errors accumulated from the time-stepping procedure becomes significant, and hence, a further decrease in errors with grid-refinement is not

observed. The observed second-order convergence is the expected behavior for using a second-order central difference scheme for the viscous terms.

5.2.2 Couette flow with constant dynamic viscosity

The test given in Jain (1973) is a couette flow test that makes the energy eq. (3.13) solvable under an assumption of constant thermal conductivity ($\kappa =$ constant) and dynamic viscosity ($\mu = \mu_o$). The lower wall is stationary, while the upper wall moves parallel to the lower wall at constant velocity U. The temperature of both walls is fixed and is kept constant.

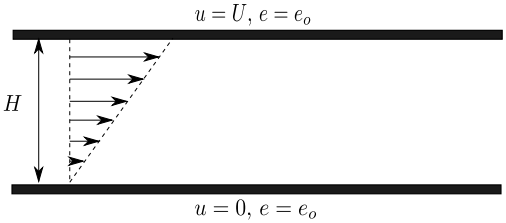

Figure 5.12: Geometry and boundary conditions for Couette flow shown in the $x - y$ plane. The lower wall is stationary, while the upper wall moves at a constant velocity U relative to the lower wall.

5.2.2.1 Derivation of the couette flow equations

Consider the governing differential equations for momentum and energy given in eqs. (3.8) and (3.13). The equations can be simplified for a two-dimensional Couette flow with isothermal walls with the following assumptions

(i) Two dimensional flow : $\frac{\partial}{\partial z}() = 0$

(ii) Incompressible flow : $\nabla \cdot \mathbf{u} = 0$

(iii) Steady state : $\frac{\partial}{\partial t}() = 0$

(iv) Fully developed in x-direction : $\frac{\partial}{\partial x}() = 0$

(v) Zero wall-normal velocity ($v = 0$)

(vi) Constant Prandtl number Pr and ratio of specific heat capacities γ.

(vii) Constant thermal conductivity (κ = constant)

(viii) Constant dynamic viscosity ($\mu = \mu_o$)

Under these assumptions, the system of equations is reduced to the form shown in eq. (5.15). In the equations, T is fluid temperature related to the fluid internal energy (e) as $e = C_v T$.

$$\begin{aligned} \frac{d}{dy}\left(\mu \frac{du}{dy}\right) &= 0 \\ \kappa \frac{d^2T}{dy^2} + \mu \left(\frac{du}{dy}\right)^2 &= 0 \end{aligned} \tag{5.15}$$

The corresponding boundary conditions for the Couette flow in the dimensional form are given in eq. (5.16). The expression for the energy equation has also previously been derived by Nahme (1940).

$$\begin{aligned} y = 0 &: \; u = 0, \; e = e_o \\ y = H &: \; u = U, \; e = e_o \end{aligned} \tag{5.16}$$

Let μ_o be the reference dynamic viscosity of the fluid corresponding to e_o. Then, the constant thermal conductivity (κ) is defined in eq. (5.17).

$$\kappa = \frac{\mu_o \gamma C_v}{Pr} \tag{5.17}$$

5.2.2.2 Analysis

The momentum equation in eq. (5.15) can be integrated to obtain the non-dimensional shearing stress τ_o as follows

$$\tau_o = \mu \frac{du}{dy} = \text{constant} = \left(\mu \frac{du}{dy}\right)_{y=0} \tag{5.18}$$

Eliminating du/dy from eqs. (5.15) and (5.18), the following modified energy equation eq. (5.19) is obtained

$$\frac{d^2 e}{dy^2} + \frac{Pr\, \tau_o^2}{\gamma\, \mu_o^2} = 0 \tag{5.19}$$

Under the assumption of constant dynamic viscosity ($\mu = \mu_o$), the eq. (5.15) is solvable analytically and is given by eq. (5.20).

$$\begin{aligned} e &= e_o + \frac{U^2\, Pr}{2\gamma} \frac{y}{H}\left(1 - \frac{y}{H}\right) \\ u &= U\left(\frac{y}{H}\right) \end{aligned} \tag{5.20}$$

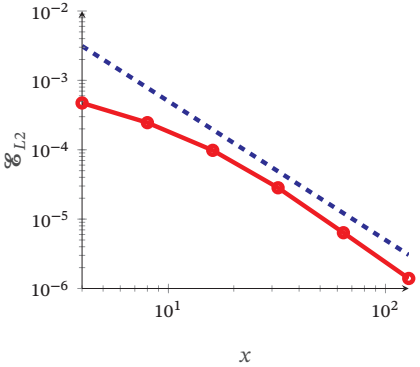

Figure 5.13: Convergence of streamwise fluid velocity in Couette flow with isothermal walls. (▬ ▬ ▬) represents the N^{-2} power law with WENO-JS and (▬) represents the L_2 error for fluid streamwise velocity compared to the analytical solution.

We run simulations starting with a uniform flow at Mach number ($Ma = 0.2$), $\gamma = 1.4$ in a domain $[2 \times 2 \times 2]$, and use a constant kinematic viscosity,

ν = constant = $U\,H/Re$. (Note: Since the entire flow is close to incompressible, the density variations are minor, and hence, constant kinematic viscosity should also imply constant dynamic viscosity). The Prandtl and Reynolds numbers are set to $Pr = 0.7$ and $Re = 10$ respectively and the wall temperatures are fixed at $e_o = U^2/(\gamma(\gamma-1)Ma^2)$. We validate the results with the analytical solution for constant dynamic viscosity given in eq. (5.20). It should be noted that the Reynolds number (Re) only affects the transient solution but not the final steady-state analytical solution. In addition, periodic boundary conditions are set along x and z directions. Validation tests are run at different resolutions and with a fixed time step of $dt = 10^{-5}$ for 2×10^6 time steps.

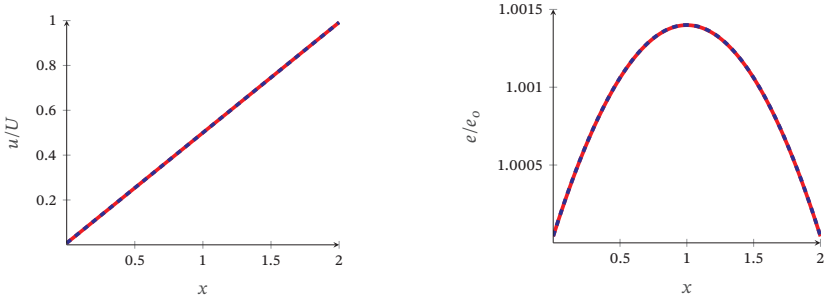

Figure 5.14: Normalized streamwise velocity and internal energy of the fluid for Couette flow compared to the analytical solution. (- - -) represents the analytical solution and (——) represents the DNS solution at $N = 128$. (a) Normalized streamwise flow velocity (b) Normalized fluid internal energy.

The convergence of streamwise fluid velocity at $t = 20$ compared to the analytical solution is shown in fig. 5.13, and the normalized streamwise velocity and internal energy are shown in fig. 5.14. A second-order convergence is observed as expected.

5.2.3 Couette flow with variable dynamic viscosity

In this more stringent Couette flow test, the flow compressibility is non-negligible, and the viscosity is a linear function of the temperature. With the

chosen viscous law, the compressible Navier-Stokes equations are reduced to a set of ordinary differential equations that can be solved numerically, for example, by using the Newton-Raphson method. This test was previously introduced by Illingworth (1950). The geometry of the current test is shown in fig. 5.15.

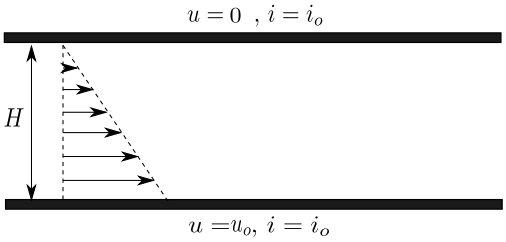

Figure 5.15: Geometry and boundary conditions for compressible Couette flow shown in the $x - y$ plane. The upper wall is stationary, while the lower wall moves at a constant velocity u_o relative to the upper wall. The specific enthalpy at the upper and lower walls is fixed at $i = i_o$.

At sufficiently low residuals, the obtained solution from the iterative procedure can be used as the reference solution to the problem. First, the Couette flow equations are stated and non-dimensionalized, following which a grid convergence test comparing the DNS results with the reference solution is performed. The following assumptions are considered

(i) Two dimensional flow : $\frac{\partial}{\partial z}() = 0$

(ii) Steady state : $\frac{\partial}{\partial t}() = 0$

(iii) Fully developed in x-direction : $\frac{\partial}{\partial x}() = 0$

(iv) Zero wall-normal velocity ($v = 0$)

(v) Constant Prandtl number Pr and ratio of specific heat capacities γ.

(vi) A linear viscosity law between dynamic viscosity and specific enthalpy ($\mu \propto i$)

Under these assumptions, the system of equations in eqs. (3.8) and (3.13) reduce to eq. (5.21).

$$\begin{aligned} \frac{d}{dy}\left(\mu\frac{du}{dy}\right) &= 0 \\ \frac{dp}{dy} &= 0 \\ \frac{\gamma}{Pr}\left[\frac{d}{dy}\left(\mu\frac{de}{dy}\right)\right] + \mu\left(\frac{du}{dy}\right)^2 &= 0 \end{aligned} \tag{5.21}$$

Let i represent the specific enthalpy per unit mass. Then, the specific internal energy (e) can be written as in eq. (5.22).

$$i = e + \frac{p}{\rho} = \frac{p}{(\gamma-1)\rho} + \frac{p}{\rho} = \frac{p\gamma}{(\gamma-1)\rho} = \gamma e \tag{5.22}$$

Substituting eq. (5.22) in eq. (5.21), we obtain

$$\frac{1}{Pr}\left[\frac{d}{dy}\left(\mu\frac{di}{dy}\right)\right] + \mu\left(\frac{du}{dy}\right)^2 = 0 \tag{5.23}$$

The details of the non-dimensionalization of the governing differential equations and their simplifications based on the mentioned assumptions are provided in appendix E. Let, the subscript 'o' represent the quantities evaluated at the bottom wall, which is the reference plate for this test. c_o be the speed of sound of the flow near the lower plate defined as $c_o = \sqrt{\gamma p_o/\rho_o}$. The Mach number ($Ma = u_o/c_o$), the Reynolds number ($Re = \rho_o u_o H/\mu_o$), and the Prandtl number (Pr) are chosen as 1, 10, and 1 respectively. The test is run with $H = 1$ and a time-step size of $dt = 10^{-5}$ for 2×10^6 steps. At $t = 0$, the initial density distribution is uniform $\rho = \rho_o = 1$, and the streamwise velocity u varies linearly between the two plates as $u = u_o(1-y/H)$, such that the initial pressure distribution is given by $p = \rho_o u^2/(\gamma Ma^2)$. The lower plate moves at a velocity $u = u_o$ relative to the stationary upper plate, and the

internal energy on both the walls is fixed at $e = e_o = (p_o/(\gamma - 1)\rho_o)$. Periodic boundary conditions are used in the streamwise and spanwise directions. Figure 5.16 shows the steady state streamwise velocity and specific enthalpy computed at the finest grid ($N = 128$) compared to the reference solution.

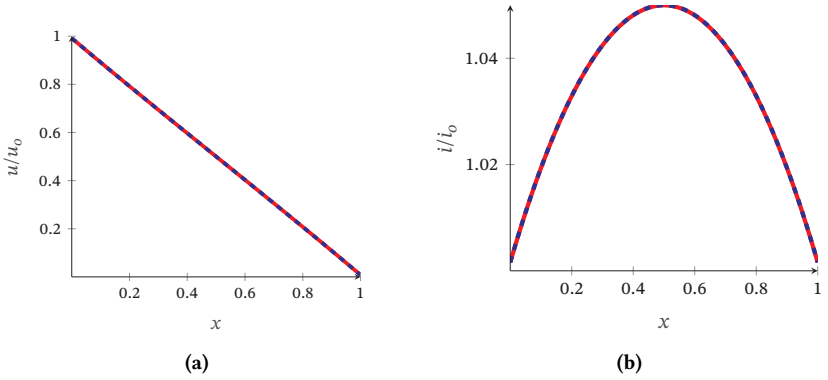

Figure 5.16: Normalized streamwise velocity and specific fluid enthalpy for compressible Couette flow compared to the reference solution. (▪▪▪) represents the reference solution and (▬) represents the DNS solution at $N = 128$. (a) Normalized streamwise flow velocity (b) Normalized fluid specific enthalpy.

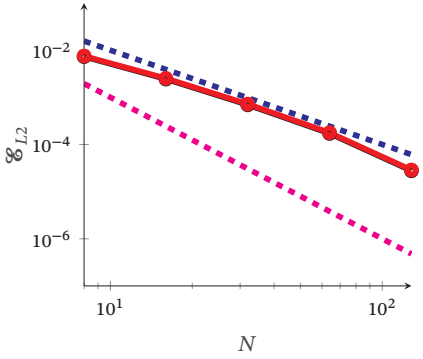

Figure 5.17: Convergence of streamwise fluid velocity and specific enthalpy for compressible Couette flow at $Ma = 1$ with isothermal walls. (▪▪▪) and (▪▪▪) represent the N^{-2} and N^{-3} power laws respectively. (▬) and (▬) represents the convergence of L_2 errors for streamwise velocity and specific enthalpy.

Figure 5.17 shows the convergence plot of L_2 errors of the specific enthalpy and the streamwise velocity compared to the reference solution. A close-to-second-order convergence is observed, attributed to the second-order numerical scheme used for the viscous terms.

5.2.4 Compressible turbulent supersonic channel flow

In the current section, a Direct Numerical Simulation of turbulent supersonic channel flow with constant wall temperatures is performed and studied. The geometry and physical parameters have previously been used by Coleman et al. (1995), and later, the DNS results were reproduced by Lechner et al. (2001) by using a pressure-velocity-entropy formulation of the compressible Navier-Stokes equations. The geometry used for the DNS run is shown in fig. 5.18.

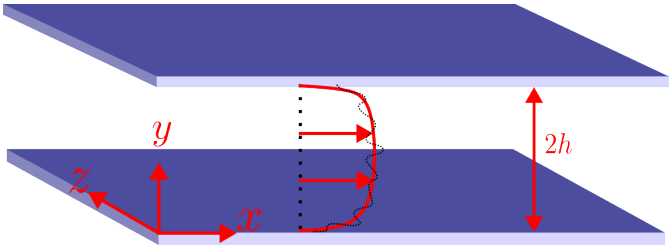

Figure 5.18: Geometry and boundary conditions for compressible wall-bounded turbulent supersonic channel flow. Periodic boundary conditions are implemented along the spanwise and streamwise directions, while a no-slip constant temperature boundary condition is imposed at the walls.

The flow inside the channel is maintained by a uniform body force equivalent to a pressure gradient term in pressure-driven flows. The source term ensures a constant total mass flux through the channel such that a statistically stationary, fully developed turbulent state can be obtained. The channel walls are cooled with respect to the bulk flow and act as an energy sink by transferring energy produced by viscous dissipation out of the channel. The Reynolds number (Re) and the Mach number (Ma) based on the bulk velocity (u_m), wall dynamic viscosity (μ_w), channel half width (h), bulk density (ρ_m),

and the wall speed of sound (c_w) are chosen as $Ma = 1.5$ and $Re = 3000$. The medium chosen is air. Hence, the Prandtl number (Pr) based on the wall dynamic viscosity (μ_w) and wall thermal conductivity (κ_w) is fixed at 0.7 and the specific heat capacity ratio (γ) is set to 1.4. The temperature-dependent dynamic viscosity (μ) follows a power-law given by $\mu \propto T^{0.7}$. The definitions of the non-dimensional parameters are summarised in eq. (5.24).

$$\begin{aligned} Ma &= u_m/c_w = 1.5 \\ Re &= \rho_m u_m h/\mu_w = 3000 \\ Pr &= \mu_w C_p/\kappa_w = 0.7 \\ \gamma &= C_p/C_v = 1.4 \end{aligned} \tag{5.24}$$

The computational domain is the same as the one used by Coleman et al. (1995) given by $L_x = 4\pi$, $L_y = 2$, and $L_z = 4\pi/3$. The domain is uniformly discretized along the wall-normal direction such that the grid spacing in wall units in the statistically stationary state is given by $\Delta y^+ = 0.42$. The DNS was started by a uniform flow field, and a localized non-uniform puff-forcing was introduced for a duration of $0.032\, h/u_\tau$ for triggering the transition to turbulence. Details of such an approach have previously been discussed by Willis and Kerswell (2008). The total time for the DNS simulation was $t_{total} = 90.41\, h/u_\tau$, where h is the channel half-width and u_τ is the friction velocity given by $u_\tau = \sqrt{\tau_w/\rho_w}$, where τ_w is the wall shear given in eq. (5.25).

$$\tau_w = \frac{\mu_w}{2}\left(\left|\frac{\mathrm{d}u}{\mathrm{d}y}\right|_{y=0} + \left|\frac{\mathrm{d}u}{\mathrm{d}y}\right|_{y=2h}\right) \tag{5.25}$$

Flow fields are temporally averaged for $12\, h/u_\tau$ time units between $78\, h/u_\tau$ and $90\, h/u_\tau$. The current results are compared with the DNS results reported by Lechner et al. (2001). $\langle\cdot\rangle$ represents the time-averaged statistic obtained by Reynolds averaging, and $(\tilde{\cdot})$ represents favre-averaging, such that the respective fluctuations are given by eq. (5.26). The averaging procedures and flow field decomposition definitions are given in appendix A.

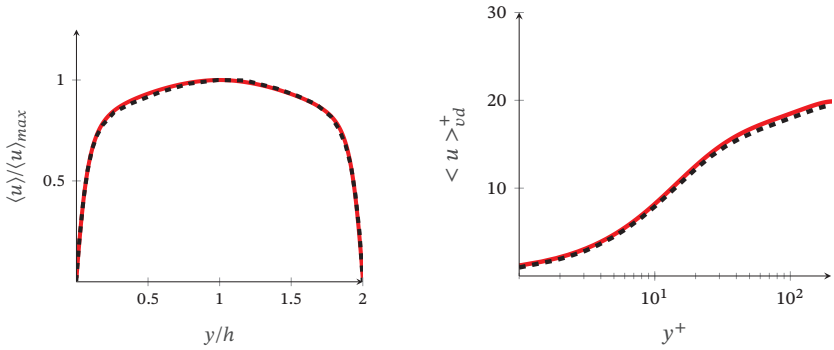

Figure 5.19: Comparison of (a) mean normalized and (b) Van Driest transformed velocity profile compared with the DNS data of Lechner et al. (2001) and Coleman et al. (1995). (▬ ▬ ▬) represents the reference solution and (▬▬) represents the time-averaged DNS solution.

$$
\begin{aligned}
U' &= U - \langle U \rangle \\
U'' &= U - \widetilde{U}
\end{aligned}
\tag{5.26}
$$

Figure 5.19 compares the normalized Reynolds averaged mean velocity, and the Van-driest transformed velocity compared to the reference solution. A good agreement is observed with the reference data. The definition of the Van Driest transformation is the same as in Coleman et al. (1995) and is given by eq. (5.27). The higher velocity gradient near the wall, as seen in fig. 5.19a, is a characteristic of wall-bounded fully developed turbulent flows owing to the enhancement of momentum transport by the fluctuating motion. This, in turn, increases the wall shear stress and leads to a flatter velocity profile compared to a laminar flow. The maximum value of the mean velocity is observed at the channel centerline. The density-weighted mean velocity obtained by Van Driest transformed velocity seems to follow a logarithmic profile approximately at $y^+ > 30$ as seen in fig. 5.19b similar to the universal incompressible logarithmic law.

$$\langle u \rangle_{vd}^{+} = \int_0^{\langle u \rangle^+} \left(\frac{\rho}{\rho_w} \right)^{1/2} \mathrm{d}\langle u \rangle^+ \tag{5.27}$$

This seems to agree with Morkovin (1962), who proposed that for Mach numbers less than 5, the difference between incompressible and compressible boundary layers can be accounted for by considering the variations of mean flow field quantities. The logarithmic profile can be attributed to the diminishing effects of viscosity outside the viscous sublayer. Figure 5.20a shows the variation of the normalized mean temperature, and fig. 5.20b shows the RMS fluctuation of temperature compared to the reference data of Lechner et al. (2001).

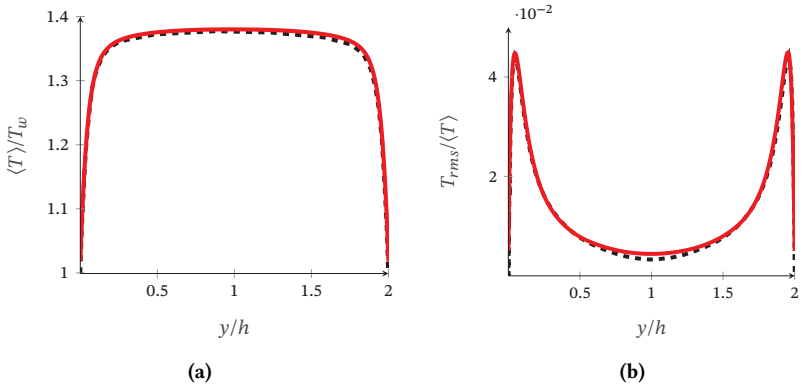

Figure 5.20: Comparison of (a) mean normalized and (b) RMS temperature profile compared with the DNS data of Lechner et al. (2001). (▬ ▬ ▬) represents the reference solution and (▬▬) represents the time-averaged DNS solution.

The cooled isothermal walls remove the heat generated by dissipation inside the channel. Figure 5.21 shows the mean density profile and its RMS fluctuation. The trend followed by the mean density profile is opposite to that of the mean temperature profile. This can be attributed to the flow being essentially isobaric. Using eq. (3.14), it is apparent that for such a flow, the wall-normal gradients of temperature and density take opposite signs. It was shown by

Lechner et al. (2001) that the large RMS fluctuations in the buffer region could mainly be attributed to the steep negative wall-normal gradients and a positive turbulent mass flux. Far from the walls, there is a significant decrease in the density and temperature fluctuations in the core of the channel as the influence of wall-induced shear diminishes, and the turbulent structures become more isotropic.

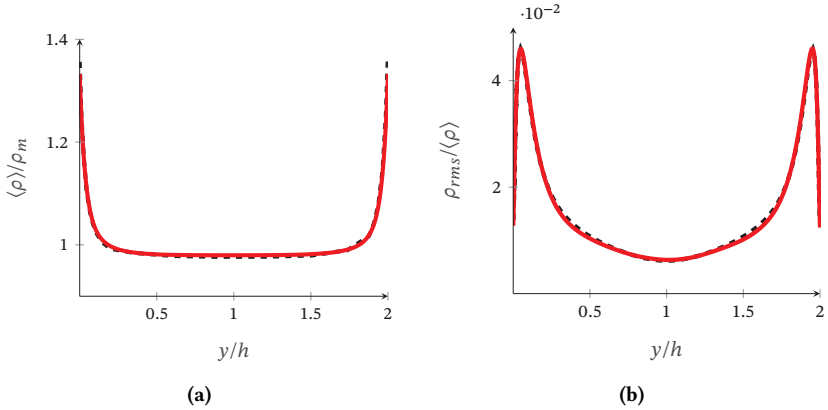

Figure 5.21: Comparison of (a) mean normalized and (b) RMS density fluctuation profile compared with the DNS data of Lechner et al. (2001). (▪ ▪ ▪) represents the reference solution and (▬) represents the time-averaged DNS solution.

Figure 5.22 shows the wall-normal profiles of mean Mach and Reynolds numbers compared to the DNS data of Coleman et al. (1995). Both the non-dimensional parameters achieve a maximum at the channel centerline and vanish at the walls. The mean centerline Mach number (Ma_c) and mean centerline Reynolds number (Re_c) take the value of 1.5 and 2760, respectively. Interestingly, the value of Re_c for the present test is lower than that of Kim et al. (1987), who reported a value of $Re_c = 3250$ at $Ma = 0$. This might be because of the increased influence of viscous effects compared to the inertial effects since the dynamic viscosity increases towards the channel centerline as seen in fig. 5.23. Figure 5.23 shows the normalized mean dynamic viscosity profile. Since $\mu \propto T^{0.7}$, the fluid's viscosity also achieves a minimum at the walls and a maximum at the channel centerline.

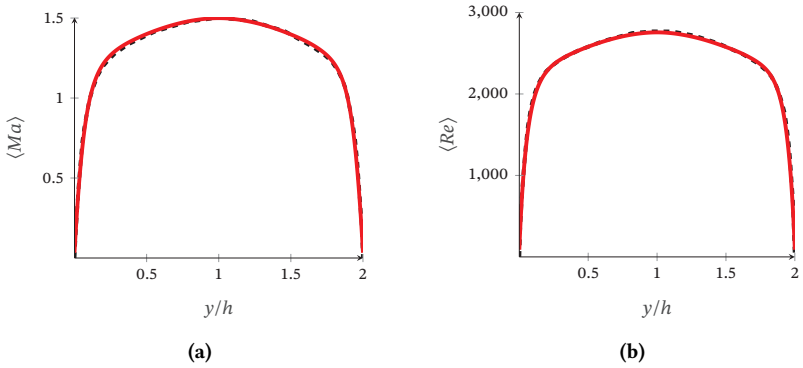

Figure 5.22: Comparison of (a) mean Mach number and (b) mean Reynolds number profile compared with the DNS data of Coleman et al. (1995). (▬ ▬ ▬) represents the reference solution and (▬) represents the time-averaged DNS solution.

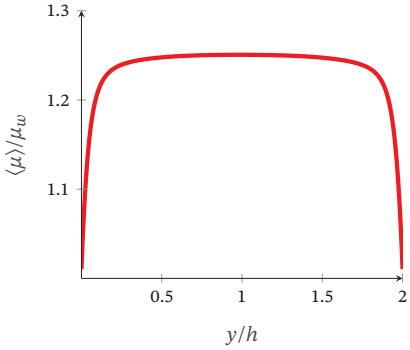

Figure 5.23: Profile of mean dynamic viscosity (▬) normalized by the wall viscosity

Figure 5.24 shows the profiles of turbulent Mach number and the mixing length. The turbulent Mach number Ma_t is defined in eq. (5.28).

$$Ma_t = \sqrt{\langle u_i' u_i' \rangle}/c \tag{5.28}$$

The turbulent Mach number peaks in the buffer region, showing the relative importance of compressibility effects in turbulent characteristics in this region. It was also previously shown by Coleman et al. (1995) that the dilatation is close to zero in the channel's core except near the walls. It was later concluded by Lechner et al. (2001) that for the same flow, the compressibility effects appeared only near the channel walls by analyzing the Reynolds stress tensor normalized with wall shear stress. They observed that the axial stress in this region was increased, and the other components were reduced compared to the incompressible counterpart by Kim et al. (1987).

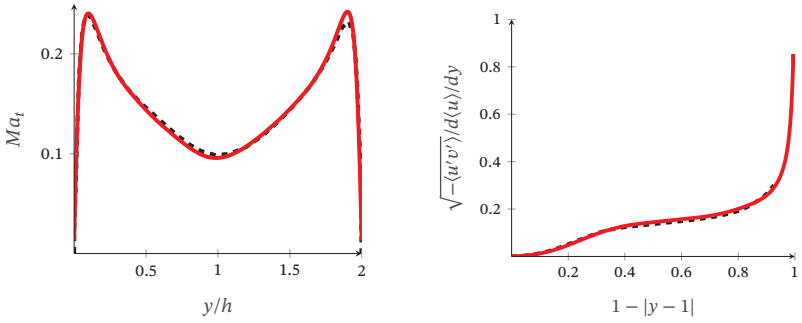

Figure 5.24: Comparison of (a) the turbulent Mach number and (b) mixing length compared with the DNS data of Coleman et al. (1995). (▪ ▪ ▪) represents the reference solution and (▬) represents the time-averaged DNS solution.

Figure 5.25 shows the contours of instantaneous streamwise velocity fluctuations. Strong streamwise fluctuations near the walls can be seen in the figure. Coleman et al. (1995) had previously demonstrated that compressibility enhances the coherence of near-wall streaks, thereby increasing the streamwise correlation length. Conversely, the spanwise spacing of these streaks remains approximately equivalent to that observed in incompressible flow. Lechner et al. (2001) defined the positive streamwise velocity fluctuations near the walls as sweeps ($u' > 0$) and the negative streamwise velocity fluctuations near

the walls as ejections ($u' < 0$). The contours of the streamwise velocity fluctuations at $y^+ = 9$ in the buffer layer are plotted in fig. 5.26. The sweeps and ejections appear alternatingly and carry high-velocity fluid to the walls while moving low-speed fluid away. It was observed by Lechner et al. (2001) that the sweeps carry mostly the positive temperature fluctuations, and the ejections carry mostly the negative temperature fluctuations.

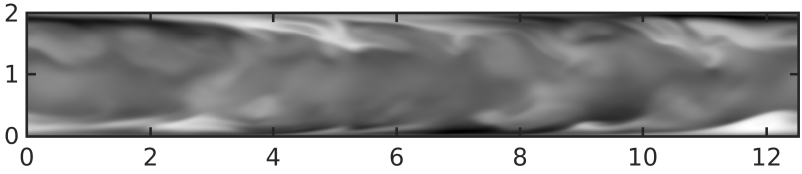

(a) $x - y$ plane

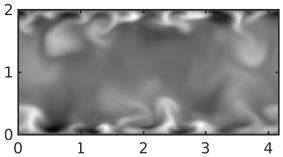

(b) $y - z$ plane

Figure 5.25: Instantaneous field of streamwise velocity fluctuation at $Re_\tau \approx 200$ and $Re_b = 3000$ plotted on a grayscale from strongly negative (black) to strongly positive (white). (a) shows the contours in the $(x - y)$ plane at $z = 0.5L_z$. (b) shows the contours in the $(y - z)$ plane at $x = 0.5L_x$.

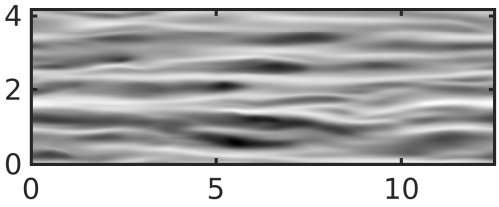

Figure 5.26: Contours of streamwise velocity fluctuations normalized with the bulk velocity (u'/u_m) at $y^+ = 9$ in the $x - z$ plane. Contours are plotted on a grayscale from strongly negative (black) to strongly positive (white).

Figure 5.27 shows the isosurfaces of the streamwise velocity fluctuations near the lower wall and gives a deeper insight into the structures of sweeps and ejections. The isosurface of the q-criterion is also plotted to show the evolution of vortices near these structures. Pointed out by Lechner et al. (2001), it can be observed that the shearing between these sweep and ejection structures generates these vortices.

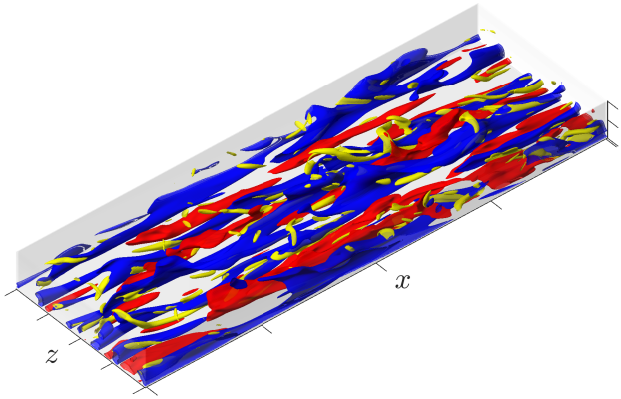

Figure 5.27: Isosurfaces of streamwise velocity fluctuations normalized with the bulk velocity (u'/u_m) and the q-criterion (q). Blue represents the isosurface of $(u'/u_m) = +0.15$ and red represents the isosurface of $(u'/u_m) = -0.15$. Yellow shows the isosurface of $q = u_m^2/h^2$.

In conclusion, Direct Numerical Simulation (DNS) of supersonic compressible wall-bounded turbulent channel flow is performed at $Ma = 1.5$, $Re = 3000$, and $Pr = 0.7$. Mean flow fields, non-dimensional quantities, and other relevant flow quantities are evaluated after the flow reaches statistical stationarity and are compared with the reference data of Coleman et al. (1995) and Lechner et al. (2001). A good agreement is obtained in the comparisons.

5.3 Inviscid two phase validation

5.3.1 Strong shock near a stationary wall

In the current validation test for the Immersed Boundary Method for Euler's equations in one dimension, a cooled gas with a constant velocity is brought to rest by a rigid stationary wall. Collision with the wall generates a strong shock wave that propagates away from the wall at a constant shock velocity. This test has been performed previously by Noh (1987) to compute the errors involved using an artificial viscosity method in the numerics involving shocks with considerable shock strengths. The flow state behind the shock can be evaluated using normal shock relations (Toro 2013).

In a domain $x \in [-0.5, 0.5]$, the wall is placed between $-0.5 < x \leq 0$. The fluid to the right of the wall travels with an initial velocity ($u_o = -1$), density ($\rho_o = 1$), and pressure ($p_o = 10^{-6}$) towards the wall, compressing the gas, heating the fluid, and generating a strong shock wave.

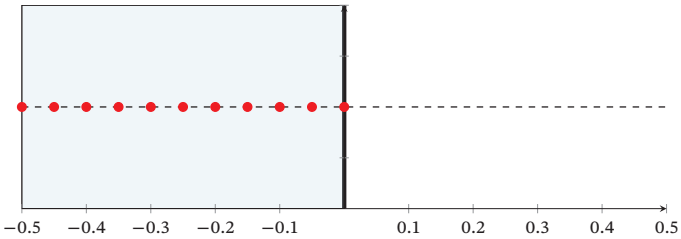

Figure 5.28: Lagrangian marker distribution for representation of a stationary wall in one-dimension. (●) represents the lagrangian markers equispaced in the wall region between $-0.5 < x \leq 0$.

Numerically, the wall is represented by a group of lagrangian markers, which are equispaced inside the wall region as shown in fig. 5.28. A no-penetration normal velocity boundary condition is implemented at the lagrangian markers, which generates a source term in the momentum equations to bring the

momentum of the fluid near the walls to zero. The details of the immersed boundary procedure are given in section 4.3.

The analytical solution involves a shock traveling towards the right with a shock velocity ($S = 1/3$). The pressure and density behind the shock are given by $\rho_l = 4$ and $p_l = 1.33$, respectively. The solution is advanced in time until $t_f = 0.6$ using a 3^{rd} order Runge Kutta scheme for temporal evolution and a 5^{th} order WENO scheme with characteristic decomposition for advection. The computed DNS solution is compared to the exact solution and is shown in fig. 5.29. An overall good agreement with the analytical solution is obtained in the smooth regions with larger deviation near the discontinuity. The L_2 errors ($\mathcal{E}_{L2}$) of the density, velocity, and pressure fields were evaluated by comparing to the exact-solution with 300 grid-points. $\mathcal{E}_{L2}$ for pressure was 0.1106, for density was 0.2414, and for velocity was 0.0664.

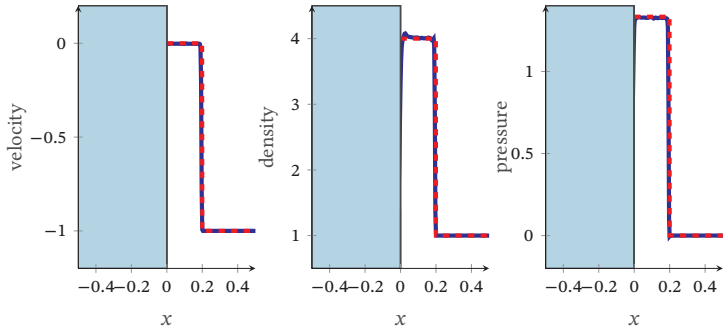

Figure 5.29: Comparison of the flow state to the right of the stationary wall computed using DNS (▬) with 300 gridpoints compared to the exact solution (▪ ▪ ▪).

5.3.2 Shock interaction with a fixed sphere

When a shock wave passes over a fixed particle, the transient pressure-induced force experienced by the particle behaves non-monotonically. The particle drag increases sharply as the shock wave sweeps over the particle, reaching a peak when the shock wave reaches the transverse grand circle before it decreases again and reaches a local minimum (given that the local

Reynolds number is sufficiently high). The local minimum of the drag is due to the diffraction of the shock wave downstream of the particle, resulting in a local negative inviscid unsteady contribution to the total drag. Afterwards, the drag increases again and reaches an asymptotic value. The viscous effects are minor compared to the pressure contributions to the peak drag during the transient within a couple of shock-interaction time scales (Behrendt et al. 2022). Shock interaction with a fixed isolated particle has been studied in previous works experimentally and numerically, for example, by Tanno et al. (2003), Sun et al. (2005), Wagner et al. (2012a), Mehta et al. (2016a), and Behrendt et al. (2022).

When the post-shock Mach number behind the shock wave is less than a critical value (Ma_{crit}), the inviscid contribution to the asymptotic long-time drag experienced by the particle goes down to zero (Behrendt et al. 2022). In such a case, the quasi-steady drag is dominated by viscous contributions. For a spherical particle, the critical Mach number is approximately 0.6. However, if the post-shock Mach number is supercritical, the long-time inviscid contributions to the quasi-steady drag will be non-zero. Hence, quasi-steady drag would have both inviscid and viscous contributions. In a supercritical flow, as the fluid accelerates near the spherical particle's convex boundary, the flow may become supersonic at some point. The fluid then adjusts to the downstream conditions through shocklets. However, if the post-shock conditions are supersonic, a bow shock forms upstream of the particle in addition to the recovery shock. These shocklets and bow shocks contribute to the non-zero inviscid contribution to the quasi-steady drag for post-shock Mach numbers greater than the critical value.

Two different cases of shock interaction with an isolated fixed particle are considered. One in which the post-shock conditions are subsonic ($Ma_s = 1.22$), and the other in which the post-shock conditions are supersonic ($Ma_s = 3$). The definition of the drag coefficient used in the current section is defined in eq. (5.29). The subscript 'ps' represents the post-shock flow condition, F_x is the total instantaneous force on the particle in the streamwise direction, and A_p is the frontal area ($A_p = \pi r^2$ for a sphere with radius r).

$$C_D = \frac{F_x}{\frac{1}{2}\rho_{ps} u_{ps}^2 A_p} \tag{5.29}$$

5.3.2.1 Shock-particle interaction: $Ma_s = 1.22$

Experiments and numerical simulations of shock interacting with an isolated spherical particle at $Ma_s = 1.22$ were performed by Sun et al. (2005). They performed experiments in air and boundary-conforming axisymmetric numerical simulations of shock-particle interactions for Reynolds number between 49 and 4.9×10^5. In the current section, DNS simulations at $Ma_s = 1.22$ are performed, with the spherical particle being represented numerically using the Immersed Boundary Procedure as explained in appendix D.

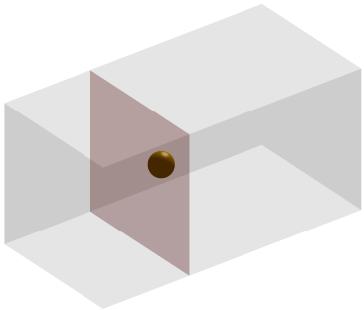

Figure 5.30: Initial geometry for the problem of shock-particle interaction at $Ma_s = 1.22$ in an inviscid flow. The spherical particle is initially centered at $x_c = [5,3,3]$. A shock wave (shown in red) is placed in the $y-z$ plane at $x = 4$.

In a computational domain, $x \in [0,12]$, $y \in [0,6]$, and $z \in [0,6]$, a fixed spherical particle of diameter ($D = 1$) is initially placed at $x_c = [5,3,3]$. A $Ma_s = 1.22$ shock is initially placed at $x_s = 4$, such that the pre-shock condition (flow state to the right of the shock wave) is ambient, and the post-shock Mach number (Ma_{ps}) is 0.312377. In these post-shock conditions, the flow

state is essentially incompressible. Free-slip, no-penetration boundary conditions are implemented at the particle surface using the immersed boundary procedure. The initial flow configuration is shown in fig. 5.30. Periodic boundary conditions are set along the transverse directions in the domain, and non-reflecting inflow-outflow boundary conditions are implemented at the boundary planes normal to the flow direction. A 5^{th} order TENO scheme for advection and a 3^{rd} order Runge Kutta scheme for time evolution is used. The shock wave was traveling at the shock speed ($u_s = Ma_s a_r$), where a_r is the speed of sound based on the preshock conditions. The instantaneous numerical schlieren computed from the density gradient magnitude of the flow at different times is given in fig. 5.31. As the shock passes over the particle, A reflected bow shock is formed and travels away from the sphere location. In fig. 5.31c, diffraction of the shock wave downstream of the particle location is visible, which results in instantaneous negative inviscid drag experienced by the particle.

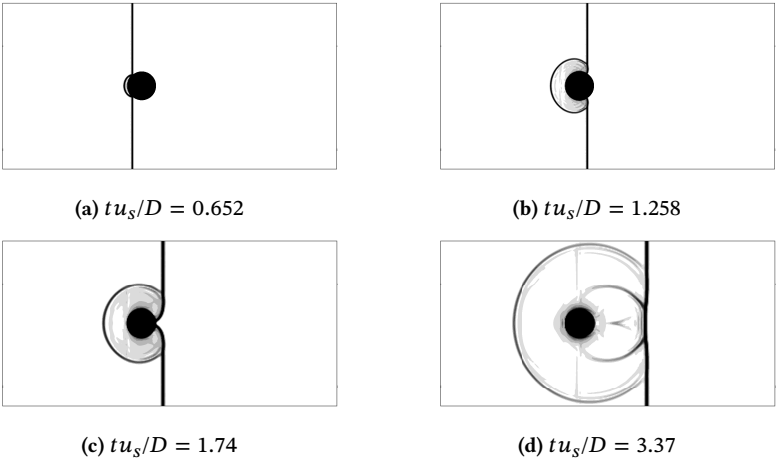

(a) $tu_s/D = 0.652$ **(b)** $tu_s/D = 1.258$

(c) $tu_s/D = 1.74$ **(d)** $tu_s/D = 3.37$

Figure 5.31: Numerical schlieren for shock-particle interaction at $Ma_s = 1.22$ in an inviscid flow showing the evolution of the reflected shock wave with time.

The transient drag experienced by the particle as the shock sweeps the particle is shown in fig. 5.32. The peak drag achieves a peak around $tu_s/D \approx 0.5$.

It is observed that the peak drag, which is dominated by the inviscid mechanisms, is well captured by the current DNS simulations at a particle resolution of $D/dx = 30$. It should be noted that although the long-time drag contribution by inviscid mechanisms is zero, the diffuse interface immersed boundary procedure introduces some additional diffusive effects. Hence, the long-time drag behaves similarly to a large Reynolds number flow state, resulting in a slight positive deviation from zero drag. It was found that the mean drag coefficient (C_D) evaluated by calculating the average between $u_s t/D_p = 10$ and $u_s t/D_p = 15$ at grid resolution of $D_p/\,\mathrm{d}x = 30$ was 0.4692. Note, that this is close to the drag coefficient in the inertial range ($10^3 < Re < 10^5$) (Crowe et al. 2011).

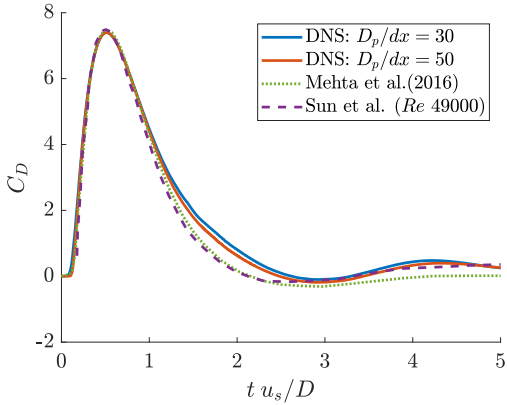

Figure 5.32: The transient drag coefficient for a spherical fixed sphere interacting with a shock at shock mach number ($Ma_s = 1.22$) in an inviscid flow. (——) and (——) represent the computed DNS solution at a resolution of $D_p/\,\mathrm{d}x = 30$ and $D_p/\,\mathrm{d}x = 50$ respectively. (.....) and (– – –) represent the results from the boundary conforming simulations of Mehta et al. (2016b) under inviscid conditions and Sun et al. (2005) at Reynolds number of ($Re = 49000$) respectively.

5.3.2.2 Shock-particle interaction: $Ma_s = 3$

In this section, a shock wave of $Ma_s = 3$ interacting with a fixed isolated particle is studied in an inviscid flow. The geometrical configuration and the

boundary conditions are the same as the one used in section 5.3.2.1. However, in this case, the post-shock condition ($Ma_{ps} = 1.35769$) is supersonic. Similar to section 5.3.2.1, the transient total drag on the particle reaches a peak and decreases henceforth. However, the quasi-steady asymptotic value of the drag does not go down to zero; rather, it settles at a positive value. The isosurface of density gradient magnitude at $u_s t/D = 4.42$ is shown in fig. 5.33. As the incident shock wave passes over the particle, a bow shock is formed upstream of the particle. The presence of the bow shock at long times contributes towards the non-zero quasi-steady drag.

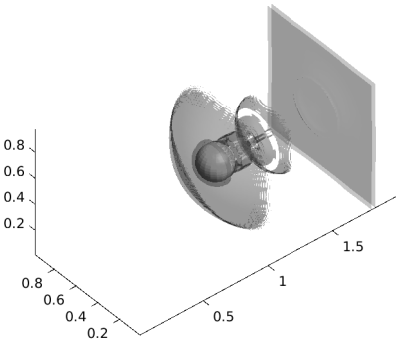

Figure 5.33: Isosurface of density-gradient magnitude for the $Ma_s = 3$ shock interacting with a spherical particle in inviscid flow.

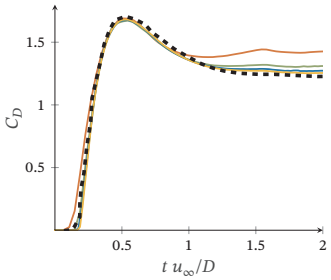

Figure 5.34: Transient drag for a shock of $Ma_s = 3$ interacting with an isolated sphere in an inviscid flow at different particle resolutions (DNS performed by Prof. Markus Uhlmann, KIT) (——) $D/dx = 24$ (——) $D/dx = 48$ (——) $D/dx = 72$ (——) $D/dx = 96$ compared to the reference solution of Mehta et al. (2016a) (▪ ▪ ▪)

Figure 5.34 shows the grid convergence plot of the transient total drag experienced by the particle as the incident shock wave traverses over the fixed spherical particle compared to the Boundary conforming results of Mehta et al. (2016a). The Direct Numerical Simulations performed to check convergence in the current test were performed by Prof. Markus Uhlmann, Karlsruhe Institute of Technology. The peak drag, dominated by pressure gradient contribution, is captured well at all the resolutions. It is also observed that the long time quasi-steady drag predictions improve at higher grid resolutions.

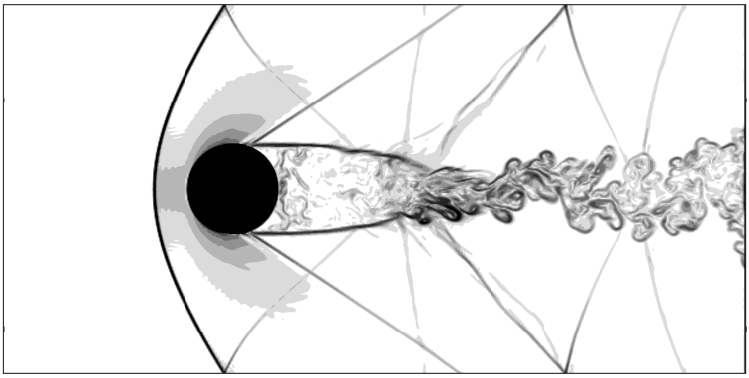

Figure 5.35: Numerical schlieren for shock of $Ma_s = 3$ interacting with a spherical particle at $u_s t/D = 16.82$. The figure shows the bow shock upstream of the particle long after the passage of the incident shock wave evaluated at $D_p/\,\mathrm{d}x = 30$.

Figure 5.35 shows the numerical schlieren at $u_s t/D = 16.82$, long after the incident shock has sweeped the particle. The flow is characterized by a bow shock upstream of the particle and an unstable wake downstream of the particle. The presence of the bow shock can be explained by the higher upstream velocity than the local acoustic velocity. Hence, the upstream flow is not forewarned about the presence of an obstacle until it is sufficiently close. The upstream flow then adjusts to the obstacle by sudden compression and change of properties over a few molecular diameters upstream of the particle, which we observe in the form of a bow shock.

5.4 Viscous two phase validation

The Navier-Stokes equations are solved on the fixed cartesian grid, and a no-slip, no-penetration boundary condition is used to represent the solid boundary. During the shock-wave interaction with an isolated fixed particle, the viscous drag contribution is especially significant at long-time quasi-steady conditions, where the pressure drag contributions are lower than the initial peak in the transient.

In the current section, a DNS of incompressible flow around a sphere is performed at a Mach number of 0.2 and Reynolds number of 240. Next, a shock wave interaction with an isolated fixed particle is performed at two different Reynolds numbers and a constant shock Mach number. The results are compared to the available boundary-conforming reference data at the same parameter point of Sun et al. (2005) and Professor Sivaramakrishnan Balachandar's group at the University of Florida through internal communication. The effect of constant temperature boundary conditions on a single particle's wake regime, drag, and lift is studied and compared to the available data of Nagata et al. (2018). Finally, the flow through a homogenous distribution of fixed particles is studied and compared with the data for the boundary-conforming simulations of Osnes et al. (2023).

5.4.1 Flow around an isolated fixed particle

5.4.1.1 Incompressible viscous flow around a sphere

Direct Numerical Simulation of viscous flow at Reynolds number of ($Re = 240$), Prandtl number ($Pr = 1$), and Mach number of ($Ma = 0.2$) is performed. The aim is to test the accuracy and applicability of the compressible DNS flow solver with the diffuse interface immersed boundary method for studying incompressible multiphase flow systems.

Since the flow does not have shock waves or sharp gradients, a finite-difference scheme based on the entire stencil (without preferential weights given to sub-stencils in schemes like WENO-JS and TENO) for positive and

negative fluxes eq. (4.11), called the 5^{th} order large stencil scheme is used. The viscous terms are discretized using a second-order central finite-difference scheme, and the time integration is through the third-order low-storage Runge Kutta method. The Mach number (Ma) and the Reynolds number (Re) are calculated based on the free-stream conditions. Inflow-outflow boundary conditions in the streamwise direction and periodic boundary conditions in the transverse directions are implemented. The internal energy at the particle surface is fixed at the value based on free-stream conditions.

At the low Mach number, the flow is essentially incompressible, and the drag and lift values computed for rigid-fixed spheres using a spectral-element flow solver by Bouchet et al. (2006) for incompressible flows can be used for comparison. At the Reynolds number of 240, chosen in the current DNS test, the flow regime is steady and non-axisymmetric at the end state. The drag and lift experienced by the sphere and the relative errors are shown in table 5.4 at different grid resolutions, and the drag convergence with grid refinement is plotted in fig. 5.36.

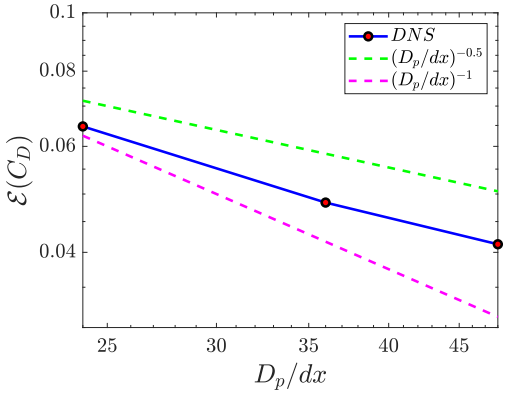

Figure 5.36: Convergence of the relative error in drag coefficient compared to Bouchet et al. (2006) for flow at $Re = 240$, $Ma = 0.2$, $Pr = 1$ over an isolated fixed sphere.

It is observed that the flow regime is captured well by the current DNS simulations. The relative errors in drag and lift coefficients compared to the reference solution at $D/dx = 48$ are 4.1 % and 5.6 %, respectively.

Table 5.4: Comparison of the drag and lift coefficients at different grid resolutions for flow at $Re = 240$, $Ma = 0.2$, $Pr = 1$ over an isolated fixed sphere with the results of Bouchet et al. (2006).

$D_p/\,\mathrm{d}x$	C_D	$C_{D,ref}$	$\mathcal{E}_{CD}$	C_L	$C_{L,ref}$	$\mathcal{E}_{C_L}$
24	0.761	0.715	0.065	0.0599	0.057	0.052
36	0.750	0.715	0.048	0.0600	0.057	0.053
48	0.744	0.715	0.041	0.0602	0.057	0.056

5.4.1.2 Shock wave interaction with a fixed sphere: $Re = 49$

The unsteady drag for an incident shock wave interacting with a fixed sphere at Reynolds number of $Re = 49$ and $Ma_s = 1.22$ is studied. The Prandtl number (Pr), shock Mach number (Ma_s), the viscous law used, and the numerical schemes used are the same as section 5.4.1.3. The choice of flow parameters is the same as the classical boundary-conforming axisymmetric simulation of Sun et al. (2005).

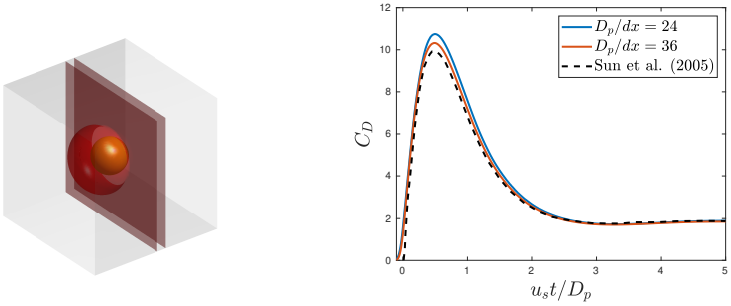

(a) **(b)**

Figure 5.37: Fixed sphere interacting with an incident shock wave of shock Mach number ($Ma_s = 1.22$) and Reynolds number ($Re = 49$): (a) Isosurface of density gradient magnitude at $u_s t/D_p = 0.8943$ (b) Convergence of transient drag with grid refinement compared to the reference solution of Sun et al. (2005).

Figure 5.37a shows the instantaneous isosurface of density gradient magnitude (in red) as the shock wave sweeps over the particle at $u_s t/D_p = 0.8943$.

A developing reflected shock wave can be seen upstream of the particle. Figure 5.37b shows the total drag coefficient computed at two different grid resolutions compared to the reference solution of Sun et al. (2005). The transient and quasi-steady drag are captured, and the computed solution agrees well and converges towards the reference solution.

5.4.1.3 Shock wave interaction with a fixed sphere: $Re = 100$

Unsteady drag on a fixed sphere is evaluated for a shock wave of shock Mach number ($Ma_s = 1.22$) and Reynolds number ($Re = 100$) using Direct Numerical Simulations. The Reynolds number is based on particle diameter, post-shock velocity, viscosity, and density. The Prandtl number of the flow is constant and is chosen as 0.7. The internal energy of the sphere is fixed at the pre-shock value throughout the simulation. In addition, Sutherland's temperature-dependent viscous law is implemented. For air as the medium, the chosen Reynolds number and Mach number would depict a diameter of the order of ten microns at standard temperatures and pressures. This would represent shock wave interaction with particles like spores, dust, and silt in nature. The transient drag is compared to the boundary-conforming results with the same parameters kindly provided by Sam Briney and Professor Sivaramakrishnan Balachandar, University of Florida.

The 5^{th} order TENO scheme (Liang et al. 2022) is used for advection, which ensures low dissipation near the shock wave. For diffusion, the second-order central finite difference scheme is used. A third-order low-storage Runge Kutta scheme (Rai and Moin 1991) is used for temporal evolution. Non-reflecting inflow-outflow boundary conditions along the direction of the incident shock wave and periodic boundary conditions in the transverse directions are implemented.

In fig. 5.38a, it is seen that the drag computed by the immersed boundary procedure converges to the boundary-conforming results for the transient peak and after the passage of the incident shock wave. Figure 5.38b shows the convergence of the relative errors in peak drag compared to the reference data with grid refinement. A close-to and slightly better than the first-order

convergence is observed. The relative error is 2.4% at the highest particle resolution of $D_p/\,\mathrm{d}x = 96$, where D_p is the diameter of the fixed sphere.

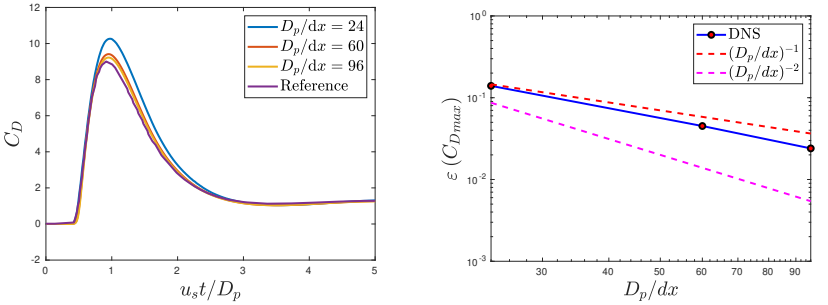

(a) **(b)**

Figure 5.38: Fixed sphere interacting with an incident shock wave of shock Mach number ($Ma_s = 1.22$) and Reynolds number ($Re = 100$): (a) Transient drag at different grid resolutions compared to the reference boundary conforming data provided by Sam Briney and Professor Sivaramakrishnan Balachandar, University of Florida (b) Convergence of relative errors in peak drag with grid refinement.

The total drag force experienced by the particle can be represented by the sum of quasi-steady, pressure-gradient, inviscid, and viscous unsteady contributions. Previously, Parmar et al. (2009) have used this idea to model the unsteady drag over a sphere for a shock wave passing over a particle. Similar to the inviscid shock-particle test at the same shock Mach number in section 5.3.2.1, as the incident shock wave sweeps the particle, the transient drag reaches a peak, which is dominated by inviscid mechanisms. The drag then decreases and settles at the quasi-steady value. It should be noted that at the low Reynolds number chosen for this test, the total drag never reaches negative values. This feature can be attributed to the viscous quasi-steady contributions dominating the inviscid unsteady contributions during the shock-wave diffraction downstream of the sphere.

Unlike in section 5.3.2.1, both the initial peak transient and the quasi-steady state are well-captured by the compressible multi-phase flow solver. Flow at large Reynolds numbers is expected to require finer grid refinement for convergence, especially to capture the quasi-steady state where the viscous

contributions are non-negligible compared to the inviscid contributions. This can be explained by the fact that at higher Reynolds number, the half-width of the three-point discrete delta stencil (Roma et al. 1999) used in the immersed-boundary procedure may become comparable to the existing physical boundary layer.

5.4.1.4 Effect of Mach number, Reynolds number, and Temperature ratio on the flow around an isolated fixed sphere

In addition to the Mach number and the Reynolds number, it was established by Nagata et al. (2018) through boundary-fitted Direct Numerical Simulations that the temperature ratio between the particle and free-stream flow can have a direct impact on the flow regime, particle drag, lift, and heat transfer. No-slip and isothermal boundary conditions were imposed on the particle in their study, and Sutherland's temperature-dependent viscous law (Sutherland 1893) was used. They defined the Temperature Ratio (TR) as the ratio of particle and free-stream temperatures, the Mach number (Ma) as the ratio of free-stream flow and acoustic velocities, and the Reynolds number (Re) based on the free-stream quantities and particle diameter. The definitions of the non-dimensional quantities are given in eq. (5.30). The subscript "∞" represents the quantities in free-stream conditions.

$$TR = \frac{T_p}{T_\infty} \qquad Ma = \frac{|\mathbf{u}_\infty|}{c_\infty} \qquad Re = \frac{\rho_\infty |\mathbf{u}_\infty| D_p}{\mu_\infty} \tag{5.30}$$

They concluded that in the range of Reynolds number ($Re = 0{-}300$) and Mach number ($Ma = 0.3 - 2$), the flow seemed to stabilize with increasing temperature ratio in subsonic conditions. For example, the flow at $Re = 250$ and $Ma = 0.8$ had unsteady periodic vortex-shedding in the wake at $TR = 0.5$, a steady non-axisymmetric flow at $TR = 0.9$, and a steady axisymmetric flow at $TR = 2$. At supersonic conditions, however, the flow was steady axisymmetric at all values of Re and TR in the parameter range. Hence, for subsonic conditions, increasing TR was similar to lowering Re on the wake regime and vice versa. This could be understood by the dependence of dynamic viscosity on the temperature through Sutherland's law. A high TR would lead to the

heating of the fluid in the sphere's vicinity, consequently increasing the fluid viscosity and decreasing the fluid density. The overall effect is an increase in the kinematic viscosity with TR. Since the viscous effects are stronger at higher TR, any flow instability, like unsteady vortex shedding, can be dampened more effectively at higher TR. This explains the stabilizing effect of TR on the particle wake.

It was observed in their study that the total drag coefficient increased with TR. However, the effect of TR on the drag in the continuum regime has traditionally been ignored by most drag correlations. The RMS amplitude of the lift forces and the non-dimensional frequency of oscillation given by the Strouhal number also decrease (in general) with increasing TR. Similar reasoning of increased viscous effects with TR can be used to explain the general behavior of drag and lift coefficients.

There are multiple Nusselt number (Nu) correlations around a fixed isolated sphere like from the works of Sauer (1951), Ranz and Marshall (1952), Whitaker (1972), Yamanaka et al. (1976), Fox et al. (1978), Feng and Michaelides (2000), Richter and Nikrityuk (2012), and Qi and Yu (2021) under a range of flow conditions. However, the literature considering the collective effect of Mach number (Ma), Reynolds number (Re), and the temperature Ratio (TR) between sphere and free-stream conditions is limited for compressible flows. It was shown from the DNS simulations of Nagata et al. (2018) that for flows where the TR is significantly different from unity, the fluid state in the sphere's vicinity can be quite different from the free-stream conditions. The Nusselt number for the sphere evaluated through their Direct Numerical Simulations compared to the classical correlations was higher at low TR and vice versa. Hence, the balance between heat transfer through forced convection and conduction should consider the local change of viscosity and fluid density to evaluate the Nusselt number. Another interesting feature observed from their DNS study was the behavior of the Nusselt number for supersonic flows at $Re = 300$. In that case, they found that for $TR > 1$ (but still sufficiently close to unity), the Nusselt number became negative. Although the free-stream temperature was lower than the sphere, the flow ahead of the shock was compressed and heated up, locally

making the fluid hotter than the sphere. Consequently, the heat transfer coefficient is negative for such a flow scenario. The complex flow patterns in a compressible flow can affect the heat transfer rate and direction based on the local variations of flow properties. Hence, they should be taken into account when modeling Nusselt number correlations.

In this section, Direct Numerical Simulations for flow around an isolated fixed particle are performed for a few parameter points from the study of Nagata et al. (2018) for different Reynolds numbers, Mach numbers, and Temperature Ratios. Professor Takayuki Nagata, from Nagoya University, is acknowledged for kindly providing the data for particle force history, averaged drag and Nusselt numbers, and local temperature profiles near the particle for the chosen parameter points. The flow patterns, drag coefficient, Nusselt number, and temperature profiles are compared to the provided reference data for the chosen parameter points.

The choice of parameter points

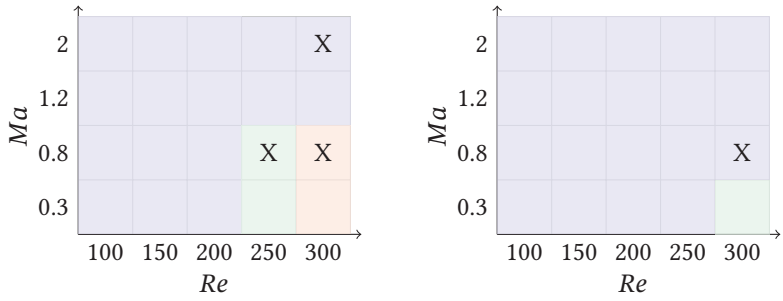

(a) Temperature ratio $(T_p/T_\infty) = 0.8$ **(b)** Temperature ratio $(T_p/T_\infty) = 2$

Figure 5.39: Choice (**X**) of free-stream Mach number (Ma), Reynolds number (Re) and Temperature Ratio (TR) chosen for comparison with boundary conforming results of Nagata et al. (2018). The different flow regimes from their DNS study are color coded as Unsteady periodic Axisymmetric Non axisymmetric.

The wake regimes for compressible flow around a fixed isolated sphere based on the freestream Mach number, Reynolds number, and Temperature ratio were characterized by Nagata et al. (2018). Four of their cases were chosen

by varying the Re, Ma, and TR to evaluate the capability of the current DNS solver in accurately capturing the wake patterns.

Starting with the base case for unsteady periodic flow pattern with $Ma = 0.8$, $Re = 300$, and $TR = 0.9$, the Ma is increased to $Ma = 2$ for the second case (steady axisymmetric), the Re is reduced to $Re = 250$ in the third case (Steady non-axisymmetric), and finally the TR is increased to $TR = 2$ in the fourth case (Steady axisymmetric). The choice of parameters is summarised in fig. 5.39.

Unsteady periodic flow: $Ma = 0.8, Re = 300, TR = 0.9$

At this choice of Re, Ma, and TR, the diffusive mechanisms are not fast enough to dampen the unsteady perturbations in the sphere's wake, leading to unsteady periodic vortex shedding in the wake of the sphere. The instantaneous wake behind the sphere is shown in fig. 5.40 as isosurface of Q-criterion. Hairpin-like structures are visible in the wake of the sphere.

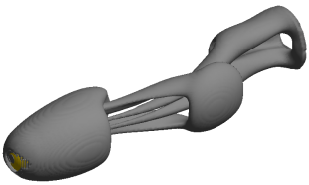

Figure 5.40: Instantaneous wake structure for flow around a fixed isolated sphere at $Re = 300$, $Ma = 0.8$, $TR = 0.9$ given by the isosurface of the second invariant of the velocity gradient tensor given by $QD_p^2/u_\infty^2 = 5 \times 10^{-4}$.

Reference quantities based on the freestream conditions are used in normalization to evaluate the Drag coefficient, Lift coefficient, and Nusselt number. The definitions of these non-dimensional quantities quantifying the fluid-particle heat and momentum exchange are given in appendix F.

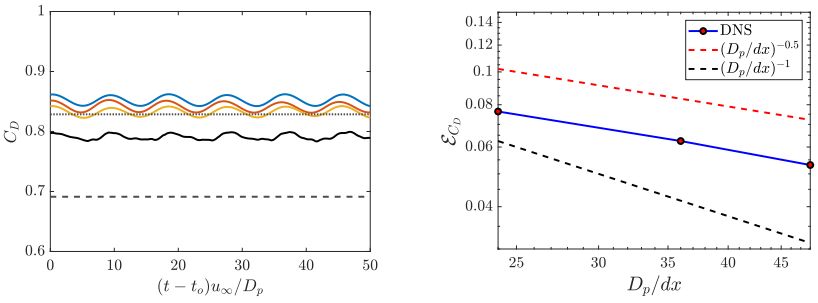

Figure 5.41: (a) Drag coefficient for flow at $Ma = 0.8$, $Re = 300$ and $TR = 0.9$ at different resolutions (——) D_p/dx = 24, (——) D_p/dx = 36, (——) D_p/dx = 48 compared to the boundary conforming DNS data of Nagata et al. (2018) (——), drag correlation by Loth et al. (2021) (. . . . .), and incompressible drag correlation by Clift and Gauvin (1971a) (– – –) (b) Convergence of relative error in drag coefficient compared to the reference data of Nagata et al. (2018) with grid refinement.

Figure 5.41 shows the convergence of drag coefficient with grid refinement and comparisons with DNS data of Nagata et al. (2018) and drag models of Loth et al. (2021) and Clift and Gauvin (1971a). The time t_o in fig. 5.41a is an arbitrary time after the flow has been established. Comparison with the incompressible drag model of Clift and Gauvin (1971a) shows that the drag coefficient over a sphere increases at $Ma = 0.8$ compared to the incompressible flow ($Ma = 0$). The effect of compressibility was considered in the model based on Mach and Reynolds number of Loth et al. (2021), which also agrees with this trend. In general, for supercritical but subsonic flows ($0.6 < Ma < 1$), the drag coefficient increases sharply with the Mach number. From the DNS simulations of Nagata et al. (2018), it was observed that the drag coefficient also increases with the temperature ratio, which can be explained by the increasing viscous effects compared to the inertial effects, which in turn reduces the local Reynolds number in the sphere's vicinity. Overall, a good agreement with the reference DNS data of Nagata et al. (2018) is obtained with 5.3 % relative error in the computed drag coefficient at $D_p/\,\mathrm{d}x = 48$. Another observation in fig. 5.41a is the unsteadiness present in the observed time-dependent drag coefficient.

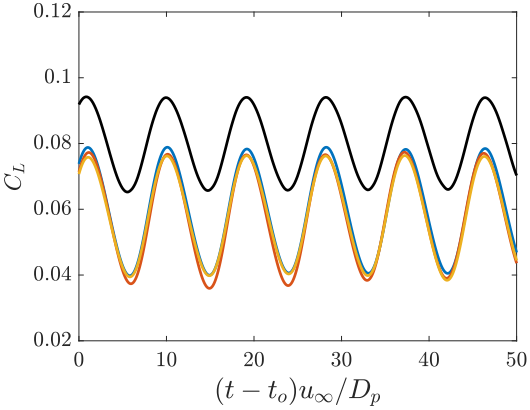

Figure 5.42: Lift coefficient (C_L) for flow around a fixed isolated sphere at $Re = 300$, $Ma = 0.8$, $TR = 0.9$ at (——) D_p/dx = 24, (——) D_p/dx = 36, (——) D_p/dx = 48 compared to the DNS results of Nagata et al. (2018) (——).

Figure 5.42 shows the lift coefficient (C_L) compared to the boundary conforming DNS results of Nagata et al. (2018). C_L oscillates periodically in time, showing the unsteady nature of the wake. The non-dimensional frequency of vortex shedding given by Strouhal Number (St) is defined in eq. (5.31), where f is the dimensional frequency of vortex shedding.

$$St = \frac{f D_p}{u_\infty} \tag{5.31}$$

The Strouhal number evaluated from the current DNS runs agrees well with the reference value from boundary-conforming results of Nagata et al. (2018). At the highest refinement ($D_p/\,\mathrm{d}x = 48$), the value of the Strouhal number is 0.1105, which is only 0.64 % higher compared to the reference value (0.1098). Although the period of oscillation was captured well, the amplitude of oscillation observed was higher than the reference data. However, the percentage error in the lift forces evaluated as $\mathscr{E}_{F_L} = (F_L - F_{L,ref})/(0.125\rho_\infty u_\infty^2 \pi D_p^2)$ is 2.41 %. Overall, a good agreement of the lift coefficient with the reference data is observed.

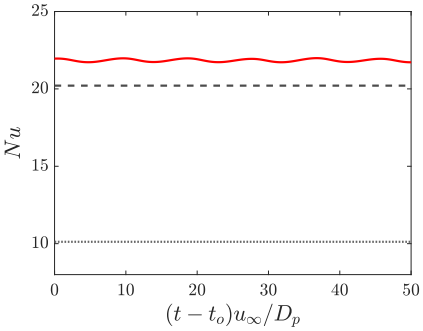

Figure 5.43: Nusselt number at $D_p/\,\mathrm{d}x = 48$ (——) for flow around a fixed isolated sphere at $Re = 300$, $Ma = 0.8$, $TR = 0.9$ compared to the DNS results of Nagata et al. (2018) (– – –) and the Mach-dependent correlation of Fox et al. (1978) (.....).

Figure 5.43 shows the Nusselt number evaluated at $D_p/\,\mathrm{d}x = 48$ compared to the DNS results of Nagata et al. (2018) and Nusselt correlation by Fox et al. (1978). The relative errors in the mean Nusselt number at this resolution compared to the DNS value of Nagata et al. (2018) is 7.6 %. It is seen that the correlation by Fox et al. (1978) gives significant errors in evaluating the Nusselt number. The reason for the increase of the Nusselt number at TR close to unity at $Ma = 0.8$ was explained to be local aerodynamic heating and local change of fluid's viscosity and density in Nagata et al. (2018), which was not considered by Fox et al. (1978). It is observed that the Nusselt number also shows an unsteady periodic behavior similar to the drag and the lift coefficients.

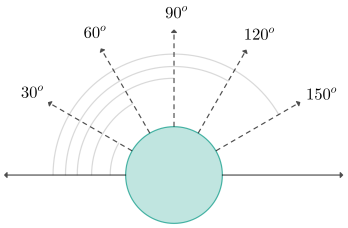

Figure 5.44: The angular positions along which the radial temperature profiles are evaluated.

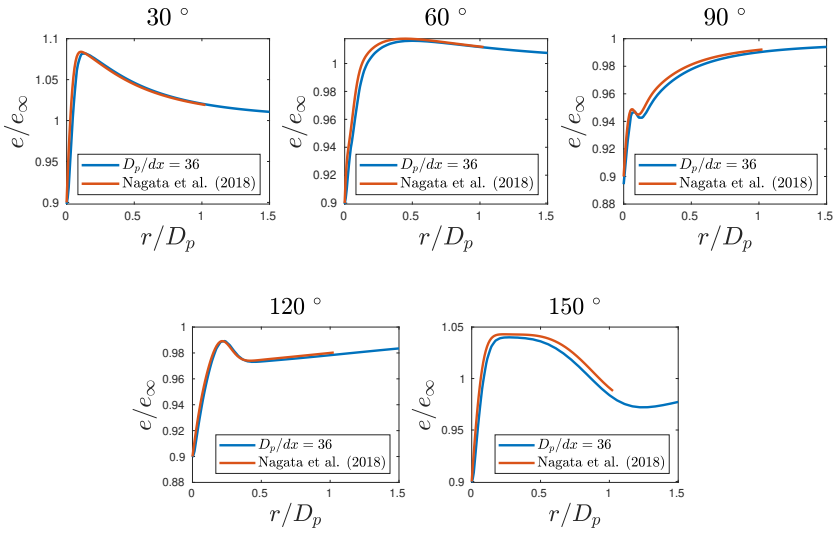

Figure 5.45: Normalized radial time-averaged temperature profiles (——) at different angular positions from the sphere surface (fig. 5.44) compared to the Boundary conforming results (Nagata et al. 2018) (——) for flow at $Re = 300$, $Ma = 0.8$, and $TR = 0.9$.

Next, the radial temperature profiles are evaluated at different angles from the axis, aligned with the streamwise direction, and passing through the sphere's center. They are compared to the temperature profiles provided by Professor Takayuki Nagata through internal communication. The different angular positions for the radial temperature profiles are shown in fig. 5.44.

Figure 5.45 shows the time-averaged normalized radial time-averaged temperature profiles for $D_p/\,\mathrm{d}x = 36$ at different angular positions compared to the boundary-conforming DNS data by Nagata et al. (2018). A good agreement with the reference results is obtained for the profiles at all angular positions. At all angular positions, a large temperature gradient is observed close to the sphere's surface, which enhances the heat transfer rate near the sphere's locality and the Nusselt number (Nu). The imposed temperature ratio (TR) contributes towards the local changes in fluid properties like density, temperature, and viscosity near the sphere surface, affecting the Nusselt number for

an isothermal particle. This strengthens the need to consider local changes in fluid properties and the effect of imposed TR for future models of Nusselt numbers in compressible flows.

Steady axisymmetric flow: $Ma = 2, Re = 300, TR = 0.9$

In their DNS studies for supersonic flows around a fixed particle, Nagata et al. (2018) found that the flow pattern was steady axisymmetric at all values of Reynolds numbers (Re) and Temperature ratios (TR). A standing bow shock is observed long upstream of the particle at the chosen parameters, a characteristic of supersonic flows around a spherical particle.

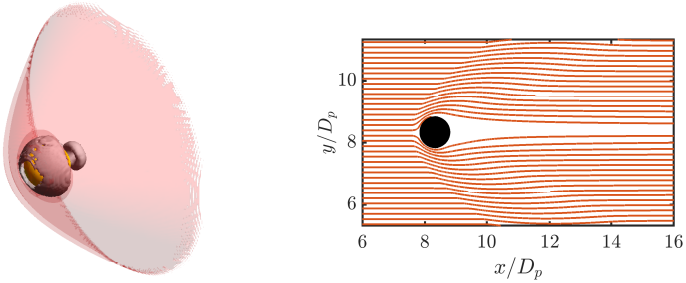

(a) **(b)**

Figure 5.46: (a) Isosurface of density gradient $|\nabla\rho|D_p/\rho_\infty = 0.1$ in red showing the presence of bow shock upstream of the particle at long times and the isosurface of $\lambda_2 \times D_p^2/u_\infty^2 = -0.01$ in gray showing the wake pattern downstream of the particle. (b) Streamlines showing the sharp velocity gradients at the bow shock's location at the z-half plane.

Figure 5.46 shows the standing bow shock using instantaneous isosurface of density gradient magnitude ($|\nabla\rho|$) and the wake using λ_2 criterion.

Table 5.5: Drag (C_D) and lift coefficients (C_L) for flow at $Ma = 2$, $Re = 300$, and $TR = 0.9$ computed at $D_p/\mathrm{d}x = 36$ around an isolated fixed sphere compared to boundary conforming results of Nagata et al. (2018) ($C_{D,ref}$) and ($C_{L,ref}$)

C_D	$C_{D,ref}$	C_L	$C_{L,ref}$
1.4271	1.3584	8.62×10^{-4}	0.0073

table 5.5 show the drag and lift coefficients evaluated at $D_p/\,\mathrm{d}x = 36$, compared to the boundary conforming results of Nagata et al. (2018). The relative error in drag coefficient compared to the Nagata et al. (2018) is 5.05 %. The error in lift-forces given $\mathscr{E}_{F_L} = (F_L - F_{L,ref})/(0.125\rho_\infty u_\infty^2 \pi D_p^2)$ is less than 1 %. The lift coefficient's low value also depicts the flow's axisymmetric nature. Overall, a good agreement with the reference data of Nagata et al. (2018) is observed. The drag coefficient obtained with the model by Loth et al. (2021) was found to be 1.2558 and that by Clift and Gauvin (1971a) was 0.6912. The drag model of Loth et al. (2021) does not consider the balance between the local effects of velocity and temperature gradients in evaluating the viscous drag coefficient. It was shown by Nagata et al. (2018) that the local effects played a major role and should be considered for drag models for compressible flow around an isothermal particle. The drag model of Clift and Gauvin (1971a) severely underpredicts the drag coefficient and is not applicable for compressible flows, where the presence of shocklets or shock waves can significantly affect the local energy and momentum exchange between the fluid and the particle. Compared to the test at $Ma = 0.8$, $Re = 300$, and $TR = 0.9$, the time-dependent unsteadiness in the flow is also significantly reduced. The flow is categorized as steady axisymmetric by Nagata et al. (2018).

Table 5.6: Nusselt number (Nu) for flow at $Ma = 2$, $Re = 300$, and $TR = 0.9$ computed at $D_p/\,\mathrm{d}x = 36$ around an isolated fixed sphere compared to boundary conforming results of Nagata et al. (2018) (Nu_{ref}).

Nu	Nu_{ref}	$\mathscr{E}_{Nu}$
97.4269	96.9357	0.0051

Table 5.6 shows the Nusselt number (Nu) computed at $D_p/\,\mathrm{d}x = 36$ compared to the reference solution of Nagata et al. (2018). A good agreement of the evaluated Nusselt number with the reference data is obtained with a relative error of 0.5 % in the mean Nusselt number. There is a large increase in the Nusselt number, which can be attributed to the heat exchange influenced by local aerodynamic heating behind the standing shock wave at TR smaller than but close to unity. At $Ma = 2$, $Re = 300$, and $Pr = 0.7$, The Nusselt number correlation of Fox et al. (1978) gives a value of 9.205. It does

not consider the complex local effects arising from the imposed temperature ratio and, therefore, severely underpredicts the Nusselt number. Hence, future Nusselt number correlations for compressible flow around an isothermal particle should consider its effects and local flow patterns around the particle for better predictions.

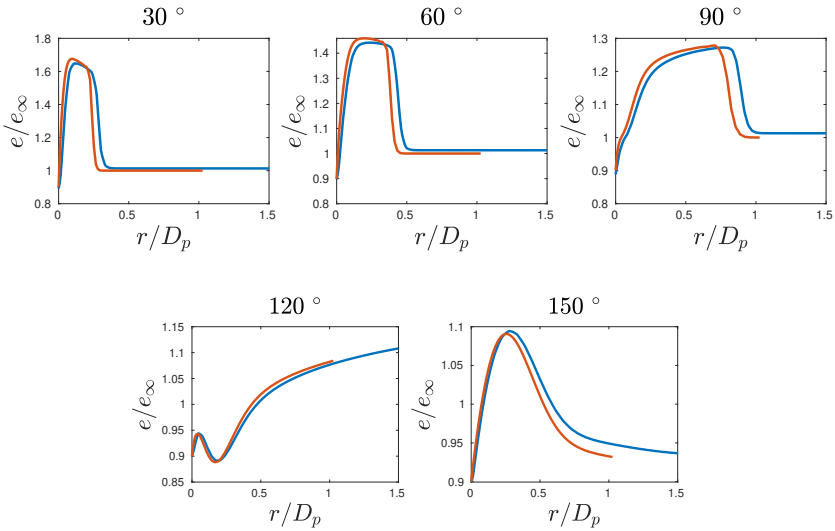

Figure 5.47: Normalized radial time-averaged temperature profiles ($Re = 300, Ma = 2, TR = 0.9$) at different angular positions from the sphere surface (——)(fig. 5.44) compared to the Boundary conforming results of Nagata et al. (2018) (——).

Figure 5.47 shows the time-averaged radial temperature profiles at different angular positions given by fig. 5.44 compared to the reference DNS data of Nagata et al. (2018) provided through internal communication. A good agreement of the temperature profiles is obtained at different angular positions.

Steady nonaxisymmetric flow: $Ma = 0.8, Re = 250, TR = 0.9$

When reducing the Reynolds number (Re) of the flow from $Re = 300$ to $Re = 250$, keeping the Mach number ($Ma = 0.8$) and Temperature ratio ($TR = 0.9$) the same, it was observed by Nagata et al. (2018) that the

flow becomes steady non-axisymmetric. Figure 5.48a shows the instantaneous double-threaded wake structure for flow at $Ma = 0.8$, $Re = 250$, and $TR = 0.9$ around an isolated fixed sphere and fig. 5.48b shows the streamlines in the time-averaged flow field. The flow is non-axisymmetric, which agrees with the observations of Nagata et al. (2018). The flow is stabilized compared to the test at $Re = 300$, keeping Ma and TR the same, which can be explained by increased viscous effects at lower values of Re.

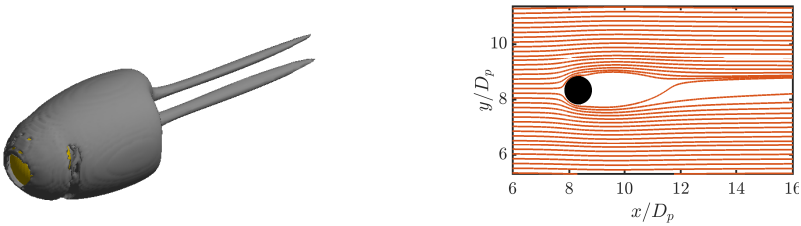

(a) **(b)**

Figure 5.48: (a) Double threaded wake behind the sphere computed through isosurface of Lambda2 criterion ($\lambda_2 \times D_p^2 = -0.01 \times u_\infty^2$) (b) Streamlines showing the non-axisymmetric wake behind the sphere.

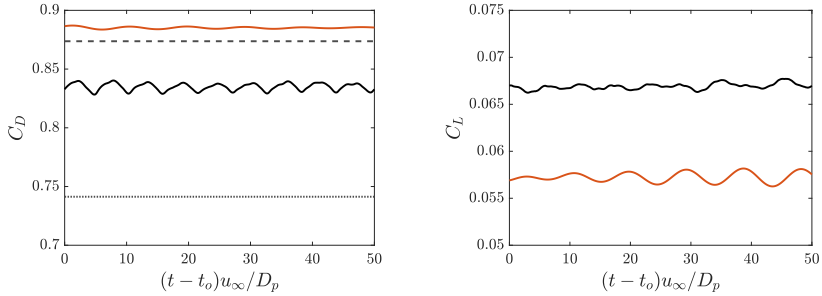

(a) **(b)**

Figure 5.49: (a) Drag coefficient (——) compared to the DNS results of Nagata et al. (2018) (——) and drag models by Loth et al. (2021) (- - -) and Clift and Gauvin (1971a) (.....) (b) Lift coefficient (——) for flow at $Ma = 0.8$, $Re = 250$, and $TR = 0.9$ around an isolated fixed sphere compared to Nagata et al. (2018) (——).

Figure 5.49 shows the drag and lift coefficient computed at $D_p/\,\mathrm{d}x = 36$ and compared to the DNS results of Nagata et al. (2018) and drag correlations of Loth et al. (2021) and Clift and Gauvin (1971a). t_o is an arbitrarily chosen time. At the chosen resolution, the relative error in drag compared to the Nagata et al. (2018) is 6.03 %. From fig. 5.49b, it is observed that the flow has a non-trivial unsteadiness. However, the amplitude of oscillation for the evaluated mean lift coefficient is suppressed compared to the case ($Ma = 0.8$, $Re = 300$, and $TR = 0.9$), and by neglecting it, the flow can approximately be categorized as steady non-axisymmetric as stated in Nagata et al. (2018). It should be noted that the lift and drag in the reference DNS data of Nagata et al. (2018) also have a non-zero periodic amplitude of oscillation in the drag and lift coefficient. However, based on their criteria for categorizing flow regimes, the current flow pattern is assumed to be steady and non-axisymmetric. The Mach and Reynolds number-dependent drag correlation of Loth et al. (2021) is slightly higher than the DNS results of Nagata et al. (2018) since they do not consider the reduced viscous effects due to the imposed temperature ratio. Overall, a good agreement with the reference DNS data for drag and lift coefficient is observed, and the flow regime is captured.

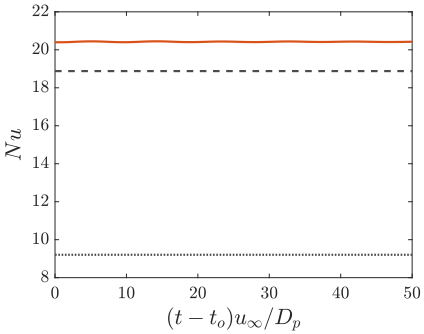

Figure 5.50: Nusselt number at $D_p/\,\mathrm{d}x = 36$ (——) for flow around a fixed isolated sphere at $Re = 250$, $Ma = 0.8$, $TR = 0.9$ compared to the DNS results of Nagata et al. (2018) (– – –) and the Mach-dependent correlation of Fox et al. (1978) (. . . . .).

Figure 5.50 shows the comparison between the computed Nusselt number at $D_p/\,\mathrm{d}x = 36$ and the values from the DNS data of Nagata et al. (2018) and

the model of Fox et al. (1978). The relative error in Nusselt number compared to the boundary conforming results of Nagata et al. (2018) is 8.17 %. The oscillation amplitude observable in the Nusselt number with time is non-zero, however small.

Next, the averaged radial temperature profiles from the sphere's surface at different angular positions from the upstream stagnation point are evaluated and compared with the boundary-conforming results from Nagata et al. (2018). The definition of the angular positions for evaluation of temperature profiles is given in fig. 5.44, and the temperature profiles are shown in fig. 5.51.

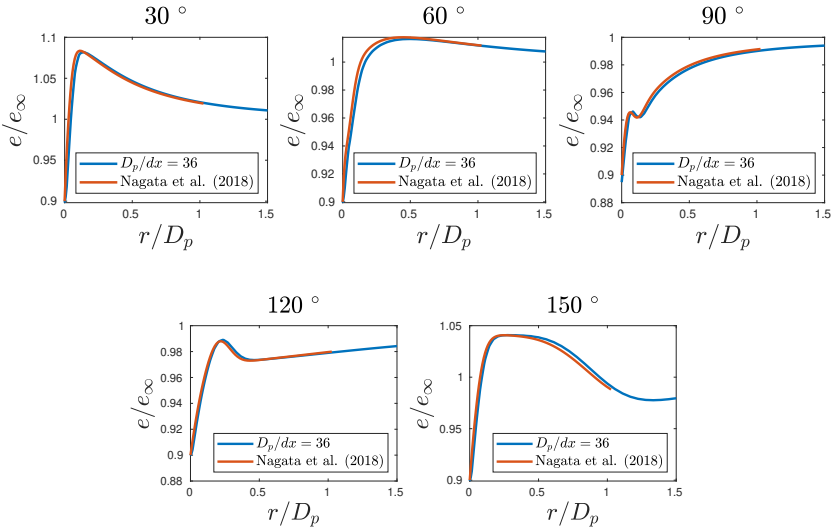

Figure 5.51: Normalized radial time-averaged temperature profiles ($Re = 250$, $Ma = 0.8$, $TR = 0.9$) (——) at different angular positions from the sphere surface (fig. 5.44) compared to the Boundary conforming results (——) by Professor Takayuki Nagata, Nagoya University by internal communication.

The qualitative features of the observed temperature profiles are similar to the test at ($Re = 300$, $Ma = 0.8$, $TR = 0.9$). Sharp temperature gradients are

observed in the sphere's locality due to aerodynamic heating, which enhances the Nusselt number's computed value.

Steady axisymmetric flow: $Ma = 0.8, Re = 300, TR = 2$

It was shown by Nagata et al. (2018) that increasing the temperature ratio (TR) stabilizes the flow. As the temperature of the particle is raised, the flow near the sphere's vicinity gets heated, raising the kinematic viscosity and effectively reducing the Reynolds number. Hence, the viscous effects become more effective in dampening the unsteadiness and stabilizing the flow. The effective reduction in the Reynolds number at a higher temperature ratio also increases the drag coefficient of the sphere.

Figure 5.52: Instantaneous wake structure for flow around a fixed isolated sphere at $Re = 300$, $Ma = 0.8$, $TR = 2$ given by the isosurface of the second invariant of the velocity gradient tensor given by $QD_p^2/u_\infty^2 = 1 \times 10^{-4}$.

Figure 5.52 shows the instantaneous wake structure given by the Q-criterion. The double-threaded wake structure downstream of the particle disappears at the choice of $Ma = 0.8$, $Re = 300$, and $TR = 2$. The wake structure is consistent with the observations of Nagata et al. (2018).

Figure 5.53a shows the drag coefficient computed at $D_p/\,\mathrm{d}x = 36$ compared to the boundary conforming DNS results of Nagata et al. (2018). t_o in the figures is an arbitrarily chosen time. It is observed that the time-dependent drag and lift coefficients have non-trivial periodic unsteadiness in the flow.

However, the oscillation amplitude is small, and Nagata et al. (2018) categorize the current flow regime as steady.

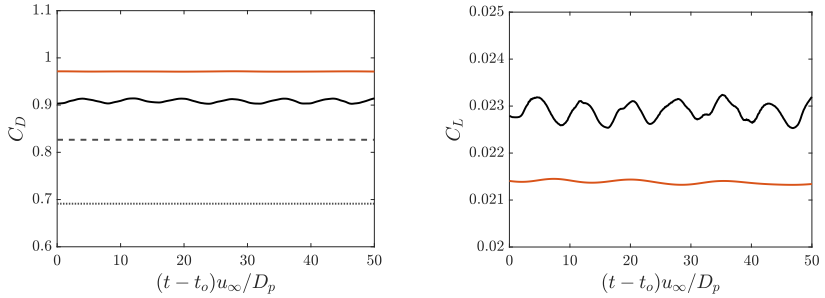

Figure 5.53: (a) Drag coefficient (——) compared to the DNS results of Nagata et al. (2018) (——) and drag models by Loth et al. (2021) (- - -) and Clift and Gauvin (1971a) (.....) (b) Lift coefficient (——) for flow at $Ma = 0.8$, $Re = 300$, and $TR = 2$ around an isolated fixed sphere compared to the boundary conforming results of Nagata et al. (2018) (——).

The drag coefficient is also compared to the incompressible drag model of Clift and Gauvin (1971a) and the compressible drag model of Loth et al. (2021). At the chosen resolution ($D_p/\,\mathrm{d}x$), a relative error of 6.89 % for the mean drag is obtained compared to the results of Nagata et al. (2018). It is observed that the incompressible correlations of Clift and Gauvin (1971a) underpredict the drag for the chosen parameters. The drag correlation does not consider the enhancement of drag-coefficient associated with compressibility effects at subsonic but supercritical flow conditions, as well as the local increase of kinematic viscosity in the vicinity of the heated particle. Hence, their drag model does not apply to the current flow test. Although the correlation of Loth et al. (2021) considers the compressibility effects, it does not consider the enhanced viscous effects near the particle. Hence, their predictions are better than Clift and Gauvin (1971a), but do not capture the local effects of heating or cooling a particle.

The lift coefficient is compared to the boundary-conforming DNS results of Nagata et al. (2018) in fig. 5.53b. A good agreement with the reference data is

obtained with a relative error of less than 1 % in the mean lift force compared to the boundary-conforming reference data. It should, however, be noted that although the flow is not entirely steady (even for the boundary-conforming reference data), and the lift coefficient has a low but finite value, the criteria by Nagata et al. (2018) categorizes the flow as steady-axisymmetric.

Figure 5.54 shows the computed Nusselt number at $D_p/\,\mathrm{d}x = 36$ compared to the reference DNS results of Nagata et al. (2018) and the correlation of Fox et al. (1978). A good agreement of the time-averaged Nusselt number compared to the reference boundary-conforming data is obtained with a relative error of 4.87 %. The Nusselt number correlation of Fox et al. (1978) overpredicts the drag for the current test since it does not consider the effects of local heating of the fluid near the particle. The increase in fluid's viscosity in the sphere's vicinity as it is heated decreases the local Reynolds number, consequently reducing the local Nusselt number.

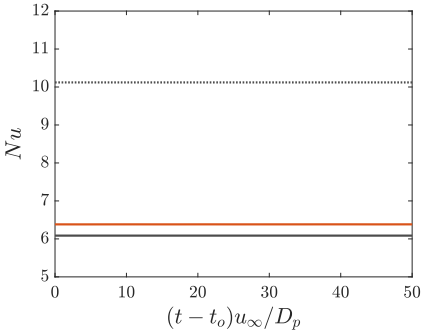

Figure 5.54: Nusselt number at $D_p/\,\mathrm{d}x = 36$ (——) for flow around a fixed isolated sphere at $Re = 300, Ma = 0.8, TR = 2$ compared to the DNS results of Nagata et al. (2018) (——) and the Mach-dependent correlation of Fox et al. (1978) (.....).

Figure 5.55 shows the radial temperature profiles at different angular positions (fig. 5.44) compared to the reference boundary conforming results of Nagata et al. (2018). A good agreement with the reference data is obtained at $D_p/\,\mathrm{d}x = 36$ for the profiles at all the angular positions. A strong temperature gradient is observed in the sphere's vicinity, which contributes to the evaluation of the local Nusselt number.

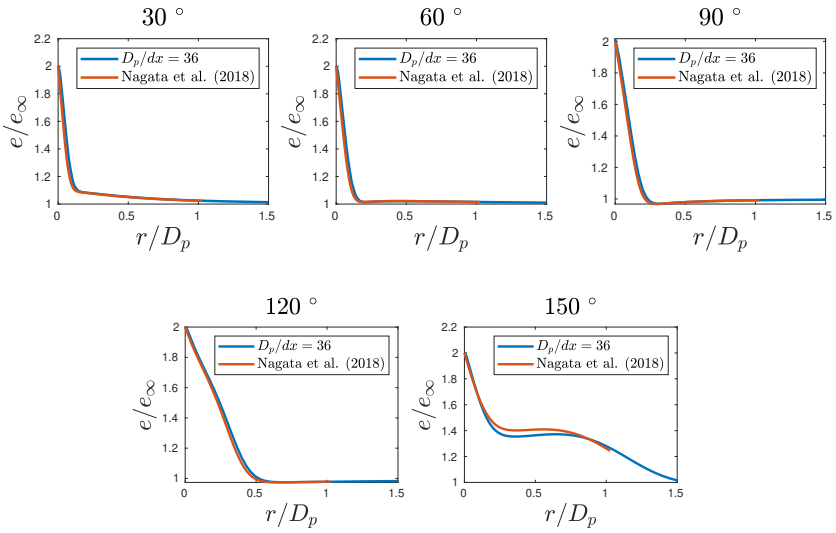

Figure 5.55: Normalized radial time-averaged temperature (——) profiles ($Re = 300$, $Ma = 0.8$, $TR = 2$) at different angular positions from the sphere surface (fig. 5.44) compared to the Boundary conforming results (——) by Professor Takayuki Nagata, Nagoya University by internal communication.

Concluding remarks

Figure 5.56 shows the comparisons of the computed drag coefficient (C_D) and the Nusselt number (Nu) with $D_p/\,\mathrm{d}x = 36$ with some incompressible and compressible models. It is observed that the effect of the imposed temperature ratio on an isothermal particle in a compressible flow can have a significant impact on the local drag and Nusselt numbers by impacting the local flow in the sphere's vicinity. To the extent of the author's knowledge, no drag and Nusselt number correlations are currently available, which consider the combined effects of Ma, Re, and TR for an isothermal particle in a compressible flow. The flow pattern in the wake of the particle is stabilized by increasing the temperature ratio (TR) and reducing the Reynolds number (TR). The flow is also stabilized at supersonic Mach numbers (Ma) with a standing bow shock upstream of the particle position. The imposed temperature ratio increases the total drag coefficient (C_D). However, the computed Nusselt number is

higher than the predicted values from the model at temperature ratios less than unity and lower than the predictions at higher values. This observation was also reported by Nagata et al. (2018). For a flow with forced convection around an isothermal fixed particle, the imposed energy boundary condition on the sphere, like isothermal, adiabatic, or fluid-solid energy balance, can affect the nature of heat transfer in the sphere's locality and the local Nusselt number. In addition, localized heating through compressibility effects also contributes, which makes modeling the Nusselt number for compressible flows more complicated than the incompressible flows.

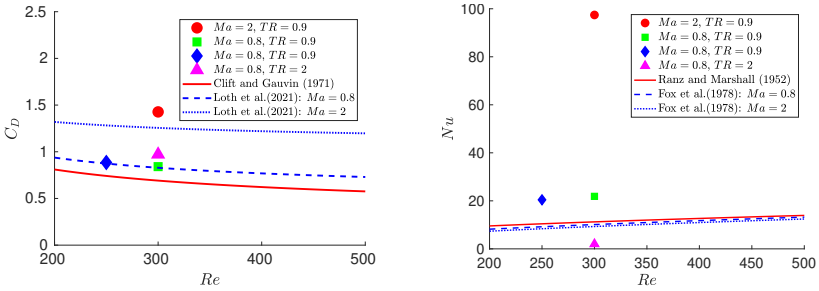

Figure 5.56: (a) Drag coefficient obtained by varying the Re, Ma, and TR compared to the drag models by Loth et al. (2021) and Clift and Gauvin (1971a) (b) Nusselt number at different Re, Ma, and TR compared to the models by Ranz and Marshall (1952) and Fox et al. (1978).

The flow patterns in a range of Reynolds numbers, Mach numbers, and imposed Temperature ratios could be captured. In addition, a good agreement was obtained with the boundary-conforming results of Nagata et al. (2018) for drag coefficients, lift coefficients, Nusselt numbers, and temperature profiles.

5.4.2 Flow through a homogenous array of fixed particles

In this section, Direct Numerical Simulation of uniform flow through a homogeneously distributed array of finite-sized fixed particles is performed at

Mach number ($Ma = 0.28$), Reynolds number ($Re = 90$), and volume fraction ($\phi = 0.05$). The results are compared to the boundary-conforming particle-resolved LES data presented in Osnes et al. (2023). Magnus Vartdal and Andreas Nygård Osnes from the Norwegian Defence Research Establishment are acknowledged for providing the particle positions, volume-averaged flow data, time-averaged normalized force data, and flow fields from their LES runs which could be used for detailed comparison. Moreover, I would also like to thank them for assisting in setting up the DNS test through information regarding their flow setup. Finally, a comparison is made with the quasi-steady drag correlation of Osnes et al. (2023).

5.4.2.1 Problem setup

The compressible Navier-Stokes equations are solved in a domain of $30D_p \times 10D_p \times 10D_p$, and finite-sized particles are distributed uniformly with a volume fraction ($\phi = 0.05$), where D_p is the diameter of the solid particle. The particle positions are the same as Osnes et al. (2023). The geometrical setup is the same as the one used in the study in Osnes et al. (2023). In the current DNS test, the solid particles are represented using the immersed boundary procedure, as explained in section 4.3. Air is considered as the medium. Hence, the specific heat capacities (γ) ratio is set to 1.4, and the flow's Prandtl number (Pr) is set to 0.7, typical of air.

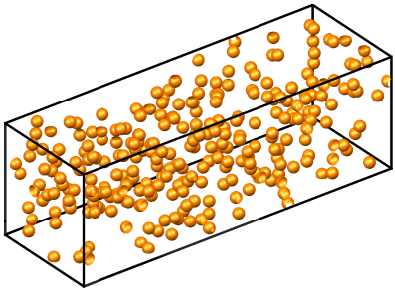

Figure 5.57: Particle arrangement used in the Direct Numerical simulation of flow over a homogeneously distributed particle array at $Ma = 0.28$, $Re = 90$, and $\phi = 0.05$

No-slip, no-penetration, and constant temperature boundary conditions are implemented on the particle surfaces using the immersed boundary procedure. The flow is driven by a volumetric forcing term, which ensures that a steady state can be obtained. The definitions of Reynolds number, Mach number, and the Volume fraction are the same as Osnes et al. (2023) and are given in eq. (5.32)

$$Ma = \frac{\widetilde{u}}{\langle c \rangle} \qquad Re = \frac{\langle \rho \rangle \widetilde{u} D_p}{\langle \mu \rangle} \qquad \phi = \frac{N \pi D_p^3}{6V} \tag{5.32}$$

The definition of the drag (C_D) and lift (C_L) coefficients are defined in eq. (5.33), which is the same as Osnes et al. (2023).

$$C_D = \frac{8\langle F_x \rangle_{t,p}}{\langle \rho \rangle \widetilde{u}^2 \pi D_p^2} \qquad C_L = \frac{8\sqrt{\langle F_y^2 \rangle_{t,p} + \langle F_z^2 \rangle_{t,p}}}{\langle \rho \rangle \widetilde{u}^2 \pi D_p^2} \tag{5.33}$$

In the eq. (5.32), $\langle \cdot \rangle$ represents the volume average of a flow quantity, and $\widetilde{\cdot}$ is the corresponding Favre average. D_p, N, and V represent the particle diameter, the total number of particles in the domain, and the volume of the domain, respectively. The other symbols have their usual meaning. For the DNS runs, the flow is initialized at $Ma = 0.3$, $Re = 100$, and with a constant volumetric force per unit mass used from Osnes et al. (2023). As the volumetric force on the fluid is balanced by the drag forces, and the solid-fluid heat exchange balances the work done by it, a steady state is eventually reached.

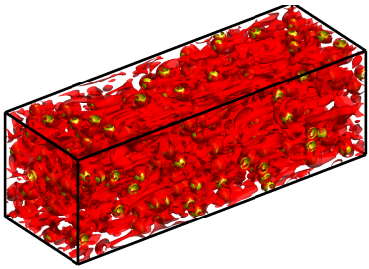

Figure 5.58: Q-criterion with $QD_p^2/\widetilde{u}^2 = 0.0014$ for the instantaneous flow at steady state for flow at $Ma \approx 0.28$ and $Re \approx 90$ and $\phi = 0.05$.

Figure 5.58 shows the isosurface of the Q-criterion at $QD_p^2/\widetilde{u}^2 = 0.0014$. Complex vortex structures can be seen arising due to the complex fluid-solid interactions in a random semi-dilute distribution of particles.

5.4.2.2 Grid convergence

Table 5.7: Grid convergence of Re, Ma, and C_D for compressible flow through a homogenous array of fixed particles compared to the boundary conforming results of Osnes et al. (2023) at steady state.

Re_{ref}	Ma_{ref}	$C_{D,ref}$	$D_p/\,\mathrm{d}x$	Re	Ma	C_D	$\mathcal{E}(Re)$	$\mathcal{E}(Ma)$	$\mathcal{E}(C_D)$
89.60	0.275	1.452	20	85.428	0.258	1.69	0.046	0.061	0.164
			40	87.479	0.264	1.59	0.024	0.038	0.099

Table 5.7 shows the convergence of the Reynolds number (Re), Mach number (Ma), and the drag coefficient (C_D) with grid refinement. $\mathcal{E}(Re)$, $\mathcal{E}(Ma)$, and $\mathcal{E}(C_D)$ represent the relative errors in Re, Ma, and C_D respectively. The convergence results are summarised in fig. 5.59.

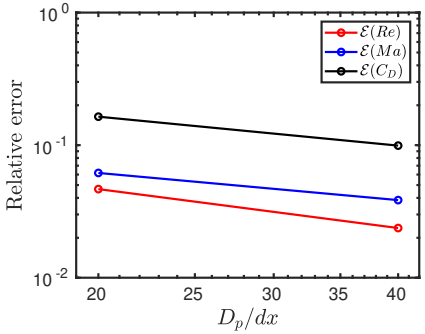

Figure 5.59: Grid convergence of Re, Ma, and C_D, when compared to the boundary conforming results of Osnes et al. (2023) at steady state.

It can be noted that although the errors in Ma and Re are small at $D_p/\,\mathrm{d}x = 40$, the relative error in the C_D is relatively higher. This is because the streamwise

forces are normalized with the reference force based on the volume-averaged and Favre-averaged quantities at steady state, which have finite errors. If, however, the non-dimensional quantity (C_B) given by eq. (5.34) is used, the relative error at $D_p/\,\mathrm{d}x = 40$ is 5.09 %.

$$C_B = \frac{\sum_{i=1}^{N} \langle F_x \rangle_t}{F_{input}} \tag{5.34}$$

C_B is the ratio of the total streamwise quasi-steady force acting on the particles and the imposed volumetric force acting on the fluid. The value of C_B at $D_p/\,\mathrm{d}x = 40$ is 1.0518. The closeness of C_B to unity shows the balance between the input volumetric force on the fluid phase and the rate of momentum loss due to fluid-solid interaction. The constant volumetric force, F_{input}, is calculated as the product of initial fluid density, the volume occupied by the fluid phase, and a constant force per unit mass.

5.4.2.3 Comparison of force coefficients and force fluctuations

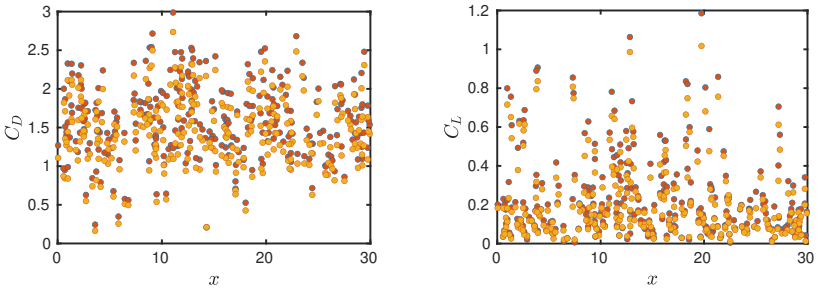

(a) (b)

Figure 5.60: (a) The drag coefficients and (b) the lift coefficients for all the particles in a flow at $Ma \approx 0.28$ and $Re \approx 90$ and $\phi = 0.05$ compared to the boundary conforming results of Osnes et al. (2023).(●) represents the DNS solution at $D_p/\,\mathrm{d}x = 40$ and (●) represents the boundary conforming results of Osnes et al. (2023).

Figure 5.60 shows the scatter plot for comparison of the individual drag and lift coefficients. The grid convergence for the relative errors in drag coefficient is given in table 5.7. The plot reveals significant spatial variance in drag and lift coefficients at the chosen parameters for the computed DNS results at $D_p/\,\mathrm{d}x = 40$ and the reference data. In order to quantify the force fluctuations, a normalized standard deviation is defined as the ratio between the standard deviation of the individual particle forces and the mean of the forces as given in eq. (5.35).

$$\sigma_N(F) = \frac{\sqrt{\sum \left(\langle F\rangle_t - \langle F\rangle_{p,t}\right)^2 / N}}{\langle F\rangle_{p,t}} \tag{5.35}$$

Table 5.8: Standard deviation of the individual streamwise forces normalized with the mean of the streamwise forces over all the particles compared to the boundary conforming results of Osnes et al. (2023).

$\sigma_{N,ref}$	$\sigma_N : D_p/\,\mathrm{d}x = 40$	$\mathfrak{E}(\sigma_N)$
0.3031	0.2936	0.0314

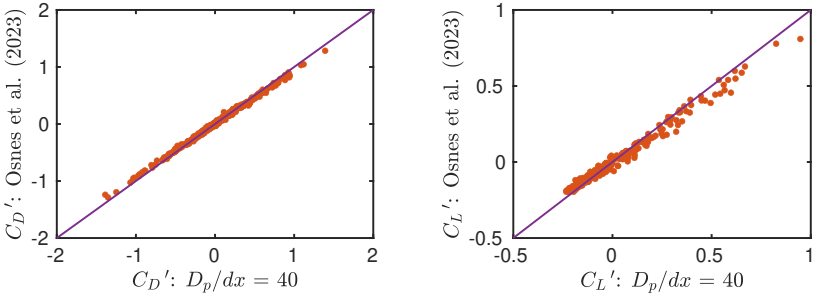

(a) **(b)**

Figure 5.61: The fluctuations (●) in (a) drag coefficients and (b) the lift coefficients for all the particles in a flow at $Ma \approx 0.28$ and $Re \approx 90$ and $\phi = 0.05$ compared to fluctuations from the boundary conforming results of Osnes et al. (2023). (——) represent a line with a slope of unity.

From table 5.8, it is observed that the standard deviation in streamwise forces is around 30 % of the mean. As seen from the table, the current DNS simulations are able to capture the spatial variance of streamwise forces from the boundary-conforming reference results. A more direct comparison of the force fluctuations is performed by comparing the streamwise and transverse force fluctuations for identical particles between the current DNS results at $D_p/\,\mathrm{d}x = 40$ and the reference data. The results are shown in fig. 5.61. This could be performed because, in the current runs, the same particle positions as that of Osnes et al. (2023) are used. A good agreement is obtained for the individual streamwise and transverse force fluctuations.

5.4.2.4 Comparison with drag model

Table 5.9: Standard deviation of the individual streamwise forces normalized with the mean of the streamwise forces over all the particles compared to the boundary conforming results of Osnes et al. (2023).

	$\langle C_D \rangle_{p,t}$	Rel. error
LES: Osnes et al. (2023)	1.452	-
Model: Osnes et al. (2023)	1.388	0.044
DNS: $D_p/\,\mathrm{d}x = 40$	1.59	0.099

Osnes et al. (2023) provided the quasi-steady drag correlation as a function of Reynolds number (Re), Mach number (Ma), and the volume-fraction (ϕ) for flow through a homogenous array of fixed particles. A brief comparison between the model, the computed drag in the reference (Osnes et al. (2023)), and the current DNS solutions at $D_p/\,\mathrm{d}x = 40$ is made in this section. The results are summarized in table 5.9. From table 5.9, it is observed that the drag model underpredicts the boundary-conforming LES results by 4.4 %.

6 Flow through particle array of finite width

As shown in section 5.4.1.4 and from the previous works of Nagata et al. (2018), it is known that the drag and lift forces, the fluid-solid heat exchange, and the flow regime are affected by the compressibility effects (given by the Mach number), the competing effects of flow viscosity and inertia (given by the Reynolds number), and the local temperature gradients (given by the particle to fluid temperature ratio). In the presence of other neighboring particles, additional interactions arise between the particle wakes and shock structures (in supersonic flows). Hence, volume fraction corrections are necessary to predict macroscopic flow quantities like averaged force coefficients and Nusselt numbers. For flow through a homogenous arrangement of particles, force models have recently been proposed in the works of Osnes et al. (2023) and Khalloufi and Capecelatro (2023).

Additional complexity arises when studying flow through inhomogeneous distributions like finite-sized particle arrays. Experimental and numerical studies through such an arrangement have previously been performed by Ling et al. (2012), Regele et al. (2014), Mehta et al. (2016b), Vartdal and Osnes (2018), Mehta et al. (2019), Osnes et al. (2019), Osnes et al. (2020), Mehta et al. (2020), and Osnes and Vartdal (2021). It is well known that the transient features for a shock wave interacting with a particle curtain include an attenuating transmitted shock and a reflected shock which strengthens over time. Eventually, a negative streamwise pressure gradient and a positive gradient of streamwise velocity are established inside the curtain. The flow inside the curtain is also characterized by spatial and temporal flow fluctuations, which depend on parameters like the choice of particle Reynolds number, the incident shock-wave Mach number, and the solid volume fraction.

Figure 6.1 shows the incident, transmitted, and reflected shock waves along with the rarefaction and contact discontinuities during the transient shock-curtain interaction in a state-space diagram. A description of the mechanisms involved in their evolution has been provided by Regele et al. (2014) in the context of inviscid flows and will be briefly discussed here for completeness. It should be noted that even for the viscous compressible flows relevant in the current work, the inviscid mechanisms play a major role during the initial transient as observed by Osnes et al. (2020).

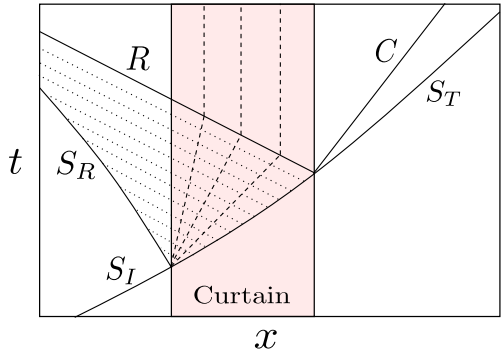

Figure 6.1: State-space diagram describing the evolution of incident shock (S_I), transmitted shock (S_T), reflected shock (S_R), rarefaction wave (R), contact discontinuity (C), expansion waves (_ _ _), and compression waves (.....) for a shock wave interacting with a fixed-particle curtain.

As the incident shock wave (S_I) interacts with the upstream edge of the particle curtain, a reflected shock (S_R) and a transmitted shock (S_T) are formed. The reflected shock travels upstream, getting strengthened over time by the compression waves, while the transmitted shock travels downstream getting attenuated inside the curtain. Propagation of the transmitted shock inside the curtain, sets up an expansion fan behind it. As the transmitted shock exits from the downstream curtain edge, a rarefaction wave (R) and a contact (C) are created. The rarefaction wave travels upstream, establishing the steady pressure-gradient inside the curtain, while the contact wave travels further downstream separating the downstream curtain-wake region.

The current work focuses on the flow through a finite-sized particle array for a given solid volume fraction and a range of Mach numbers while keeping the Reynolds number constant at $\mathcal{O}(100)$. The effect of increasing the curtain width and changing the volume fraction is also explored. The definitions of the non-dimensional parameters are given in section 6.1. Next, the local flow behavior inside the curtain is studied using particle-conditioned averaging at different positions along the streamwise direction. One-dimensional spectra and two-point correlation functions are evaluated in the wake of the particle curtain, and the efficacy of available average-force models developed for homogeneous distributions is tested in the inhomogeneous arrangement. Finally, the performance of a simple one-dimensional model by Ling et al. (2012) is compared against the current DNS results.

6.1 Flow setup and configuration

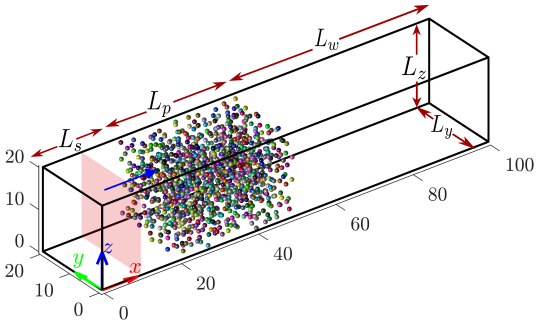

Figure 6.2: Particle arrangement for shock-wave interaction with a particle array of finite width. The dimensions in the figure are represented as normalized values with respect to the particle diameter (D_p). L_p is the width of the particle-curtain, L_w refers to the length of the downstream region and L_s refers to the length of the upstream region.

Direct Numerical Simulations of compressible viscous flow through a random array of fixed particles of finite width are performed. The particles in the context of the current chapter refer to spheres of diameter D_p. The current runs are initialized using the shock Mach number (Ma_s), particle Reynolds number

based on post-shock quantities (Re_{ps}), solid volume fraction (ϕ), the Prandtl number (Pr), and the solid to post-shock fluid temperature ratio (TR_{ps}). The temperature of the particle (T_p) is fixed and set to the initial pre-shock value. The lengths of the region upstream (L_s) and downstream (L_s) of the particle array are constant in all the runs and are fixed at ($L_s = 20D_p$) and ($L_w = 50D_p$), respectively. The width of the particle curtain is given by L_p. The geometrical setup used for the current runs is shown in fig. 6.2, where the lengths are non-dimensionalized by the particle diameter D_p.

$$Ma_s = \frac{u_s}{a_R} \qquad Re_{ps} = \frac{\rho_{ps} u_{ps} D_p}{\mu_{ps}} \tag{6.1}$$

$$\phi = \frac{N\pi D_p^3}{6L_pL_yL_z} \qquad TR_{ps} = \frac{T_p}{T_{ps}} \tag{6.2}$$

The non-dimensional parameters based on post-shock reference quantities used to initialize the DNS and to analyze the transient flow are given in eq. (6.1). The subscript "ps" refers to the post-shock quantities, a_R is the pre-shock speed of sound, u_s is the shock velocity, and N is the total number of particles inside the array. However, it should be noted that the definitions of the non-dimensional parameters based on post-shock reference quantities are not directly indicative of the flow at late times, where the inflow conditions have been modified by the reflected shock wave. Hence, local-to-particle reference quantities or those based on the final established inflow conditions will be used below in the presentation of flow at late times. The choice of the non-dimensional parameters, grid resolution ($D_p/\Delta x$), and the relevant geometrical dimensions of the domain are summarized in table 6.1.

The flow is initialized with a shock wave initially located $0.7D_p$ upstream of the particle array for all the DNS runs at $Ma_s = 1.22$ and $Ma_s = 1.66$, separating the post-shock left and pre-shock right states. The initial transient state can be studied and compared for these two shock Mach numbers. For the cases where the post-shock flow is supersonic ($M260L_{30,ps}$ and $M260_{30,ps}$), the interaction of the strong reflected shock wave with the supersonic inflow boundary made the solution unstable. Instead, the flow was initialized with

uniform post-shock conditions of $Ma_s = 2.6$ to study the late-time flow dynamics. The post-shock conditions based particle Reynolds number (Re_{ps}) is fixed at 100 for all the tests, while the solid volume fraction (ϕ) is set to 5 % in all the cases except $M166C_{30}$. $M166C_{30}$ is the case with the same choice of parameters as $M166_{30}$, except the volume fraction, which is reduced by half. The case $M260L_{30,ps}$ has the same choice of parameters as $M260_{30,ps}$, but with a two-thirds increase in the length of the curtain. The transverse boundaries are periodic, and subsonic or supersonic inflow/outflow-boundary conditions as discussed in section 4.2 are used at the upstream and downstream boundaries based on the local value of the Mach number. The Prandtl number ($Pr = 0.7$) and the ratio of specific heat ($\gamma = 1.4$) are kept constant for all the cases.

Table 6.1: Parameters for the simulations of shock interaction with an array of fixed particles with finite thickness: Shock Mach number Ma_s, Reynolds number Re_{ps}, volume fraction ϕ, Temperature ratio T_p/T_{ps}, Wake region length L_w, Tranverse region length L_y, L_z, resolution $D_p/\Delta x$, and Prandtl number Pr.

Type	Ma_s	Re_{ps}	ϕ	T_p/T_{ps}	L_p	$L_y = L_z$	$D_p/\Delta x$	Pr
$M122_{20}$	1.22	100	0.05	0.87	$30D_p$	$20D_p$	20	0.7
$M122_{30}$	1.22	100	0.05	0.87	$30D_p$	$20D_p$	30	0.7
$M122_{40}$	1.22	100	0.05	0.87	$30D_p$	$20D_p$	40	0.7
$M122_{50}$	1.22	100	0.05	0.87	$30D_p$	$20D_p$	50	0.7
$M166_{30}$	1.66	100	0.05	0.70	$30D_p$	$20D_p$	30	0.7
$M166C_{30}$	1.66	100	0.025	0.70	$30D_p$	$20D_p$	30	0.7
$M260_{30,ps}$	2.6	100	0.05	0.45	$30D_p$	$20D_p$	30	0.7
$M260L_{30,ps}$	2.6	100	0.05	0.45	$50D_p$	$20D_p$	30	0.7

No-slip, no-penetration, and constant-temperature thermal boundary conditions are used at the particle surface using the immersed boundary procedure explained in section 4.3.1. In addition, the fluid viscosity is related to the fluid

temperature using Sutherland's temperature-dependent viscosity law, as explained in eq. (C.8).

6.2 Grid convergence

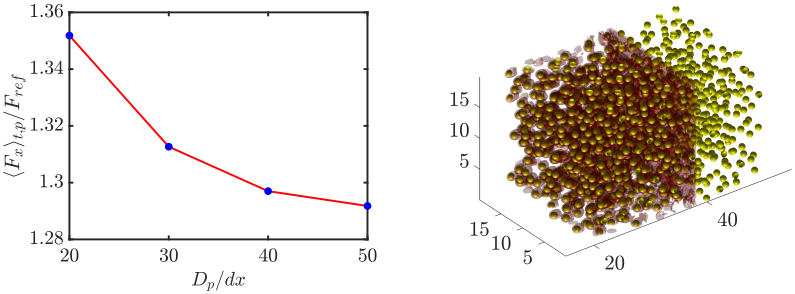

(a) **(b)**

Figure 6.3: (a) Grid convergence of time and particle averaged force $\langle F_x \rangle_{t,p}$ normalized by a reference force $F_{ref} = \rho_{ps} u_{ps}^2 \pi D_p^2/8$ after reaching statistical stationarity for a shock of $Ma_s = 1.22$ interacting with a fixed-particle array. The subscript 'ps' refers to post-shock conditions (b) Isosurface of the density gradient magnitudes ($\nabla\rho$) for the same case at $u_s t/D_p = 19.52$.

In order to check the sensitivity of the current DNS runs to the grid size, a self-convergence test is performed. For the case with $Ma_s = 1.22$, the grid resolution is successively increased from $D_p/\Delta x = 20$ for the case $M122_{20}$ till $D_p/\Delta x = 50$ for $M122_{50}$. Recall that the grid spacing is equal along the streamwise and transverse directions for the immersed boundary procedure (explained in section 4.3.1) used in the current work (which means, $\Delta x = \Delta y = \Delta z$).

Figure 6.3a shows the convergence of the time and particle-averaged force $\langle F_x \rangle_{t,p}$ along the streamwise direction at late times normalized with the post-shock condition based reference force given by $F_{ref} = 0.125\rho_{ps} u_{ps}^2 \pi D_p^2$. At $D_p/\Delta x = 30$, the normalized force on the particles differs from the finest case at $D_p/\Delta x = 50$ by approximately 2 %. Hence, for the rest of the numerical

runs, $D_p/\Delta x = 30$ was chosen as a good compromise between desired accuracy and computational resources.

6.3 Transient flow

In the current section, the transient flow features inside the curtain as the incident shock wave interacts with the fixed-particle array are analyzed for cases with $Ma_s = 1.22$ and $Ma_s = 1.66$. Recall that the case with $Ma_s = 2.6$ has been initialized differently. The development of the mean flow fields, attenuation of the incident shock wave, the strengthening of the reflected shock wave, and the velocity fluctuations inside the curtain are examined, and the effect of the solid volume fraction and the shock Mach numbers are discussed.

Figure 6.3b shows the isosurface of the magnitude of density gradients $|\nabla\rho|$ for shock wave of $Ma_s = 1.22$, $Re_{ps} = 100$, and $\phi = 0.05$ interacting with the fixed particle array at $u_s t/D_p = 19.52$. Strong density gradients are established inside the particle curtain as the incident shock wave interacts with the fixed particle array. The post-shock conditions are essentially incompressible ($Ma_{ps} = 0.3124$ for $Ma_s = 1.22$). However, although small in magnitude, density gradients are present due to minor but finite compressibility effects even at the low Mach number. Later, in section 6.4.1, the density profiles inside the particle array are compared for different shock Mach numbers at late times. Finite density gradients are also observed to persist along the particle array at late times. Although small compared to cases with higher Ma_s, the streamwise density gradients are non-zero for $Ma_s = 1.22$.

6.3.1 Development of flow fields

Figure 6.4 shows the instantaneous numerical schlieren for the shock-wave at $Ma_s = 1.66$ traversing through the fixed particle array at $u_s t/D_p = 11.09, 33.03$ and 55.98 in the y-half plane. The numerical schlieren for shock-wave at $Ma_s = 1.22$ traversing through the fixed particle array at $u_s t/D_p = 13.03, 26.19$ and 39.25 are shown in fig. 6.6 at the same

plane. The numerical schlieren is defined the same as Mehta et al. (2020) and shown in eq. (6.3).

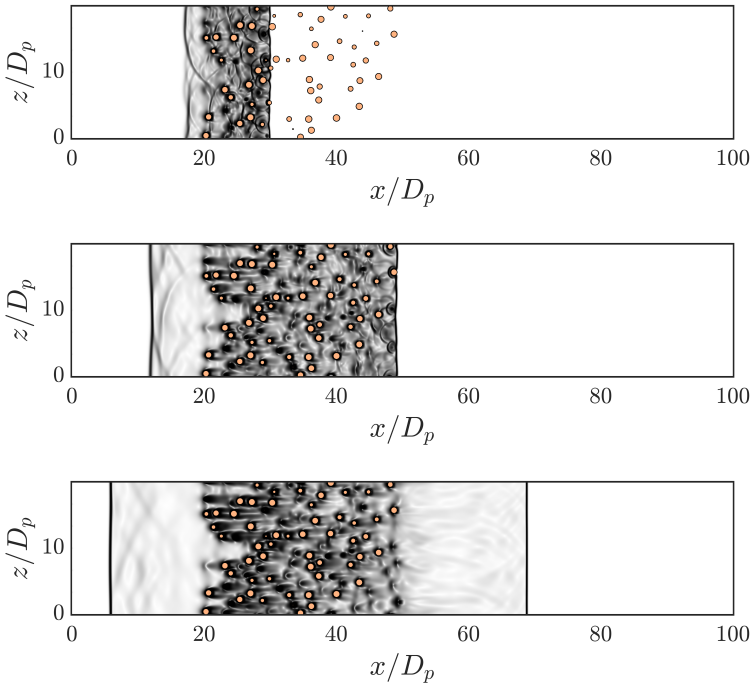

Figure 6.4: Instantaneous numerical schlieren given by eq. (6.3) for shock wave of $Ma_s = 1.66$ traversing through a fixed-particle curtain at (Top) $u_s t/D_p$ = 11.09, (Middle) $u_s t/D_p$ = 33.03, (Bottom) $u_s t/D_p$ = 55.98 in the y-half plane.

$$S_{num} = \exp\left(\frac{-100\,|\nabla\rho|}{\max(|\nabla\rho|)}\right) \tag{6.3}$$

Individual reflected bow shocks are produced as the incident shock interacts with the fixed-particle array, coalescing over time into a planar reflected shock

wave upstream of the fixed-particle array. Strong density gradients eventually develop near the particles and persist after the incident shock wave is transmitted through the particle curtain.

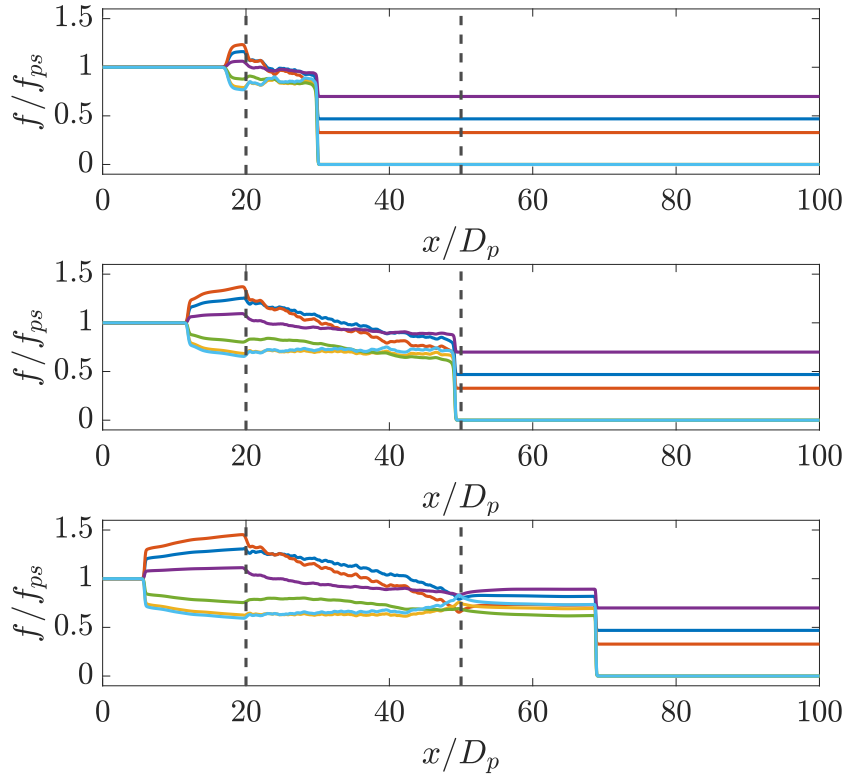

Figure 6.5: Instantaneous $y-z$ plane-averaged flow fields normalized with post-shock conditions for shock wave of $Ma_s = 1.66$ ($M166_{30}$) traversing through a fixed-particle curtain at (Top) $u_s t/D_p$ = 11.09, (Middle) $u_s t/D_p$ = 33.03, (Bottom) $u_s t/D_p$ = 55.98. (——) $\langle\rho\rangle_{y,z}/\rho_{ps}$, (——) $\langle p\rangle_{y,z}/p_{ps}$, (——) $\widetilde{u}_{y,z}/u_{ps}$, (——) $\langle T\rangle_{y,z}/T_{ps}$, (——) $\langle Re\rangle_{y,z}/Re_{ps}$, (——) $\langle Ma\rangle_{y,z}/Ma_{ps}$.

Compared to the case $M166_{30}$ shown in fig. 6.4, it is observed that the strength of the reflected shock is lower for $M122_{30}$ shown in fig. 6.6. This is later confirmed by the by the comparisons between the instantaneous $y-z$ plane

averaged profiles normalized with post-shock quantities for the cases $M122_{30}$ and $M166_{30}$ as shown in fig. 6.7 and fig. 6.5 respectively. The profiles show lower density and pressure gradients near the reflected shock for the case $M122_{30}$ compared to the case $M166_{30}$. $\langle\cdot\rangle_{y,z}$ represents the phase-average as defined in eq. (A.7) in the transverse plane.

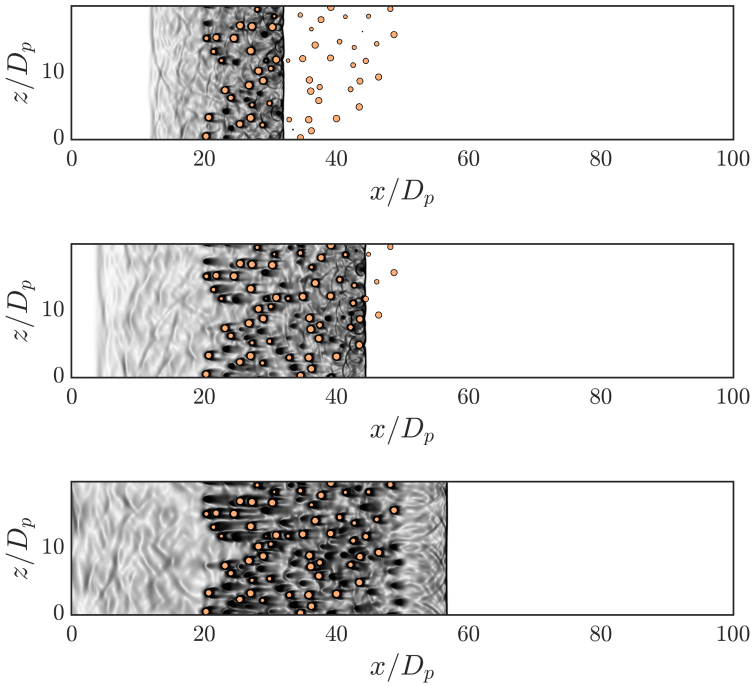

Figure 6.6: Instantaneous numerical schlieren given by eq. (6.3) for shock wave of $Ma_s = 1.22$ traversing through a fixed-particle curtain at (Top) $u_s t/D_p$ = 13.03, (Middle) $u_s t/D_p$ = 26.19, (Bottom) $u_s t/D_p$ = 39.25 in the y-half plane.

As the incident shock wave interacts with the particle curtain, it is attenuated by the combined effects of the particle drag and the fluid viscosity. It was shown by Osnes et al. (2020) that the attenuation by viscous effects can be significant compared to the particle effects, especially at lower volume fractions.

Since the incident shock wave is not entirely attenuated inside the particle curtain, a transmitted shock wave can be observed to emerge downstream of the particle array. It was observed that the transmitted shock crosses the downstream edge of the particle curtain at approximately $u_s t/D_p = 32.1227$ for the case $M122_{30}$ and $u_s t/D_p = 34.0907$ for $M166_{30}$.

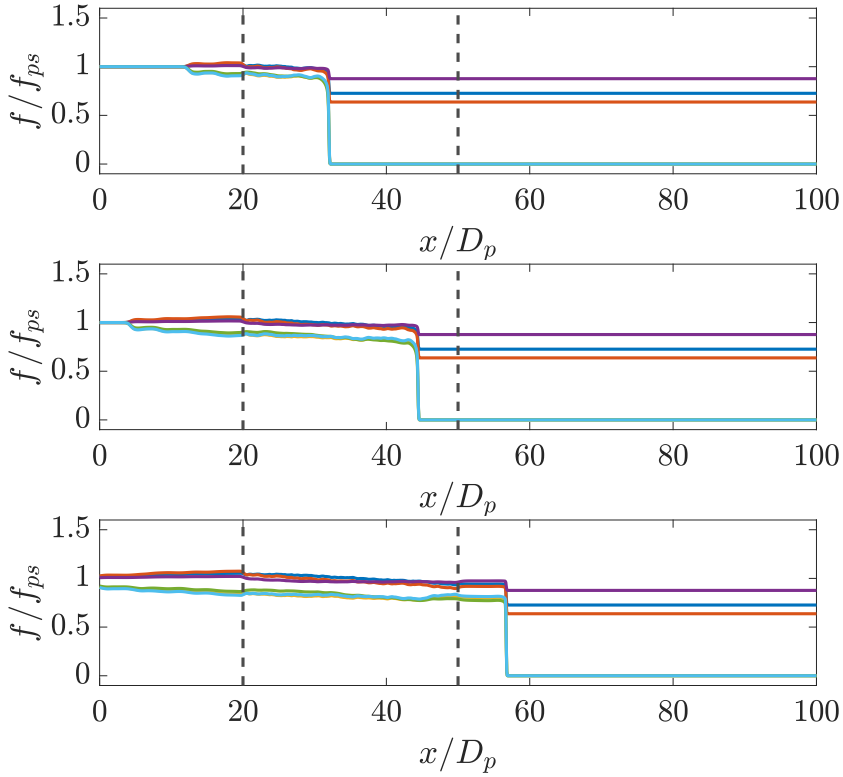

Figure 6.7: Instantaneous $y-z$ plane-averaged flow fields normalized with post-shock conditions for shock wave of $Ma_s = 1.22$ traversing through a fixed-particle curtain at (Top) $u_s t/D_p$ = 13.034, (Middle) $u_s t/D_p$ = 26.194, (Bottom) $u_s t/D_p$ = 39.251. (——) $\langle\rho\rangle_{y,z}/\rho_{ps}$, (——) $\langle p\rangle_{y,z}/p_{ps}$, (——) $\widetilde{u}_{y,z}/u_{ps}$, (——) $\langle T\rangle_{y,z}/T_{ps}$, (——) $\langle Re\rangle_{y,z}/Re_{ps}$, (——) $\langle Ma\rangle_{y,z}/Ma_{ps}$.

The presence of a non-zero solid volume fraction creates flow constrictions inside the particle array. Inside the curtain, the density, temperature, and pressure of the flow decrease along the particle array. At the same time, the velocity of the flow increases to satisfy mass conservation. The Mach number of the flow increases as the fluid passes through the particle array. After the incident shock wave is transmitted through the particle array, a rarefaction wave is created that propagates upstream, halts the propagation of the expansion fan and establishes steady flow-field gradients throughout the particle array. The propagating rarefaction wave also dictates the inflow conditions at late times seen by the particle array. This mechanism has been explained by Regele et al. (2014) for their inviscid two-dimensional numerical simulations.

The presence of viscous effects introduces additional pressure losses due to frictional effects, which adds further complexity. However, the qualitative flow features are governed majorly by the compressibility effects for $M166_{30}$ with $Ma_s = 1.66$ compared to the case $M122_{30}$ with $Ma_s = 1.22$. For the case $M122_{30}$ as shown in fig. 6.7, the pressure, density, streamwise velocity, and pressure gradients remain low inside the curtain. The effect of flow acceleration is observed to be more significant near the downstream edge of the particle array for the case $M166_{30}$ compared to $M122_{30}$. This observation is consistent with the works of Osnes et al. (2019), Osnes et al. (2020), and Osnes and Vartdal (2021). Downstream of the particle array, the pressure, density, and temperature increase, while the velocity decreases over a short distance before settling at the flow state behind the transmitted shock. This effect is more pronounced for the case $M166_{30}$ compared to $M122_{30}$. Let us define an expansion length (L_e), which is the distance from the downstream curtain edge, where the magnitude of the normalized pressure-gradient downstream of the particle-curtain, $(D_p/p_{ps})\,\Delta\langle p\rangle_{y,z}/\Delta x$ first drops below 0.001. It was observed that L_e was $6.77D_p$ for $M166_{30}$ at $u_s t/D_p = 55.98$, and $1.23D_p$ for $M122_{30}$ at $u_s t/D_p = 39.25$. A similar trend is also later observed at late times as shown in fig. 6.21b, where the expansion length for $M166_{30}$ was found to be higher than $M122_{30}$.

Upstream of the particle array, the reflected shock wave travels upstream and strengthens over time. This flow feature is shown later in section 6.3.3. The

flow behind the reflected shock is compressed, increasing the density, temperature and pressure while reducing the velocity. The Mach number and Reynolds number are also reduced behind the reflected shock.

6.3.2 Shock wave delay and attenuation

Figure 6.9a shows the transient drag coefficient ($C_{D,ps}$) obtained by normalizing the streamwise force by the post-shock based reference force for the particles located most upstream, closest to the middle and the most downstream of a particle curtain for the case $M166_{30}$. The post-shock-based average Nusselt numbers for the same particles are shown in fig. 6.9b. The definition of $C_{D,ps}$ and Nu_{ps} for the m^{th} particle is given in eq. (6.4). In eq. (6.4), κ_w is the thermal conductivity of the fluid near the surface of a particle, T_p is the wall temperature, T_{ps} is post-shock temperature, and $\overline{q}$ is the average heat flux. Details for Nusselt number evaluation are given in appendix F.

$$C_{D,ps}^{(m)} = \frac{F_x^{(m)}}{0.125\rho_{ps}u_{ps}^2\pi D_p^2} \qquad Nu_{ps}^{(m)} = \frac{D_p}{\kappa_w\,(T_p - T_{ps})}\,\overline{q}^{\,(m)} \tag{6.4}$$

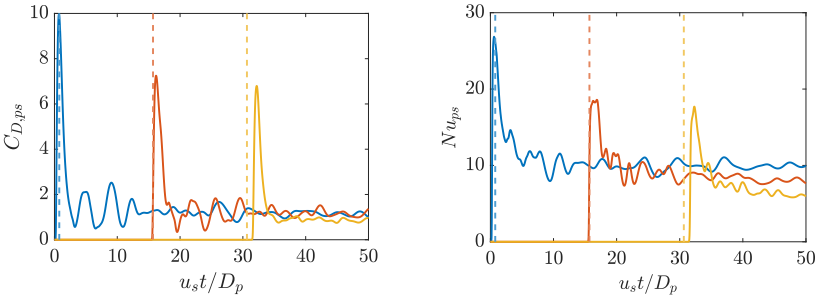

Figure 6.8: Time history of the (a) drag coefficient ($C_{D,ps}$) and (b) Nusselt number (Nu_{ps}) obtained through normalization with post-shock conditions for a shock wave at $Ma_s = 1.22$ ($M122_{30}$) traversing through the (——) most upstream particle, (——) particle closest to the center of the curtain, and (——) the most downstream particle. - - -, - - - and - - - are the expected times for the incident shock waves to reach the location of the particle-center in absence of the particle array.

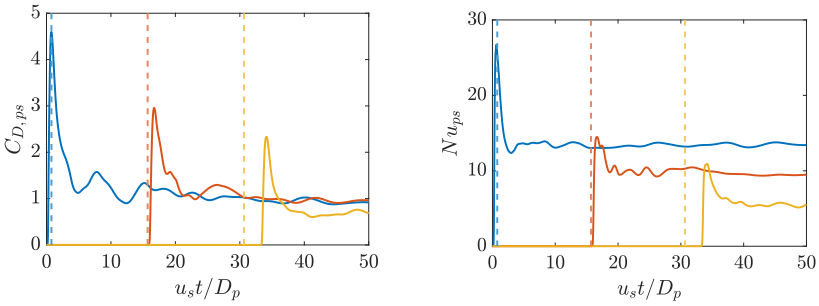

Figure 6.9: Time history of the (a) drag coefficient ($C_{D,ps}$) and (b) Nusselt number (Nu_{ps}) obtained through normalization with post-shock conditions for a shock wave at $Ma_s = 1.66\,(M166_{30})$ traversing through the (——) most upstream particle, (——) particle closest to the center of the curtain, and (——) the most downstream particle. - - -, - - - and - - - are the expected times for the incident shock waves to reach the location of the particle-center in absence of the particle array.

It is observed that as the shock wave sweeps the particle array, the peak drag coefficient and the peak Nusselt number experienced by the particles decrease with the streamwise position along the particle array. This is a consequence of the attenuation of the incident shock wave by means of the particle forces and viscous effects. In addition to the attenuation, the incident shock speed also reduces along the particle array. Hence, the expected arrival time of the incident shock wave near the particle is delayed. The delay in the arrival of the incident shock is more pronounced for the downstream particles as compared to the particles further upstream.

$$\tau_d = \frac{u_s\, t\,|^{(m)}_{C_{D,peak}}}{D_p} - \frac{x_p^{(m)} - x_{s,i}}{D_p} \tag{6.5}$$

To quantify the delay of the incident shock wave along the particle array, a non-dimensional delay time τ_d is defined as the difference between the normalized times taken for the drag coefficient to reach its peak and the unattenuated incident shock wave to reach the center of a particle of index m.

The reference time used for normalization is the shock-particle time scale, $t_s = D_p/u_s$. The definition of the non-dimensional delay time is given in eq. (6.5). In eq. (6.5), $t\,|^{(m)}_{C_{D,peak}}$ is the time taken for the drag of a particle of index m to reach its peak, $x_p^{(m)}$ is the streamwise position of the particle's center, and $x_{s,i}$ is the initial position of the incident shock wave.

6.3.2.1 Effect of Shock Mach number (Ma_s)

The peak drag-coefficients, peak Nusselt numbers, and the non-dimensional delay times for the particle most upstream, closest to the middle, and the most downstream in the array are summarized in tables 6.2 and 6.3.

Table 6.2: The peak drag coefficients ($C^{(m)}_{D,peak}$), Nusselt numbers ($Nu^{(m)}_{peak}$) and non-dimensional delay times ($\tau_d^{(m)}$) for the most upstream ($m = 1$), most to the middle ($m = 2$), and most downstream ($m = 3$) particles in a particle array for the case $M122_{30}$.

m	$x_p^{(m)}/D_p$	$C^{(m)}_{D,peak}$	$\frac{C^{(m)}_{D,peak}-C^{(1)}_{D,peak}}{C^{(1)}_{D,peak}}$	$Nu^{(m)}_{peak}$	$\frac{Nu^{(m)}_{peak}-Nu^{(1)}_{peak}}{Nu^{(1)}_{peak}}$	$\tau_d^{(m)}$
1	20.06	9.96	-	26.86	-	-0.0476
2	34.99	7.25	0.2721	18.59	0.3076	0.4855
3	49.95	6.79	0.3177	17.69	0.3411	1.5578

It is observed that the particles further downstream experience a higher delay in the arrival of the incident shock wave. In addition, the delay for the most upstream particle is negative. This can be explained by the fact that the peak drag for a shock loading on a sphere occurs upstream of its transverse grand circle. This phenomenon has also been observed by Tanno et al. (2003) and Osnes and Vartdal (2022). In addition, the attenuation of $Nu^{(m)}_{peak}$ is relatively larger than the attenuation of $C^{(m)}_{D,peak}$.

Table 6.3: The peak drag coefficients ($C_{D,peak}^{(m)}$), Nusselt numbers ($Nu_{peak}^{(m)}$) and non-dimensional delay times ($\tau_d^{(m)}$) for the most upstream ($m = 1$), most to the middle ($m = 2$), and most downstream ($m = 3$) particles in a particle array for the case $M166_{30}$.

m	$x_p^{(m)}/D_p$	$C_{D,peak}^{(m)}$	$\frac{C_{D,peak}^{(m)} - C_{D,peak}^{(1)}}{C_{D,peak}^{(1)}}$	$Nu_{peak}^{(m)}$	$\frac{Nu_{peak}^{(m)} - Nu_{peak}^{(1)}}{Nu_{peak}^{(1)}}$	$\tau_d^{(m)}$
1	20.06	4.49	-	26.68	-	-0.0314
2	34.99	2.96	0.3566	14.48	0.4574	1.01
3	49.95	2.33	0.4920	10.91	0.5911	3.4595

Comparing tables 6.2 and 6.3, it is observed that the non-dimensional delay time (τ_d) is higher for $M166_{30}$ compared to $M122_{30}$. The fractional decrease in peak drag coefficient ($C_{D,peak}^{(m)}$) for the downstream particles is also more prominent at the higher Ma_s. The same trend is also observed for the fractional change in the peak Nusselt numbers ($Nu_{peak}^{(m)}$). In addition, it was observed that similar to $M122_{30}$, the fractional decrease in ($Nu_{peak}^{(m)}$) downstream is more significant compared to ($C_{D,peak}^{(m)}$).

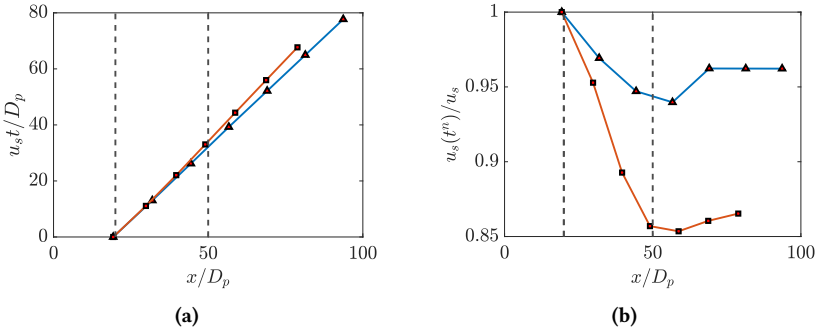

Figure 6.10: Comparison of the (a) Non-dimensionalized space-time diagram and (b) shock velocity as a function of streamwise distance non-dimensionalized by incident non-attenuated shock velocity for incident shock wave with Mach numbers (——) $M122_{30}$, (——) $M166_{30}$ sweeping through a fixed-particle array.

Figure 6.10a shows the non-dimensionalized space-time diagram for shock wave of $Ma_s = 1.22$ and $Ma_s = 1.66$ passing through a fixed particle array. here u_s is the initial unattenuated shock speed at $t = 0$. Let t^n represent the time corresponding to the transient shock wave location ($x_s(t^n)$) for the n^{th} sample at which the shock-wave location is evaluated as shown in fig. 6.10a. Then, the shock-velocity corresponding to the n^{th} sample is defined as $u_s(t^n) = (x_s(t^n) - x_s(t^{n-1})/(t^n - t^{n-1}))$, where $n = 1,2,...N_s$, and $n = 0$ represents the nominal value corresponding to $t = 0$ and the unattenuated shock velocity u_s.

Based on the definition, the shock velocity ($u_s(t^n)$) normalized with the incident unattenuated shock velocity (u_s) is shown in fig. 6.10b. It is observed that the magnitude of the shock velocity (u_s) is reduced to a larger amount inside the curtain for the case $M166_{30}$ with $Ma_s = 1.66$ compared to case $M122_{30}$ with $Ma_s = 1.22$. From the fig. 6.10b, it is observed that shortly after the incident shock wave is transmitted through the particle array, the acceleration of the transmitted shock changes sign and its velocity increases. This is caused by the increase in the fluid pressure downstream of the particle array as seen in fig. 6.5c.

$$u_{s,lag} = \frac{u_s - \min(u_s(t^n))}{u_s} \tag{6.6}$$

In order to quantify the reduction in the shock velocity through shock wave attenuation, a non-dimensional shock-velocity lag ($u_{s,lag}$) is defined, which measures the difference between the initial incident shock velocity and its minimum velocity downstream of the particle array inside the domain as in eq. (6.6). The value of $u_{s,lag}$ for the case $M122_{30}$ is 0.0378 and for $M166_{30}$, it measures 0.1347.

Figure 6.11a shows the individual peak drag coefficients ($C_{D,peak}$) for all the particles as a function of their streamwise positions for $Ma_s = 1.22$ and $Ma_s = 1.66$. In addition, the curves for slab-averaged mean drag coefficients, $\langle C_{D,peak} \rangle_{slab}$ (with the averaging defined in eq. (A.15)) and the drag values

one standard deviation more and less than the mean given by $\langle C_{D,peak}\rangle_{slab} \pm \sigma_{C_{D,peak,slab}}$ are plotted for $M122_{30}$ and $M166_{30}$. Here, $\sigma_{slab}\,(C_{D,peak})$ represents the standard deviation of the peak drag for the particles located inside a given slab. The slab averages are computed over a bin-width of D_p. It is observed that the fractional drop in the peak drag ($C_{D,peak}\ \downarrow$) given by eq. (6.7) was 0.2909 for $M122_{30}$ and 0.4712 for $M166_{30}$. This again confirms that the incident shock wave attenuation is stronger for $M166_{30}$, with the higher incident shock Mach number.

$$C_{D,peak}\ \downarrow = \frac{\langle C_{D,peak}\rangle_{slab}\,|_{x/D_p=20} - \langle C_{D,peak}\rangle_{slab}\,|_{x/D_p=50}}{\langle C_{D,peak}\rangle_{slab}\,|_{x/D_p=20}} \tag{6.7}$$

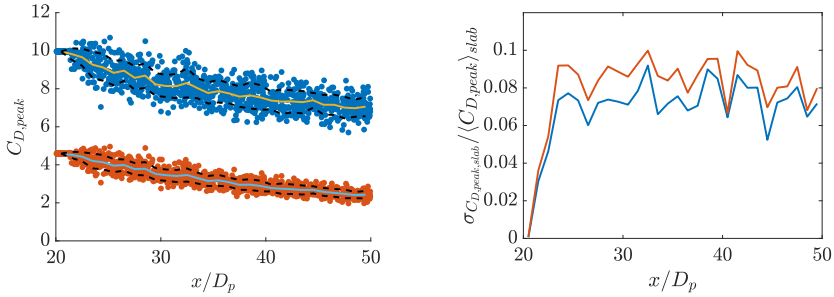

(a) **(b)**

Figure 6.11: (a) The individual peak drag coefficients ($C_{D,peak}$) obtained through normalization with post-shock quantities as a function of the particle positions inside the particle curtain for incident shock wave Mach numbers (●) $M122_{30}$, (●) $M166_{30}$. (——) and (——) are the respective slab-averaged mean values and (- - -) represents the peak drag value one-standard deviation more and less than the mean value. (b) The standard-deviation ($\sigma_{C_{D,peak,slab}}$) of $C_{D,peak}$ for the particles over x-slabs of width D_p normalized with the slab averaged value of peak drag coefficient ($\langle C_{D,peak}\rangle_{slab}$) averaged over the x-slabs for (——) $M122_{30}$, (——) $M166_{30}$.

Figure 6.11b shows the streamwise variation of the standard deviation in the peak drag coefficients evaluated over streamwise slabs ($\sigma_{C_{D,peak,slab}}$) normalized with the slab-averaged peak-drag coefficient ($\langle C_{D,peak} \rangle_{slab}$). It is observed that the normalized standard deviation in the peak drag coefficient achieves the least value upstream of the particle array and is higher for the case $M166_{30}$ compared to the case $M122_{30}$ at all positions inside the particle array. The lower value at the upstream edge of the curtain can be explained by the fact that all the particles located in the region approximately experience the effect of the unattenuated shock in similar flow conditions. However, as the shock propagates along the curtain, the attenuation of the shock wave varies based on the local particle arrangement, flow conditions, and the varying drag forces exerted by the particles on the fluid, resulting a larger fluctuation of the peak drag coefficient inside the particle curtain.

The maximum value for the standard deviation in the peak drag coefficient normalized by the mean given by $\max(\sigma_{C_{D,peak,slab}}/\langle C_{D,peak} \rangle_{slab})$ was found to be 0.0919 for $M122_{30}$ and 0.0998 for $M166_{30}$ at $x/D_p = 32.5$ for both the cases. Although the maximum normalized standard deviation was 8.6 % higher for the case $M166_{30}$ compared to $M122_{30}$, they occurred at the same streamwise location inside the curtain. This suggests that the streamwise fluctuation in the peak drag coefficient is dependent on the local particle arrangement inside the curtain.

Figure 6.12 shows the evolution of the normalized pressure ratio across the incident shock wave as it sweeps the particle array for $M122_{30}$ and $M166_{30}$. The shock wave is first identified as the streamwise position where the $y-z$ plane-averaged density gradients reach a peak. The pressure ratio is then evaluated as the ratio of pressure half a particle diameter behind and ahead of the shock front. The pressure ratio across the incident shock wave is directly linked to the shock strength and the shock velocity as seen in eq. (2.5) and fig. 2.3. It is observed that the pressure ratio across the incident shock wave is attenuated by a larger extent for case $M166_{30}$ compared to $M122_{30}$. Let the fractional change in pressure ratio across the incident shock wave inside the curtain be defined as in eq. (6.8).

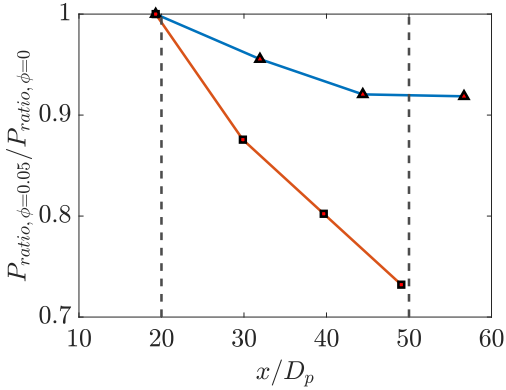

Figure 6.12: The pressure ratio across the shock wave ($P_{ratio,\phi=0.05}$) normalized with the pressure ratio across the initial unattenuated shock ($P_{ratio,\phi=0}$) as a function of streamwise position for shock waves with (——) $Ma_s = 1.22$ ($M122_{30}$), (——) $Ma_s = 1.66$ ($M166_{30}$) traversing a fixed particle curtain

$$P_{ratio,frac} = 1 - \frac{\min(P_{ratio,\phi=0.05})\,|_{x/D_p<50}}{P_{ratio,\phi=0}} \tag{6.8}$$

The value of $P_{ratio,frac}$ for $M122_{30}$ is 0.08 and for $M166_{30}$, it is 0.27. Hence, it can be concluded that the pressure ratio across the incident shock is attenuated to a larger extent inside the particle array for higher incident shock-wave Mach numbers (Ma_s).

The instantaneous slab averaged post-shock conditions based drag coefficient ($\langle C_{D,ps}\rangle_{slab}$) at $u_s t/D_p = 10$ and $u_s t/D_p = 25$ are shown for $M122_{30}$ and $M166_{30}$ in fig. 6.13. $\langle C_{D,ps}\rangle_{slab}$ peaks in the x-slab where the incident shock wave is present at the chosen time. Behind the incident shock, the particles inside the curtain have a lower value of $\langle C_{D,ps}\rangle_{slab}$ as compared to the peak value. It is seen that the peak value of $\langle C_{D,ps}\rangle_{slab}$ is higher for the case $M122_{30}$ compared to $M166_{30}$. In addition, the peak $\langle C_{D,ps}\rangle_{slab}$ reduces at later times at both the shock Mach numbers. Finally, the increased effects of shock delay at higher Ma_s ($M166_{30}$) can be observed using the fact that, for

this case, the peak $\langle C_{D,ps}\rangle_{slab}$ occurs at a lower streamwise position compared to $M122_{30}$ at the same instance of time. The effect is more prominent at later times as the shock velocity inside the curtain is further decreased.

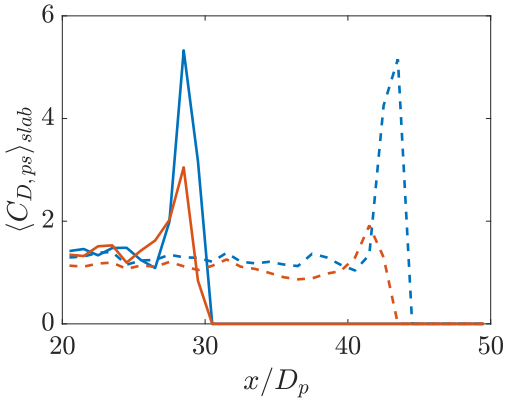

Figure 6.13: Slab averaged drag coefficient $\langle C_{D,ps}\rangle_{slab}$ evaluated at solid volume fraction $\phi = 0.05$ for an incident shock wave interacting with a fixed particle curtain at (——) $u_s t/D_p = 10$, $M122_{30}$, (– – –) $u_s t/D_p = 25$, $M122_{30}$, (——) $u_s t/D_p = 10$, $M166_{30}$, (– – –) $u_s t/D_p = 25$, $M166_{30}$.

6.3.2.2 Effect of solid volume fraction

Table 6.4: The peak drag coefficients ($C^{(m)}_{D,peak}$), Nusselt numbers ($Nu^{(m)}_{peak}$) and non-dimensional delay times ($\tau^{(m)}_d$) for the particle most upstream ($m = 1$), closest to the center of the curtain ($m = 2$), and most downstream ($m = 3$) in a particle array for the case $M166C_{30}$.

m	$x^{(m)}_p/D_p$	$C^{(m)}_{D,peak}$	$\frac{C^{(m)}_{D,peak}-C^{(1)}_{D,peak}}{C^{(1)}_{D,peak}}$	$Nu^{(m)}_{peak}$	$\frac{Nu^{(m)}_{peak}-Nu^{(1)}_{peak}}{Nu^{(1)}_{peak}}$	$\tau^{(m)}_d$
1	20.08	4.5940	-	26.71	-	-0.0176
2	35.00	4.0418	0.1202	21.89	0.4574	0.5456
3	49.86	3.2705	0.2881	16.91	0.5911	1.6078

The case $M166C_{30}$ has half the number of particles distributed uniformly in the curtain volume occupied by $M166_{30}$ while keeping the other parameters the same. In table 6.4, the peak drag coefficients ($C_{D,peak}^{(m)}$), the peak Nusselt numbers ($Nu_{peak}^{(m)}$) and the non-dimensional delay times ($\tau_d^{(m)}$) for the most upstream, most to the middle, and most downstream particles inside the particle-array are summarized for case $M166C_{30}$. When compared to table 6.3, the incident shock wave is observed to be attenuated less at the lower volume fraction ($\phi = 0.025$). This is seen in the fractional decrease in ($C_{D,peak}^{(m)}$) and ($Nu_{peak}^{(m)}$) inside the particle array, which are lower for $M166C_{30}$ compared to $M166_{30}$. In addition, the non-dimensional delay times (τ_d) are lower for $M166C_{30}$ compared to $M166_{30}$.

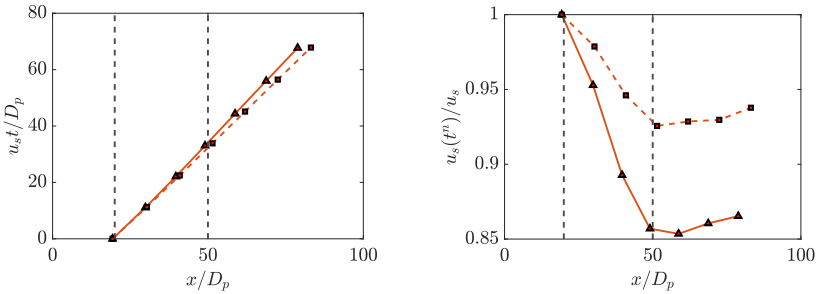

Figure 6.14: Comparison of the (a) Non-dimensionalized space-time diagram and (b) shock velocity as a function of streamwise distance non-dimensionalized by incident non-attenuated shock velocity for incident shock Mach number $Ma_s = 1.66$ with solid volume fractions (——) $\phi = 0.05$ ($M166_{30}$) and (- - -) $\phi = 0.025$ ($M166C_{30}$).

Figure 6.14a shows the non-dimensionalized space-time diagrams comparing the shock wave positions for $M166C_{30}$ and $M166_{30}$ as a function of time. The incident shock wave is observed to travel a larger distance along the streamwise direction at a lower volume fraction. This phenomenon is clearer by looking at fig. 6.14b, which shows that the shock velocity experiences a higher magnitude of deceleration in the larger solid volume fraction case ($M166_{30}$). For both the cases ($M166_{30}$ and $M166C_{30}$), as the incident shock wave is transmitted downstream of the particle array, the acceleration changes sign

and becomes positive. In addition, the shock-velocity lag ($u_{s,lag}$) defined in eq. (6.6) for the case $M166C_{30}$ is 0.0744. $u_{s,lag}$ for the case $M166C_{30}$ is larger than $M122_{30}$ but smaller than $M166_{30}$.

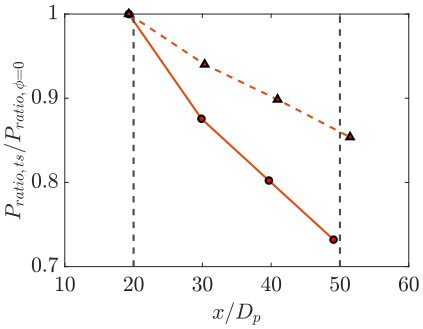

Figure 6.15: The pressure ratio across the shock wave ($P_{ratio,ts}$) normalized with the pressure ratio across the initial unattenuated shock ($P_{ratio,\phi=0}$) as a function of streamwise distance for shock waves with $Ma_s = 1.66$ and solid volume fractions (——) $\phi = 0.05$ ($M166_{30}$) and (- - -) $\phi = 0.025$ ($M166C_{30}$) traversing through the fixed particle curtain.

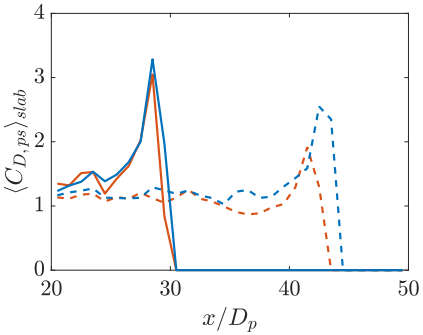

Figure 6.16: Slab averaged drag coefficient $\langle C_{D,ps}\rangle_{slab}$ evaluated for shock wave with incident shock Mach number $Ma_s = 1.66$ interacting with a fixed particle curtain at (——) $u_s t/D_p = 10$, $\phi = 0.05$ ($M166_{30}$), (- - -) $u_s t/D_p = 25$, $\phi = 0.05$ ($M166_{30}$), (——) $u_s t/D_p = 10$, $\phi = 0.025$ ($M166C_{30}$), (- - -) $u_s t/D_p = 25$, $\phi = 0.025$ ($M166C_{30}$).

The normalized pressure ratio across the shock wave ($P_{ratio,ts}/P_{ratio,\phi=0}$) is shown in fig. 6.15 for $M166_{30}$ and $M166C_{30}$. The pressure ratio across the shock wave as it travels along the particle array is observed to decrease to a smaller extent at the lower volume fraction ($M166C_{30}$) compared to ($M166_{30}$). This can be explained by a stronger attenuation at the higher solid volume fraction. Figure 6.16 shows the comparison for instantaneous slab averaged drag coefficient ($\langle C_{D,ps}\rangle_{slab}$) between $M166_{30}$ and $M166C_{30}$ at $u_s t/D_p = 10$ and $u_s t/D_p = 25$. ($\langle C_{D,ps}\rangle_{slab}$) peaks in the x-slab where the shock wave is present at the chosen time. Similar to fig. 6.13, the slab average forces decrease behind the location of the incident shock wave, after being swept by it. Comparisons between $M166_{30}$ and $M166C_{30}$ show that the effects of shock delay and attenuation are smaller at the lower volume fraction ($M166C_{30}$).

6.3.3 Behavior of reflected shock wave

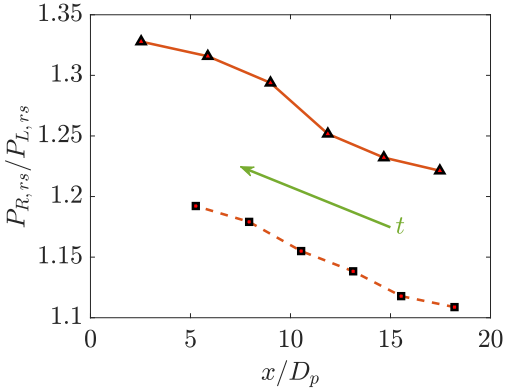

Figure 6.17: The pressure ratio across the reflected shock ($P_{R,rs}/P_{L,rs}$) after the shock wave with $Ma_s = 1.66$ and solid volume fractions (——) $\phi = 0.05$ ($M166_{30}$) and (- - -) $\phi = 0.025$ ($M166C_{30}$) has traversed through a fixed particle curtain. The green arrow shows the direction of increasing time.

Figure 6.17 shows the pressure ratio across the reflected shock wave for $M166_{30}$ and $M166C_{30}$ as a function of the streamwise position. When the incident shock wave traverses through the particle array, a planar reflected

shock wave is generated that travels in the upstream direction. The reflected shock wave is identified as a peak in the magnitude of the $y-z$ plane-averaged density gradients upstream of the particle array. Following this, the pressure ratio across the reflected shock is evaluated between the pressures half a particle diameter behind and ahead of the reflected shock. In fig. 6.17, it is observed that the reflected shock wave strengthens, as it moves in the upstream direction for both the cases $M166_{30}$ and $M166C_{30}$. In addition, the strength of the reflected shock is seen to be larger for $M166_{30}$ compared to $M166C_{30}$. It is concluded that the strength of the reflected shock wave is larger for higher solid volume fractions. The pressure ratio across the reflected shock increased by 7.52 % for the case $M166C_{30}$ between $x/D_p = 5.26$ and $x/D_p = 18.2$, and by 8.72 % between $x/D_p = 2.53$ and $x/D_p = 17.467$ for the case $M166_{30}$.

The drag forces exerted by the particles on the fluid media creates a resistance for the flow to pass through the curtain. Consequently, pressure is built up upstream of the particle curtain, strengthening the reflected shock wave over time. The reasoning behind higher strengths of the reflected shock at lower Reynolds number was explained by Osnes et al. (2020). The phenomenon was explained based on the increase in total streamwise resistive forces on the fluid due to viscous effects, resulting in a higher pressure buildup. A similar explanation can be be extended to the current comparison between volume fractions given in fig. 6.17. The total drag forces on the fluid in the more dilute volume-fraction case $M166C_{30}$ are lower compared to the higher volume fraction case $M166_{30}$. Consequently, the strength of the reflected shock is also lower for the lower solid volume fraction case at a given streamwise location upstream of the particle curtain.

6.3.4 Velocity fluctuations

Flow through a random arrangement of particles in an array generates spatial flow fluctuations which would otherwise be absent in a single phase flow at low Reynolds numbers (in the current work $Re_{ps} = 100$). It was shown by Mehrabadi et al. (2015) that these “pseudo-turbulent” flow structures

have different spatial and time-scales compared to classical single phase-turbulence. Hence, they should be modeled and approached differently. The pseudo-turbulent spatial velocity fluctuations from the $y-z$ plane averaged values is considered in this section. The kinetic energy based on these pseudo-turbulent fluctuations will be called the pseudo-turbulent kinetic energy (PTKE) based on the $y-z$ plane averaged velocities and represented by ($\mathcal{K}_{y,z}$).

In the context of compressible flows, it is convenient to define a Favre averaged quantity for non-conservative flow variable like velocity denoted by $\widetilde{(\cdot)}_{y,z}$. The fluctuation with respect to the Favre-average quantity is then denoted by $(\cdot)''_{y,z}$. The details of the averaging procedures are described in appendix A. If the velocity field ($\mathbf{u}$) is given by $\mathbf{u} = [u, v, w]$, then the pseudo turbulent kinetic energy ($\mathcal{K}_{y,z}$) is defined in eq. (6.9).

$$\mathcal{K}_{y,z} = \frac{1}{2}\left(\widetilde{u''_{y,z}u''_{y,z}} + \widetilde{v''_{y,z}v''_{y,z}} + \widetilde{w''_{y,z}w''_{y,z}}\right) \tag{6.9}$$

6.3.4.1 Effect of solid volume fraction

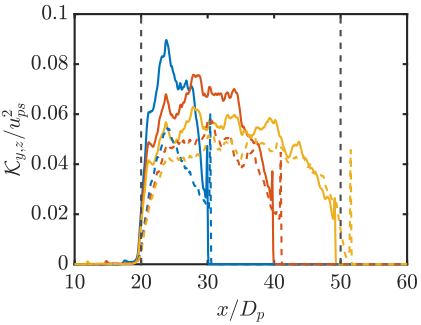

Figure 6.18: Normalized pseudo-turbulent kinetic energy ($\mathcal{K}_{y,z}/u_{ps}^2$) for shock wave with $Ma_s = 1.66$ and solid volume fractions $\phi = 0.05$ ($M166_{30}$) at (——) $u_s t/D_p = 11.0898$ (——) $u_s t/D_p = 22.0672$ (——) $u_s t/D_p = 33.0362$ and $\phi = 0.025$ at (- - -) $u_s t/D_p = 11.2731$ (- - -) $u_s t/D_p = 22.4767$ (- - -) $u_s t/D_p = 33.8567$. Here, $\mathcal{K}$ represents the individual components of the pseudo-turbulent contributions without summation.

Figure 6.18 shows the comparisons between $M166_{30}$ and $M166C_{30}$ for instantaneous post-shock velocity normalized PTKE profiles as the incident shock waves traverses through the particle array. From fig. 6.18, it is observed that for both $M166_{30}$ and $M166C_{30}$, the peak in the magnitude of PTKE decreases as the incident shock wave traverses further downstream along the particle array. In addition, the peak magnitude of PTKE is lower for lower volume fractions.

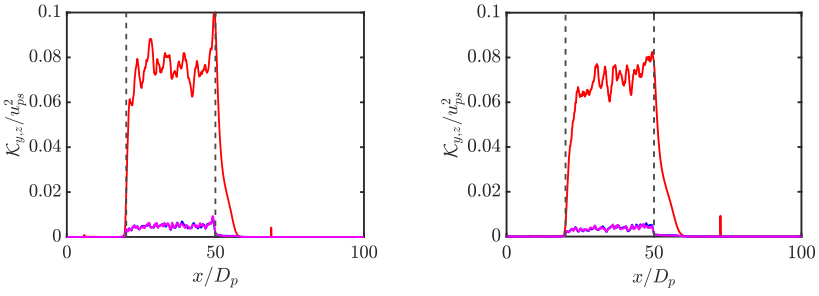

Figure 6.19: Comparison of the contributions to the normalized pseudo-turbulent kinetic energy for shock wave with $Ma_s = 1.66$ and solid volume fractions (a) $\phi = 0.05$, at $u_s t/D_p = 55.98$ ($M166_{30}$) and (b) $\phi = 0.025$ at $u_s t/D_p = 56.4584$ ($M166C_{30}$) interacting with a particle curtain. Contributions to the total pseudo-turbulent kinetic energy are given by (——) $0.5\,\widetilde{u''_{y,z}u''_{y,z}}$, (——) $0.5\,\widetilde{v''_{y,z}v''_{y,z}}$ and (——) $0.5\,\widetilde{w''_{y,z}w''_{y,z}}$.

Figure 6.19a and fig. 6.19b show the contributions to the normalized PTKE from the different velocity components at $u_s t/D_p \approx 56$ for case $M166_{30}$ and $M166C_{30}$ respectively. The streamwise contributions to the PTKE are close to an order of magnitude larger than the transverse contributions for both the solid volume fractions. In addition, the pseudo-turbulent fluctuations are larger near the downstream end of the particle-array. Comparing between the two volume fraction cases, it is observed that $M166_{30}$ in general is comparatively higher than $M166C_{30}$ inside the curtain, but the peak near the downstream curtain edge is clearly higher for $M166_{30}$. The closeness of the PTKE contributions inside the curtain can be explained as follows. As the reflected shock wave is weaker for $M166C_{30}$ compared to $M166_{30}$ (as shown

in fig. 6.17), the transient flow velocity seen by the curtain near the upstream edge will be slightly higher for $M166C_{30}$ at a given instance of time. Consequently, the pseudo turbulent flow fluctuations locally are also enhanced in the bulk of the curtain and become comparable to $M166_{30}$, which has twice the solid volume fraction. At the downstream edge of the curtain, the flow locally gets choked for both the cases (will be shown at late times for both the cases in section 6.4.5), but exhibit a stronger flow acceleration for the case $M166_{30}$, resulting in a sharper peak in the PTKE.

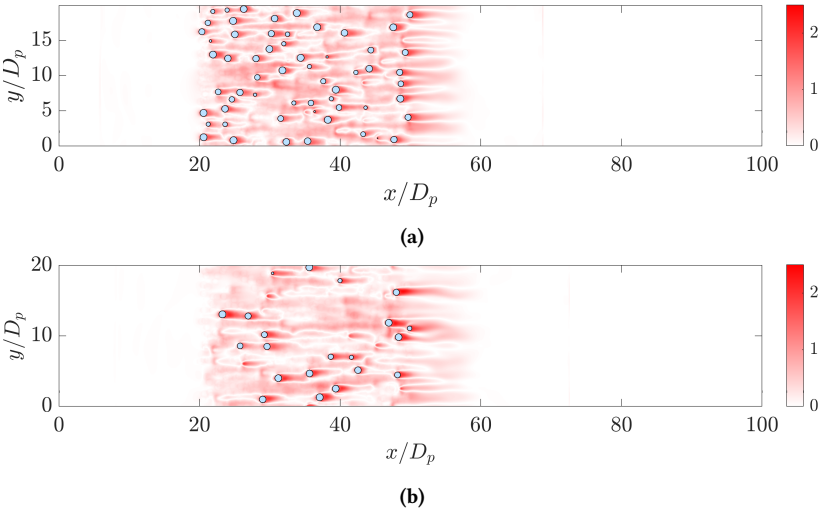

Figure 6.20: The normalized magnitude of streamwise velocity fluctuations ($|u_{z=0.5L_z} - \widetilde{u}_z|/u_{ps}$) with respect to the favre averaged velocity (averaged along the z direction) computed in the $x-y$ plane for the case (a) $M166_{30}$ (b) $M166C_{30}$ at $u_s t/D_p = 56$.

Figure 6.20 shows the normalized absolute value of the streamwise velocity fluctuations given by $|u_{z=0.5L_z} - \widetilde{u}_z|/u_{ps}$ for the case $M166_{30}$ and $M166C_{30}$, where u_{ps} and u_s are the post-shock and shock velocities respectively. It corresponds to the same cases and at the same times as in figs. 6.19a and 6.19b. Here, $\widetilde{u}_z$ represents the Favre average over the z-plane given by $\widetilde{u}_z = \langle \rho u \rangle_z / \langle \rho \rangle_z$, and $\langle \cdot \rangle_z$ represents the phase average in the z-plane. The

figures reveal strong spatial streamwise fluctuations that exist inside and over a short distance downstream of the particle array. This leads to the large streamwise contribution to PTKE as observed in figs. 6.19a and 6.19b. In addition, the contour plots reveal that the largest spatial fluctuations on the chosen plane are produced in the wake of the particles.

6.4 Long time behavior: Shock wave - Particle curtain interaction

Long after the incident shock wave has passed over the particle array, the temporal fluctuations at the chosen post-shock Reynolds number ($Re_{ps} = 100$) become negligible (refer to table 6.5), and the spatial fluctuations dominate. Hence, in this section, only the effects of pseudo-turbulent fluctuations caused by spatial inhomogeneity inside the particle array are considered. Table 6.5 shows the normalized standard deviation in time (σ_t) for the mean streamwise force on the curtain ($\sigma_t(\langle F_x \rangle_p)$) and the forces on the most upstream ($\sigma_t(F_{x,us})$), middle ($\sigma_t(F_{x,mid})$), and downstream ($\sigma_t(F_{x,ds})$) particles in the array.

Table 6.5: Normalized standard deviation (σ_t) in time for the total mean streamwise force on the curtain ($\sigma_t(\langle F_x \rangle_p)$) and the most upstream ($F_{x,us}$), middle ($F_{x,mid}$), and downstream particles ($F_{x,ds}$) in the curtain obtained at late times over more than $10 D_p/u_\infty$ time units.

Type	$\frac{\sigma_t(\langle F_x \rangle_p)}{\lvert\langle F_x \rangle_{p,t}\rvert}$	$\frac{\sigma_t(F_{x,us})}{\lvert\langle F_{x,us} \rangle_t\rvert}$	$\frac{\sigma_t(F_{x,mid})}{\lvert\langle F_{x,mid} \rangle_t\rvert}$	$\frac{\sigma_t(F_{x,ds})}{\lvert\langle F_{x,ds} \rangle_t\rvert}$
$M122_{30}$	1.5×10^{-5}	2.38×10^{-4}	3.55×10^{-4}	6.53×10^{-4}
$M166_{30}$	4.49×10^{-5}	1.78×10^{-4}	1.68×10^{-4}	3.97×10^{-4}
$M166C_{30}$	9.67×10^{-5}	1.45×10^{-4}	1.05×10^{-4}	9.81×10^{-4}
$M260_{30,ps}$	4.37×10^{-5}	2.3×10^{-4}	2.69×10^{-4}	1.72×10^{-4}
$M260L_{30,ps}$	1.26×10^{-4}	2.085×10^{-4}	2.7×10^{-4}	8.53×10^{-5}

Table 6.5 confirms that the temporal fluctuations of streamwise particle-forces are negligibly small compared to the mean at all the chosen shock Mach numbers (Ma_s) and volume fractions (ϕ). Therefore, temporal averaging will not be necessary in the present section.

The inflow conditions at the late times are modified by the reflected shock and hence, strongly depend on its strength. The modified inflow state at late times is then denoted by the subscript "∞". Table 6.6 show the normalized primitive variables for the inflow state at late times. The stronger the reflected shock is, higher are the post-shock normalized density, pressure, and temperature. Conversely, the post-shock normalized streamwise velocity at the inflow is smaller when the strength of the reflected shock is larger. This also means that it is not possible to control the late-time inflow state with the present setup.

Table 6.6: Density (ρ), streamwise velocity (u), pressure (p), and temperature (T) for the inflow state at late times normalized with the post-shock values at the respective chosen shock Mach number (Ma_s).

Type	$\frac{\rho_\infty}{\rho_{ps}}$	$\frac{u_\infty}{u_{ps}}$	$\frac{p_\infty}{p_{ps}}$	$\frac{T_\infty}{T_{ps}}$
$M122_{30}$	1.0362	0.8222	1.0511	1.0143
$M166_{30}$	1.2614	0.4993	1.3852	1.0981
$M166C_{30}$	1.1850	0.6371	1.2685	1.0705
$M260_{30,ps}$	1.6040	0.3707	1.9570	1.2201
$M260L_{30,ps}$	1.6421	0.3357	2.0383	1.2338

6.4.1 Flow fields

The slab-averaged density, streamwise velocity, pressure, and temperature normalized with the late-time inflow conditions are shown in fig. 6.21 for $M122_{30}, M166_{30}$ and $M260_{30,ps}$ as a function of normalized streamwise distance. The slab-average is performed over x-slabs of width D_p which span the entire transverse domain. The details of the slab-averaging procedure is given in appendix A.1.1.

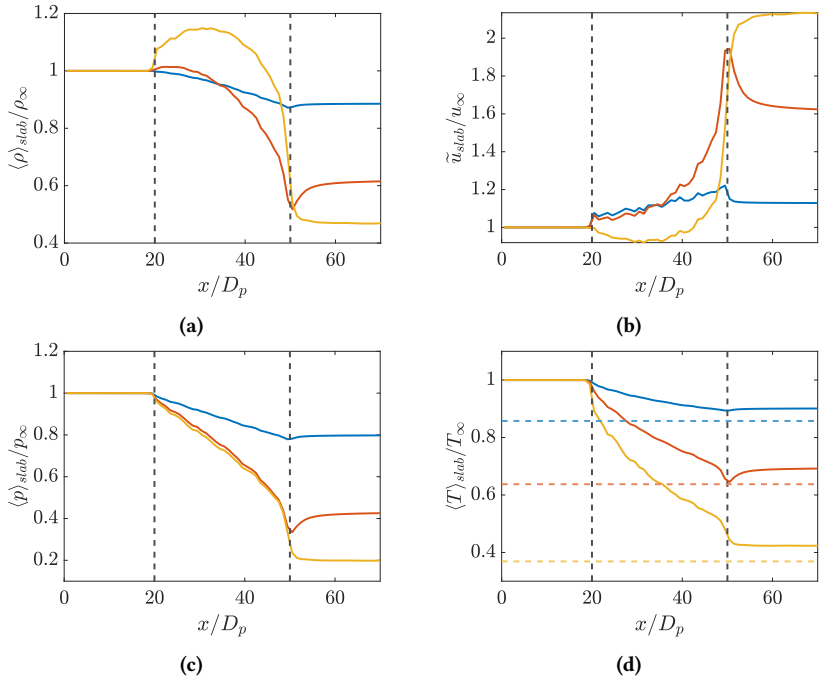

Figure 6.21: Slab averaged flow-field profiles for (a) Density (b) velocity (c) Pressure (d) Temperature normalized with inflow conditions at late times as a function of normalized streamwise distance for the cases (——) $M122_{30}$ (——) $M166_{30}$ (——) $M260_{30,ps}$. The dashed lines in (d) represent particle-to-inflow temperature ratio T_p/T_∞, and their colors correspond to the cases for which they are computed.

At late times, the temperature ratio between the particle and the inflow conditions is such that $T_p/T_\infty = 0.86$ for $M122_{30}$, $T_p/T_\infty = 0.64$ for $M166_{30}$, and $T_p/T_\infty = 0.37$ for $M260_{30,ps}$. Hence, from fig. 6.21d, it is observed that the fluid is cooled by the particle for all the three cases along the streamwise distance inside the curtain. In addition, the magnitude of the temperature gradients are higher for $M260_{30,ps}$ compared to $M122_{30}$ and $M166_{30}$, especially near the upstream edge of the particle-curtain. Since, the thermal conductivity (κ) is higher for $M260_{30,ps}$ based on the Sutherland's law (eq. (C.8)) and the conductivity-viscosity relation (eq. (3.16)), the magnitudes of the local heat-flux (eq. (F.6)) to the particles will also be higher for $M260_{30,ps}$ at the

steady state, especially at the upstream edge of the particle curtain. Near the downstream edge but still inside the particle curtain, a strong flow acceleration occurs for the high Mach number cases $M166_{30}$ and $M260_{30,ps}$. This effect is visible as a stronger magnitude of negative temperature gradients for these cases in the region. Downstream of the particle array, the temperature increases again for $M122_{30}$ and $M166_{30,ps}$ but decreases for $M260_{30,ps}$. It should be noted that the slab-averaged mean flow reaches sonic conditions near the downstream edge of the curtain (refer to fig. 6.23b below), but remains subsonic throughout for $M122_{30}$ and $M166_{30}$. However, we will see in figs. 6.29 and 6.30 that for the cases $M166_{30}$ and $M260_{30,ps}$, the flow may be choked locally and achieve sonic conditions at the curtain-exit. Hence, for $M166_{30}$, although the slab averaged flow quantities are subsonic throughout the curtain, locally, the flow may be supersonic near the downstream edge of the curtain.

The slab-averaged normalized pressure profiles in fig. 6.21c show that a negative pressure gradient is established at late-times inside the curtain that facilitates the fluid-flow through the curtain. The mechanism for establishment of the negative pressure-gradients is explained in the introduction of the chapter in chapter 6. The pressure gradient decreases strongly near the downstream edge (but still inside) of the particle curtain, as the fluid flows through the constrictions for $M166_{30}$ and $M260_{30,ps}$ with high local Mach numbers, but has a gentler decrease for $M122_{30}$. Downstream of the particle curtain, the slab-averaged pressure increases over a short distance for $M122_{30}$ and $M166_{30}$ but decreases for $M260_{30,ps}$ before approaching constancy. This can be explained by drawing analogies from a converging-diverging nozzle to approximately explain the phenomena. Near the downstream edge of the particle-curtain (but inside), the fluid accelerates as seen in fig. 6.21b through constrictions created by the particles inside the curtain (analogous to reduced area in the converging section of the converging-diverging nozzle). The strong flow acceleration can cause it to reach choked flow conditions locally for $M166_{30}$ and $M260_{30,ps}$. Downstream of the particle array, the fluid experiences an increase in the effective cross-sectional area (analogous to the diverging section of the converging-diverging nozzle). The downstream conditions (far from

the curtain) for $M260_{30,ps}$ are such that, the flow reacts to the increase in effective cross-sectional area with further flow-expansion and decrease in the static pressure similar to under-expanded supersonic jets at the nozzle exit. Conversely, for the case $M166_{30}$, the pressure far downstream of the curtain is high enough, such that the locally supersonic flow at the curtain-exit undergoes a weak shock to achieve subsonic conditions as seen in fig. 6.29. Afterwards, the velocity reduces and the static pressure increases, typical of subsonic jets. For $M122_{30}$, the flow is locally subsonic throughout the curtain and the flow at the curtain-exit reacts with an increase in static pressure and a decrease in the flow velocity, typical of subsonic jets. It should be remembered that the analogies are approximate and the flow through the particle array is a non-isentropic process. The slab-averaged pressures in fig. 6.21c seem to approach a consistent choked flow pressure-profile for $M166_{30}$ and $M260_{30,ps}$ inside the curtain, which is consistent with the local Mach number profiles seen in fig. 6.29.

The density of the flow inside the curtain (refer to fig. 6.21a) is affected by the combined effects of the existing pressure and internal energy gradients. The density (ρ) is related to the specific internal energy (e) and the pressure (p) through eq. (3.14). Consequently, the density gradient as a function of these gradient-terms are shown in eq. (6.10).

$$\frac{\partial \rho}{\partial x} = \frac{1}{(\gamma - 1)e^2}\left[e\frac{\partial p}{\partial x} - p\frac{\partial e}{\partial x}\right] \tag{6.10}$$

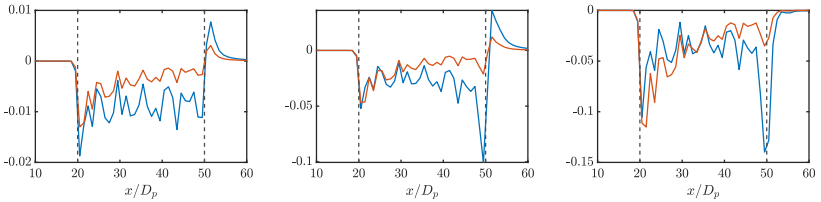

(a) $M122_{30}$ **(b)** $M166_{30}$ **(c)** $M260_{30,ps}$

Figure 6.22: Slab averaged dimensional (——) pressure gradient term ($e\,\partial p/\partial x$) and (——) internal energy gradient term ($p\,\partial e/\partial x$) for the cases (a) $M122_{30}$, (b) $M166_{30}$ and (c) $M260_{30,ps}$.

Equation (6.10) reveals that the pressure-gradient and the internal energy gradient terms are competing in nature to determine the mean density gradients in a flow. The slab-averaged terms $e\,\partial p/\partial x$ and $p\,\partial e/\partial x$ for the three cases $M122_{30}$, $M166_{30}$, and $M260_{30,ps}$ are shown in fig. 6.22. From fig. 6.22, it is observed that the pressure-gradient term is lower than the internal energy gradient term throughout the curtain for the case $M122_{30}$. Hence, from eq. (6.10), it is apparent that the density gradient remains negative, and consequently the density decreases along the width of the curtain.

For the case $M166_{30}$ and more prominently in $M260_{30,ps}$, at the upstream edge of the curtain, the internal-energy gradient term is lower than the pressure-gradient term. However, along the curtain-width, the pressure gradient term crosses over and becomes lower than the internal-energy gradient term. Hence, for these cases, the density first increases along the streamwise distance inside the curtain, reaches a maximum, and then decreases further downstream. At the downstream edge of the particle curtain (but inside), the density gradients in the flow are especially governed by the strong negative-pressure gradients, especially for $M166_{30}$ and $M260_{30,ps}$ owing to the strong flow acceleration in this region.

The behavior of the density profiles in fig. 6.21a is reflected in the slab-averaged streamwise velocity profiles given in fig. 6.21b. At late times, to satisfy mass-conservation principles, the velocity profiles show a trend which is opposite to that of the density profiles inside the curtain.

Figure 6.23 shows the slab-average based profiles of the non-dimensional quantities, namely the Reynolds number ($\langle Re\rangle_{slab}$), Mach number ($\langle Ma\rangle_{slab}$) and the temperature ratio ($T_p/\langle T\rangle_{slab}$). The definitions of the non-dimensional quantities is given in eq. (6.11).

$$\langle Re\rangle_{slab} = \frac{\langle \rho\rangle_{slab}\widetilde{u}_{slab}D_p}{\langle \mu\rangle_{slab}} \qquad \langle Ma\rangle_{slab} = \frac{\widetilde{u}_{slab}}{\langle c\rangle_{slab}}$$
$$\langle TR\rangle_{slab} = \frac{T_p}{\langle T\rangle_{slab}} \tag{6.11}$$

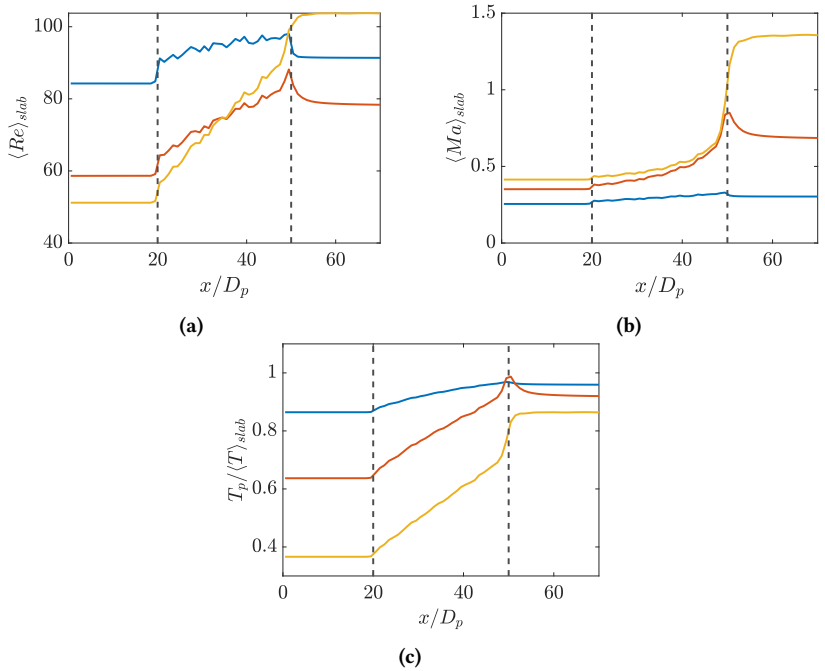

Figure 6.23: Slab averaged Non-dimensional quantities for (a) Reynolds number (b) Mach number (c) Temperature ratio for the cases (——) $M122_{30}$ (——) $M166_{30}$ (——) $M260_{30,ps}$

From fig. 6.23, it is observed that the Reynolds number based on slab averaged quantities increases with streamwise position for the cases $M122_{30}$, $M166_{30}$ and $M260_{30,ps}$. At the upstream edge of the particle curtain, the Reynolds number is lowest for $M260_{30,ps}$ but highest for $M122_{30}$. However, the rate of increase in the mean Reynolds number is highest for $M260_{30,ps}$. Since, the mass flow rate through the curtain is constant, the Reynolds number trend can be explained by the change in the dynamic viscosity due to the variation of the fluid temperature along the width of the curtain. At the upstream end of the curtain The fluid temperature is highest for $M260_{30,ps}$ as seen in fig. 6.23c, and the lowest for $M122_{30}$. Consequently, from the Sutherland's law eq. (C.8), the fluid viscosity is highest for $M260_{30,ps}$ and lowest for $M122_{30}$, explaining the Reynolds number trend at the upstream edge of

the curtain. Furthermore, along the width of the curtain, the magnitude of the temperature gradients are highest for $M260_{30,ps}$ and lowest for $M122_{30}$. Consequently, the fluid cools much faster for $M260_{30,ps}$ compared to $M122_{30}$ along the curtain-width. From the Sutherland's law, the dynamic viscosity of the fluid decreases at a higher rate for $M260_{30,ps}$ compared to $M122_{30}$ and consequently, its Reynolds number increases at a faster rate.

From fig. 6.23b, it is observed that the slab-averaged mean flow remains subsonic throughout the curtain-width for $M122_{30}$ and $M166_{30}$. However, for $M260_{30,ps}$, the mean flow reaches sonic conditions at the downstream edge of the curtain. The strong flow acceleration near the downstream edge of the particle-curtain (but still inside) causes the Mach number to increase sharply for $M166_{30}$ and $M260_{30}$. Conversely, the Mach number has a gentler slope for $M122_{30}$ throughout. Downstream of the particle curtain, the mean Mach number increases for $M260_{30,ps}$, and decreases for $M122_{30}$ and $M166_{30}$ before achieving a constant value. The behavior can be understood by drawing analogies from a converging diverging nozzle as explained previously in the section.

Since, the mean flow is subsonic for $M166_{30}$ and $M122_{30}$, the fluid reacts to the effective increase in cross-sectional area by a decrease in the Mach number. Conversely, the mean flow is supersonic for $M260_{30,ps}$ in the region, and the Mach number increases downstream of the curtain.

Figure 6.24 shows the numerical schlieren given by eq. (6.3) for the cases $M122_{30}$, $M166_{30}$, and $M260_{30,ps}$. The magnitude of the density gradients represented by the numerical schlieren are negligible upstream of the particle-curtain. However, strong density gradients form near the particle boundaries inside the curtain. For $M122_{30}$ and $M166_{30}$, where the mean flow is subsonic at the downstream-edge of the curtain as seen in fig. 6.21b, subsonic jet like structures are observed, along which the flow velocity reduces, and the pressure increases before attaining the ambient value. Interestingly, for the case $M260_{30,ps}$, the flow in the wake of the particle-curtain transitions to a series of alternating standing oblique shocks and expansion fans similar to what is observed in supersonic under-expanded jets (Tam 1995). The flow accelerates and the pressure decreases further to adapt to the ambient

flow conditions downstream through this mechanism. The asymmetry in the shock-cells seen for $M260_{30,ps}$ as shown in fig. 6.24c at late times are possibly a consequence of the asymmetric downstream front of the particle-curtain. If the downstream edge of the curtain is thought of as a series of spatially distributed nozzle exits, the random distribution of the particles in this region may change its effective parameters like the ratio of exit area to its throat area, consequently affecting the nature of shock cells locally in the wake. The effect of the downstream front of the curtain on the shock-cell distribution is interesting to study. However, it is outside the scope of the current work.

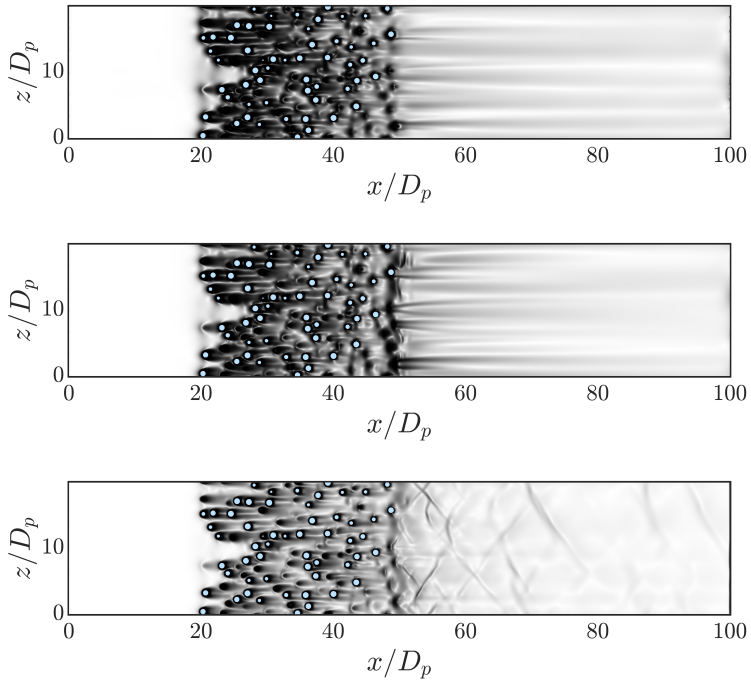

Figure 6.24: Numerical schlieren at late times for (Top) $M122_{30}$, (Middle) $M166_{30}$, and (Bottom) $M260_{30,ps}$ in the y-half plane.

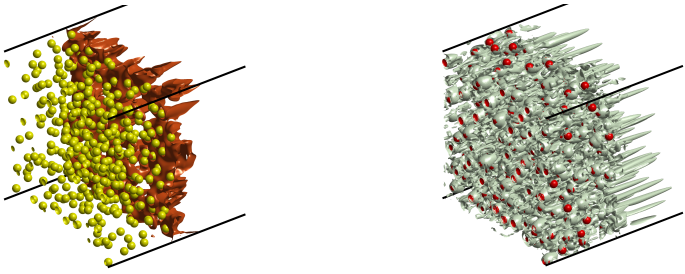

(a) **(b)**

Figure 6.25: (a) Isosurface of the local Mach number at $Ma = 1$ revealing the choked flow conditions at the downstream edge of the curtain for $M166_{30}$. (b) Isosurface of the wake of the particle curtain using the λ_2 criterion ($\lambda_2 D_p^2/u_\infty^2 = -0.01$)

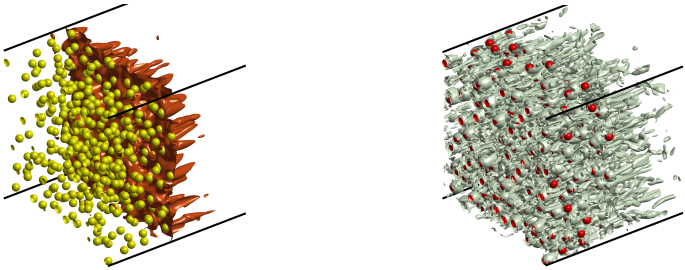

(a) **(b)**

Figure 6.26: (a) Isosurface of the local Mach number at $Ma = 1$ revealing the choked flow conditions at the downstream edge of the curtain for $M260_{30,ps}$. (b) Isosurface of the wake of the particle curtain using the λ_2 criterion ($\lambda_2 D_p^2/u_\infty^2 = -0.01$)

Figures 6.25a and 6.26a show the isosurface of the local Mach number defined as $Ma = u/\sqrt{\gamma p/\rho}$ at $Ma = 1$ for the cases $M166_{30}$ and $M260_{30,ps}$ respectively. The isosurfaces show that for both the cases, the flow achieves sonic conditions and becomes choked at the downstream edge of the particle-curtain. It is also observed that a larger fraction of the downstream cross-sectional area is choked for $M260_{30,ps}$ compared to $M166_{30}$. However, downstream of the curtain for the case $M260_{30,ps}$, the entire flow becomes supersonic through fluid friction. In contrast, in case of $M166_{30}$, although large

fraction of the cross-sectional area of the flow become choked at the downstream curtain edge, local pockets exist in the transverse plane, through which the flow remains entirely subsonic along the streamwise direction throughout the domain. These features are explained in more detail in section 6.4.5.4. The wake structures behind the particle curtain visualized using the λ_2-criterion for the case $M166_{30}$ appear elongated as shown in fig. 6.25b. However, the coherent elongated structures are not seen for $M260_{30,ps}$ as seen in fig. 6.26b. This reflects the difference in the dynamics of the wake region as was seen in fig. 6.24.

Figures 6.28 to 6.30 show the contours of instantaneous density (ρ/ρ_∞), streamwise velocity (u/u_∞), pressure (p/p_∞), temperature (T/T_{infty}), Reynolds number ($\rho u D_p/\mu$), and Mach number ($u/\sqrt{\gamma p/\rho}$) for the cases $M122_{30}$, $M166_{30}$, and $M260_{30,ps}$ on the y-mid plane. It should be noted that the definitions of Reynolds (Re) and Mach numbers (Ma) are different from eq. (6.11). Rather than slab-averaged quantities, local velocity, density, viscosity, and pressure are used to compute the flow profiles.

For the case of $M122_{30}$, it is observed that the density and the static pressure decrease gradually with streamwise distance inside the curtain. Since the particles are at a lower temperature than the upstream fluid, they cool the hot fluid as it passes through the curtain. The velocity, local Reynolds number, and the local Mach number profiles show the subsonic jets through which the expanded flow adjusts to the downstream conditions. In addition, it is seen that the local flow remains subsonic throughout the domain.

For the case $M166_{30}$, stronger flow gradients are observed downstream of the curtain compared to $M122_{30}$. Although, the slab-average-based Mach number ($\langle Ma \rangle_{slab}$) is subsonic at the downstream front as seen in fig. 6.23b, the Mach number contours as observed in fig. 6.29f reveal locally choked-flow and supersonic regions downstream of the curtain.

For the case $M260_{30,ps}$, the flow behind the curtain adjusts to the downstream conditions through a series of standing oblique shocks and expansion-fans creating asymmetric shock-cell patterns as observed from fig. 6.30. Although locally subsonic flow may exist at the downstream edge of the particle curtain,

especially in the individual particle wakes, the mean flow is mostly governed by supersonic flow mechanisms. However, as will be explained below, the flow becomes entirely supersonic further downstream of the curtain for the case $M260_{30,ps}$.

The isocontours of sonic Mach numbers for the cases $M166_{30}$ and $M260_{30,ps}$ are shown as solid black lines in figs. 6.29f and 6.30f respectively. For the case $M166_{30}$, locally supersonic pockets of flow are observed downstream of the curtain, which confirms the presence of co-existing subsonic and supersonic flow regions near the downstream edge of the curtain. In contrast, the entirety of the flow at the visualized cross-section of the curtain attains supersonic conditions for the case $M260_{30,ps}$ (observed as a corrugated contour), through a combined effect of choking at the downstream curtain edge and momentum exchange with the surrounding supersonic flow through fluid friction further downstream. Although visualized only in the y-half plane, the feature was generalized in section 6.4.5.4.

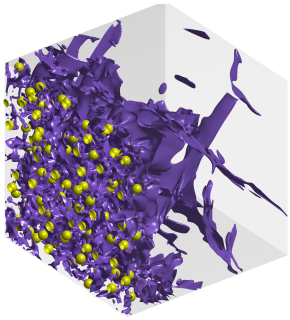

Figure 6.27: Isosurface of density gradient magnitudes given by $|\nabla\rho|D_p/\rho_{ps} = 0.01$ for the case $M260_{30,ps}$ showing oblique density waves in the wake of the particle curtain.

Figure 6.27 shows the oblique density waves, which are a part of the asymmetric shock cell-structures through the isosurface of density gradient magnitudes for $M260_{30,ps}$. Similar flow structures are seen in the under-expanded supersonic jets as discussed previously in the section.

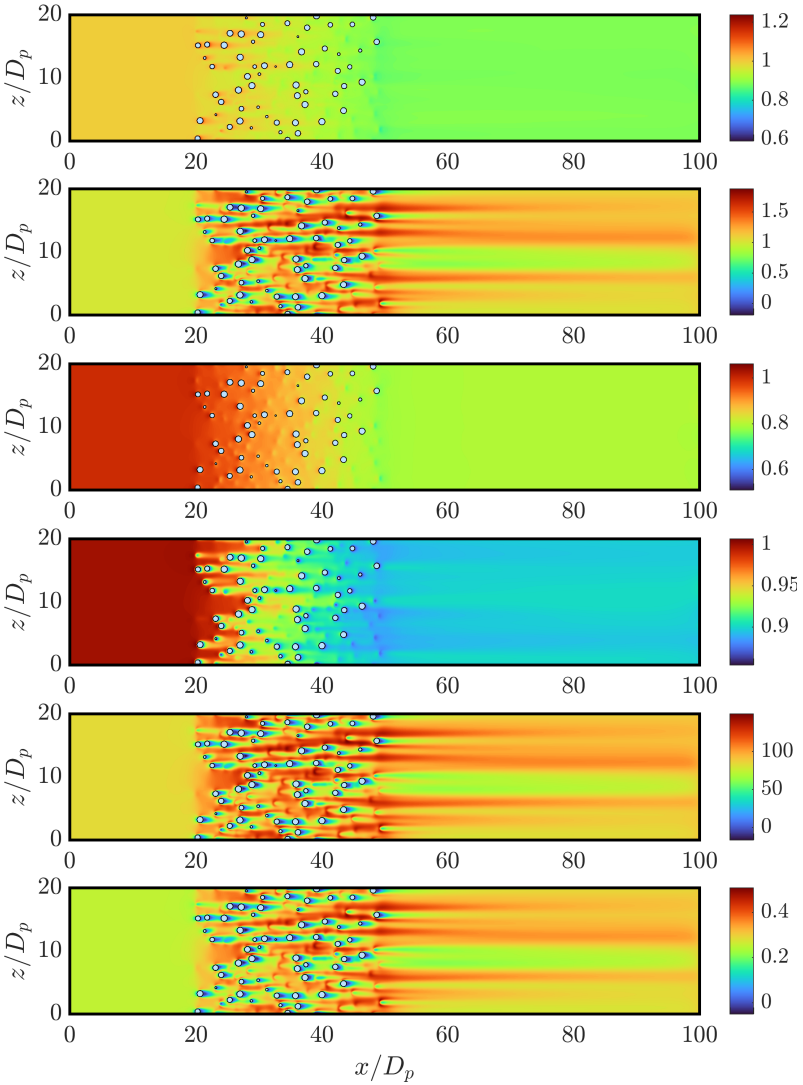

Figure 6.28: Contours of instantaneous flow fields for $M122_{30}$ in the y-half plane. From top to bottom: (a) Normalized density (ρ/ρ_∞) (b) Normalized streamwise velocity (u/u_∞) (c) Normalized static pressure (p/p_∞) (d) Normalized temperature (T/T_∞) (e) local Reynolds number $(\rho u D_p/\mu)$ (f) local Mach number $(u/\sqrt{\gamma p/\rho})$ at late times.

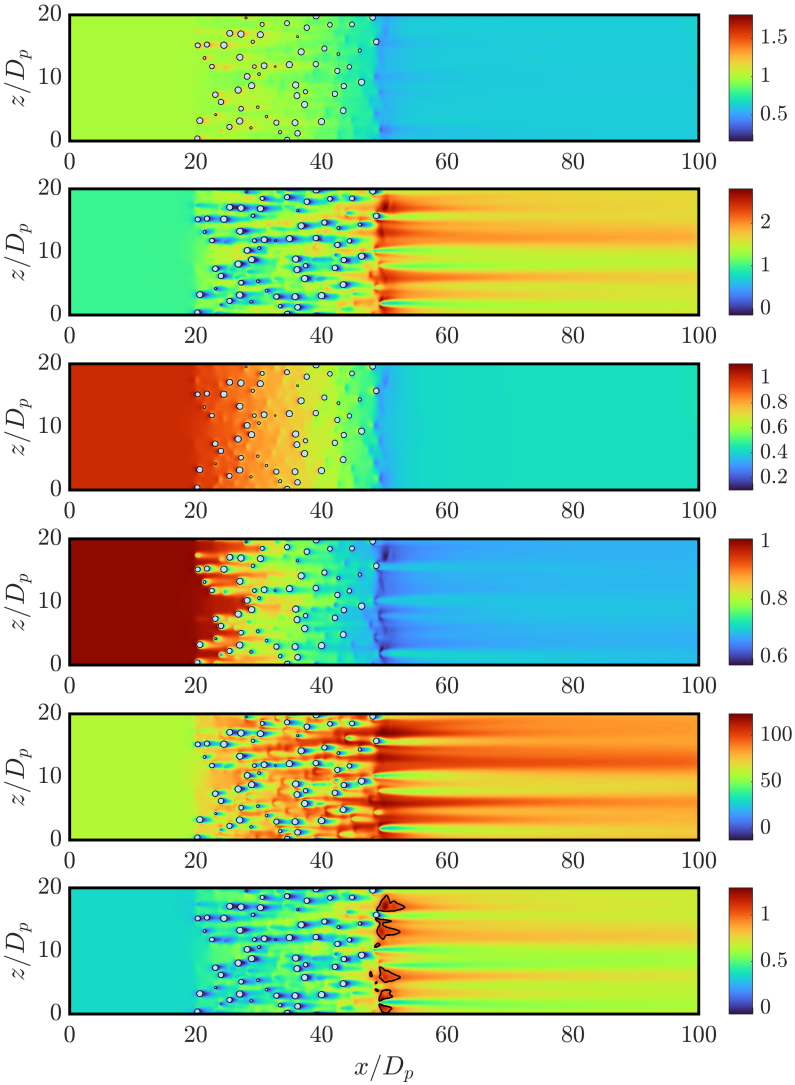

Figure 6.29: Contours of instantaneous flow fields for $M166_{30}$ in the y-half plane. From top to bottom: (a) Normalized density (ρ/ρ_∞) (b) Normalized streamwise velocity (u/u_∞) (c) Normalized static pressure (p/p_∞) (d) Normalized temperature (T/T_∞) (e) local Reynolds number $(\rho u D_p/\mu)$ (f) local Mach number $(u/\sqrt{\gamma p/\rho})$ at late times. (____) represents the $(Ma = 1)$ iso-contour.

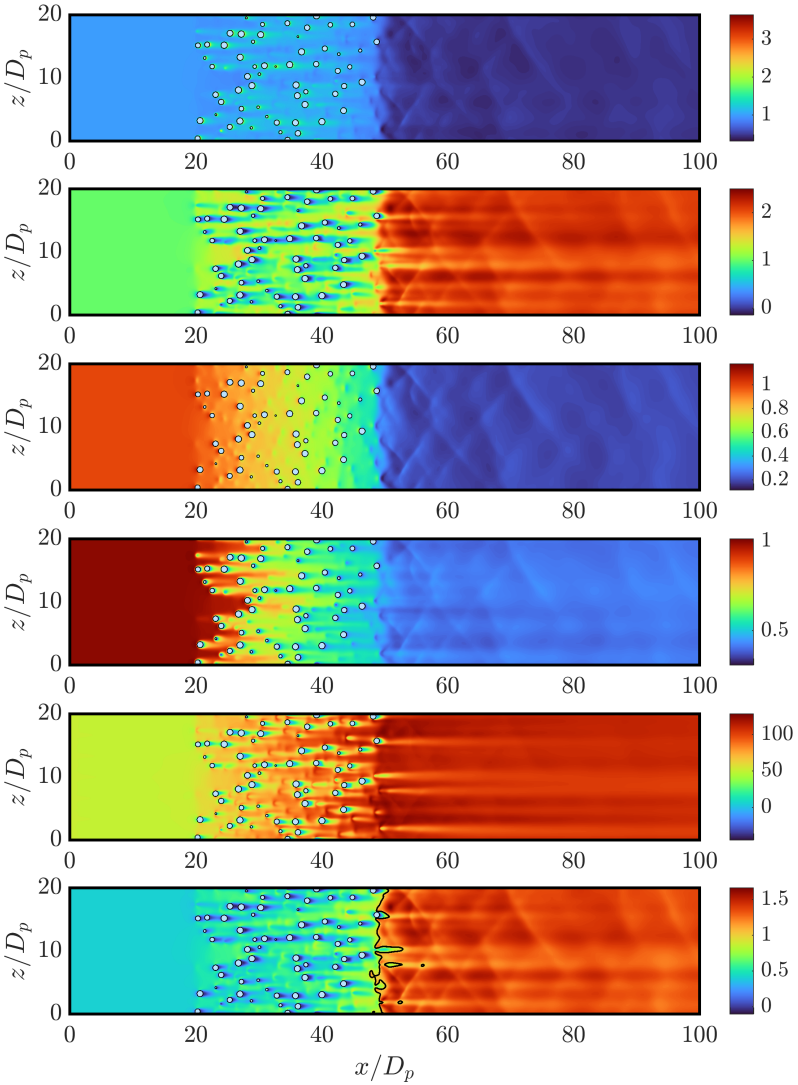

Figure 6.30: Contours of instantaneous flow fields for $M260_{30,ps}$ in the y-half plane. From top to bottom: (a) Normalized density (ρ/ρ_∞) (b) Normalized streamwise velocity (u/u_∞) (c) Normalized static pressure (p/p_∞) (d) Normalized temperature (T/T_∞) (e) local Reynolds number $(\rho u D_p/\mu)$ (f) local Mach number $(u/\sqrt{\gamma p/\rho})$ at late times. (____) represents the $(Ma = 1)$ iso-contour.

6.4.2 Particle conditioned local flow

In the current section, the mean local flow near the particles are studied using the particle-conditioned averaging of flow fields. Since, the flow is inhomogeneous in the streamwise (x) direction, the particle curtain is divided into six x-slabs of width $5D_p$ each spanning the transverse domain. The Eulerian flow-fields are then averaged in the particle-frame of reference over the particles present inside the slab to evaluate the particle-conditioned average. The average calculated in this way shows the average behavior of the flow in the vicinity of particles inside the slab. The details of the particle-conditioned averaging procedure is shown in appendix A.1.4. The x-slabs are wide enough to have enough particle samples for a smooth averaged flow field. On an average, 188 particles are present in each of the slabs.

Before proceeding, the shifted coordinate system with respect to the reference particle's center position $\mathbf{X}_c = [x_c, y_c, z_c]$ is defined. If $\mathbf{X} = [x, y, z]$ represent the original coordinate system, then the particle-center shifted system ($\widetilde{\mathbf{X}}$) is described by eq. (6.12).

$$\widetilde{\mathbf{X}} = \mathbf{X} - \mathbf{X}_c \tag{6.12}$$

Hence, the reference particle corresponding to each of the x-slabs will share the same shifted coordinate system ($\widetilde{\mathbf{X}}$). In this section, the particle-conditioned velocity and temperature fields in the x-slabs near the respective reference particle will be discussed and their behavior along the inhomogeneous streamwise direction inside the curtain will be described.

6.4.2.1 Particle conditioned velocity fields

Let the streamwise velocity (u) conditioned on the particles present in the x-slab located between $x/D_p = x_1$ and $x/D_p = x_2$ and normalized with the late-time inflow velocity u_∞ be represented as $\langle u_{x/D_p = x_1, x_2} \rangle_{pc}/u_\infty$. Then for the six slabs, $x_1 = [20, 25, 30, 35, 40, 45]$ and $x_2 = [25, 30, 35, 40, 45, 50]$.

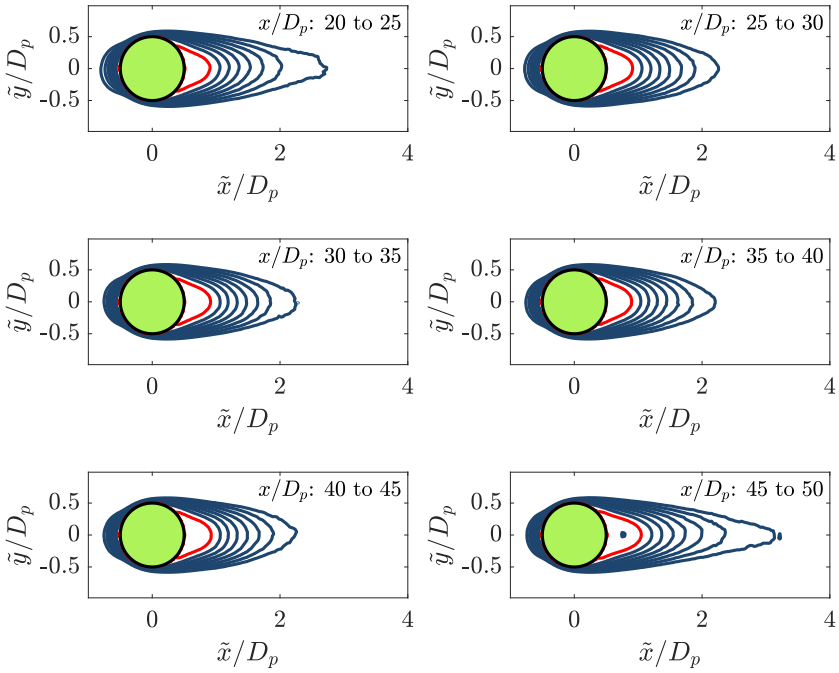

Figure 6.31: Normalized particle-conditioned average streamwise fluid-velocity contours $\langle u_{x/D_p=x_1,x_2}\rangle_{pc}/u_\infty$ for the case $M122_{30}$. $x_1 = [20, 25, 30, 35, 40, 45]$ and $x_2 = x_1 + 5$. The iso-contour lines (——) represent the normalized fluid velocity with values ranging between $[-0.1 : 0.1 : 0.7]$. The isocontour in red (——) represents the extent of the recirculation region.

Figures 6.31 to 6.33 show the wake at different x-slab positions using isocontours of $\langle u_{x/D_p=x_1,x_2}\rangle_{pc}/u_\infty$ for the case $M122_{30}$, $M166_{30}$, and $M260_{30,ps}$ respectively. It is observed that the average wake behavior represented by the velocity isocontours is approximately aligned with the center line passing through the sphere center fir the three cases. In addition, the bound on the recirculation region near the representative particles are identified as the contour where $\langle u_{x/D_p=x_1,x_2}\rangle_{pc}/u_\infty = 0$.

For the case $M122_{30}$, the velocity contours with values in the range $[-0.1 : 0.1 : 0.7]$ appear stretched for the the slab represented by $x_1 = 45$ and $x_2 = 50$ compared to the ones further upstream. In contrast, for the case

$M166_{30}$ and $M260_{30,ps}$, the contours in the same range appear more stretched at the upstream slab location given by $x_1 = 20$ compared to the most downstream slab. This can be attributed to the strong flow acceleration near the downstream edge of the curtain for $M166_{30}$ and $M260_{30,ps}$.

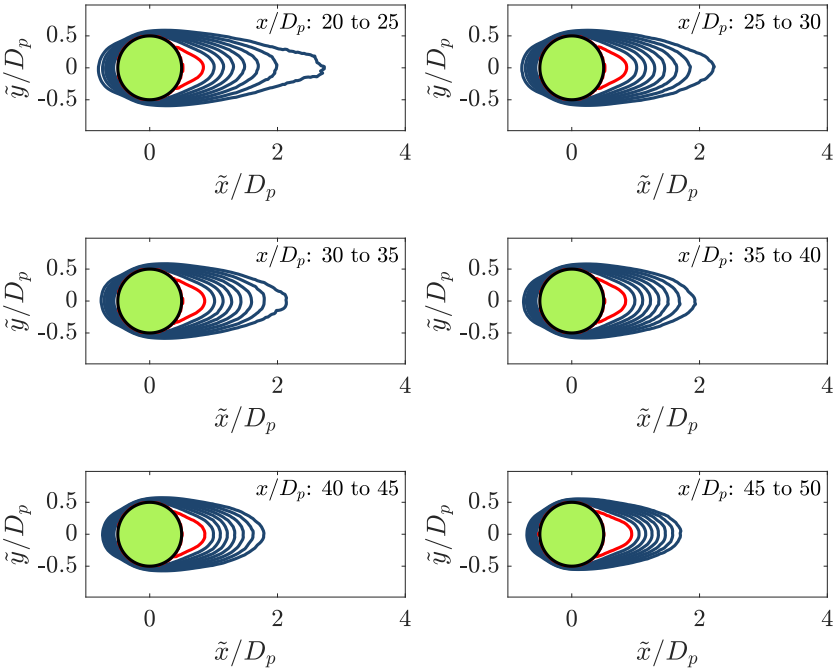

Figure 6.32: Normalized particle-conditioned average streamwise fluid-velocity contours $\langle u_{x/D_p=x_1,x_2}\rangle_{pc}/u_\infty$ for the case $M166_{30}$. $x_1 = [20, 25, 30, 35, 40, 45]$ and $x_2 = x_1 + 5$. The iso-contour lines (——) represent the normalized fluid velocity with values ranging between $[-0.1 : 0.1 : 0.7]$. The isocontour in red (——) represents the extent of the recirculation region.

It should be remembered that a strong flow acceleration at the downstream edge of the particle curtain for the cases $M166_{30}$ and $M260_{30,ps}$, results in a strong variation of flow properties even over a streamwise distance of D_p. However, since the width of the downstream slab is $5D_p$, the particle-conditioning procedure averages out the flow field changes and

is not an accurate representation of the flow near the particles located at either the upstream or the downstream edges of the most-downstream slab ($x_1 = 45$, $x_2 = 50$). Hence, ideally, the slab width should be reduced in future works(especially near the downstream edge of the particle curtain) to obtain a more accurate representation of the flow using particle-conditioned averages. In order to maintain enough samples for smooth fields while maintaining the same solid volume fraction, ideally, the transverse domain lengths L_y and L_z would simultaneously need to be increased.

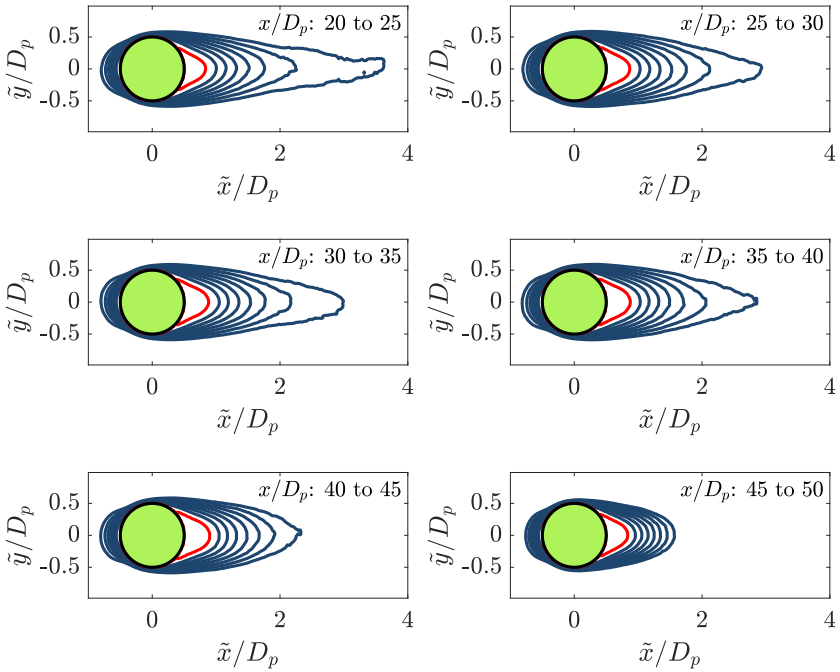

Figure 6.33: Normalized particle-conditioned average streamwise fluid-velocity contours $\langle u_{x/D_p=x_1,x_2}\rangle_{pc}/u_\infty$ for the case $M260_{30,ps}$. $x_1 = [20, 25, 30, 35, 40, 45]$ and $x_2 = x_1 + 5$. The iso-contour lines (——) represent the normalized fluid velocity with values ranging between $[-0.1 : 0.1 : 0.7]$. The iso-contour in red (——) represents the extent of the recirculation region.

The recirculation length (L_r) given by the maximum distance between the downstream stagnation point and the extent of the recirculation region along the particle centerline parallel to the streamwise direction are summarized in table 6.7 and are plotted in fig. 6.34. It is observed to be longer for the most downstream slab compared to the most upstream slab by 36.19 % for the case $M122_{30}$ and 29.35 % for the case $M166_{30}$. However, in contrast to the cases $M122_{30}$ and $M166_{30}$, the recirculation length (L_r) does not show a significant increase for the particle representative of the most downstream slab compared to the most upstream slab.

Table 6.7: Normalized recirculation lengths (L_r/D_p) obtained through particle-conditioned average at different streamwise slab locations given by $x_1 = [20, 25, 30, 35, 40, 45]$

Case	L_r/D_p					
	$x_1 = 20$	$x_1 = 25$	$x_1 = 30$	$x_1 = 35$	$x_1 = 40$	$x_1 = 45$
$M122_{30}$	0.4021	0.4126	0.4127	0.3963	0.4216	0.5476
$M166_{30}$	0.3387	0.3587	0.3603	0.3421	0.3612	0.4381
$M260_{30,ps}$	0.3343	0.3676	0.3822	0.3756	0.3985	0.3357

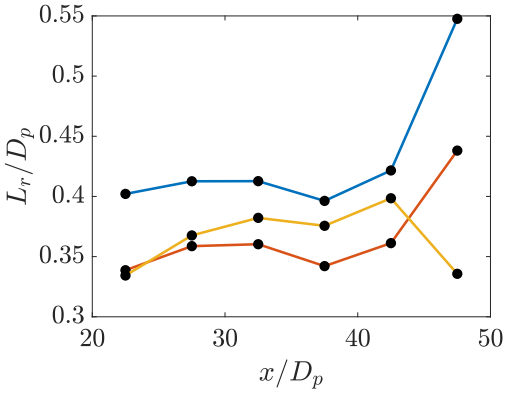

Figure 6.34: The normalized recirculation lengths (L_r/D_p) for the cases (——) $M122_{30}$, (——) $M166_{30}$, and (——) $M260_{30,ps}$ as a function of normalized streamwise positions (x/D_p) at different x-slab locations.

It was noted by Nagata et al. (2018) that the recirculation lengths for flow around an isolated isothermal particle depended on the free-stream Reynolds number (Re_∞), Mach number (Ma_∞), and the particle to free-stream fluid temperature ratio (TR_∞). They observed that for supersonic flows at $Re_\infty = 100$, the recirculation length (L_r) decreased with increasing TR_∞. In addition, the recirculation lengths for the supersonic flows were lower than for subsonic flows at $Re = 100$ for TR_∞ between 0.5 and 2. A similar observation is made while comparing the cases $M122_{30}$ and $M260_{30,ps}$, for which the Reynolds number in the current DNS are closer to 100 as seen in fig. 6.23a. In the case $M260_{30,ps}$, for which the flow is choked downstream of the particle-curtain, the recirculation length is smaller than the case $M122_{30}$, where the flow remains subsonic. In addition, for the case $M260_{30,ps}$, there is a dip in the recirculation length (L_r) at the most downstream slab where the flow becomes supersonic and the local temperature ratio increases (figs. 6.23b and 6.23c), consistent with the observations of Nagata et al. (2018). Finally, the recirculation lengths in the current DNS in presence of neighboring particles is significantly reduced compared to an isolated particle. For example, the normalized recirculation length for an isolated particle at $Ma_\infty = 0.3, Re_\infty = 100$ and $TR_\infty = 0.9$ as observed by Nagata et al. (2018) was approximately 0.85, which makes the prediction for $M122_{30}$ at the most downstream slab 35.58 % smaller than the isolated particle case.

Figure 6.35 shows the particle-conditioned streamwise velocity along the particle centerline parallel to the streamwise direction at different x-slab locations for the cases $M122_{30}$ (fig. 6.35a), $M166_{30}$ (fig. 6.35b), and $M260_{30,ps}$ (fig. 6.35c). For all the three cases, the effective normalized inflow velocity seen by the particles of the most upstream slab is close to unity as expected. However, flow acceleration occurs downstream of the curtain for the three cases, and the inflow velocity seen by the particles near the downstream edge of the curtain is higher than what is seen by the particles further upstream.

For the cases $M166_{30}$ and $M260_{30,ps}$, strong flow acceleration occurs at the downstream edge of the particle-curtain as seen in fig. 6.21b, and a strong streamwise velocity gradient exists. Hence, for these cases, the particle-conditioned streamwise velocity can exceed the respective inflow velocity

seen by the representative particle over a few multiples of particle-diameter, especially for the slabs close to the downstream edge of the curtain.

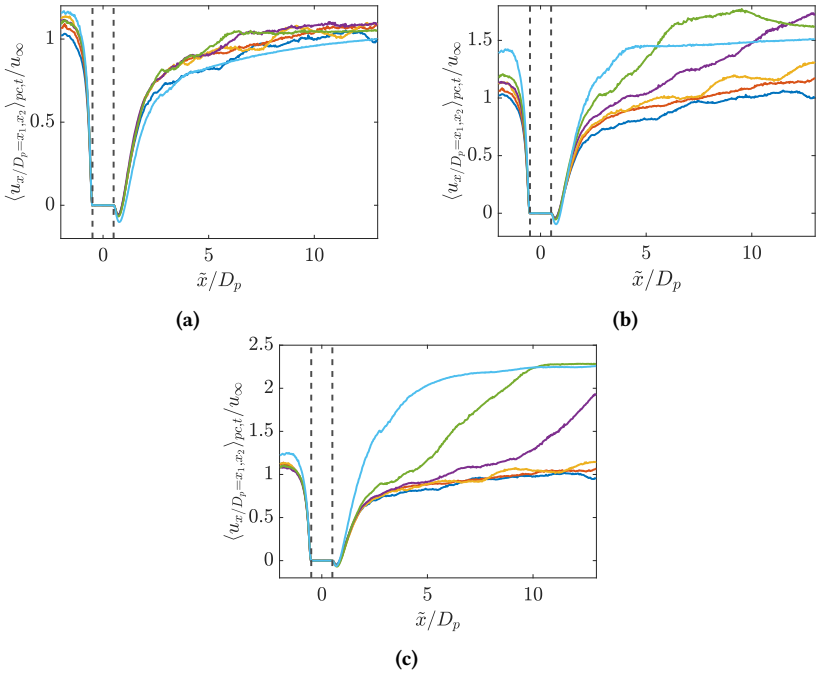

Figure 6.35: Particle-conditioned streamwise velocity ($\langle u_{x/D_p=x_1,x_2}\rangle_{pc}/u_\infty$) on the center line passing through the particle center and parallel to the x-axis for the cases (a) $M122_{30}$ (b) $M166_{30}$ and (c) $M260_{30,ps}$, where (——) $x_1 = 20$, $x_2 = 25$, (——) $x_1 = 25$, $x_2 = 30$, (——) $x_1 = 30$, $x_2 = 35$, (——) $x_1 = 35$, $x_2 = 40$, (——) $x_1 = 40$, $x_2 = 45$, and (——) $x_1 = 45$, $x_2 = 50$.

Let $\hat{u}_d(x_1, x_2)$ represent the velocity deficit for the representative particle of a x-slab located between $x/D_p = x_1$ and $x/D_p = x_2$ and computed along the particle centerline. The definition of $\hat{u}_d(x_1, x_2)$ is shown in eq. (6.13), where $\langle u_{x/D_p=x_1,x_2}\rangle_{pc,\infty}$ represents the respective inflow velocity seen by the representative particle, such that $\langle u_{x/D_p=x_1,x_2}\rangle_{pc,\infty} = \langle u_{x/D_p=x_1,x_2}\rangle_{pc}\big|_{\min(\tilde{x}/D_p)}$ along the particle centerline. In eq. (6.13), $\hat{u}_d(x_1, x_2)$ is calculated along the particle-centerline from the downstream edge of the representative particle

until $\langle u_{x/D_p=x_1,x_2}\rangle_{pc}$ exceeds $\langle u_{x/D_p=x_1,x_2}\rangle_{pc,\infty}$. The condition is enforced since, near the downstream edge of the particle-curtain, the flow may experience strong flow acceleration, such that the particle-conditioned flow velocity for a representative particle may quickly exceed its perceived inflow velocity over a distance in the order of a few particle diameters, especially in the cases $M166_{30}$ and $M260_{30,ps}$.

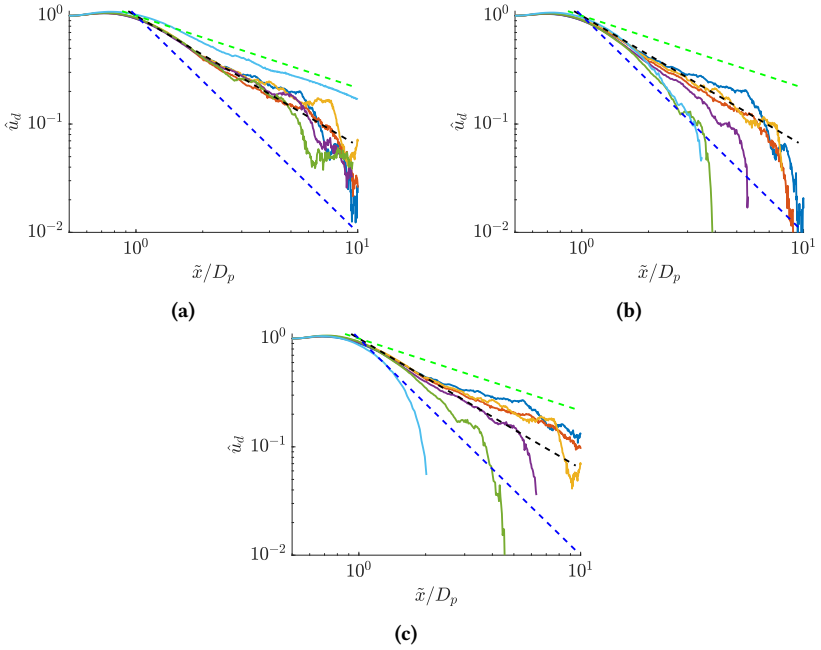

Figure 6.36: Velocity deficit ($\hat{u}_d$) evaluated on the center line passing through the particle center and parallel to the x-axis for the cases (a) $M122_{30}$ (b) $M166_{30}$ and (c) $M260_{30,ps}$ The colors representing the plots for velocity deficit have the same meaning as fig. 6.35. The dashed lines represent the decay rates proportional to (- - -) $\tilde{x}^{-2/3}$, (- - -) $\tilde{x}^{-1.1}$ and (- - -) $\tilde{x}^{-2}$

$$\hat{u}_d(x_1,x_2) = \frac{\langle u_{x/D_p=x_1,x_2}\rangle_{pc,\infty} - \langle u_{x/D_p=x_1,x_2}\rangle_{pc}}{\langle u_{x/D_p=x_1,x_2}\rangle_{pc,\infty}} \tag{6.13}$$

Figure 6.36 shows the velocity deficit ($\hat{u}_d$) evaluated for the cases $M122_{30}$, $M166_{30}$, and $M260_{30,ps}$ at different x-slab locations on a logarithmic scale. A few interesting observations are made. In the case $M122_{30}$, $\hat{u}_d$ follows a decay rate proportional to approximately $\widetilde{x}^{-1.1}$ for the representative particles of the five most upstream slabs located at $x_1 = 20, 25, 30, 35$, and 40 until a downstream distance of $\widetilde{x}/D_p = 5$.

A decay rate close to -1 was also found by Doychev (2014) for incompressible flow around a stationary homogeneous distribution of particles in a triply periodic domain at $Re_\infty = 141,245$ and a volume fraction of $\phi_p = 0.005$. For the most downstream slab ($x_1 = 45$), the $\hat{u}_d$ for the representative particle follows a decay rate closer to $\widetilde{x}^{-2/3}$, which is similar to the decay rates observed in turbulent wakes (Pope 2000).

For the case $M166_{30}$, as seen in fig. 6.36b, $\hat{u}_d$ decays at the rate $\widetilde{x}^{-1.1}$ until $\widetilde{x}/D_p = 6$ at the x-slab positions given by $x_1 = 25$ and 30. The decay rate deviates and is higher for the representative particles located downstream in the x-slabs given by $x_1 = 35, 40$, and 45. This is interesting since, unlike the case $M122_{30}$, the decay-rate becomes faster for the particles closer to the downstream edge of the curtain compared to the bulk. This can be attributed to the strong flow acceleration for the case $M166_{30}$ at the downstream edge of the curtain. In fact, the decay rate at the x-slab locations given by $x_1 = 40$ and 45 are closer to $\widetilde{x}^{-2}$ between $\widetilde{x}/D_p = 1$ and $\widetilde{x}/D_p = 3$. For the most upstream slab given by $x_1 = 20$, however, the decay rate deviates and becomes slower than $\widetilde{x}^{-1.1}$ between approximately $\widetilde{x}/D_p = 3$ and $\widetilde{x}/D_p = 6$.

In the case $M260_{30,ps}$, the spectrum of decay rates observed in the inhomogeneous setup widens even further. For example, approximately between $\widetilde{x}/D_p = 2$ and 4, the decay rate of $\hat{u}_d$ for x-slab given by $x_1 = 35$ is close to $\widetilde{x}^{-1.1}$. However, the decay rates at the slabs given by $x_1 = 20, 25$, and 30 are slower. In comparison, the decay rate in the slab given by $\widetilde{x}/D_p = 40$ which is further downstream, shows a decay rate closer to $\widetilde{x}^{-2}$ at a similar distance from the center of the representative particle. Finally, the slab located most downstream at $x_1 = 45$ does not show any clear power law and decays the fastest.

6.4.2.2 Particle conditioned temperature fields

Temperature contours

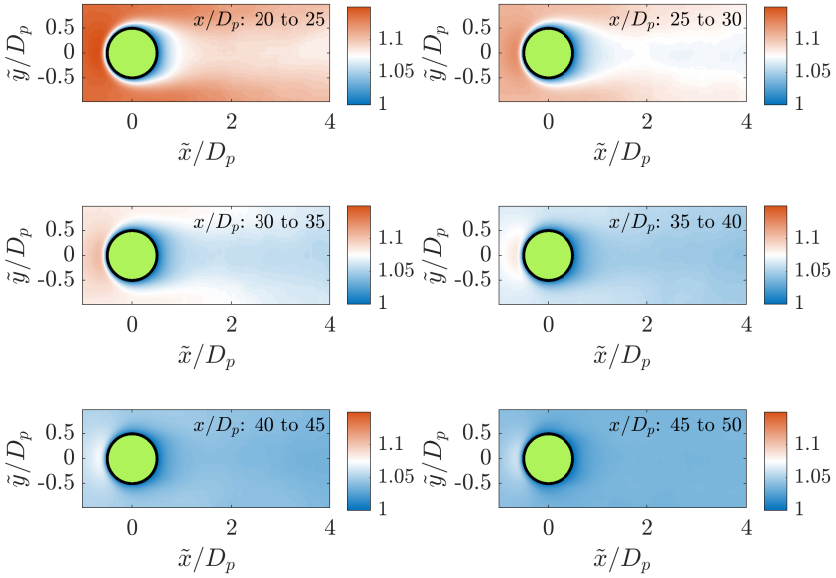

Figure 6.37: Normalized Particle-conditioned average fluid temperature contours $\langle T_{x/D_p=x_1,x_2}\rangle_{pc}/T_p$ for the case $M122_{30}$. $x_1 = [20, 25, 30, 35, 40, 45]$ and $x_2 = x_1 + 5$.

Figures 6.37 to 6.39 show the contours of the particle conditioned temperature profiles normalized with the imposed particle temperature ($\langle T_{x/D_p=x_1,x_2}\rangle_{pc}/T_p$) for the cases $M122_{30}$, $M166_{30}$, and $M260_{30,ps}$ respectively. The figures show the established thermal boundary layers near the particle as the fluid flow through the curtain. It is observed that the particles located further along the streamwise direction inside the curtain are exposed to lower upstream temperatures for the cases $M122_{30}$, $M166_{30}$, and $M260_{30,ps}$. This is expected since the fluid gets cooled along the particle curtain as seen in fig. 6.21d. In

addition, the perceived upstream temperature for the representative particle at a given x-slab location is lowest for $M122_{30}$ and highest for $M260_{30,ps}$. This is because the inflow temperatures (T_∞) for the case $M260_{30,ps}$ is highest among the three cases as observed from fig. 6.23c

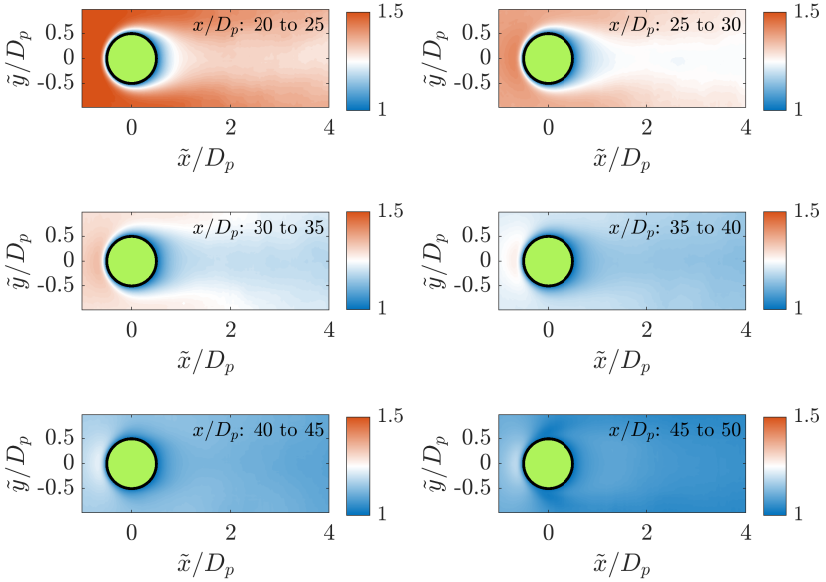

Figure 6.38: Normalized particle-conditioned average fluid temperature contours $\langle T_{x/D_p=x_1,x_2}\rangle_{pc}/T_p$ for the case $M166_{30}$. $x_1 = [20, 25, 30, 35, 40, 45]$ and $x_2 = x_1 + 5$.

In general, lower radial temperature gradients are observed along a vector aligned with the positive x axis measured from the particle surface as compared to along the cross-stream and the negative x directions. This feature is observed for all three cases and at different slab locations. Hence, the flow in the locality of the particles are cooler in the particle wake region. The streamwise temperature gradients near the upstream and downstream stagnation points will be quantified below.

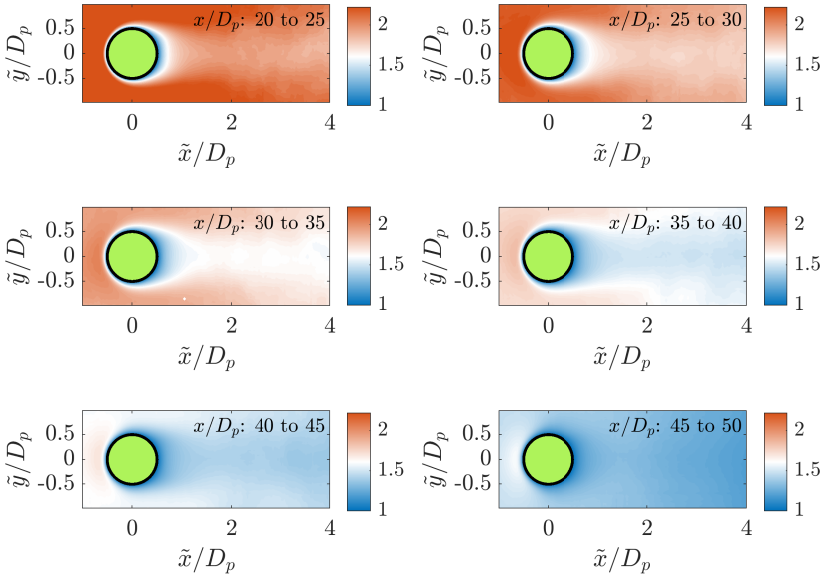

Figure 6.39: Normalized particle-conditioned average fluid temperature contours $\langle T_{x/D_p=x_1,x_2}\rangle_{pc}/T_p$ for the case $M260_{30,ps}$. $x_1 = [20, 25, 30, 35, 40, 45]$ and $x_2 = x_1 + 5$.

Normalized temperature profiles

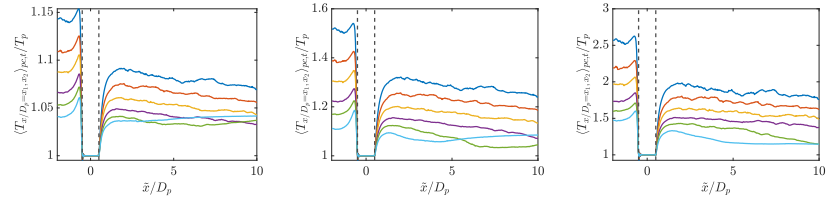

Figure 6.40: Profiles of normalized particle-conditioned average fluid temperature $\langle T_{x/D_p=x_1,x_2}\rangle_{pc}/T_p$ for the cases (a) $M122_{30}$ (b) $M166_{30}$ and (c) $M260_{30,ps}$. $x_1 = [20, 25, 30, 35, 40, 45]$ and $x_2 = x_1 + 5$ along the particle centerline parallel to the streamwise axis. The colors of the contour plot have the same meaning as in fig. 6.35.

Table 6.8: Normalized particle conditioned temperature gradient magnitudes for the case $M122_{30}$ at different streamwise slab locations given by $x_1 = [20, 25, 30, 35, 40, 45]$ near the upstream stagnation point ($\tilde{x}/D_p = -0.5$) and downstream stagnation point ($\tilde{x}/D_p = 0.5$).

$\tilde{x}/D_p$	$(D_p/T_p) \mid \Delta\langle T_{x/D_p=x_1,x_2}\rangle_{pc}/\Delta\tilde{x} \mid$					
	$x_1 = 20$	$x_1 = 25$	$x_1 = 30$	$x_1 = 35$	$x_1 = 40$	$x_1 = 45$
-0.5	1.5811	1.3336	1.148	0.936	0.7854	0.6844
$+0.5$	0.3556	0.2922	0.2449	0.1994	0.1677	0.1496

Table 6.9: Normalized particle conditioned temperature gradient magnitudes for the case $M166_{30}$ at different streamwise slab locations given by $x_1 = [20, 25, 30, 35, 40, 45]$ near the upstream stagnation point ($\tilde{x}/D_p = -0.5$) and downstream stagnation point ($\tilde{x}/D_p = 0.5$).

$\tilde{x}/D_p$	$(D_p/T_p) \mid \Delta\langle T_{x/D_p=x_1,x_2}\rangle_{pc}/\Delta\tilde{x} \mid$					
	$x_1 = 20$	$x_1 = 25$	$x_1 = 30$	$x_1 = 35$	$x_1 = 40$	$x_1 = 45$
-0.5	5.4777	4.4550	3.7201	2.9538	2.4333	2.1198
$+0.5$	1.2493	0.9850	0.7980	0.6217	0.505	0.4015

Table 6.10: Normalized particle conditioned temperature gradient magnitudes for the case $M260_{30,ps}$ at different streamwise slab locations given by $x_1 = [20, 25, 30, 35, 40, 45]$ near the upstream stagnation point ($\tilde{x}/D_p = -0.5$) and downstream stagnation point ($\tilde{x}/D_p = 0.5$).

$\tilde{x}/D_p$	$(D_p/T_p) \mid \Delta\langle T_{x/D_p=x_1,x_2}\rangle_{pc}/\Delta\tilde{x} \mid$					
	$x_1 = 20$	$x_1 = 25$	$x_1 = 30$	$x_1 = 35$	$x_1 = 40$	$x_1 = 45$
-0.5	18.5049	14.9397	12.4859	9.9936	8.2867	7.2693
$+0.5$	4.6597	3.7074	3.0367	2.4091	2.0044	1.5223

Figures 6.40a to 6.40c show the particle conditioned temperature profiles along the particle centerline, which is parallel to the streamwise axis.

The corresponding magnitudes of the normalized temperature gradients ($|\,(D_p/T_p)\,\Delta\langle T_{x/D_p=x_1,x_2}\rangle_{pc}/\Delta\tilde{x}\,|$) are shown in tables 6.8 to 6.10 respectively. The temperature peaks just upstream of the particle location before dropping to the imposed particle-temperature, creating a strong negative temperature gradient. The magnitude of the negative temperature gradient is higher for the particles located closer to the upstream-edge of the curtain compared to those which are located further downstream. In addition, magnitude of the negative temperature gradient is highest for $M260_{30,ps}$ and lowest for $M122_{30}$ at a given x-slab location.

At the downstream stagnation point of the representative particle for a given x-slab location, the temperature increases again along the streamwise direction, achieving another peak, before decreasing again. As the temperature increases from the downstream stagnation point of the representative particles, a positive temperature gradient is established along the streamwise direction. In general, it was observed that the magnitude of the positive temperature gradients established near the downstream stagnation point were smaller than the magnitudes of the negative temperature gradients established near the upstream stagnation point for a given case and at a given x-slab location.

6.4.3 Particle forces and heat transfer

In this section, the forces and the nature of the heat transfer and their variance for the particles inside the curtain is studied. At late times, the post-shock quantities do not have a physical significance, since the inflow conditions have been modified by the reflected shock waves. Hence, different from eq. (6.4), it is more appropriate to define the Drag coefficient and the Nusselt number based on the local reference quantities. Two different approaches are used to compute the drag coefficient and the Nusselt numbers. The first definition based on the local slab-averaged quantities given in eq. (6.14) and the second one based on the local hemispherical shell averaged quantities given in eq. (6.15).

$$\begin{aligned}
\langle C_D \rangle_{slab} &= \frac{\sum_{m=1}^{N_s} \langle F_x^{(m)} \rangle}{0.125 N_s \langle \rho \rangle_{slab} \langle u \rangle_{slab}^2 \pi D_p^2} \\
\langle Nu \rangle_{slab} &= \frac{D_p}{N_s \kappa_w \left(T_w - \langle T \rangle_{slab} \right)} \sum_{m=1}^{N_s} \langle \overline{q}^{(m)} \rangle
\end{aligned} \tag{6.14}$$

$$\begin{aligned}
\langle C_D^{(m)} \rangle_{shell} &= \frac{\langle F_x^{(m)} \rangle}{0.125 \langle \rho^{(m)} \rangle_{shell} \langle u^{(m)} \rangle_{shell}^2 \pi D_p^2} \\
\langle Nu^{(m)} \rangle_{shell} &= \frac{D_p}{\kappa_w \left(T_w - \langle T^{(m)} \rangle_{shell} \right)} \langle \overline{q}^{(m)} \rangle
\end{aligned} \tag{6.15}$$

The procedures for slab and hemispherical shell averaging are given in appendix A. In eq. (6.14), the slab width (B_x) chosen is given by $B_x = D_p$ and N_s is the total number of particles in a given slab (s). In eq. (6.15), (m) is the index of a particle for which hemispherical shell-averaging is performed. The hemispherical shell averaging provides a more local insight into the individual particle drag coefficients, Nusselt numbers, and associated variance along the inhomogeneous streamwise direction. A sketch representing the hemispherical shell volume over which the averaging is performed is shown in fig. 6.41.

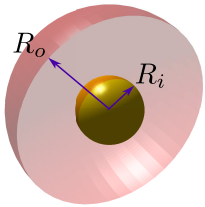

Figure 6.41: Visualization of the hemispherical shell volume (in red) upstream of a sphere with inner radius R_i (same as the sphere radius R) and the outer radius R_o.

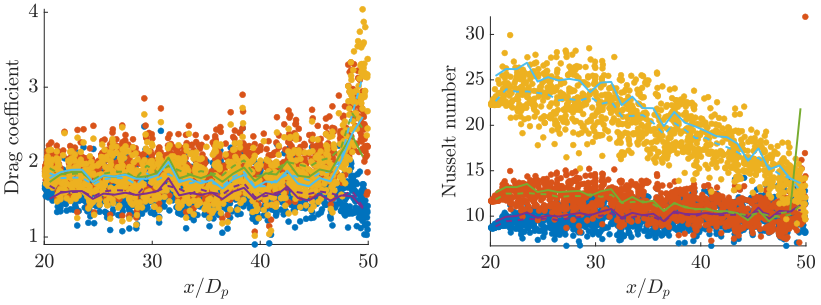

Figure 6.42: (a) Drag coefficient and Nusselt number (b) for flow through a finite-sized particle array. The scatter plot of individual particle shell-averaged Drag coefficients and Nusselt numbers are shown as (●) $\langle f^{(m)} \rangle_{shell}$ for $M122_{30}$, (●) $\langle f^{(m)} \rangle_{shell}$ for $M166_{30}$, (●) $\langle f^{(m)} \rangle_{shell}$ for $M260_{30}$. The slab-averaged Drag coefficients and Nusselt numbers are given by (——) $\langle f \rangle_{slab}$ for $M122_{30}$, (——) $\langle f \rangle_{slab}$ for $M166_{30}$, (——) $\langle f \rangle_{slab}$ for $M260_{30,ps}$. Finally, the shell-averaged Drag coefficients and Nusselt numbers averaged inside the slab are given by (- - -) $\langle f \rangle_{shell,slab}$ for $M122_{30}$, (- - -) $\langle f \rangle_{shell,slab}$ for $M166_{30}$, (- - -) $\langle f \rangle_{shell,slab}$ for $M260_{30,ps}$. A slab width of D_p is used for slab averaging. f represents the Drag coefficient or the Nusselt number, wherever applicable.

Figure 6.42a shows the comparison between the cases $M122_{30}$, $M166_{30}$, and $M260_{30,ps}$ for slab-averaged ($\langle C_D \rangle_{slab}$) and hemispherical shell averaged ($\langle C_D^{(m)} \rangle_{shell}$) Drag coefficients. Similarly, fig. 6.42b shows the comparison between the cases $M122_{30}$, $M166_{30}$, and $M260_{30,ps}$ for slab-averaged ($\langle Nu \rangle_{slab}$) and hemispherical shell averaged ($\langle Nu^{(m)} \rangle_{shell}$) Nusselt numbers. In addition, to make a direct comparison between the shell-averaged and slab-averaged quantities, shell-averaged Drag coefficients and Nusselt numbers averaged inside the slab of width D_p are evaluated and defined in eq. (6.16), where m is the particle index and N_s is the total number of particles inside a given slab of width D_p.

$$\langle C_D \rangle_{shell,slab} = \langle \langle C_D \rangle_{shell} \rangle_{slab} \tag{6.16}$$

$$\langle Nu \rangle_{shell,slab} = \langle \langle Nu \rangle_{shell} \rangle_{slab} \tag{6.17}$$

6.4.3.1 Behavior of the Drag coefficient

It is observed for the case $M122_{30}$, where the flow remains locally subsonic throughout the curtain, there is no significant observed variation of $\langle C_D \rangle_{slab}$ along the particle-curtain. Although the Reynolds number for the case shows a small increase along the curtain as shown in fig. 6.23a, its effect on the Drag coefficient is compensated by the increase in Mach number and particle-to-fluid temperature ratio as seen in figs. 6.23b and 6.23c. The local peaks and troughs in the corresponding profile are due to the local variation of solid volume-fraction (ϕ) along the curtain, whose footprint can also be observed in the other two cases ($M166_{30}$ and $M260_{30,ps}$). For the cases $M166_{30}$ and $M260_{30,ps}$, $\langle C_D \rangle_{slab}$ have a larger value compared to $M122_{30}$ throughout the curtain. An interesting feature observed in the cases $M166_{30}$ and $M260_{30,ps}$ is a sharp peak in the slab-average based Drag coefficient at the downstream edge of the curtain, where the flow can be locally choked and achieve supersonic velocities further downstream. This flow-feature was also observed by Osnes et al. (2019) at late times with the shock Mach number of $Ma_s = 2.6$, although they used a much higher Reynolds number in their LES study of $\mathcal{O}(1000)$. This hints at the increase in drag coefficient downstream to depend on inviscid mechanisms. Osnes et al. (2019) state that the effect is based on the sharp increase in Mach number as the flow accelerates rapidly downstream of the particle curtain. It is now established from the previous works of Nagata et al. (2016) for single particles and Osnes et al. (2023) in a multi-particle system that the total drag coefficient increases sharply in the high subsonic-regime. Indeed, in the current work, as discussed in section 6.4.1, the local flow Mach number may quickly increase from a low subsonic value upstream of the curtain to choking conditions near the downstream edge of the particle curtain as a result of the strong flow acceleration for the cases $M166_{30}$ and $M260_{30,ps}$.

It was noted by Nagata et al. (2018) that the Drag coefficient of an isolated particle in viscous compressible flows depends on the Mach number, Reynolds number and the particle-to-flow Temperature ratio. They had observed that the Drag coefficient (C_D) increased with increasing the Temperature ratio (TR) and the Mach number (Ma), but decreased with the increasing Reynolds

number (*Re*). The complex interplay of the three non-dimensional parameters can also be seen in the present inhomogeneous distribution of multiple particles in a finite-sized array. From fig. 6.42, it is observed that the average Drag coefficient for the particles present in the bulk (not including the region near the downstream edge of the particle array) are the lowest for $M122_{30}$, increases for $M166_{30}$, but decreases in comparison to $M166_{30}$ by a small amount for the case $M260_{30,ps}$. This observation can be explained as follows. Let us refer to fig. 6.23.

The Reynolds number in the bulk is lower and the Mach number is higher for the cases $M166_{30}$ and $M260_{30,ps}$ compared to $M122_{30}$. Although, the Temperature Ratio is higher for $M122_{30}$ compared to the other two cases, it's effect is presumably less significant compared to the combined effects of Mach and Reynolds numbers. Hence, the Drag coefficient for the cases $M166_{30}$ and $M260_{30,ps}$ are higher compared to $M122_{30}$ in the bulk. Between the cases $M166_{30}$ and $M260_{30,ps}$, the Reynolds number and the Mach number effects are presumably smaller compared to the thermal effects. Since the Temperature ratio for the case $M260_{30,ps}$ is much smaller than $M166_{30}$ in the bulk, a slight decrease in the Drag-coefficient is observed for $M260_{30,ps}$ compared to $M166_{30}$.

At the downstream edge of the particle curtain, as previously mentioned, strong flow acceleration occurs for $M166_{30}$ and $M260_{30,ps}$ and the Drag coefficient is dictated by compressibility effects. Hence, the Drag coefficients for $M166_{30}$ and $M260_{30,ps}$ are higher compared to $M122_{30}$. The observed peak in Drag coefficient at the downstream edge of the curtain is higher for the case $M260_{30,ps}$ compared to $M166_{30}$. This is also possibly explained by the fact that a larger cross-section of the flow gets locally choked for the case $M260_{30,ps}$ compared to $M166_{30}$ as seen in figs. 6.25a and 6.26a. We will see in section 6.5 how accurately the standard models are capable of predicting the evolution of average drag coefficient.

The local hemispherical shell averaging reveals strong variation in the individual drag coefficients along the particle curtain for the cases $M122_{30}$, $M166_{30}$, and $M260_{30,ps}$ as seen in fig. 6.42a. In addition, the general trend followed

by the slab-averaged Drag coefficients ($\langle C_D \rangle_{slab}$) is captured by the shell-averaged Drag coefficients averaged inside the slab ($\langle C_D \rangle_{shell,slab}$). However, it is observed that the peak in the Drag coefficient at the downstream edge of the particle curtain obtained from $\langle C_D \rangle_{shell,slab}$ is higher than from $\langle C_D \rangle_{slab}$.

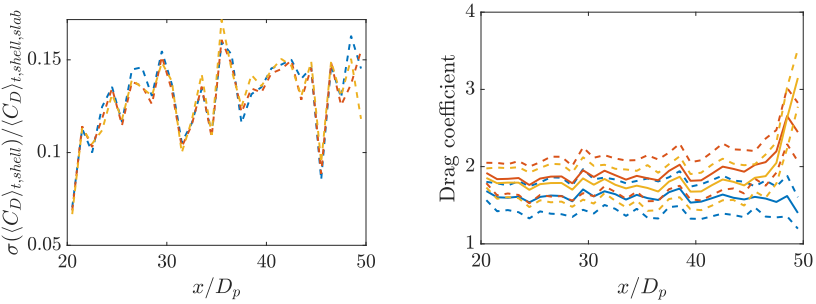

Figure 6.43: (a) Comparison of the standard deviation of the Drag coefficient obtained through shell averaging inside a bin of width D_p ($\sigma(\langle C_D \rangle_{shell})$) normalized with the mean of the shell-averaged Drag coefficient inside the slab ($\langle C_D \rangle_{shell,slab}$) for the cases (- - -) $M122_{30}$, (- - -) $M166_{30}$ and (- - -) $M260_{30,ps}$. (b) shows the profiles of $\langle C_D \rangle_{shell,slab}$ for the cases (——) $M122_{30}$, (——) $M166_{30}$, and (——) $M260_{30,ps}$ respectively. The dashed lines represent the value of Drag coefficient one standard deviation above and below the corresponding mean value, and the color is the same for the case for which the mean ($\langle C_D \rangle_{shell,slab}$) is computed.

The hemispherical shell-averaging procedure also allows to quantify the local variance of Drag coefficient along the particle curtain. The normalized standard deviation $\sigma(\langle C_D \rangle_{shell}) / \langle C_D \rangle_{shell,slab}$ of the particle forces in streamwise x-slabs is given in fig. 6.43a. It is observed that the the normalized standard deviation does not differ by much between the cases $M122_{30}$, $M166_{30}$, and $M260_{30,ps}$. Hence, it is presumed that at the late times, the force fluctuations inside the particle curtain have a similar dependency on the local particle arrangement irrespective of the Mach number. In all three cases, a general increase in the normalized standard deviation is observed near the upstream edge of the particle curtain until about $x/D_p \approx 25$. Beyond $x/D_p \approx 25$, the profile does not show appreciable increase in the normalized standard deviation (apart from the local peaks and troughs which are a function of the local

solid volume fraction). Later in section 6.5, comparisons are made between the current DNS and the available models.

Before proceeding, it should be remarked that the evaluation of the drag coefficient (C_D) and the Nusselt number (Nu) have a fundamentally different meaning. While the drag coefficient measures the total force on the particles compared to the dynamic pressure force, the Nusselt number compares the effective heat transfer rate by convection compared to conduction. Hence, the trends shown by the two non-dimensional parameters are expected to be different inside the curtain. A force coefficient measuring the total drag force on the particle compared to the Stokes drag is defined in appendix H and some trends are discussed.

6.4.3.2 Behavior of the Nusselt number

Comparing the profiles in fig. 6.42b, it is observed that the Nusselt number obtained through local slab averaging ($\langle Nu \rangle_{slab}$) and the shell-averaged Nusselt numbers averaged inside the slab ($\langle Nu \rangle_{shell,slab}$) are highest for the case $M260_{30,ps}$ and lowest for $M122_{30}$ at the upstream edge of the curtain.

Near the downstream edge of the particle curtain, the Nusselt number values are much closer. However, for the case $M166_{30}$, a sharp increase in the Nusselt number is observed at the downstream edge of the particle curtain. This can be observed through the scatter plot of $\langle Nu \rangle_{shell}$ for $M166_{30}$ in fig. 6.42b, where the particles close to the downstream edge of the curtain may locally reach a Temperature ratio ($T_p/\langle T \rangle_{shell}$) sufficiently close to unity (fig. 6.23c), such that the conductive heat transfer rate is diminished compared to the total rate of heat transfer. Consequently, the Nusselt number increases for $M166_{30}$ in the region. In fact, for the outlier with maximum value of $\langle Nu \rangle_{shell,slab}$ for the case $M166_{30}$ as seen in fig. 6.42b has a local Temperature ratio ($T_p/\langle T \rangle_{shell}$ = 0.988).

In the bulk flow (neglecting the possible local effects at the downstream edge of the curtain), the Nusselt number follows a smoother trend for the three cases. For $M122_{30}$, a gradual increase in the Nusselt number is observed

along the streamwise direction. In contrast, the Nusselt numbers for the cases $M166_{30}$ and $M260_{30,ps}$ decrease with the streamwise position along the curtain in the bulk. As noted by Nagata et al. (2018), similar to the drag coefficient, the Nusselt number for the particles are also a function of the local Mach number, Reynolds number, and the Temperature ratio. However, the dependence on the three non-dimensional parameters is more complex. Nonetheless, some general comparisons and remarks can be made. It was observed by Nagata et al. (2018) that at a Mach number of 0.3, the Nusselt number for an isolated particle increased on decreasing temperature ratio. This is consistent with the current results at the upstream edge of the curtain. Although, the Nusselt number also increases with increasing Reynolds number, the thermal effects are presumably more important at the upstream edge of the particle curtain in comparison to the Reynolds number effects due to high magnitudes of the particle-to-flow temperature gradients in the region, especially for $M166_{30}$ and $M260_{30,ps}$.

For the case $M122_{30}$, the positive gradient of the Nusselt number along the curtain is governed by the competing effects of increasing Reynolds number and the Temperature ratios as stated by Nagata et al. (2018) at a Mach number of 0.3. The gradual increase in the Nusselt number for $M122_{30}$ is possibly because of the stronger dependence of Nusselt number on the Reynolds number compared to the Temperature ratio along the curtain. In contrast, the thermal effects seem to be more important compared to the Reynolds number along the curtain for the cases $M166_{30}$ and $M260_{30,ps}$ (Note that the mean flow remains low subsonic for all three cases in the bulk of the curtain, except close to its downstream edge as seen in fig. 6.23b). Consequently, the Nusselt number decreases along the streamwise distance along the curtain in the bulk for the cases $Ma166_{30}$ and $M260_{30,ps}$. Another observation by Nagata et al. (2018) is that for a Mach number of 0.8, the Nusselt numbers at Temperature ratio 0.5 and 0.9 for an isolated particle are nearly equal. Something similar is observed at the downstream edge of the curtain for the cases $M166_{30}$ and $M260_{30,ps}$. The Nusselt number for these two cases at the downstream edge of the curtain are also similar, although the local particle-to-fluid temperature ratios are quite different as seen in fig. 6.23c.

Figure 6.44a shows the normalized standard deviation of the Nusselt number ($\sigma(\langle Nu\rangle_{shell})/\langle Nu\rangle_{shell,slab}$) as a function of the streamwise position along the curtain. Like the Drag coefficient, it is observed that the normalized standard deviation is similar between the cases $M122_{30}$, $M166_{30}$, and the $M260_{30,ps}$ in the bulk. However, for the case $M166_{30}$, a sharp peak in the standard deviation is observed at the downstream edge of the curtain due to the peak in the Nusselt numbers for some particles whose particle-to-fluid Temperature ratio is sufficiently close to unity. The general trend of the normalized standard deviation in the bulk (excluding the downstream edge of the curtain) is an increase with the streamwise position along the curtain. However, the rate of increase seems to decrease along the particle curtain inside the bulk.

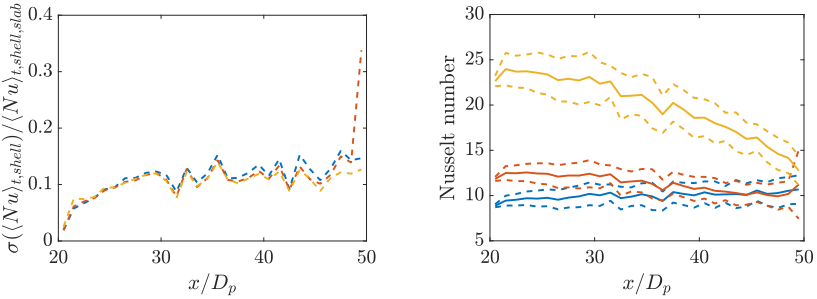

Figure 6.44: (a) Comparison of the standard deviation of the Nusselt number obtained through shell averaging inside a bin of width D_p ($\sigma(\langle Nu\rangle_{shell})$) normalized with the mean of the shell-averaged Nusselt number inside the slab ($\langle Nu\rangle_{shell,slab}$) for the cases (- - -) $M122_{30}$, (- - -) $M166_{30}$ and (- - -) $M260_{30,ps}$. (b) shows the profiles of $\langle Nu\rangle_{shell,slab}$ for the cases (——) $M122_{30}$, (——) $M166_{30}$, and (——) $M260_{30,ps}$ respectively. The dashed lines represent the value of Nusselt number one standard deviation above and below the corresponding mean value, and the color is the same for the case for which the mean ($\langle Nu\rangle_{shell,slab}$) is computed.

Finally, the shell and slab averaged Nusselt numbers ($\langle Nu\rangle_{shell,slab}$) for the three cases along with the values one standard deviation higher and lower than the mean are plotted in fig. 6.44b. It is observed from fig. 6.42b that the Nusselt number calculated through the local shell-averaging ($\langle Nu\rangle_{shell,slab}$)

in general has a smaller value compared to the ones evaluated by local slab-averaging ($\langle Nu \rangle_{slab}$) along the particle curtain. It is possibly because of the fact that the local temperature evaluated by shell averaging ($\langle T^{(m)} \rangle_{shell}$) near a particle of index m are slightly higher compared to the the slab-averaged temperature ($\langle T \rangle_{slab}$) inside which the particle is located. This is because for a flow with negative temperature gradients along the curtain, the hemispherical shell averaging only considers the upstream flow as locally seen by the particle, compared to the slab averaged temperature which considers an average of the temperature variations inside the entire slab.

6.4.4 Effect of curtain width

In order to characterize the effects of the curtain-width, L_p for the case $M260_{30,ps}$ is increased from $30D_p$ to $50D_p$ while keeping the other parameters constant. This case is denoted by $M260L_{30,ps}$ in table 6.1.

6.4.4.1 Comparison of mean flow profiles

The slab-averaged mean density, streamwise velocity, pressure, and Temperature profiles for the two cases are plotted in fig. 6.45. The flow fields are normalized with the inflow conditions at the curtain inlet and are plotted on a rescaled streamwise coordinate system given by $\hat{x} = (x - x_{p,o})/L_p$, where $x_{p,o}$ is the streamwise location of the curtain inlet and L_p is the curtain length specific to the case. It should be noted that there are no significant flow field gradients upstream of the curtain at late times. Hence, the normalization with the curtain inlet conditions is approximately equivalent to normalization with the respective free-stream conditions given in table 6.6 and the flow fields shown in fig. 6.45 can be thought of as being normalized with the free-stream conditions. Figure 6.45d reveals that the normalized temperature ($\langle T \rangle_{slab}/T_{p,o}$) decreases to a lower value for the case with the longer curtain-width ($M260_{30,ps}$). This is to be expected since the fluid gets cooled further by the particles along the curtain for a longer curtain width. The normalized pressure profiles given in fig. 6.45c look similar between the two cases. In addition, the flow gets choked at the downstream edge of the curtain (as will be

later shown in fig. 6.46b) in both the cases and the pressure gradients inside the curtain adjust to the choking conditions downstream.

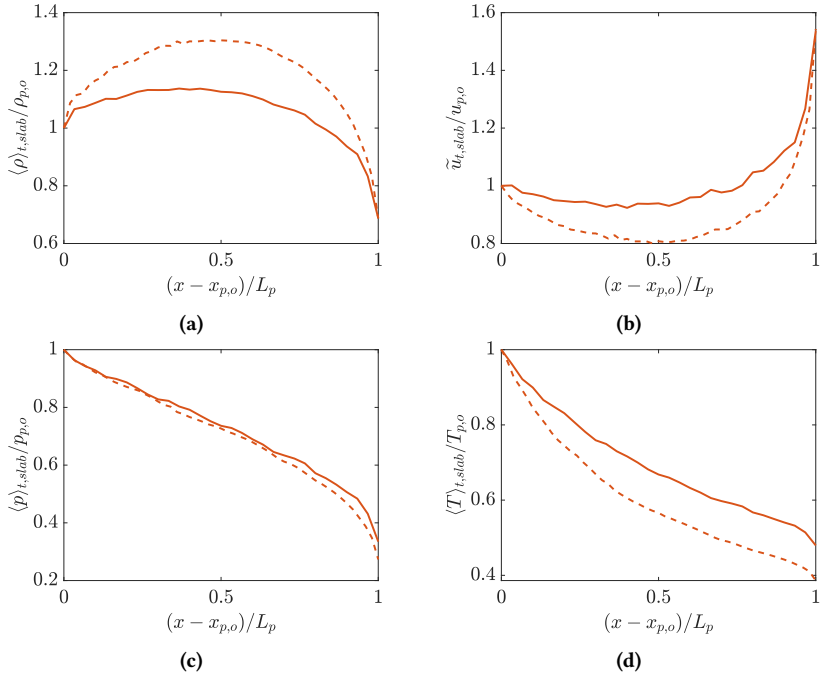

Figure 6.45: Comparison of slab averaged flow-field profiles for (a) Density, (b) velocity, (c) Pressure, and (d) Temperature normalized with conditions at the curtain upstream position at late times as a function of scaled and normalized streamwise distance between cases $M260_{30,ps}$ (——) and $M260L_{30,ps}$ (– – –). The subscript "p,o" denotes the curtain upstream location.

The normalized density profiles for $M260_{30,ps}$ and $M260L_{30,ps}$ are given in fig. 6.45a. For both the cases, the normalized density first increases along the curtain, achieves a maximum and then decreases further. The reason for this behavior depends on combined effect of local pressure and temperature gradients and is explained in section 6.4.1. It is interesting to note that the normalized density profiles achieve an approximately equal value at the downstream

edge of the curtain. However, this feature was not captured for the streamwise density along the curtain by varying curtain-widths using the simplistic one-dimensional model (refer to section 6.5.2) for the case $M166_{30}$. A deeper investigation of the curtain-dependence on the flow features is recommended in future research, but is currently outside the scope of the current work. The normalized velocity given by fig. 6.45b first decreases, achieves a local minimum, and then increases further along the curtain in both cases. This trend is opposite to that of the density profiles, which is to be expected in order to satisfy mass conservation principles. Similar to the density profiles, the normalized velocity profiles also achieve an approximately equal value at the downstream curtain edge for the cases $M260_{30,ps}$ and $M260L_{30,ps}$.

6.4.4.2 Comparison of Non-dimensional parameters

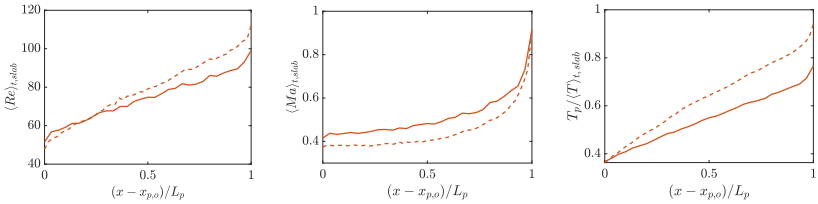

Figure 6.46: Comparison of slab averaged profiles for (a) Reynolds number, (b) Mach number, and (c) at late times as a function of scaled and normalized streamwise distance between cases $M260_{30,ps}$ (——) and $M260L_{30,ps}$ (- - -). $x_{p,o}$ denotes the curtain upstream location.

The profiles for the slab averaged Reynolds number $\langle Re \rangle_{slab}$, Mach number $\langle Ma \rangle_{slab}$, and the particle-to-fluid Temperature Ratio $T_p/\langle T \rangle_{slab}$ are shown in figs. 6.46a to 6.46c respectively for the cases $M260_{30,ps}$ and $M260L_{30,ps}$. It is observed that $\langle Re \rangle_{slab}$ is lower at the curtain inlet for the case $M260L_{30,ps}$ compared to $M260_{30,ps}$. However, at the downstream edge of the curtain, it achieves a higher value of Reynolds number compared to $M260_{30,ps}$. This can be explained by the nature of the temperature profiles given in fig. 6.45d. Since, the fluid is cooled to a larger extent in case of $M260L_{30,ps}$ compared to

$M260_{30,ps}$ at the downstream curtain edge, based on the Sutherland's law eq. (C.8), the flow is also more viscous for $M260_{30,ps}$. Consequently, its Reynolds number is also higher at the downstream particle curtain edge. At the upstream edge of the particle curtain, the fluid is slightly hotter for the case $M260L_{30,ps}$ compared to $M260_{30,ps}$ as seen from table 6.6. With the same argument, the Reynolds number behavior at the upstream edge of the particle curtain can also be explained.

The slab averaged Mach numbers $\langle Ma \rangle_{slab}$ achieve a low-subsonic value at the upstream edge of the particle curtain for both the cases $M260L_{30,ps}$ and $M260_{30,ps}$. Hence, the compressibility effects are small in this region. In addition, the Mach number is smaller at the upstream edge of the curtain for the case $M260L_{30,ps}$ compared to $M260_{30,ps}$. The Mach number profiles maintain a small positive gradient along the curtain until the downstream edge, where a strong flow acceleration occurs for both the cases. The Mach number profiles seem to achieve a choked flow condition for both the cases at the downstream edge of the curtain. This feature is analogous to the choking of the flow near the throat of a converging diverging nozzle at sufficiently large upstream-to-downstream pressure ratios, irrespective of the length of the converging section.

The slab averaged temperature ratio ($T_p/\langle T \rangle_{slab}$) profiles show that the fluid is slightly more cooled for the case $M260_{30,ps}$ at the upstream edge of the curtain compared to $M260L_{30,ps}$. However, at the downstream edge, the trend flips and the $M260L_{30,ps}$ has colder fluid compared to $M260_{30,ps}$, consistent with previous discussions.

6.4.4.3 Comparison of particle forces and heat transfer

Figure 6.47a shows the Drag coefficient based on slab averaged quantities ($\langle C_D \rangle_{slab,t}$) for the cases $M260_{30,ps}$ and $M260L_{30,ps}$. Both the cases seem to show a similar trend along the particle curtain when plotted on the rescaled coordinate system. A strong flow acceleration occurs near the downstream edge of the curtain in both cases. The downstream edge particle drag coefficient is also approximately equal in both the cases. This is expected since the

solid volume fraction, Reynolds number and Mach number in the region are similar as shown in figs. 6.46a and 6.46b.

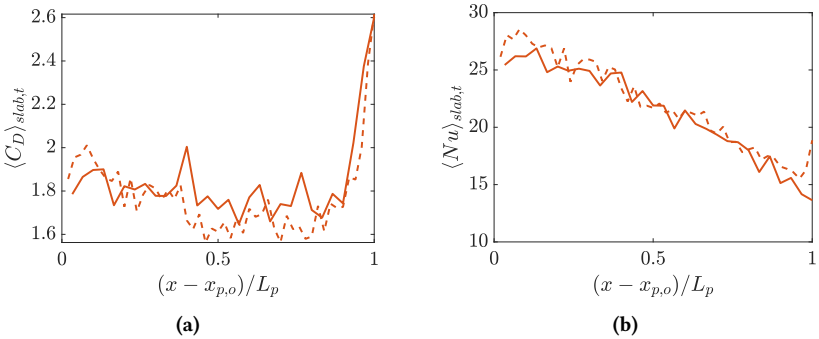

Figure 6.47: Comparison of slab averaged profiles for (a) Drag coefficient and (b) Nusselt number at late times as a function of scaled and normalized streamwise distance between cases $M260_{30,ps}$ (——) and $M260L_{30,ps}$ (- - -). $x_{p,o}$ denotes the curtain upstream location.

The Nusselt number based on slab averaged quantities is shown in fig. 6.47b for the cases $M260_{30,ps}$ and $M260L_{30,ps}$. The Nusselt number in the bulk (except the downstream curtain edge) look similar for both cases. In both cases, the Nusselt number decreases along the curtain in the bulk. However, near the downstream edge of the curtain, the fluid for the case $M260L_{30,ps}$ shows an increase in Nusselt number. Analogous to the case $M166_{30}$ as seen from fig. 6.42b, the fluid is sufficiently cooled at the downstream edge of the longer curtain, such that the conductive rate of heat transfer is reduced compared to the total heat transfer rate, resulting in an enhanced Nusselt number locally.

6.4.5 Effect of volume fraction

In this section the effect of volume-fraction on the flow dynamics at late times is studied for the case $M166_{30}$. The solid volume fraction (ϕ) for the case $M166_{30}$ is reduced from $\phi = 0.05$ to 0.25 while keeping the other parameters constant. This case with a lower solid volume fraction is represented as $M166C_{30}$ and the relevant parameters for the case are shown in table 6.1.

6.4.5.1 Comparison of mean flow profiles

Figure 6.48 show the slab-averaged profiles of the density, streamwise velocity, pressure and temperature for the cases $M166_{30}$ and $M166C_{30}$ normalized with the respective inflow conditions. The inflow conditions for the two cases are described in table 6.6.

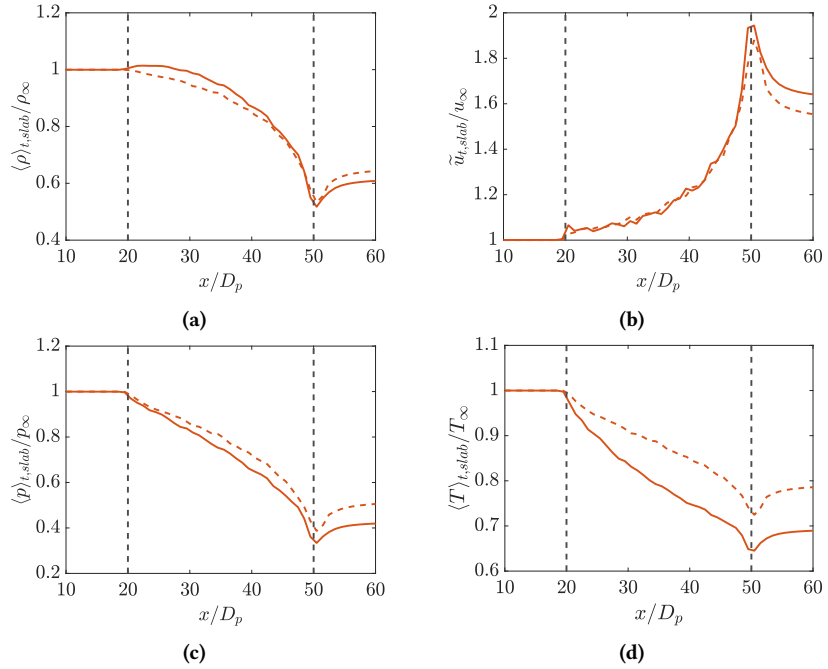

Figure 6.48: Comparison of slab averaged flow-field profiles for (a) Density, (b) velocity, (c) Pressure, and (d) Temperature normalized with inflow conditions at late times given by table 6.6 as a function of normalized streamwise distance between cases $M166_{30}$ (——) and $M166C_{30}$ (- - -).

The slab averaged profiles in fig. 6.48d, show a negative temperature gradient for the two cases along the streamwise distance inside the curtain. However, $M166C_{30}$ has a smaller magnitude of temperature gradient along the curtain compared to $M166_{30}$. Consequently, the slab-averaged temperature is higher

for the case $M166C_{30}$ compared to $M166_{30}$ at the downstream edge of the curtain. Hence, the fluid is cooled to a smaller extent by the particles for a more dilute distribution of particles. Intuitively, a smaller number of particles (as in the case $M166C_{30}$ compared to $M166_{30}$) results in a smaller rate of total heat exchange between the two phases inside the curtain.

Figure 6.48c gives the slab averaged pressure profiles for the cases $M166_{30}$ and $M166C_{30}$. Although both the cases show a negative pressure gradient inside the curtain, the magnitude of pressure-gradient is smaller for the case $M166C_{30}$ compared to $M166_{30}$. It should be remarked that the pressure gradient will depend on the fluid viscosity and the local flow velocity (Muskat 1934), in addition to the solid volume fraction. As seen from fig. 6.48d and table 6.6, in general, the fluid temperature remains higher for the lower Mach number case ($M166C_{30}$) compared to $M166_{30}$ inside the curtain. From Sutherland's viscosity law, the fluid is also in general more viscous inside the curtain for $M166C_{30}$. Consequently, it contributes positively to the pressure-gradient magnitudes for the coarser case and compensates for the effect of a more dilute particle arrangement. Hence, even at lower solid volume fractions, the pressure-gradient magnitudes appear similar for the two cases. It should be noted that the closeness of the pressure profiles are probably not a general feature. The pressure gradients inside the curtain will depend on the cumulative effects of the imposed temperature conditions on the particles, the inflow conditions to the curtain, the viscous law used, and the solid volume fraction.

The slab-averaged velocity profiles along the curtain are shown for the two cases in fig. 6.48b. The velocity increases along the curtain for both the cases. Inside the curtain, the normalized profiles for velocity look identical in the bulk (excluding the region near the downstream edge of the curtain). Close to the downstream edge however, the slab averaged velocity profiles achieve a smaller value for the case $M166C_{30}$ compared to $M166_{30}$.

The normalized density profiles for the two cases are shown in fig. 6.48a. Density decreased throughout the particle curtain for the case $M166C_{30}$, however, density increased initially for $M166_{30}$ near the upstream edge of the curtain,

before decreasing further. Consequently, near the upstream edge of the curtain, smaller density gradients are observed for the case $M166C_{30}$ compared to the $M166_{30}$.

6.4.5.2 Comparison of Non-dimensional parameters

Figure 6.49a shows the slab-average based Reynolds number as a function of the streamwise position along the curtain for the case $M166_{30}$ and $M166C_{30}$. The Reynolds number increases for both the cases along the curtain as the fluid is cooled by the particles, reducing the fluid viscosity. In addition, it is observed that the slab-averaged Reynolds number for the case $M166C_{30}$ is higher than $M166_{30}$ throughout the curtain.

The slab-average based Mach number ($\langle Ma \rangle_{slab}$) is higher for the case $M166C_{30}$ compared to $M166_{30}$ as seen in fig. 6.49b. This is because of the inflow conditions at late times, which are setup by the initial reflected shock wave for the case $M166C_{30}$ already has a higher Mach number compared to $M166_{30}$. Strong flow acceleration occurs for both the cases at the downstream edge of the curtain resulting in a strong increase in the average Mach number in the region. In both the cases, flow gets locally choked at the downstream curtain edge.

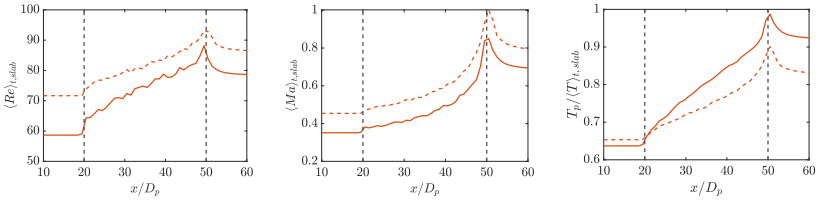

Figure 6.49: Comparison of slab averaged profiles for (a) Reynolds number, (b) Mach number, and (c) at late times as a function of normalized streamwise distance between the cases $M166_{30}$ (——) and $M166C_{30}$ (– – –).

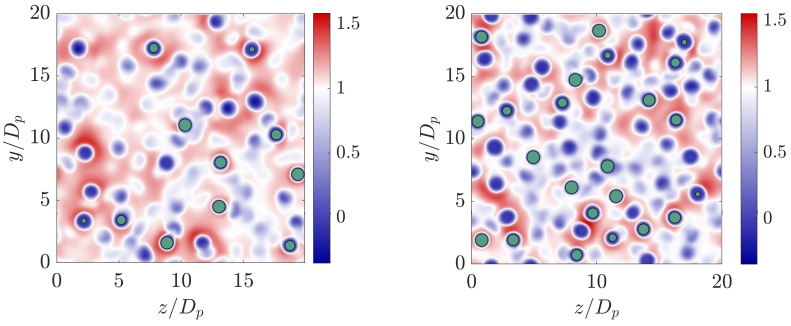

Figure 6.50: Contours of the local Mach number at the cross section corresponding to the downstream edge of the curtain given by $x = L_s + L_p$ for the cases (a) $M166C_{30}$ and (b) $M166_{30}$ at late times. The blue color corresponds to subsonic regions and the red color represent locally supersonic regions.

The contours of the local Mach number at the downstream edge of the curtain for both the cases are shown in fig. 6.50. Indeed, it is observed that a larger cross-section at the downstream edge of the curtain is supersonic for the case $M166C_{30}$ compared to $M166_{30}$. The particle-to-fluid temperature ratio is given in fig. 6.49c. It is observed that the temperature ratio increases for both the cases along the curtain. In addition, The profiles confirm that although the free-stream temperature is lower for the case $M166C_{30}$, the fluid temperature is higher than $M166_{30}$ at the downstream curtain edge.

6.4.5.3 Comparison of particle forces and heat transfer

Figure 6.51a shows the slab-average based drag coefficient for the case $M166_{30}$ and $M166C_{30}$. The Drag coefficient in general was observed to be lower in the case $M166C_{30}$ compared to $M166_{30}$. This effect arises from the combined effect of the higher Reynolds number, smaller particle-to-fluid temperature ratio and a smaller magnitude of the pressure gradient along the curtain for the case $M166C_{30}$.

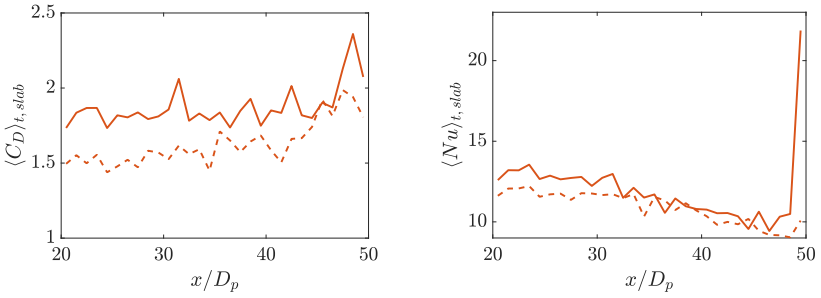

Figure 6.51: Slab averaged profiles for (a) Drag coefficient and (b) Nusselt number at late times as a function of normalized streamwise distance for cases $M166_{30}$ (——) and $M166C_{30}$ (- - -).

The slab-average based Nusselt number for the two cases are shown in fig. 6.51b. The Nusselt number decreases along the particle-curtain inside the bulk (excluding the downstream edge of the curtain) for both the cases but show an increase at the downstream curtain edge. As previously discussed, the increase in Nusselt number downstream of the curtain are presumably based on the reduced rate of conductive to total heat transfer rate as the temperature ratio becomes sufficiently close to unity. However, the Nusselt number in general remains smaller inside the curtain for the case $M166C_{30}$ compared to $M166_{30}$.

6.4.5.4 Comparison of subsonic and supersonic regions

Figure 6.52 shows the cross-sectional regions in the $y-z$ plane where the flow reaches sonic conditions for the cases $M166_{30}$ and $M166C_{30}$ at late times. From the contour plots, it is apparent that a larger cross-section of the flow reaches $Ma = 1$. To quantify this feature, a fractional area (A^*_{sup}) is defined as in eq. (6.18). In eq. (6.18), $A_{sonic,yz}$ is the cross-sectional area in the $y-z$ plane, along which the flow achieves sonic conditions. The value of A^*_{sonic} was observed to be 0.6974 for $M166_{30}$ and 0.8816 for the case $M166C_{30}$ respectively.

$$A^*_{sonic} = \frac{A_{sonic,yz}}{A_{total,yz}} \tag{6.18}$$

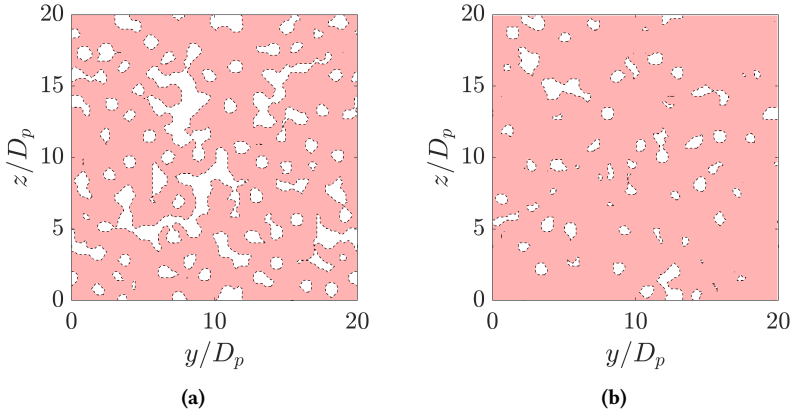

Figure 6.52: Comparison of regions which achieve sonic Mach numbers (in red) compared to the regions which remain subsonic throughout (in white) for the cases (a) $M166_{30}$ and (b) $M166C_{30}$ at late times in the $y-z$ plane.

Hence, it is concluded that for the cases $M166_{30}$ and $M166C_{30}$, only a fraction of the cross-sectional area becomes choked along the streamwise direction. As a short note, for the case $M260_{30,ps}$, even though only a fraction of the total area is choked at the downstream edge of the curtain, the flow still achieves supersonic conditions further downstream along the curtain through fluid friction as shown in fig. 6.30f.

6.4.6 Statistics in the curtain wake

It was shown in table 6.5 that the temporal fluctuations in the flow fields are small compared to the spatial fluctuations for all the test cases considered

in the study at late times. Hence, in this section, the statistics for pseudo-turbulent fluctuations of the flow field arising from inhomogeneous particle distribution are discussed. First the streamwise variation of the pseudo-turbulent fluctuations are visualized by plotting the profiles of PTKE in the wake of the curtain (also inside the curtain) at late times for the cases $M122_{30}$, $M166_{30}$, and $M260_{30,ps}$. In addition, statistical tools like joint probability density functions, energy spectra and two point correlations are used to discuss the spatial fluctuations of relevant flow quantities and their interdependence in the wake of the curtain.

6.4.6.1 Velocity fluctuations

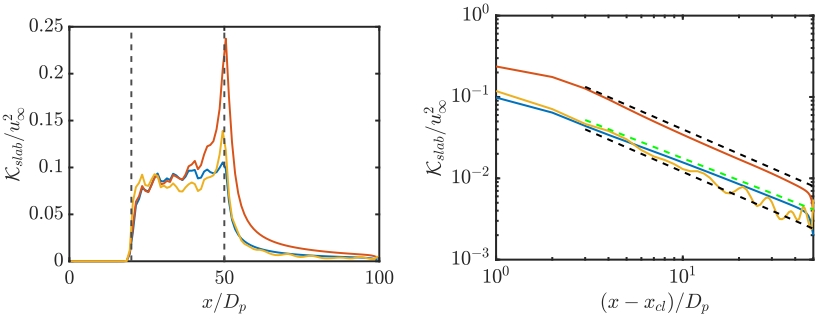

Figure 6.53: (a) Comparison of slab averaged based Normalized pseudo-turbulent kinetic energy (PTKE) ($\mathcal{K}_{slab}/u_\infty^2$) and (b) decay of PTKE downstream of the curtain. x_{cl} represents the location of the downstream edge of the curtain. The black dashed line (- - -) represents a x^{-1} decay and the green line (- - -) represents a $x^{-0.9}$ decay. The different cases are represented by (——) $M122_{30}$, (——) $M166_{30}$, and (——) $M260_{30,ps}$.

Figure 6.53a shows the streamwise distribution of the normalized pseudo turbulent kinetic energy given by $\mathcal{K}_{slab}/u_\infty^2$ at late times for the cases $M122_{30}$, $M166_{30}$, and $M260_{30,ps}$, where $\mathcal{K}_{slab}$ is given by eq. (6.19) and $u''_{slab} = u - \widetilde{u}_{slab}$.

$$\mathcal{K}_{slab} = \frac{1}{2}\left(\widetilde{u''_{slab}u''_{slab}} + \widetilde{v''_{slab}v''_{slab}} + \widetilde{w''_{slab}w''_{slab}}\right) \tag{6.19}$$

With the chosen normalization, a few interesting features are observed. In all the three cases, the PTKE is high inside the particle curtain and decays in its wake. For the case $M122_{30}$, a gradual increase in PTKE is observed along the streamwise direction inside the curtain. In contrast, for the cases $M166_{30}$ and $M260_{30,ps}$, a peak in PTKE is observed near the downstream curtain edge as the flow undergoes sharp acceleration. With the chosen normalization, the peak at the downstream edge observed was highest for the case $M_{166_{30}}$ and smallest for $M122_{30}$. In fact, the peak value of the normalized PTKE for the case $M166_{30}$ was 70.6 % higher than the peak of $M260_{30,ps}$ and 125.14 % higher than the peak normalized PTKE value of $M122_{30}$. However, the large peak observed for the normalized PTKE in the case $M166_{30}$ is an artefact of choosing u_∞ as the chosen reference quantity. As seen in table 6.6, the inflow conditions are different for the three cases and are sensitive to the strength of the transient reflected shock.

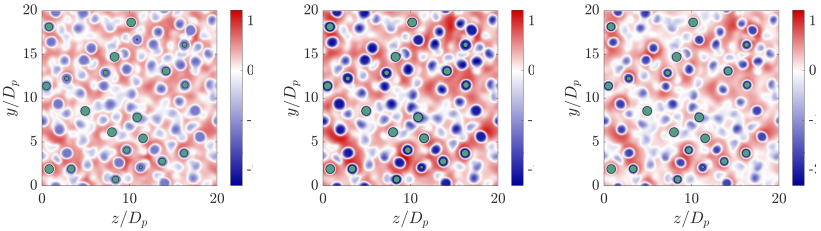

Figure 6.54: Comparison of normalized fluctuation contours $u''_{y,z/u_\infty}$ for $M122_{30}$, $M166_{30}$, and $M260_{30,ps}$ are shown in (a), (b), and (c) respectively. Here, the fluctuation with respect to the plane averaged mean is given by $u''_{y,z} = u - \widetilde{u}_{y,z}$ evaluated at $x/D_p = 50$.

Figure 6.53b shows the decay of the normalized PTKE between $x/D_p = 50$ and $x/D_p = 100$ for the three cases on the log scale. The case $M166_{30}$

shows a decay of normalized PTKE proportional to x^{-1} approximately in the region given by $(x - x_{cl})/D_p > 1$, where x_{cl} is the position of the downstream curtain edge. The case $M260_{30,ps}$ also approximately shows a power law decay proportional to x^{-1} in the region $(x - x_{cl})/D_p \in [1,10]$. Beyond $(x - x_{cl})/D_p > 10$, the profile shows an oscillatory nature, because of the presence of shock-cells for the case $M260_{30,ps}$ in the wake of the curtain as seen in fig. 6.24c. In fact, it approximately matches the wavelength of the shock cells ($\approx 8D_p$), as seen in fig. 6.30c. It was observed through In the case $M122_{30}$, a smaller decay proportional to $x^{-0.9}$ was instead observed in the range $(x - x_{cl})/D_p > 1$.

Figure 6.54 shows the normalized streamwise velocity fluctuation u''/u_∞ for the three cases, where now $u''_{y,z} = u - \widetilde{u}_{y,z}$ at $(x/D_p = 50)$. From the contours, it can be seen that negative fluctuations occur in the wake of the individual particles where the local flow velocity magnitude reaches a smaller value compared to the cross-sectional mean. Similarly, positive fluctuations are observed mostly in the interstitial spaces between the particles which cause a nozzle effect.

Let us define a pseudo-turbulent Reynolds number (Re_t) as in eq. (6.20) based on the PTKE for velocity scale and the particle diameter as the length scale.

$$Re_t = \frac{\langle \rho \rangle_{slab} D_p \sqrt{\mathcal{K}_{slab}}}{\langle \mu \rangle_{slab}} \tag{6.20}$$

Figure 6.55 shows the streamwise variation of the pseudo-turbulent Reynolds number (Re_t) for the cases $M122_{30}$, $M166_{30}$, and $M260_{30,ps}$. It is observed that Re_t is low for all three cases inside the curtain of the order $\mathcal{O}(10)$. In addition, Re_t showed an increasing trend along the curtain for the cases $M166_{30}$ and $M260_{30,ps}$. Increasing PTKE in addition to decreasing viscous effects along the particle curtain (As the fluid is cooled along the particle curtain, the viscous effects become weaker based on the Sutherland's viscosity law) contribute towards this trend. Another interesting observation is the oscillatory nature of Re_t in the wake of the particle curtain for the case with the highest

post-shock Mach number (Ma_{ps}), which can be explained by the presence of shock-cells in the domain.

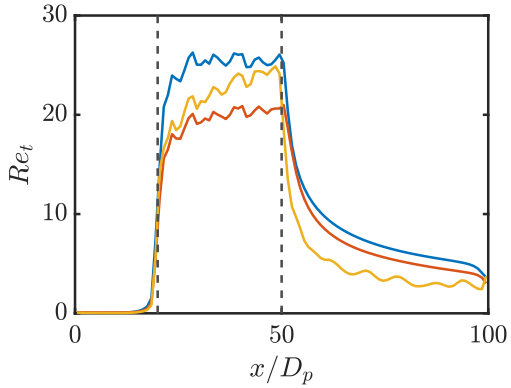

Figure 6.55: Pseudo-turbulent Reynolds number (Re_t) as a function of streamwise distance with length scale based on particle diameter and the velocity scale based on PTKE ($\mathcal{K}_{slab}$) in x-slabs of width $B_x = D_p$ for the cases (——) $M122_{30}$ (——) $M166_{30}$, and (——) $M260_{30,ps}$.

6.4.6.2 Some definitions for curtain wake statistics

It is noted that the current flow setup has an inhomogeneity along the streamwise x-direction and a statistical homogeneity along the transverse y and z directions. Furthermore, the flow has negligible temporal fluctuations at late times as seen in table 6.5 and can be approximately assumed steady. Keeping this in mind, the wake region given by $x > L_p + L_s$, is divided into three x-slabs similar to appendix A.1.1 with slab upstream edge locations given by $x_1/D_p = [50.5,\ 60.5,\ 70.5]$ of width $B_x/D_p = 5$ each. The spatial statistics are then analyzed individually in each of the slabs.

Before proceeding, some mathematical definitions are discussed in the present section. Let us define the position vector ($\mathbf{x}$) as $\mathbf{x} = [x, y, z]$, the velocity vector ($\mathbf{u}$) as $\mathbf{u} = [u_1, u_2, u_3]$ and a separation vector ($\mathbf{r}$) given by $\mathbf{r} = [r_x, r_y, r_z]$. Then following Pope (2000), a two point velocity covariance is defined as in eq. (6.21). The corresponding two-point spatial correlation function is defined

in eq. (6.22). In eqs. (6.21) and (6.22), the spatial fluctuation for a velocity component u'' in a given slab is defined as $u''_{slab} = u - \widetilde{u}_{slab}$ and $\alpha, \beta \in [1, 2, 3]$.

$$C_{\alpha\beta}(\mathbf{r}) = \langle\, u''_\alpha(\mathbf{x})\, u''_\beta(\mathbf{x}+\mathbf{r}) \,\rangle_{slab} \tag{6.21}$$

$$R_{\alpha\beta}(\mathbf{r}) = \frac{C_{\alpha\beta}(\mathbf{r})}{C_{\alpha\beta}(0)} \tag{6.22}$$

For example, with such a definition, the two point correlation function for identical velocity component ($\alpha = \beta$) with a separation along y can then be represented as in eq. (6.23).

$$R_{\alpha\alpha}(r_y) = \frac{\langle\, u''_\alpha(\mathbf{x})\, u''_\alpha(\mathbf{x}+r_y\mathbf{j}) \,\rangle_{slab}}{\langle\, u''_\alpha(\mathbf{x})\, u''_\alpha(\mathbf{x}) \,\rangle_{slab}} \tag{6.23}$$

the one-dimensional energy spectrum as a function of k_y is defined in eq. (6.24).

$$E_{\alpha\alpha}(k_y) = \left\langle \widehat{u}_\alpha(x, k_y, z)\, \widehat{u}^*_\alpha(x, k_y, z) \right\rangle_{x,z} \tag{6.24}$$

In eq. (6.24), $\widehat{u_\alpha}^*$ represents the complex conjugate of $\widehat{u_\alpha}$. In the current section, k_y represents the wave-number vector related to the wavelength (λ_y) as $k_y = 2\pi/\lambda_y$. Definitions along the wave-number $k_z = 2\pi/\lambda_z$ can be defined in a similar way.

6.4.6.3 Two point correlations and premultiplied energy spectra

Figure 6.56, fig. 6.57, and fig. 6.58 show the plots for the two point correlations and the corresponding pre-multiplied spectra along y and z for the cases $M122_{30}$, $M166_{30}$, and $M260_{30,ps}$ at different x-slab locations given by $x_1/D_p = 50.5, 60.5$, and 70.5. As a remark, the two transverse directions are homogeneous and the difference between the correlation along y and z

are because of the particle statistics. In much larger domains and larger particle samples, it is expected for the correlations along the two directions to become more similar.

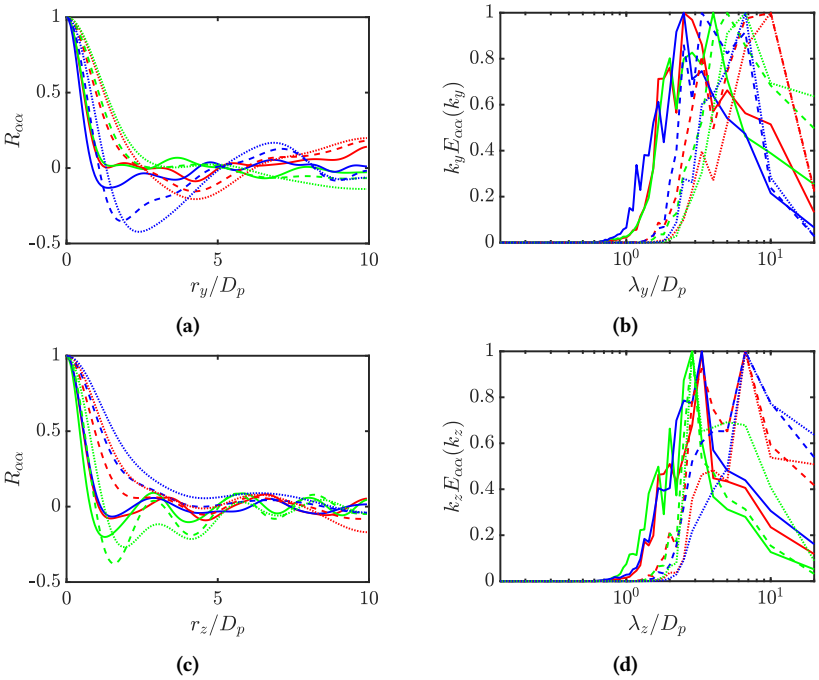

Figure 6.56: Comparison of the two point correlations and the corresponding pre-multiplied spectra for the case $M122_{30}$ along y in (a), (b), and along z in (c), (d). The solid lines (——), (——), and (——) represent R_{11}, R_{22}, and R_{33} at the x-slab given by $x_1/D_p = 50.5$. The dashed lines (– – –), (– – –), and (– – –) represent R_{11}, R_{22}, and R_{33} at $x_1/D_p = 60.5$, and the dotted lines (.....), (.....), and (.....) represent R_{11}, R_{22}, and R_{33} in slabs located at $x_1/D_p = 70.5$.

$R_{22}(r_z)$ and $R_{33}(r_y)$ are referred as the transverse-cross correlations, $R_{22}(r_y)$ and $R_{33}(r_z)$ as the transverse-aligned correlations, and $R_{11}(r_y)$ and $R_{11}(r_z)$ as the axial-cross correlations. In addition, let us define the velocity fluctuations to become de-correlated at the separation distance where the correlation coefficient first reaches zero.

It was observed that R_{11}, R_{22}, and R_{33} de-correlated at longer separation distances along y and z for the x-slabs located further downstream for the cases $M122_{30}$ and $M166_{30}$. However, a clear trend for the de-correlation distances were not found for the case $M260_{30,ps}$. As an example, for the case $M122_{30}$, $R_{33}(r_y)$ de-correlated at $r_y/D_p = 0.87$ for the slab given by $x_1/D_p = 50.5$, at $r_y/D_p = 1.07$ for the slab given by $x_1/D_p = 60.5$, and at $r_y/D_p = 1.33$ for the slab given by $x_1/D_p = 70.5$.

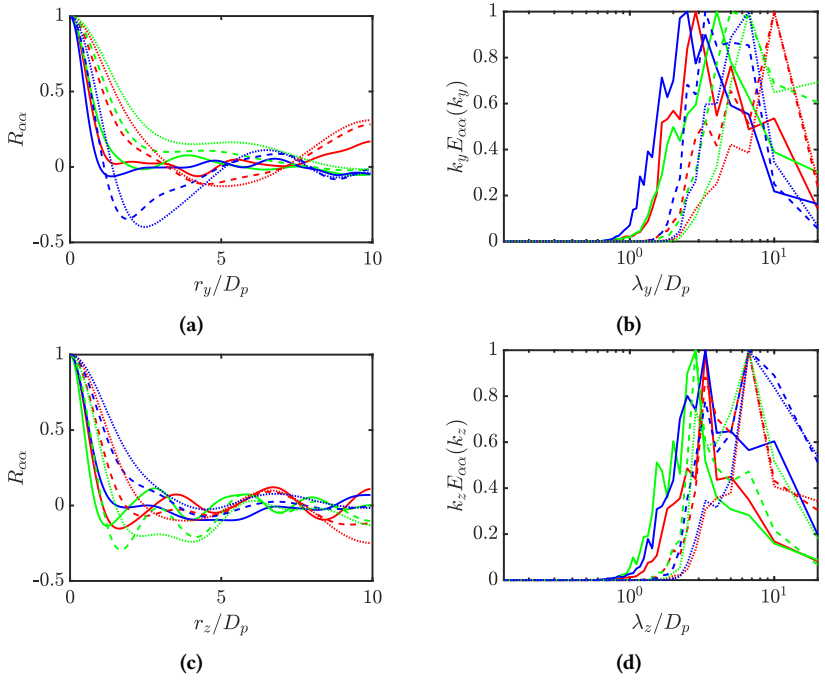

Figure 6.57: Comparison of the two point correlations and the corresponding pre-multiplied spectra for the case $M166_{30}$ along y in (a), (b), and along z in (c), (d). The solid lines (——), (——), and (——) represent R_{11}, R_{22}, and R_{33} at the x-slab given by $x_1/D_p = 50.5$. The dashed lines (– – –), (– – –), and (– – –) represent R_{11}, R_{22}, and R_{33} at $x_1/D_p = 60.5$, and the dotted lines (.....), (.....), and (.....) represent R_{11}, R_{22}, and R_{33} in slabs located at $x_1/D_p = 70.5$.

The transverse-cross correlations were found to be weaker than the axial-cross and transverse-aligned components for the cases $M122_{30}$ and $M166_{30}$. More notably, the trend reversed in the case of $M260_{30,ps}$, such that the transverse cross correlations were observed to be stronger and have larger de-correlation distances compared to the axial-cross and transverse aligned components. The stronger correlations for the transverse-cross components are related to the presence of shock-cells in the curtain wake. In fact, the de-correlation distances for the transverse-cross correlation were close to $r_z/D_p = 8$, which is approximately equal to the wavelength of the shock-cells as discussed in section 6.4.6.1.

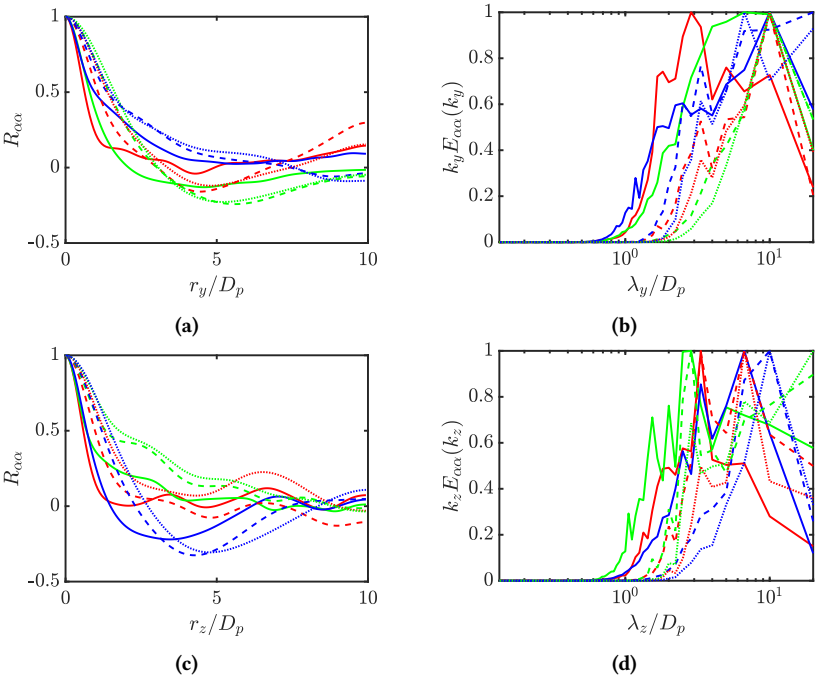

Figure 6.58: Comparison of the two point correlations and the corresponding pre-multiplied spectra for the case $M260_{30,ps}$ along y in (a), (b), and along z in (c), (d). The solid lines (——), (——), and (——) represent R_{11}, R_{22}, and R_{33} at the x-slab given by $x_1/D_p = 50.5$. The dashed lines (– – –), (– – –), and (– – –) represent R_{11}, R_{22}, and R_{33} at $x_1/D_p = 60.5$, and the dotted lines (.....), (.....), and (.....) represent R_{11}, R_{22}, and R_{33} in slabs located at $x_1/D_p = 70.5$.

The pre-multiplied spectra along y and z for the cases $M122_{30}$ and $M166_{30}$ show that the energy of the smaller length scales are resolved well. A peak in the pre-multiplied spectra is captured at all the x-slab locations and across all spectra components for the two cases. In addition, for the two cases, it is observed that the peak in the pre-multiplied energy spectra always occurs approximately in the range of $\lambda/D_p \in [1,10]$ at all x-slab locations and for all spectra components. In contrast, for the case $M260_{30,ps}$, although a peak in the premultiplied spectra for the transverse-aligned and cross-axial components was observed in the range $\lambda/D_p \in [1,10]$, the transverse domain size ($L_y/D_p = 20$) was insufficient to clearly capture a peak for the transverse-cross component in the more downstream slabs. This feature is possibly observed because of the large scale flow structures like the shock cells, which are present in the case $M260_{30,ps}$.

6.4.6.4 Energy spectra

Figures 6.59a to 6.59c show the one-dimensional energy spectra along y for the cases $M122_{30}$, $M166_{30}$, and $M260_{30,ps}$ respectively at different x-slab locations given by $x_1/D_p = [50.5, 60.5, 70.5]$. It is observed that the for the three cases, the one-dimensional spectra show a much stronger decay at large wavenumbers in the x-slabs, which are located further downstream compared to the slab which is located closest to the downstream edge of the particle curtain. In addition, the cross-axial component of the one-dimensional energy spectrum given by $E_{11}(k_y)$ is larger than the transverse-aligned $E_{22}(k_y)$, and the transverse-cross component $E_{33}(k_y)$ for $M122_{30}$, $M166_{30}$, and $M260_{30,ps}$ at all the slab locations and across a wide range of wavenumbers. A k^{-3} decay has previously been seen in dispersed particulate (Doychev 2014) and bubbly flows (Risso 2011). In the current work, the k^{-3} decay in the wake of the particle curtain is only observed in a narrow range of wavenumbers. For example, in the most upstream slab, the k_y^{-3} subrange is only observed approximately around $k_y D_p = 3$ for all components of the spectra (E_{11}, E_{22}, and E_{33}) and for all the three cases.

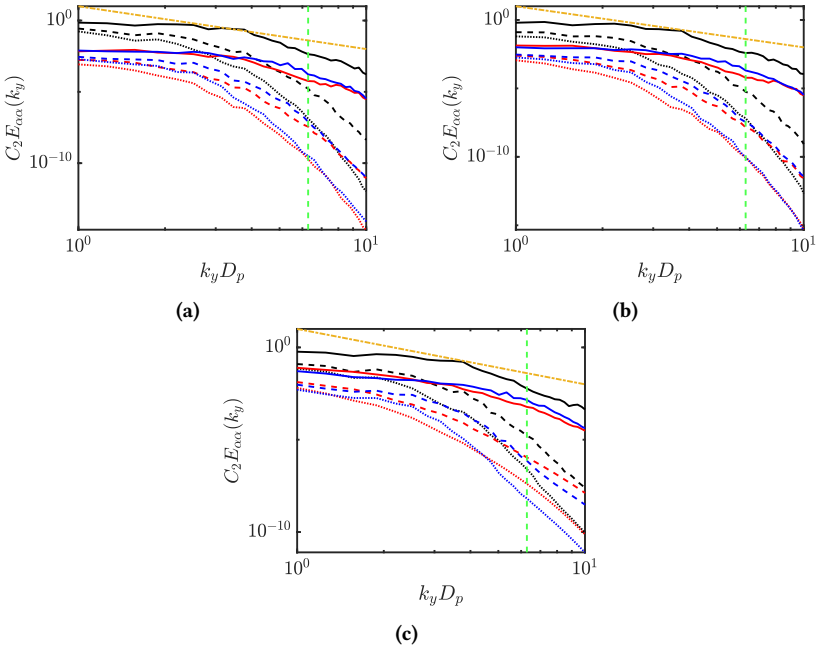

Figure 6.59: Comparison of the one-dimensional energy spectra for the cases (a) $M122_{30}$, (b) $M166_{30}$, and (c) $M260_{30,ps}$ as a function of the wavenumbers along y (k_y). (——), (——), (——) represent the spectra of E_{11}, E_{22}, and E_{33} in the slab located between $x/D_p = [50.5, 55.5]$ respectively. (- - -), (- - -), (- - -) represent the spectra of E_{11}, E_{22}, and E_{33} in the slab located between $x/D_p = [60.5, 65.5]$ respectively. (.....), (.....), (.....) represent the spectra of E_{11}, E_{22}, and E_{33} in the slab located between $x/D_p = [70.5, 75.5]$ respectively. (- - -) and (- - -) represent the slopes proportional to k_y^{-3} and k_y^{-2} respectively. (- - -) represents the wavenumber corresponding to the particle diameter.

6.4.6.5 Probability density functions of velocity fluctuations

Figure 6.60 show the the probability distribution functions of velocity fluctuations normalized with their respective rms value at different x-slab locations given by $x_1/D_p = [50.5, 60.5, 70.5]$ of width $B_x = 5D_p$ each. The probability density functions were computed by taking the slices from the joint p.d.fs of $u'' - v''$ and $v'' - w''$ at $v'' = 0$.

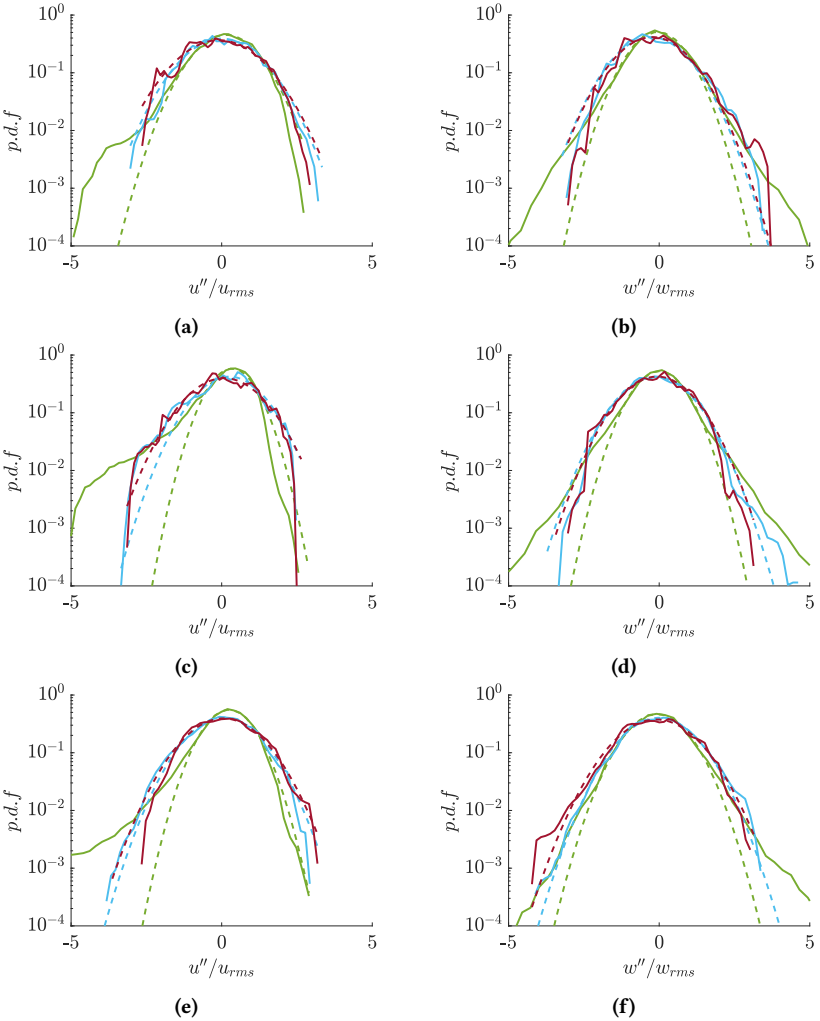

Figure 6.60: Probability density functions for velocity fluctuations normalized by their rms value in slabs of width $B_x = 5D_p$ located at (——) $x_1/D_p = 50.5$, (——) $x_1/D_p = 60.5$, and (——) $x_1/D_p = 70.5$. The different cases are represented by (a), (b) $M122_{30}$, (c), (d) $M166_{30}$, and (e), (f) $M260_{30,ps}$. The dashed lines represent the fitted gaussian curve with the colors representing the respective slab location.

Here, $u'' = u - \widetilde{u}_{slab}$, is the streamwise fluctuation and $w'' = w - \widetilde{w}_{slab}$ represents the cross-stream fluctuation. The rms values of u and w are represented by $u_{rms} = \sqrt{\langle u''u''\rangle_{slab}}$ and $w_{rms} = \sqrt{\langle w''w''\rangle_{slab}}$ respectively.

It is observed that the high-probability events in the $p.d.f$ corresponding to the low fluctuation magnitudes approximately follow a gaussian distribution. However, larger fluctuations are not accurately predicted by the gaussian distribution. In addition, the streamwise fluctuations exhibit a wide tail for $M122_{30}$, $M166_{30}$, and $M260_{30,ps}$ near the slab close to the downstream end of the particle curtain. Hence at this location, negative velocity fluctuations are more likely compared to the predictions by a gaussian distribution. This trend is most likely affected by the wake of the particles near the downstream edge of the curtain. This also shows the anisotropic nature of the flow in the region.

6.5 Comparison with models

From the previous works of Ling et al. (2011), Parmar et al. (2011), Parmar et al. (2012), and Ling et al. (2012) that the total force acting on an isolated particle in the limit of finite Mach and Reynolds numbers can be decomposed into quasi-steady ($\mathbf{F}_{qs}$), stress-gradient ($\mathbf{F}_{sg}$), added-mass ($\mathbf{F}_{am}$), and the viscous unsteady ($\mathbf{F}_{vu}$) contributions. Hence, the total force on a particle could be expressed as in eq. (6.25).The expressions of the different contributions for a spherical particle are given by eqs. (6.26) to (6.29).

$$\mathbf{F}_{total} = \mathbf{F}_{qs} + \mathbf{F}_{sq} + \mathbf{F}_{am} + \mathbf{F}_{vu} \tag{6.25}$$

$$\mathbf{F}_{qs} = \frac{1}{8} C_D \rho (\mathbf{u} - \mathbf{u}_p) |\mathbf{u} - \mathbf{u}_p| \pi D_p^2 \tag{6.26}$$

$$\mathbf{F}_{sg} = \frac{\pi D_p^3}{6} \rho \frac{\mathrm{D}\mathbf{u}}{\mathrm{D}t} \tag{6.27}$$

$$\mathbf{F}_{am} = \frac{\pi D_p^3}{6} \int_{-\infty}^{t} K_{iu}\left(\frac{t-\chi}{\tau_{iu}}, Ma\right)\left(\frac{\mathrm{D}(\rho\mathbf{u})}{\mathrm{D}t} - \frac{\mathrm{d}(\rho\mathbf{u}_p)}{\mathrm{d}t}\right)_{t=\chi} \frac{\mathrm{d}\chi}{\tau_{iu}} \tag{6.28}$$

$$\mathbf{F}_{vu} = \frac{3}{2} D_p^2 \sqrt{\pi\nu\tau_{vu}} \int_{-\infty}^{t} K_{vu}\left(\frac{t-\chi}{\tau_{vu}}, Ma, Re\right)\left(\frac{\mathrm{D}(\rho\mathbf{u})}{\mathrm{D}t} - \frac{\mathrm{d}(\rho\mathbf{u}_p)}{\mathrm{d}t}\right)_{t=\chi} \frac{\mathrm{d}\chi}{\tau_{vu}} \tag{6.29}$$

In the above equations, C_D is the quasi-steady drag coefficient,˘ is the velocity of the fluid phase given by $\mathbf{u} = [u, v, w]$, ρ is the fluid density, p is the particle velocity, K_{iu} is the inviscid unsteady kernel, K_{vu} is the viscous unsteady kernel, τ_{vu} and τ_{iu} are viscous and inviscid time-scales relevant to the flow problem. Following the works of Auton et al. (1988) and Parmar et al. (2012), $\mathrm{d}/\mathrm{d}t$ is a time derivative following the particle, while $\mathrm{D}/\mathrm{D}t = \partial/\partial t + \mathbf{u} \cdot \nabla$ denotes a time derivative following the fluid element also known as the material derivative. In eqs. (6.28) and (6.29), $\mathrm{d}(\rho \mathbf{u}_p)/\mathrm{d}t$ is the time derivative of density-weighted particle velocity.

A simplification of the added mass force was introduced by Parmar et al. (2012) by separately integrating over the inviscid unsteady kernel (K_{iu}) yielding an effective added-mass coefficient ($C_{am,eff}$) analogous to incompressible flows. With the introduced simplification, the added mass force $\mathbf{F}_{am}$ in eq. (6.28) can be simplified to:

$$\mathbf{F}_{am} = C_{am,eff} \frac{\pi D_p^3}{6} \left(\frac{\mathrm{D}(\rho \mathbf{u})}{\mathrm{D}t} - \frac{\mathrm{d}(\rho \mathbf{u}_p)}{\mathrm{d}t} \right) \tag{6.30}$$

As given in Ling et al. (2012), the effective added-mass coefficient ($C_{am,eff}$) for a spherical particle depends on compressibility effects and the local volume fraction (in sufficiently dense particle clouds). They introduced Mach corrections (Eames et al. 2008) and volume fraction corrections (Zuber 1964) to the standard added mass coefficient ($C_{am,std}$) for incompressible flows. Their correlation for $C_{am,eff}$ is represented by eq. (6.31). In the correlation, Ma_p is the particle Mach number and ϕ_p is the local particle volume fraction.

$$C_{am,eff} = C_{am,std}\, \eta_1(Ma_p)\, \eta_2(\phi_p) \tag{6.31}$$

The simple one-dimensional model by Ling et al. (2012) was used to study shock wave-interaction with a fixed-particle curtain, where the continuum phase was treated in the Eulerian framework and the particles were tracked in a Lagrangian framework. Simplifications to the different contributions shown in eqs. (6.27) to (6.29) were used to approximate the forces on the computational particles used in their work. In their model, a few assumptions were

made, which are summarized as follows. The continuous phase was treated as inviscid, and the viscous contributions were only considered for the fluid-particle momentum and heat exchange. With this assumption, the stress-gradient and added mass contributions could be simplified and expressed in terms of the pressure-gradient existing in the flow. In addition, their model neglects the contributions of the pseudo-turbulent Reynolds stress ($\widetilde{u_i'' u_i''}$) in their momentum and energy equations. The governing equations for the fluid phase used in the model simplified for fixed particles are given in eqs. (6.32) to (6.34) for completeness.

In the equations, the superscript "g" represents the continuum phase, F^{gp} is the inter-phase momentum exchange term, Q^{gp} is the interphase heat exchange term, and G^{gp} corresponds to the energy transferred between the two phases due to F^{gp}. The reader is suggested to refer to the original article for the details of the models used for the source terms. It is now known from the works of Osnes et al. (2019) and Regele et al. (2014) that the Reynolds stress terms, which arises from the volume averaging procedure can contribute significantly to the fluid momentum and energy, and hence should not be neglected. Osnes et al. (2019) recently introduced a simple model for the pseudo-turbulent Reynolds stress in terms of the separated flow regions, where the flow approximately achieves the particle velocity, especially in the particle wakes. However, the models for the Reynolds stress terms are still in their infancy, and detailed analysis of the microstructure in a random particle distribution should be performed in future work to model the pseudo-turbulent Reynolds stress terms.

$$\frac{\partial(\rho^g \phi^g)}{\partial t} + \frac{\partial(\rho^g \phi^g u_g)}{\partial x} = 0 \tag{6.32}$$

$$\frac{\partial(\rho^g \phi^g u^g)}{\partial t} + \frac{\partial(\rho^g \phi^g u^g u^g)}{\partial x} = -\frac{\partial p^g}{\partial x} + F^{gp} \tag{6.33}$$

$$\frac{\partial(\rho^g \phi^g E^g)}{\partial t} + \frac{\partial(\rho^g \phi^g u^g E^g)}{\partial x} = -\frac{\partial(u^g p^g)}{\partial x} + G^{gp} + Q^{gp} \tag{6.34}$$

Quasi steady drag force in an assembly of particles may be influenced by neighboring effects like wake-wake or shock-wake interactions. Hence, models based on solid volume fraction corrections is one of the approaches used to evaluate the quasi-steady drag correlations. Recently, quasi-steady drag correlations have been introduced for homogeneous random distributions of particles by Osnes et al. (2023). Their drag correlation is summarized in eq. (6.35).

$$C_{D,model}(Re, Ma, \phi) = \frac{C_{D,single}}{1-\phi} + f_1(Re, \phi) + f_2(Ma, \phi) \tag{6.35}$$

In eq. (6.35), $C_{D,single}$ is the drag coefficient for an isolated particle given by Loth et al. (2021), $f_1(Re, \phi)$ represent the volume fraction corrections introduced by Tenneti et al. (2011), and $f_2(Ma, \phi)$ is an additional correction term introduced by Osnes et al. (2023) to account for the finite compressibility effects in an assembly of particles.

In the present section, first, the recent quasi-steady drag correlations by Osnes et al. (2023) in addition to the stress-gradient and added mass contributions as shown in eqs. (6.26) to (6.29) are used to compare with the particle forces obtained through the DNS in the current work. Next, the one-dimensional model by Ling et al. (2012) is run with the equivalent numerical conditions in the 1D setup for the cases $M122_{30}$ and $M166_{30}$. The mean flow fields at late times for the two cases are compared between the model and the available DNS results and the differences in results obtained by the two approaches are discussed.

6.5.1 *A priori* modeling: Comparison of particle forces

In the section, the recent model by eq. (6.35), was used for *a priori* modeling of the quasi-steady drag forces on the particles. In their work, the model was used for homogeneous particle distributions. However, its efficacy for non-homogeneous distribution is tested. The quasi-steady drag contribution in addition to the contributions from the stress-gradients and added mass contributions are used to evaluate the total modeled drag forces on the particles locally inside the curtain. The modeled total drag forces are then compared

with the drag forces directly obtained through the DNS for the cases $M122_{30}$, $M166_{30}$, and $M260_{30,ps}$. The approach is summarized as follows.

- **Evaluation of the total model drag coefficient**
  - First, the local hemispherical shell-averaged Mach number ($\langle Ma^{(m)} \rangle_{shell}$) and Reynolds number ($\langle Re^{(m)} \rangle_{shell}$) are evaluated for all the particles in the curtain, where "m" is the particle index. The details of the hemispherical shell averaging procedure is summarized in appendix A.1.2.
  - The shell averaged Mach number ($\langle Re^{(m)} \rangle_{shell}$) and Reynolds number ($\langle Re^{(m)} \rangle_{shell}$), and the global volume fraction (ϕ) given in table 6.1 are then fed to the quasi steady drag correlation given in eq. (6.35) to obtain the modeled quasi steady drag coefficient ($C^{(m)}_{D,quasi,model}$) for the individual particles.
  - The stress gradient and the added-mass force contributions are evaluated across x-slabs of width D_p, and all the particles present inside the x-slab are assigned that same value. With this approach, the added mass ($F^{(m)}_{am}$) and stress gradient ($F^{(m)}_{sg}$) forcing terms are evaluated for all the particles inside the curtain in a piecewise constant fashion.
  - Next, the added mass ($F^{(m)}_{am}$) and stress gradient ($F^{(m)}_{sg}$) forcing terms are normalized with the local hemispherical shell averaged reference force (as shown in eq. (6.15)) to obtain the drag contributions from the added mass ($C^{(m)}_{D,am}$) and the stress gradient ($C^{(m)}_{D,sg}$) terms.
  - The total modeled drag is evaluated as

$$C^{(m)}_{D,model} = C^{(m)}_{D,quasi,model} + C^{(m)}_{D,sg} + C^{(m)}_{D,am}$$

  - The total modeled drag coefficient ($C^{(m)}_{D,model}$) for the particles are also averaged over slabs of slab width D_p to evaluate a shell and slab averaged model drag coefficient ($\langle C_{D,model} \rangle_{slab}$) similar to eq. (6.16).

- **Evaluation of the total drag coefficient from DNS**
  - The drag forces for the individual particles are obtained directly from the immersed boundary procedure. The total drag coefficient from the DNS is then evaluated based on the shell-averaged reference force, similar to the model and is shown in eq. (6.15).
  - Similar to the model, a shell and slab averaged drag coefficient is also evaluated as given in eq. (6.16).

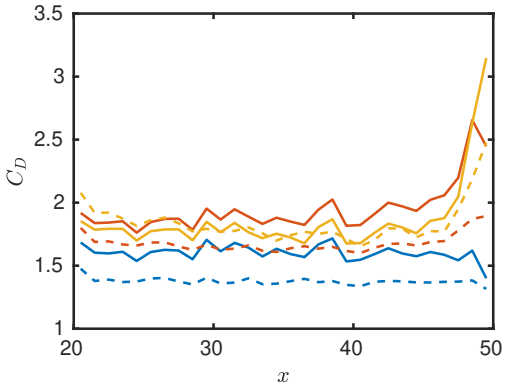

Figure 6.61: Comparison of the total drag coefficient based on the model by Osnes et al. (2023) ($\langle C_{D,model}\rangle_{slab}$) with the drag coefficient obtained from DNS ($\langle C_D\rangle_{shell,slab}$) along the particle curtain from the DNS for the cases (——) $M122_{30}$, (——) $M166_{30}$, and (——) $M260_{30,ps}$. The dashed lines with the same colors represent the drag coefficients for the three cases for the model.

Figure 6.61 shows the comparison of the drag coefficient obtained by shell and slab averaging $\langle C_D\rangle_{shell,slab}$ compared to the total model drag coefficient $\langle C_{D,model}\rangle_{slab}$ for the cases $M122_{30}$, $M16630$, and $M260_{30,ps}$ along the streamwise distance inside the curtain. It is observed that the model does not accurately capture the sharp increase in the drag coefficient at the end of the curtain for the cases $M166_{30}$ and $M260_{30,ps}$. In addition, the model does not capture the decrease in the the drag coefficient in the bulk of the curtain for $M260_{30,ps}$ compared to the case $M166_{30}$. This feature is possibly strongly influenced by temperature effects inside the curtain, which are not considered in the current models. In order to quantify the difference between the forces evaluated along the curtain by the DNS and the model, a normalized deviation

measure $\Theta_{slab}(C_D)$ is introduced as in eq. (6.36).

$$\Theta_{slab}(C_D) = \frac{\sqrt{\sum (\langle C_D \rangle_{shell,slab} - \langle C_{D,model} \rangle_{slab})^2 / N_{slab}}}{\langle \langle C_D \rangle_{shell,slab} \rangle} \tag{6.36}$$

In eq. (6.36), $N_{slab} = L_p/D_p$ is the total number of slabs along the streamwise direction and $\langle \langle C_D \rangle_{shell,slab} \rangle$ represents the averaged over all the slabs. $\Theta_{slab}(C_D)$ was observed to be 0.149 for $M122_{30}$, 0.155 for $M166_{30}$, and 0.146 for $M260_{30,ps}$.

Next, the nature of the drag coefficient is analyzed locally near the individual particles for the three cases. Figure 6.62a compares the individual drag coefficients local to the particles obtained from the model ($C_{D,model}^{(m)}$) and from DNS ($\langle C_D^{(m)} \rangle_{shell}$) for the cases $M122_{30}$, $M166_{30}$, and $M260_{30,ps}$. A larger spread in the drag coefficient obtained from DNS ($\langle C_D^{(m)} \rangle_{shell}$) is observed for all three cases compared to the model ($C_{D,model}^{(m)}$).

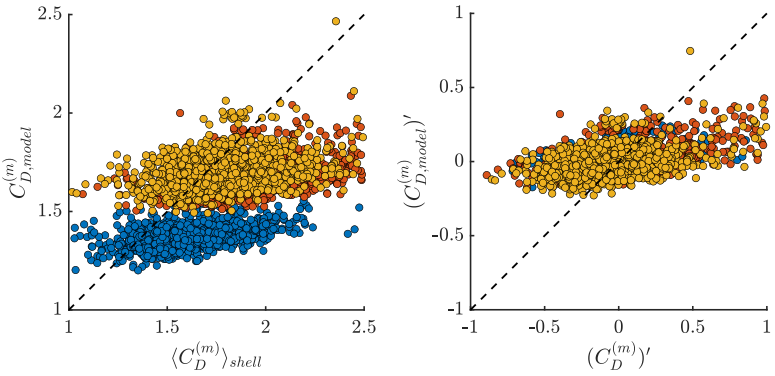

Figure 6.62: (a) Comparison between the drag coefficient obtained from DNS ($\langle C_D^{(m)} \rangle_{shell}$) and the model ($C_{D,model}^{(m)}$). (b) Comparison between the fluctuation in drag coefficient obtained from the model ($(C_{D,model}^{(m)})'$) and from DNS ($(C_D^{(m)})'$). The different cases are represented as (●) $M122_{30}$, (●) $M166_{30}$, and (●) $M260_{30,ps}$.

Let us define the fluctuation of the m^{th} drag coefficient with respect to the average over all particles as $(C_D^{(m)})' = \langle C_D^{(m)} \rangle_{shell} - \langle \langle C_D^{(m)} \rangle_{shell} \rangle_p$ and from the model as $(C_{D,model}^{(m)})' = C_{D,model}^{(m)} - \langle C_{D,model}^{(m)} \rangle_p$. Figure 6.62b shows the comparison between the model and DNS data.

$$\varphi_{model} = \frac{\sqrt{\langle (C_{D,model}^{(m)})' \, (C_{D,model}^{(m)})' \rangle_p}}{\langle C_{D,model}^{(m)} \rangle_p}$$
$$\varphi_{DNS} = \frac{\sqrt{\langle (C_D^{(m)})' \, (C_D^{(m)})' \rangle_p}}{\langle \langle C_D^{(m)} \rangle_{shell} \rangle_p} \tag{6.37}$$

In order to quantify the deviation of the drag coefficient fluctuations obtained by the model compared to the current DNS results, a quantity "φ" is defined which measures the root mean square drag coefficient fluctuations for the model or the DNS, normalized with the respective mean over all the particles as in eq. (6.37). φ for the drag coefficients obtained from the model and the DNS are summarized in table 6.11.

Table 6.11: The root mean square drag coefficient fluctuations obtained from the model/DNS, normalized with the respective mean over all the particles.

Case	φ_{model}	φ_{DNS}
$M122_{30}$	0.0470	0.1363
$M166_{30}$	0.0554	0.1616
$M260_{30,ps}$	0.06842	0.2079

From fig. 6.62b and table 6.11, it is apparent that the drag coefficient fluctuations about the mean obtained from the DNS is not captured by the force model. It was observed that in all three cases, φ_{model} was severely underpredicted compared to φ_{DNS}. The streamwise variation of the particle drag coefficient is dependent on the Mach number, Reynolds number, temperature

boundary conditions on the particle and the local particle microstructure inside the curtain. Future quasi-steady drag models can possibly be improved by considering their combined effect.

6.5.2 *A posteriori* modeling: Comparison with a one-dimensional model

6.5.2.1 Mean flow profiles

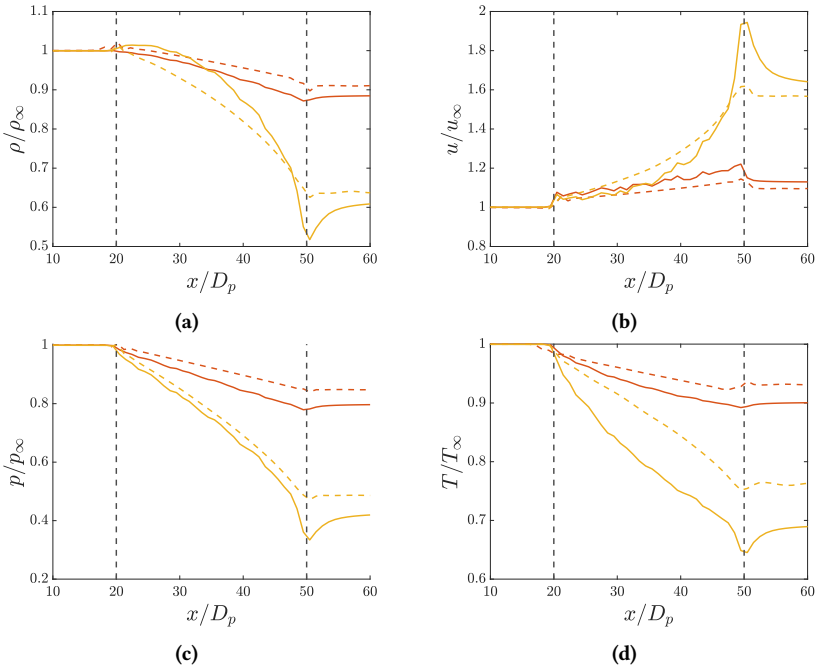

Figure 6.63: Comparison of mean flow-field profiles obtained by one-dimensional model of Ling et al. (2012) and present three dimensional Direct Numerical Simulations. The flow fields (a) Density (b) velocity (c) Pressure (d) Temperature normalized with inflow conditions are plotted at late times as a function of normalized streamwise distance for the cases (——) $M122_{30}$ (DNS), (– – –) $M122_{30}$ (Model), (——) $M166_{30}$ (DNS), (– – –) $M166_{30}$ (Model).

The one-dimensional model by Ling et al. (2012) is used in the present work to compare the late-time mean flow profiles with the results from the DNS. It should be noted that F^{gp} in eq. (6.33), the viscous unsteady terms are neglected for the late time analysis in the current work. Hence, F^{gp} is the sum of the quasi-steady, stress-gradient, and the added-mass contributions. Figure 6.63 shows the mean density, velocity, pressure, and temperature profiles along the streamwise direction normalized with the respective inflow conditions. It is observed that the general trend of the different primitive flow variables are followed by the one-dimensional model.

In the normalized density profiles given in fig. 6.63a, smaller density gradient magnitudes are observed inside the curtain for the model compared to the DNS results for the case $M122_{30}$, such that at the downstream edge of the curtain, the normalized density evaluated by the model is 5.17 % higher compared to the DNS results. For the case $M166_{30}$, the initial positive gradient seen in the density profiles from the DNS results are not captured by the model, which shows a monotonous decrease in density along the curtain. in addition, the strong density gradient magnitude observed at the downstream curtain edge is not captured by the model. For instance, the normalized density at the downstream edge of the curtain for the case $M166_{30}$ evaluated by the model is 18.18 % higher than the DNS results. Looking at the normalized velocity profiles in fig. 6.63b, similar but opposite trends are observed compared to the density profiles for the model and DNS results. For example, for the case $M166_{30}$, positive but smaller velocity gradients are observed by the model compared to the DNS. fig. 6.63c shows the comparison for the normalized pressure profiles between the one-dimensional model and the DNS results. From the normalized pressure profiles, it is seen that the pressure gradients inside the curtain evaluated by the model is smaller compared to the the DNS results in both the cases $M122_{30}$ and $M166_{30}$, such that at the downstream edge of the curtain, the normalized pressure evaluated by the model are 8.97 % and 34.9 % higher respectively. Similar to the pressure profiles, as seen in fig. 6.63d, the models under-predict the normalized temperature gradients inside the curtain compared to the DNS results for $M122_{30}$ and $M166_{30}$. For instance, the normalized temperature at the downstream curtain edge is 4.04

% and 15.9 % higher for the cases $M122_{30}$ and $M166_{30}$ respectively for the model in comparison to the DNS.

Figure 6.64 shows the comparison for the Reynolds number and Mach number profiles between the one-dimensional model and the DNS results for the cases $M122_{30}$ and $M166_{30}$. The model generally capture the qualitative trends for Reynolds number and the Mach number for both the cases. However, in general, the Reynolds number is under-predicted for $M122_{30}$ but is over-predicted for $M166_{30}$ inside the curtain at late times. At the upstream edge of the curtain, the Reynolds number is under-predicted for the case $M122_{30}$ by 6.6 % and over-predicted for the case $M166_{30}$ by 8.64 %. The Reynolds number is under-predicted for the case $M122_{30}$ by 8.19 %, but much closer for the case $M166_{30}$ with a 1.1 % under-prediction by the model at the downstream curtain edge.

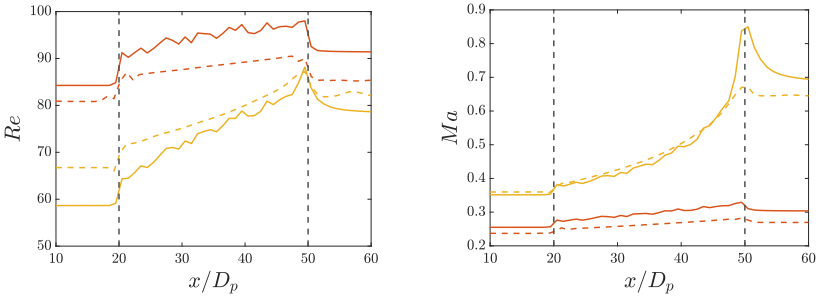

Figure 6.64: Comparison of profiles for non-dimensional parameters obtained by one-dimensional model of Ling et al. (2012) and present three dimensional Direct Numerical Simulations. (a) represents the Reynolds number (Re) and (b) represents the Mach number (Ma) plotted at late times as a function of normalized streamwise distance for the cases (——) $M122_{30}$ (DNS), (– – –) $M122_{30}$ (Model), (——) $M166_{30}$ (DNS), (– – –) $M166_{30}$ (Model).

The Mach number profiles are shown in fig. 6.64b. For the case $M122_{30}$, the model under-predicts the Mach number along the curtain. In comparison, for the case $M166_{30}$, the Mach number is predicted well by the model until approximately $x/D_p = 45$, beyond which the the sharp increase due to strong flow acceleration downstream is not captured.

It is seen that the one-dimensional model by Ling et al. (2012) captures the general flow trends observed by the the mean flow from the DNS results inside the curtain. However, the strong flow acceleration at the downstream curtain edge for the cases with high incident shock wave Mach numbers at late times is not captured by the model. Nevertheless, the one-dimensional model can be used as a tool to set up numerical simulations on a much larger scale in two or three dimensions.

7 Summary, conclusions and outlook

Dynamics of compressible flow though dispersed solid media find several applications industrially and occur ubiquitously in nature. Some examples include attenuation of shock waves using solid obstacles (Chaudhuri et al. 2013), two-phase dynamics inside volcanic conduits during eruptions (Bercovici and Michaut 2010), and explosion of dusty matter (Johnston et al. 2016). Understanding the complex nature of interphase interaction experimentally in such flows poses significant challenges owing to the sensitivity of experimental conditions and the small acoustic timescales. To this end, a compressible particle-resolved DNS (PR-DNS) solver coupled with a diffuse-interphase immersed boundary procedure is developed to study the flow dynamics and the nature of solid-fluid momentum and heat exchange in compressible particulate flows. Although significant progress has been made in the understanding of compressible particulate flows in the past decade, much remains to be explored, for example, the nature of heat transfer in finite-sized particle-arrays, pseudo-turbulence in the wake of the particle-curtain, and understanding of localized flow in fixed-particle clouds.

The aim of the current work is three-fold. First, to validate the developed PR-DNS solver against available numerical and experimental reference data for single-phase compressible flows and two-phase flows near isolated particles and through particle clouds. Second, to answer some of the mentioned unanswered questions related to the physics of compressible flows through fixed-particle arrays. Finally, to provide a high-fidelity database of particle-resolved Direct Numerical Simulations through fixed particle arrays. Although, the current work is associated with the study of fixed-particles, the established framework can easily be extended to study mobile-particulate flows in future.

Since, flows at higher Mach numbers involve small acoustic timescales, future extensions to study mobile particles will benefit significantly compared to boundary-fitted methods that require continuous re-meshing. The findings from the current work are summarized in the following sections and an outlook of possible future research in compressible particulate-flows is discussed.

7.1 Summary of validation tests

A series of validation tests were performed for the developed compressible DNS solver. Inviscid smooth flow single-phase validation tests including advection of linear density perturbation and isentropic vortex show a 5^{th} order grid-convergence rate. This is expected since a 5^{th} order advection scheme is used in the current work. Inviscid one-dimensional and two-dimensional tests with discontinuities like the sod-shock tube problem, the Lax problem, and the shock density wave interaction show that the advection schemes used in the current work resolve the discontinuities in the flow problems well.

In the current work, a second order central difference scheme is used for the diffusive terms. Taylor-Green Vortices with constant kinematic viscosity were validated against the incompressible analytical solution in the limit of a low Mach number ($Ma = 0.3$). Next, compressible Couette flow with constant and variable dynamic viscosities, and with fixed-wall temperatures were validated against the available analytical or reference solutions. In all the single phase viscous validation tests, a second order grid convergence rate was observed as expected. Finally, a more complex validation for compressible turbulent supersonic channel flow was performed for a Reynolds number ($Re = 3000$) and a Mach number ($Ma = 1.5$). At the final developed turbulent state, relevant flow profiles were compared against the available reference data from Coleman et al. (1995) and Lechner et al. (2001). A good agreement was observed with the reference data for the mean flow profiles and flow-field fluctuations. Hence, it is concluded that the DNS solver used in the present work performs well for single-phase compressible flow problems.

Next, the implemented diffuse-interface immersed boundary procedure was tested for inviscid and viscous compressible two-phase flows, and compared with available reference data. First a one-dimensional inviscid test was considered, where a cooled gas with constant velocity was brought to rest by collision with a rigid wall. Analytical solution can be obtained for this test, and comparisons against it showed a good agreement. Next, three dimensional tests for an incident shock-wave interacting with a fixed isolated particle were conducted for different shock-wave Mach numbers (Ma_s) in viscous and inviscid settings. It is well established from the works of Tanno et al. (2003) and Sun et al. (2005) that shock-wave loading on an incident particle may result in a transient drag, which is much higher than the quasi-steady value. The peak drag was captured by the current comparison tests with good level of accuracy and converged to the boundary fitted reference data upon grid resolution. The final test for flow near an isolated particle involved comparison with the boundary conforming DNS results from Nagata et al. (2018). In their work, they had compared the collective effect of free-stream Reynolds number, Mach number, and particle-to-fluid temperature ratio for an isolated particle on the particle drag, Nusselt number, flow fields, and the steadiness of the wake. Four different parameter were chosen, and a good agreement was obtained with the reference data for the chosen cases. The general observations were as follows. The particle-wake became more stable at higher particle-to-fluid temperature ratio, and free-stream Mach numbers, but became more unsteady at higher free-stream Reynolds number. The particle drag coefficient also increased with the free-stream Mach number and the imposed particle-to-fluid temperature ratio, but decreased at higher Reynolds number. Nusselt number has a more complex dependence on the temperature ratio and the Mach number, but increased with the Reynolds number.

The final validation was performed for flow through a homogenous array of fixed particles given by Osnes et al. (2023), who used a boundary-conforming particle-resolved LES approach. In their work, the fluid through the particle distribution was driven by a constant uniform volumetric force, and the fluid viscosity followed a temperature dependent power law. One of the parameter sets from their work was chosen for comparison, for which, the geometrical setup and the particle arrangement was kept identical to the reference.

Hence, a rigorous comparison of the particle forces and its corresponding fluctuations within the homogenous arrangement could be performed. With appropriate normalization, a good agreement of the mean particle forces and force-fluctuations with the reference data could be obtained.

7.2 Summary of flow through finite-sized fixed particle arrays

The flow through a finite-sized fixed particle array (curtain) using particle resolved Direct Numerical Simulations is discussed. Flow-dynamics during the initial transient while an incident shock-wave interacts with the array as well as at late times on a time scale long after the shock wave has transmitted through the curtain are studied. The post-shock Mach numbers (Ma_{ps}) were varied while keeping the post-shock condition based Reynolds number ($Re_{ps} = 100$), the Prandtl number (Pr), and the particle temperature (T_p) fixed. The initial flow in all the numerical tests were such that the flow post-shock temperatures were higher than the particle temperature, and hence, the fluid was cooled through interphase heat exchange as it traversed through the curtain. Two different solid volume fractions ($\phi = 0.05$ and $\phi = 0.025$) were chosen in the current work, and the consequent differences between the two choices in the flow-fields, the nature of particle forces, and heat transfer along the particle-array were discussed. Furthermore, the effects of a wider particle-array was also studied for the case with a supersonic post-shock Mach number.

The transient flow behavior

As the incident shock wave interacts with the fixed-particle curtain, a region of high-pressure and temperature is created upstream of the particle array through coalescence of individual reflected bow shocks, resulting in a reflected planar shock wave that travels in the direction opposite to the incident shock. At the same time, the strength of the incident shock wave is attenuated

as it passes through the curtain through cumulative effects of fluid viscosity and particle drag forces. The observed flow feature is consistent with the previous works of Mehta et al. (2018) and Osnes et al. (2020). The effect of shock attenuation is seen as a decrease in the peak drag coefficients and Nusselt numbers, in addition to larger delays in the arrival of the incident shock wave at the particle locations along the array. It was observed that the attenuation inside the curtain was stronger at higher incident shock Mach numbers and solid volume fractions.

While the incident shock wave is attenuated along the curtain, it was observed that the strength of the planar reflected shock wave increases over time as it travels upstream. This phenomenon was also observed by Vartdal and Osnes (2018) and Osnes et al. (2019) in viscous flows, who attributed the reflected shock strength to be a dependent on the the force imparted on the fluid through particle-drag and existing Reynolds stresses inside the particle-curtain. In the current work, it was observed that strength of the reflected shock-wave was lower over time for smaller solid volume fractions.

The peak in the pseudo-turbulent kinetic energy (PTKE) given by eq. (6.9), decreases over time inside the curtain, as the incident shock traverses through the particle-curtain. At the same time, a larger fraction of the curtain volume achieve finite spatial fluctuations. It was also seen that the peak in the transient PTKE values are lower at smaller solid volume fractions at similar times as the incident shock interacts with the particle curtain. By decomposing the PTKE contributions into its components, it is observed that the streamwise velocity fluctuations have a dominant contribution towards the total PTKE, while the transverse contributions were approximately an order of magnitude smaller. The dominant streamwise contributions to the PTKE can be explained by the separated flow regions in the particle wakes, where the streamwise flow locally achieves a small magnitude (for a fixed particle array). At the higher solid volume fraction ($\phi = 0.5$), a strong peak in the PTKE was observed for the test with an incident shock Mach number of 1.66 after the incident shock wave had crossed the particle curtain. However, the sharp peak was not apparent at a smaller solid volume fraction ($\phi = 0.025$) at the

downstream curtain edge. This can be explained by the stronger flow acceleration at higher solid volume fractions, resulting in much higher streamwise velocities. As the flow with such high streamwise velocities is brought to rest at the downstream curtain edge, large streamwise spatial fluctuations could be observed resulting in the sharp peak in PTKE at high solid volume fractions, with sufficiently high incident shock Mach numbers (Ma_s).

Late time flow behavior

Next, the flow behavior and the nature of particle forces and heat transfer at late times, long after the incident shock wave has transmitted through the particle array is discussed. The general trend observed from the mean flow involved a decrease in the static pressure and the flow temperature along the particle curtain. For the two cases with higher initial post-shock Mach numbers (Ma_{ps}), the flow was observed to choke at the downstream edge of the curtain. Hence, interestingly, the mean pressure profiles looked similar for the two cases. To understand this, analogies can be drawn from a flow through a converging-diverging nozzle, for which the choked flow pressure profile remains unchanged if the geometry of the nozzle is fixed (analogous to having similar particle distributions in the current work). The rate of decrease of the flow temperature along the curtain was also observed to be higher with a higher post-shock Mach number. This behavior could be explained by the long-time inflow conditions, which are dependent on the strength of the respective reflected shock waves. At higher post-shock Mach numbers, the reflected shocks were stronger, and consequently the inflow conditions were hotter at late times. This resulted in a larger temperature-gradient between the inflow and the particles, leading to a higher heat transfer rate for the cases with larger post-shock Mach numbers. The mean profiles for the density and velocity were more complex and dependent on the cumulative effects of the local pressure and temperature gradients existing in the flow. Nevertheless, the density and velocity profiles approximately followed an opposite trend to satisfy mass conservation principles.

The flow Reynolds number and the Mach numbers showed an increasing trend for cases with different initial post-shock Mach numbers. For the cases, where the flow was choked near the downstream curtain edge, a sharp increase in the flow Mach number was observed, which can be attributed to the strong flow acceleration in the region.

From the numerical schlieren diagrams at late times, jetting structures could be observed near the downstream edge of the curtain for all three cases. Subsonic jetting structures were observed for the cases, for which the flow achieved subsonic Mach numbers downstream of the particle curtain. In addition, series of alternating oblique shocks and expansion fans were visible for the case with the highest initial post-shock Mach number, analogous to shock cell structures in under-expanded jets. The nature of the flow downstream is governed by the initial transmitted shock, which sets up the back-pressure downstream of the curtain for the different cases.

The flow near the particles inside the curtain could be understood locally by looking into the flow conditioned on the particle positions at different streamwise positions along the particle array. From the local velocity contours, approximately symmetric recirculation regions were found for all the cases and at different streamwise locations along the curtain. From the local streamwise velocity plots near the particle, it was identified that the flow could achieve much higher streamwise velocities than what is seen by the particle by means of flow acceleration locally through constrictions (especially for cases where the flow undergoes strong acceleration near the downstream curtain edge). From the particle-conditioned temperature fields, it was observed that strong temperature-gradients existed close to the particle boundaries, especially near the upstream stagnation point. The observed temperature gradients were stronger for the cases with higher initial post shock Mach numbers at different streamwise locations. In addition, the magnitude of the temperature gradients near the particle surface were higher for particles located closer to the upstream edge of the particle curtain. This is expected, since the particles located closer to the upstream curtain-edge will experience flows which are hotter compared to the particles located further downstream.

The particle forces and heat-exchange were studied for the particles inside the curtain locally using reference forces based on slab and hemispherical-shell averaging procedures. The drag coefficient for the flow with the smallest post-shock Mach number (which is effectively incompressible), did not show any increasing or decreasing trend along the curtain. However, for the two cases with higher post-shock Mach numbers, strong flow acceleration occurred near the downstream edge of the curtain, leading to a sharp increase in the drag coefficient in the region for these cases. The standard deviation of the particle-forces with appropriate normalization shows that the variance of the particle forces had a strong dependence on the particle arrangement. This hints at the possibility to use the information of local flow micro-structure for improved drag prediction models similar to the works of Akiki et al. (2017).

The local Nusselt numbers showed a small increasing trend along the streamwise distance for the case with lowest post-shock Mach number but a decreasing trend for the cases with higher post-shock Mach numbers. The Nusselt number has a complex dependence on the local flow Reynolds number, Mach number, and particle-to-fluid temperature ratio. An effort was made to explain the observed Nusselt number trends based on the local variation of these non-dimensional quantities. Similar to the variance of the particle forces, the normalized variance of the Nusselt number also showed a strong dependence on the local particle distribution in the bulk of the particle curtain.

The effect of the curtain width was studied for the case with supersonic post-shock Mach numbers by increasing the curtain width by two-thirds while keeping the other parameters the same. It was observed that the normalized flow temperature reached a smaller value for the case with the longer curtain width at the downstream edge, since the flow experiences a larger surface area for heat exchange. Consequently, the Reynolds number are higher for the case with the larger curtain width at the downstream edge. The Mach number profiles show that the flow approaches choked flow conditions at the downstream edge of the curtain in both the cases. In addition, the drag coefficient and the Nusselt number plotted in rescaled coordinates looked similar in both cases.

The effect of the solid volume fraction was studied by reducing the solid volume fraction by half for the case with the intermediate shock Mach number. It was observed that the gradients of the normalized temperature profiles along the curtain were lower for the case with the smaller solid volume fraction, due to a smaller effective surface area for heat solid-fluid heat exchange. It was also observed that the particle drag coefficient and Nusselt numbers were in general lower along the curtain for the case with a smaller solid volume fraction.

The statistics in the wake of the particle curtain were studied using statistical tools like two-point correlations and energy spectra. The Pseudo-Turbulent Kinetic Energy defined in eq. (6.9) showed a decay rate close to unity with the streamwise position in the wake of the particle curtain in all three cases. The two point correlations and the corresponding pre multiplied spectra were evaluated in finite-sized slabs at different streamwise positions behind the particle-curtain. For the two cases with smaller post-shock Mach numbers, the transverse-cross components de-correlated over smaller separation distances, but for the case with the largest post-shock Mach number, the correlation was stronger for the same component. This could be explained by the alternating oblique wave structures behind the particle curtain.

The current DNS results were also compared with the one-dimensional model of Ling et al. (2012), modified for fixed particles. The general trends observed by the DNS were captured by the simplistic model. However, the strong flow acceleration at the downstream edge of the curtain, for the case with higher post-shock Mach number was not captured. However, it should be remembered that the one-dimensional model uses inviscid flow equations, except for interphase momentum and heat exchange. Furthermore, the contribution of pseudo-turbulent Reynolds stress ($\widetilde{u''u''}$) were neglected. Future efforts for a one-dimensional model could be improved by incorporating these additional contributions. In addition, the total drag coefficient obtained from the DNS were compared to the force model based on the recent quasi-steady drag correlations of Osnes et al. (2023). Although, a good agreement with the mean drag coefficient between the model and the DNS was observed, the spread in

the drag coefficient across the curtain was under-predicted by the model. Improvements in variance of the particle force models can benefit by considering the effect of local distribution of neighboring particles.

7.3 Outlook into future research

The theory of compressible flow through multi-particle systems is an evolving subject. Experimental efforts to study such flow problems have traditionally been met with multiple challenges due to the limitations in resolving fast acoustic waves, sensitivity of the experimental setup, and the limited optical visibility of the localized flow inside the particle suspensions. However, recent advancements made in experimental techniques like pulse-burst particle image velocimetry (DeMauro et al. 2017), and Tomographic X-ray particle tracking velocimetry (Mäkiharju et al. 2022) can contribute towards gaining a better understanding of compressible particulate flows. Future experimental efforts can be made to identify localized flow structures and establish a database for the particle forces and the nature of heat-transfer inside homogeneous or inhomogeneous particle distributions. The research community will significantly benefit from such efforts in developing improved drag and Nusselt number models. The database can also serve as a reference to validate numerical approaches to similar flow problems.

Recent interest in the field has been propelled by the advances in numerical techniques for compressible particulate flows. Especially, particle-resolved numerical methods have shed more light into the local flow structures, and relevant flow mechanisms. In the current work, a similar effort was made to understand the flow through a fixed particle curtain through a PR-DNS coupled with a diffuse-interface immersed boundary procedure. Since, the current work is limited to the study of fixed-particles, a straightforward possibility is the extension of the current numerical framework to mobile particles. To the author's knowledge, there is surprisingly limited literature for particle-resolved numerical studies of isolated as well as multi-particle systems with particle mobility. Future efforts can be made to understand the physics relevant to the flow problems with mobile particles, including a better

understanding of the particle trajectories, clustering, segregation, and pattern formation.

In the current work, the boundary conditions on the particles were treated as isothermal, no-slip, and no-penetration for two-phase flow problems with fluid viscosity. The current numerical framework can be extended to different thermal boundary conditions in an immersed boundary sense, including adiabatic conditions and fluid-solid energy balance on the particle surface to study compressible flow through multi-particle systems.

Another knowledge gap observed was the limited literature on Nusselt number correlations, taking the cumulative effects of Reynolds number, Mach number, and the particle-to-fluid temperature ratio. To the author's knowledge, there are currently no established Nusselt number correlations for compressible multi-particle systems, characterizing the effect of thermal boundary conditions, compressibility effects, and the flow Reynolds number. Furthermore, it was observed that the existing drag models for flow through particle suspensions do not capture the variance of the spatial flow fluctuations. It is apparent from the current work that the spatial fluctuations present in the flow in the limit of low Reynolds number, have a strong dependence on the particle distribution. Improvements in the existing drag models can be obtained by considering the effects of the local-particle microstructure similar to the work of Akiki et al. (2017).

The flow through a fixed-particle curtain may get choked at the downstream edge of the curtain. The choking phenomenon depends not only on the solid volume fraction, but also on the initial post-shock quantities, which contribute towards the establishment of the flow conditions in the wake of the particle curtain at late times. In a random arrangement, it was observed that choked flow at the downstream edge can exist alongside locally subsonic regions. Hence, it would be interesting to characterize the effect of the initial post-shock conditions (or incident shock Mach number) on the fraction of the downstream cross-sectional area that gets choked. Finally, the current work can be extended to a wider range of Reynolds number, Mach number, and solid volume fractions, to study the flow through inhomogeneous particle arrays at late times.

Bibliography

Aizik, F; Ben-Dor, G; Elperin, T; Igra, O; Mond, M and Gronig, H (1995): "Attenuation law of planar shock waves propagating through dust-gas suspensions". In: *AIAA journal* 33.5, pp. 953–955. doi: https://doi.org/10.2514/3.12382 (cit. on p. 18).

Akiki, G; Jackson, TL and Balachandar, S (2017): "Pairwise interaction extended point-particle model for a random array of monodisperse spheres". In: *Journal of Fluid Mechanics* 813, pp. 882–928. doi: https://doi.org/10.1017/jfm.2016.877 (cit. on pp. 23, 224, 227).

Al Jahdali, R; Dalcin, L; Boukharfane, R; Nolasco, IR; Keyes, DE and Parsani, M (2022): "Optimized explicit Runge–Kutta schemes for high-order collocated discontinuous Galerkin methods for compressible fluid dynamics". In: *Computers Mathematics with Applications* 118, pp. 1–17. doi: https://doi.org/10.1016/j.camwa.2022.05.006 (cit. on p. 52).

Anderson, JD (2003): Modern Compressible Flow With Historical Perspective 3rd Ed. McGraw Hill (cit. on pp. 7, 9).

Annamalai, S and Balachandar, S (2017): "Faxén form of time-domain force on a sphere in unsteady spatially varying viscous compressible flows". In: *Journal of Fluid Mechanics* 816, pp. 381–411. doi: https://doi.org/10.1017/jfm.2017.77 (cit. on p. 23).

Auton, TR; Hunt, JCR and Prud'Homme, M (1988): "The force exerted on a body in inviscid unsteady non-uniform rotational flow". In: *Journal of Fluid Mechanics* 197, pp. 241–257. doi: https://doi.org/10.1017/S0022112088003246 (cit. on p. 206).

Bailey, AB and Hiatt, J (1972): "Sphere drag coefficients for a broad range of Mach and Reynolds numbers". In: *AIAA Journal* 10.11, pp. 1436–1440. doi: https://doi.org/10.2514/3.50387 (cit. on p. 15).

Bailey, AB and Starr, RF (1976): "Sphere drag at transonic speeds and high Reynolds numbers". In: *AIAA Journal* 14.11, pp. 1631–1631. doi: https://doi.org/10.2514/3.7262 (cit. on pp. 15, 21).

Baranwal, A; Donzis, DA and Bowersox, RDW (2023): "Mach number and wall thermal boundary condition effects on near-wall compressible turbulence". In: *arXiv preprint arXiv:2307.03265*. doi: https://doi.org/10.48550/arXiv.2307.03265 (cit. on p. 12).

Baumgart, A and Blanquart, G (2023): "A numerical extension of the spatially-filtered Euler equations for contact discontinuities". In: *Journal of Computational Physics* 491, p. 112353. doi: https://doi.org/10.1016/j.jcp.2023.112353 (cit. on p. 38).

Bechert, DW and Stahl, B (1988): "Excitation of instability waves in free shear layers Part 2. Experiments". In: *Journal of Fluid Mechanics* 186, pp. 63–84. doi: https://doi.org/10.1017/S0022112088000047 (cit. on p. 38).

Behrendt, J; Balachandar, S; Garno, J and McGrath, TP (Jan. 2022): "Modeling of shock-induced force on an isolated particle in water and air". In: *Physics of Fluids* 34.1, p. 016108. doi: https://doi.org/10.1063/5.0067801 (cit. on pp. 20, 42, 82).

Bercovici, D and Michaut, C (2010): "Two-phase dynamics of volcanic eruptions: compaction, compression and the conditions for choking". In: *Geophysical Journal International* 182.2, pp. 843–864. doi: https://doi.org/10.1111/j.1365-246X.2010.04674.x (cit. on p. 217).

Borges, R; Carmona, M; Costa, B and Don, WS (2008): "An improved weighted essentially non-oscillatory scheme for hyperbolic conservation laws". In: *Journal of Computational Physics* 227.6, pp. 3191–3211. doi: https://doi.org/10.1016/j.jcp.2007.11.038 (cit. on p. 35).

Bouchet, G; Mebarek, M and Dušek, J (2006): "Hydrodynamic forces acting on a rigid fixed sphere in early transitional regimes". In: *European Journal of Mechanics - B/Fluids* 25.3, pp. 321–336. doi: https://doi.org/10.1016/j.euromechflu.2005.10.001 (cit. on pp. 89, 90).

Briassulis, G; Agui, JH and Andreopoulos, Y (2001): "The structure of weakly compressible grid-generated turbulence". In: *Journal of Fluid Mechanics* 432, pp. 219–283. doi: https://doi.org/10.1017/S0022112000003402 (cit. on p. 13).

Britan, A; Elperin, T; Igra, O and Jiang, JP (1995): "Acceleration of a sphere behind planar shock waves". In: *Experiments in Fluids* 20.2, pp. 84–90. doi: https://doi.org/10.1007/BF01061585 (cit. on p. 16).

Buchmüller, P and Helzel, C (2014): "Improved Accuracy of High-Order WENO Finite Volume Methods on Cartesian Grids". In: *Journal of Scientific Computing* 61.2, pp. 343–368. doi: https://doi.org/10.1007/s10915-014-9825-1 (cit. on pp. 49, 52).

Cebeci, T and Bradshaw, P (1977): "Momentum transfer in boundary layers". In: *Washington* (cit. on p. 15).

Chan, J; Shukla, K; Wu, X; Liu, R and Nalluri, P (2024): "High order entropy stable schemes for the quasi-one-dimensional shallow water and compressible Euler equations". In: *Journal of Computational Physics* 504, p. 112876. doi: https://doi.org/10.1016/j.jcp.2024.112876 (cit. on p. 38).

Chang, CC and Lei, SY (1996): "On the sources of aerodynamic forces: steady flow around a cylinder or a sphere". In: *Proceedings of the Royal Society of London. Series A: Mathematical, Physical and Engineering Sciences* 452.1954, pp. 2369–2395. doi: https://doi.org/10.1098/rspa.1996.0128 (cit. on p. 15).

Chaudhuri, A; Hadjadj, A; Sadot, O and Ben-Dor, G (2013): "Numerical study of shock-wave mitigation through matrices of solid obstacles". In: *Shock Waves* 23, pp. 91–101. doi: https://doi.org/10.1007/s00193-012-0362-2 (cit. on p. 217).

Chojnicki, K; Clarke, AB and Phillips, JC (2006): "A shock-tube investigation of the dynamics of gas-particle mixtures: Implications for explosive volcanic eruptions". In: *Geophysical Research Letters* 33.15. doi: https://doi.org/10.1029/2006GL026414 (cit. on pp. 1, 3).

Clift, R and Gauvin, WH (1971a): "Motion of entrained particles in gas streams". In: *The Canadian Journal of Chemical Engineering* 49.4, pp. 439–448. doi: https://doi.org/10.1002/cjce.5450490403 (cit. on pp. 20, 97, 102, 104, 105, 108, 111).

Clift, R and Gauvin, WH (1971b): "MOTION OF PARTICLES IN TURBULENT GAS STREAMS". eng. In: *BRITISH CHEMICAL ENGINEERING* 16.2-3, 229– (cit. on p. 21).

Cogo, M; Baù, U; Chinappi, M; Bernardini, M and Picano, F (2023): "Assessment of heat transfer and Mach number effects on high-speed turbulent boundary layers". In: *Journal of Fluid Mechanics* 974, A10. doi: https://doi.org/10.1017/jfm.2023.791 (cit. on p. 38).

Coleman, GN; Kim, J and Moser, RD (1995): "A numerical study of turbulent supersonic isothermal-wall channel flow". In: *Journal of Fluid Mechanics* 305, pp. 159–183. doi: https://doi.org/10.1017/S0022112095004587 (cit. on pp. 11, 12, 62, 71–73, 75–77, 79, 218).

Crowe, CT; Schwarzkopf, JD; Sommerfeld, M and Tsuji, Y (2011): Multiphase Flows with Droplets and Particles (2nd ed.) CRC Press. doi: https://doi.org/10.1201/b11103 (cit. on p. 85).

Daniel, KA and Wagner, JL (2022): "The shock-induced dispersal of particle curtains with varying material density". In: *International Journal of Multiphase Flow* 152, p. 104082. doi: https://doi.org/10.1016/j.ijmultiphaseflow.2022.104082 (cit. on p. 18).

DeMauro, EP; Wagner, JL; Beresh, SJ and Farias, PA (June 2017): "Unsteady drag following shock wave impingement on a dense particle curtain measured using pulse-burst PIV". In: *Phys. Rev. Fluids* 2 (6), p. 064301. doi: https://doi.org/10.1103/PhysRevFluids.2.064301 (cit. on pp. 18, 226).

DeMauro, EP; Wagner, JL; DeChant, LJ; Beresh, SJ and Turpin, AM (2019): "Improved scaling laws for the shock-induced dispersal of a dense particle curtain". In: *Journal of Fluid Mechanics* 876, pp. 881–895. doi: https://doi.org/10.1017/jfm.2019.550 (cit. on p. 18).

Doychev, T (2014): "The dynamics of finite-size settling particles". PhD thesis. doi: https://doi.org/10.5445/IR/1000044615 (cit. on pp. 169, 202).

Dutt, P (1988): "Stable Boundary Conditions and Difference Schemes for Navier–Stokes Equations". In: *SIAM Journal on Numerical Analysis* 25.2, pp. 245–267. doi: https://doi.org/10.1137/0725018 (cit. on p. 38).

Eames, I; Parmar, M; Haselbacher, A and Balachandar, S (2008): "On the unsteady inviscid force on cylinders and spheres in subcritical compressible flow". In: *Philosophical Transactions of the Royal Society A: Mathematical, Physical and Engineering Sciences* 366.1873, pp. 2161–2175. doi: https://doi.org/10.1098/rsta.2008.0027 (cit. on pp. 23, 206).

Emanuel, G and Jones, JP (1968): "Compressible flow through a porous plate". In: *International Journal of Heat and Mass Transfer* 11.5, pp. 827–836. doi: https://doi.org/10.1016/0017-9310(68)90127-0 (cit. on p. 13).

Feng, ZG and Michaelides, EE (2000): "A numerical study on the transient heat transfer from a sphere at high Reynolds and Peclet numbers". In: *International Journal of Heat and Mass Transfer* 43.2, pp. 219–229. doi: https://doi.org/10.1016/S0017-9310(99)00133-7 (cit. on p. 94).

Fox, TW; Rackett, CW and Nicholls, JA (1978): "Shock wave ignition of magnesium powders". In: *Shock tube and shock wave research; Eleventh International Symposium* (cit. on pp. 24, 94, 99, 102, 105, 106, 109, 111).

Foysi, H; Sarkar, S and Friedrich, R (2004): "Compressibility effects and turbulence scalings in supersonic channel flow". In: *Journal of Fluid Mechanics* 509, pp. 207–216. doi: https://doi.org/10.1017/S0022112004009371 (cit. on p. 11).

Fu, L; Hu, XY and Adams, NA (2016): "A family of high-order targeted ENO schemes for compressible-fluid simulations". In: *Journal of Computational Physics* 305, pp. 333–359. doi: https://doi.org/10.1016/j.jcp.2015.10.037 (cit. on pp. 35, 36, 282).

Garcia-Villalba, M; Kidanemariam, AG and Uhlmann, M (2012): "DNS of vertical plane channel flow with finite-size particles: Voronoi analysis, acceleration statistics and particle-conditioned averaging". In: *International Journal of Multiphase Flow* 46, pp. 54–74. doi: https://doi.org/10.1016/j.ijmultiphaseflow.2012.05.007 (cit. on p. 251).

Gerolymos, GA and Vallet, I (2014): "Pressure, density, temperature and entropy fluctuations in compressible turbulent plane channel flow". In: *Journal of fluid mechanics* 757, pp. 701–746. doi: https://doi.org/10.1017/jfm.2014.431 (cit. on p. 12).

Ghaboussi, J and Wilson, EL (1973): "Flow of compressible fluid in porous elastic media". In: *International Journal for Numerical Methods in Engineering* 5.3, pp. 419–442. doi: https://doi.org/10.1002/nme.1620050311 (cit. on p. 14).

Gray, WG and Lee, PCY (1977): "On the theorems for local volume averaging of multiphase systems". In: *International Journal of Multiphase Flow* 3.4, pp. 333–340. doi: https://doi.org/10.1016/0301-9322(77)90013-1 (cit. on p. 246).

Grinstein, FF; Oran, ES and Boris, JP (1987): "Direct numerical simulation of axisymmetric jets". In: *AIAA Journal* 25.1, pp. 92–98. doi: https://doi.org/10.2514/3.9586 (cit. on p. 39).

Harten, A; Engquist, B; Osher, S and Chakravarthy, SR (1997): "Uniformly High Order Accurate Essentially Non-oscillatory Schemes, III". In: *Journal of Computational Physics* 131.1, pp. 3–47. doi: https://doi.org/10.1006/jcph.1996.5632 (cit. on p. 35).

Henderson, CB (1976): "Drag coefficients of spheres in continuum and rarefied flows". In: *AIAA journal* 14.6, pp. 707–708. doi: https://doi.org/10.2514/3.61409 (cit. on p. 21).

Houim, RW and Oran, ES (2015): "Numerical simulation of dilute and dense layered coal-dust explosions". In: *Proceedings of the Combustion Institute* 35.2, pp. 2083–2090. doi: https://doi.org/10.1016/j.proci.2014.06.032 (cit. on p. 3).

Hugoniot, H (1887): "Mémoire sur la propagation du mouvement dans un fluide indéfini (Première partie)". In: *Journal de Mathématiques Pures et Appliquées* 3, pp. 477–492 (cit. on p. 9).

Illingworth, CR (1950): "Some solutions of the equations of flow of a viscous compressible fluid". In: vol. 46. 3, pp. 469–478. doi: https://doi.org/10.1017/S0305004100025986 (cit. on pp. 62, 68).

Jain, NC (1973): "On the plane couette flow of a variable viscosity fluid". In: vol. 78. 6, pp. 247–256. doi: https://doi.org/10.1007/BF03048093 (cit. on pp. 61, 64).

Jiang, GS and Shu, CW (1996): "Efficient Implementation of Weighted ENO Schemes". In: *Journal of Computational Physics* 126.1, pp. 202–228. doi: https://doi.org/10.1006/jcph.1996.0130 (cit. on pp. 35, 54).

Johnston, HG; Chowdhury, AY; Mannan, MS and Petersen, EL (2016): "Effect of coal-limestone mixtures on dust dispersion behind a moving shock wave". In: *Journal of Loss Prevention in the Process Industries* 44, pp. 551–563. doi: https://doi.org/10.1016/j.jlp.2016.07.006 (cit. on pp. 1, 3, 217).

Jones, DL; Goyer, GG and Plooster, MN (1968): "Shock wave from a lightning discharge". In: *Journal of Geophysical Research (1896-1977)* 73.10, pp. 3121–3127. doi: https://doi.org/10.1029/JB073i010p03121 (cit. on p. 3).

Jourdan, G; Houas, L; Igra, O; Estivalezes, JL; Devals, C and Meshkov, EE (2007): "Drag coefficient of a sphere in a non-stationary flow: new results". In: *Proceedings of the Royal Society A: Mathematical, Physical and Engineering Sciences* 463.2088, pp. 3323–3345. doi: https://doi.org/10.1098/rspa.2007.0058 (cit. on p. 16).

Kassoy, DR; Adamson, TC Jr. and Messiter, AF (Apr. 1966): "Compressible Low Reynolds Number Flow around a Sphere". In: *The Physics of Fluids* 9.4, pp. 671–681. doi: https://doi.org/10.1063/1.1761732 (cit. on p. 15).

Kendall, MAF (2002): "The delivery of particulate vaccines and drugs to human skin with a practical, hand-held shock tube-based system". In: *Shock Waves* 12.1, pp. 23–30. doi: https://doi.org/10.1007/s001930200126 (cit. on p. 1).

Khalloufi, M and Capecelatro, J (2023): "Drag force of compressible flows past random arrays of spheres". In: *International Journal of Multiphase Flow* 165, p. 104496. doi: https://doi.org/10.1016/j.ijmultiphaseflow.2023.104496 (cit. on pp. 3, 19, 118).

Kim, J; Moin, P and Moser, R (1987): "Turbulence statistics in fully developed channel flow at low Reynolds number". In: *Journal of Fluid Mechanics* 177, pp. 133–166. doi: https://doi.org/10.1017/S0022112087000892 (cit. on pp. 75, 77).

Kundu, PK; Cohen, IM and Dowling, DR (2015): Fluid mechanics. Academic press. doi: https://doi.org/10.1016/C2012-0-00611-4 (cit. on pp. 27, 28).

Lattanzi, AM; Tavanashad, V; Subramaniam, S and Capecelatro, J (2022): "Fluid-mediated sources of granular temperature at finite Reynolds numbers". In: *Journal of Fluid Mechanics* 942, A7. doi: https://doi.org/10.1017/jfm.2022.351 (cit. on p. 24).

Lax, PD and Liu, XD (1998): "Solution of Two-Dimensional Riemann Problems of Gas Dynamics by Positive Schemes". In: *SIAM Journal on Scientific Computing* 19.2, pp. 319–340. doi: https://doi.org/10.1137/S1064827595291819 (cit. on pp. 60, 61).

Lechner, R; Sesterhenn, J and Friedrich, R (Jan. 2001): "Turbulent supersonic channel flow". In: *Journal of Turbulence* 2.1, p. 001. doi: https://doi.org/10.1088/1468-5248/2/1/001 (cit. on pp. 11, 12, 71–75, 77–79, 218).

Liang, T; Xiao, F; Shyy, W and Fu, L (2022): "A fifth-order low-dissipation discontinuity-resolving TENO scheme for compressible flow simulation". In: *Journal of Computational Physics* 467, p. 111465. doi: https://doi.org/10.1016/j.jcp.2022.111465 (cit. on pp. 35, 51, 91).

Lighthill, MJ and Newman, MHA (1953): "On boundary layers and upstream influence. I. A comparison between subsonic and supersonic flows". In: *Proceedings of the Royal Society of London. Series A. Mathematical and Physical Sciences* 217.1130, pp. 344–357. doi: https://doi.org/10.1098/rspa.1953.0067 (cit. on p. 15).

Ling, Y; Balachandar, S and Parmar, M (Mar. 2016): "Inter-phase heat transfer and energy coupling in turbulent dispersed multiphase flows". In: *Physics of Fluids* 28.3, p. 033304. doi: https://doi.org/10.1063/1.4942184 (cit. on p. 24).

Ling, Y; Haselbacher, A and Balachandar, S (2011): "Importance of unsteady contributions to force and heating for particles in compressible flows: Part 1: Modeling and analysis for shock–particle interaction". In: *International Journal of Multiphase Flow* 37.9, pp. 1026–1044. doi: https://doi.org/10.1016/j.ijmultiphaseflow.2011.07.001 (cit. on pp. 23, 24, 205).

Ling, Y; Wagner, JL; Beresh, SJ; Kearney, SP and Balachandar, S (2012): "Interaction of a planar shock wave with a dense particle curtain: Modeling and experiments". In: *Physics of Fluids* 24.11. doi: https://doi.org/10.1063/1.4768815 (cit. on pp. ii, v, 23, 118, 120, 205, 206, 208, 213–216, 225, 280, 281).

Liu, Y and Kendall, MAF (2006): "Numerical analysis of gas and micro-particle interactions in a hand-held shock-tube device". In: *Biomedical Microdevices* 8.4, pp. 341–351. doi: https://doi.org/10.1007/s10544-006-9596-z (cit. on p. 2).

Loth, E (2008): "Compressibility and Rarefaction Effects on Drag of a Spherical Particle". In: *AIAA Journal* 46.9, pp. 2219–2228. doi: https://doi.org/10.2514/1.28943 (cit. on p. 21).

Loth, E; Daspit, JT; Jeong, M; Nagata, T and Nonomura, T (2021): "Supersonic and Hypersonic Drag Coefficients for a Sphere". In: *AIAA Journal* 59.8, pp. 3261–3274. doi: 10.2514/1.J060153 (cit. on pp. 21, 24, 25, 97, 102, 104, 105, 108, 111, 208).

Mach, E and Salcher, P (1887): "Photographische Fixirung der durch Projectile in der Luft eingeleiteten Vorgänge". In: *Annalen der Physik* 268.10, pp. 277–291. doi: https://doi.org/10.1002/andp.18872681008 (cit. on p. 1).

Mäkiharju, SA; Dewanckele, J; Boone, M; Wagner, C and Griesser, A (2022): "Tomographic X-ray particle tracking velocimetry: Proof-of-concept in a creeping flow". In: *Experiments in Fluids* 63, pp. 1–12. doi: https://doi.org/10.1007/s00348-021-03362-w (cit. on p. 226).

Marble, FE (1970): "Dynamics of Dusty Gases". In: *Annual Review of Fluid Mechanics* 2.Volume 2, 1970, pp. 397–446. doi: https://doi.org/10.1146/annurev.fl.02.010170.002145 (cit. on p. 18).

Martin, MP (2000): "Shock-capturing in LES of high-speed". In: *Annual Research Briefs-2000*, p. 193 (cit. on p. 35).

Mehrabadi, M; Tenneti, S; Garg, R and Subramaniam, S (2015): "Pseudo-turbulent gas-phase velocity fluctuations in homogeneous gas-solid flow: fixed particle assemblies and freely evolving suspensions". In: *Journal of Fluid Mechanics* 770, pp. 210–246. doi: https://doi.org/10.1017/jfm.2015.146 (cit. on p. 142).

Mehta, Y; Jackson, TL and Balachandar, S (2020): "Pseudo-turbulence in inviscid simulations of shock interacting with a bed of randomly distributed particles". In: *Shock Waves* 30, pp. 49–62. doi: https://doi.org/10.1007/s00193-019-00905-3 (cit. on pp. 118, 125, 246).

Mehta, Y; Jackson, TL; Zhang, J and Balachandar, S (Mar. 2016a): "Numerical investigation of shock interaction with one-dimensional transverse array of particles in air". In: *Journal of Applied Physics* 119.10, p. 104901. doi: https://doi.org/10.1063/1.4943616 (cit. on pp. 16, 18, 82, 86, 87).

Mehta, Y; Neal, C; Jackson, TL; Balachandar, S and Thakur, S (Sept. 2016b): "Shock interaction with three-dimensional face centered cubic array of particles". In: *Phys. Rev. Fluids* 1 (5), p. 054202. doi: https://doi.org/10.1103/PhysRevFluids.1.054202 (cit. on pp. 3, 18, 42, 85, 118).

Mehta, Y; Neal, C; Salari, K; Jackson, TL; Balachandar, S and Thakur, S (2018): "Propagation of a strong shock over a random bed of spherical particles". In: *Journal of Fluid Mechanics* 839, pp. 157–197. doi: https://doi.org/10.1017/jfm.2017.909 (cit. on p. 221).

Mehta, Y; Salari, K; Jackson, TL and Balachandar, S (2019): "Effect of Mach number and volume fraction in air-shock interacting with a bed of randomly distributed spherical particles". In: *Physical Review Fluids* 4.1, p. 014303. doi: https://doi.org/10.1103/PhysRevFluids.4.014303 (cit. on pp. 3, 19, 118).

Michaelides, EE; Sommerfeld, M and van Wachem, B (2022): Multiphase flows with droplets and particles. CRC Press. doi: https://doi.org/10.1201/9781003089278 (cit. on p. 246).

Miura, H; Glass, II and Young, AD (1982): "On a dusty-gas shock tube". In: *Proceedings of the Royal Society of London. A. Mathematical and Physical Sciences* 382.1783, pp. 373–388. doi: https://doi.org/10.1098/rspa.1982.0107 (cit. on p. 18).

Moriche, M; Uhlmann, M and Dušek, J (2021): "A single oblate spheroid settling in unbounded ambient fluid: A benchmark for simulations in steady and unsteady

wake regimes". In: *International Journal of Multiphase Flow* 136, p. 103519. DOI: https://doi.org/10.1016/j.ijmultiphaseflow.2020.103519 (cit. on p. 44).

Morinishi, Y; Tamano, S and Nakabayashi, K (2004): "Direct numerical simulation of compressible turbulent channel flow between adiabatic and isothermal walls". In: *Journal of Fluid Mechanics* 502, pp. 273–308. DOI: https://doi.org/10.1017/S0022112003007705 (cit. on p. 12).

Morkovin, M V (1962): "Effects of compressibility on turbulent flows". In: *Mécanique de la Turbulence* 367.380, p. 26 (cit. on p. 74).

Muskat, M (1934): "The flow of compressible fluids through porous media and some problems in heat conduction". In: *Physics* 5.3, pp. 71–94. DOI: https://doi.org/10.1063/1.1745233 (cit. on pp. 13, 189).

Nagata, T; Nonomura, T; Takahashi, S; Mizuno, Y and Fukuda, K (May 2016): "Investigation on subsonic to supersonic flow around a sphere at low Reynolds number of between 50 and 300 by direct numerical simulation". In: *Physics of Fluids* 28.5, p. 056101. DOI: https://doi.org/10.1063/1.4947244 (cit. on pp. 16, 42, 177).

Nagata, T; Nonomura, T; Takahashi, S; Mizuno, Y and Fukuda, K (2018): "Direct numerical simulation of flow around a heated/cooled isolated sphere up to a Reynolds number of 300 under subsonic to supersonic conditions". In: *International Journal of Heat and Mass Transfer* 120, pp. 284–299. DOI: https://doi.org/10.1016/j.ijheatmasstransfer.2017.12.042 (cit. on pp. 17, 21, 25, 42, 88, 93–95, 97–109, 111, 118, 166, 177, 181, 219).

Nahme, R (1940): "Beiträge zur hydrodynamischen Theorie der Lagerreibung". In: *Ingenieur-Archiv* 11.3, pp. 191–209. DOI: https://doi.org/10.1007/BF02086920 (cit. on p. 65).

Naumann, A (1953): "Luftwiderstand von Kugeln bei hohen Unterschallgeschwindigkeiten". In: *Allgem. Wärmetechnik* 4, pp. 217–221 (cit. on p. 14).

Noh, WF (1987): "Errors for calculations of strong shocks using an artificial viscosity and an artificial heat flux". In: *Journal of Computational Physics* 72.1, pp. 78–120. DOI: https://doi.org/10.1016/0021-9991(87)90074-X (cit. on p. 80).

Oliger, J and Sundström, A (1978): "Theoretical and Practical Aspects of Some Initial Boundary Value Problems in Fluid Dynamics". In: *SIAM Journal on Applied Mathematics* 35.3, pp. 419–446. DOI: https://doi.org/10.1137/0135035 (cit. on p. 38).

Olim, M; Ben-Dor, G; Mond, M and Igra, O (Oct. 1990): "A general attenuation law of moderate planar shock waves propagating into dusty gases with relatively high loading ratios of solid particles". In: *Fluid Dynamics Research* 6.3-4, p. 185. doi: https://doi.org/10.1016/0169-5983(90)90061-3 (cit. on p. 18).

Osnes, AN and Vartdal, M (2021): "Performance of drag force models for shock-accelerated flow in dense particle suspensions". In: *International Journal of Multiphase Flow* 137, p. 103563. doi: https://doi.org/10.1016/j.ijmultiphaseflow.2021.103563 (cit. on pp. 118, 129).

Osnes, AN and Vartdal, M (Apr. 2022): "Mach and Reynolds number dependency of the unsteady shock-induced drag force on a sphere". In: *Physics of Fluids* 34.4, p. 043303. doi: https://doi.org/10.1063/5.0086399 (cit. on pp. 17, 132).

Osnes, AN; Vartdal, M; Khalloufi, M; Capecelatro, J and Balachandar, S (2023): "Comprehensive quasi-steady force correlations for compressible flow through random particle suspensions". In: *International Journal of Multiphase Flow* 165, p. 104485. doi: https://doi.org/10.1016/j.ijmultiphaseflow.2023.104485 (cit. on pp. i, ii, iv, v, 3, 19, 23, 24, 42, 88, 112–118, 177, 208, 210, 219, 225).

Osnes, AN; Vartdal, M; Omang, MG and Reif, BAP (Jan. 2020): "Particle-resolved simulations of shock-induced flow through particle clouds at different Reynolds numbers". In: *Phys. Rev. Fluids* 5 (1), p. 014305. doi: https://doi.org/10.1103/PhysRevFluids.5.014305 (cit. on pp. 3, 19, 118, 119, 127, 129, 142, 221).

Osnes, AN; Vartdal, Magnus; Omang, Marianne Gjestvold and Reif, BAP (2019): "Computational analysis of shock-induced flow through stationary particle clouds". In: *International Journal of Multiphase Flow* 114, pp. 268–286. doi: https://doi.org/10.1016/j.ijmultiphaseflow.2019.03.010 (cit. on pp. 3, 19, 118, 129, 177, 207, 221).

Parmar, M; Haselbacher, A and Balachandar, S (2009): "Modeling of the unsteady force for shock-particle interaction". In: *Shock Waves* 19.4, pp. 317–329. doi: https://doi.org/10.1007/s00193-009-0206-x (cit. on pp. 23, 92).

Parmar, M; Haselbacher, A and Balachandar, S (2010): "Improved drag correlation for spheres and application to shock-tube experiments". In: *Aiaa Journal* 48.6, pp. 1273–1276. doi: https://doi.org/10.2514/1.J050161 (cit. on pp. 16, 21).

Parmar, M; Haselbacher, A and Balachandar, S (Feb. 2011): "Generalized Basset-Boussinesq-Oseen Equation for Unsteady Forces on a Sphere in a Compressible Flow". In: *Phys. Rev. Lett.* 106 (8), p. 084501. doi: https://doi.org/10.1103/PhysRevLett.106.084501 (cit. on pp. 20, 23, 205).

Parmar, M; Haselbacher, A and Balachandar, S (2012): "Equation of motion for a sphere in non-uniform compressible flows". In: *Journal of Fluid Mechanics* 699, pp. 352–375. doi: https://doi.org/10.1017/jfm.2012.109 (cit. on pp. 20, 23, 24, 205, 206).

Poinsot, TJ and Lele, SK (1992): "Boundary conditions for direct simulations of compressible viscous flows". In: *Journal of Computational Physics* 101.1, pp. 104–129. doi: https://doi.org/10.1016/0021-9991(92)90046-2 (cit. on pp. 38–40, 42).

Poinsot, TJ; Trouve, AC; Veynante, DP; Candel, SM and Esposito, EJ (1987): "Vortex-driven acoustically coupled combustion instabilities". In: *Journal of Fluid Mechanics* 177, pp. 265–292. doi: https://doi.org/10.1017/S0022112087000958 (cit. on p. 38).

Pope, SB (2000): Turbulent Flows. Cambridge University Press. doi: https://doi.org/10.1017/CBO9780511840531 (cit. on pp. 169, 197).

Qi, Z and Yu, AB (2021): "A new correlation for heat transfer in particle-fluid beds". In: *International Journal of Heat and Mass Transfer* 181, p. 121844. doi: https://doi.org/10.1016/j.ijheatmasstransfer.2021.121844 (cit. on p. 94).

Rai, MM and Moin, P (1991): "Direct simulations of turbulent flow using finite-difference schemes". In: *Journal of Computational Physics* 96.1, pp. 15–53. doi: https://doi.org/10.1016/0021-9991(91)90264-L (cit. on pp. 34, 40, 54, 91, 282).

Rankine, WJM (1870): "XV. On the thermodynamic theory of waves of finite longitudinal disturbance". In: *Philosophical Transactions of the Royal Society of London* 160, pp. 277–288. doi: https://doi.org/10.1098/rstl.1870.0015 (cit. on p. 9).

Ranz, WE and Marshall, JR (1952): "WR: Evaporation from drops". In: *Chemical engineering progress* 48, pp. 141–146 (cit. on pp. 94, 111).

Regele, JD; Rabinovitch, J; Colonius, T and Blanquart, G (2014): "Unsteady effects in dense, high speed, particle laden flows". In: *International Journal of Multiphase Flow* 61, pp. 1–13. doi: https://doi.org/10.1016/j.ijmultiphaseflow.2013.12.007 (cit. on pp. 42, 118, 119, 129, 207).

Richter, A and Nikrityuk, PA (2012): "Drag forces and heat transfer coefficients for spherical, cuboidal and ellipsoidal particles in cross flow at sub-critical Reynolds numbers". In: *International Journal of Heat and Mass Transfer* 55.4, pp. 1343–1354. doi: https://doi.org/10.1016/j.ijheatmasstransfer.2011.09.005 (cit. on p. 94).

Risso, Frédéric (2011): "Theoretical model for k- 3 spectra in dispersed multiphase flows". In: *Physics of fluids* 23.1. doi: https://doi.org/10.1063/1.3530438 (cit. on p. 202).

Roma, AM; Peskin, CS and Berger, MJ (1999): "An Adaptive Version of the Immersed Boundary Method". In: *Journal of Computational Physics* 153.2, pp. 509–534. doi: https://doi.org/10.1006/jcph.1999.6293 (cit. on pp. 44, 45, 93).

Sauer, FM (1951): "Convective Heat Transfer from Spheres in a Free-Molecule Flow". In: *Journal of the Aeronautical Sciences* 18.5, pp. 353–354. doi: https://doi.org/10.2514/8.1954 (cit. on pp. 24, 94).

Schiller, L and Naumann, A (1933): "Fundamental calculations in gravitational processing". In: *Zeitschrift Des Vereines Deutscher Ingenieure* 77, pp. 318–320 (cit. on p. 20).

Schlichting, H and Kestin, J (1961): Boundary layer theory. Vol. 121. Springer. doi: https://doi.org/10.1007/978-3-662-52919-5 (cit. on p. 14).

Schwarzkopf, JD and Horwitz, JA (2015): BHR equations re-derived with immiscible particle effects. Tech. rep. Los Alamos National Lab.(LANL), Los Alamos, NM (United States). doi: https://doi.org/10.2172/1179062 (cit. on p. 246).

Sciacovelli, L; Cinnella, P and Gloerfelt, X (2017): "Direct numerical simulations of supersonic turbulent channel flows of dense gases". In: *Journal of Fluid Mechanics* 821, pp. 153–199. doi: https://doi.org/10.1017/jfm.2017.237 (cit. on p. 12).

Shu, CW (2016): "High order WENO and DG methods for time-dependent convection-dominated PDEs: A brief survey of several recent developments". In: *Journal of Computational Physics* 316, pp. 598–613. doi: https://doi.org/10.1016/j.jcp.2016.04.030 (cit. on pp. 35, 49).

Shu, CW and Osher, S (1988): "Efficient implementation of essentially non-oscillatory shock-capturing schemes". In: *Journal of Computational Physics* 77.2, pp. 439–471. doi: https://doi.org/10.1016/0021-9991(88)90177-5 (cit. on p. 58).

Silber, EA; Boslough, M; Hocking, WK; Gritsevich, M and Whitaker, RW (2018): "Physics of meteor generated shock waves in the Earth's atmosphere – A review". In: *Advances in Space Research* 62.3, pp. 489–532. doi: https://doi.org/10.1016/j.asr.2018.05.010 (cit. on pp. 1, 3).

Singh, N; Kroells, M; Li, C; Ching, E; Ihme, M; Hogan, CJ and Schwartzentruber, TE (2022): "General Drag Coefficient for Flow over Spherical Particles". In: *AIAA Journal* 60.2, pp. 587–597. doi: https://doi.org/10.2514/1.J060648 (cit. on p. 21).

Skews, BW; Bredin, MS and Efune, M (2007): "Drag measurement in unsteady compressible flow Part 2: Shock wave loading of spheres and cones". In: *Shock* 1.1.2, pp. 1–3 (cit. on p. 16).

Sommerfeld, M (1985): "The unsteadiness of shock waves propagating through gas-particle mixtures". In: *Experiments in Fluids* 3.4, pp. 197–206. doi: https://doi.org/10.1007/BF00265101 (cit. on p. 17).

Spalart, PR; Moser, RD and Rogers, MM (1991): "Spectral methods for the Navier-Stokes equations with one infinite and two periodic directions". In: *Journal of Computational Physics* 96.2, pp. 297–324. doi: https://doi.org/10.1016/0021-9991(91)90238-G (cit. on p. 34).

Sridharan, P; Jackson, TL; Zhang, J and Balachandar, S (Feb. 2015): "Shock interaction with one-dimensional array of particles in air". In: *Journal of Applied Physics* 117.7, p. 075902. doi: https://doi.org/10.1063/1.4913217 (cit. on p. 18).

Sun, M; Saito, T; Takayama, K and Tanno, H (2005): "Unsteady drag on a sphere by shock wave loading". In: *Shock Waves* 14.1, pp. 3–9. doi: https://doi.org/10.1007/s00193-004-0235-4 (cit. on pp. 16, 23, 42, 82, 83, 85, 88, 90, 91, 219).

Sutherland, W (1893): "LII. The viscosity of gases and molecular force". In: *The London, Edinburgh, and Dublin Philosophical Magazine and Journal of Science* 36.223, pp. 507–531. doi: https://doi.org/10.1080/14786449308620508 (cit. on p. 93).

Takagi, S; Fu, L; Wakimura, H and Xiao, F (2022): "A novel high-order low-dissipation TENO-THINC scheme for hyperbolic conservation laws". In: *Journal of Computational Physics* 452, p. 110899. doi: https://doi.org/10.1016/j.jcp.2021.110899 (cit. on pp. 35, 54, 58).

Tam, CKW (1995): "Supersonic jet noise". In: *Annual review of fluid mechanics* 27.1, pp. 17–43. doi: https://doi.org/10.1146/annurev.fl.27.010195.000313 (cit. on p. 153).

Tan, S and Shu, CW (2010): "Inverse Lax-Wendroff procedure for numerical boundary conditions of conservation laws". In: *Journal of Computational Physics* 229.21, pp. 8144–8166. doi: https://doi.org/10.1016/j.jcp.2010.07.014 (cit. on p. 39).

Tanno, H; Itoh, K; Saito, T; Abe, A and Takayama, K (2003): "Interaction of a shock with a sphere suspended in a vertical shock tube". In: *Shock Waves* 13.3, pp. 191–200. doi: https://doi.org/10.1007/s00193-003-0209-y (cit. on pp. 16, 82, 132, 219).

Tenneti, S; Garg, R and Subramaniam, S (2011): "Drag law for monodisperse gas–solid systems using particle-resolved direct numerical simulation of flow past fixed assemblies of spheres". In: *International Journal of Multiphase Flow* 37.9, pp. 1072–1092. doi: https://doi.org/10.1016/j.ijmultiphaseflow.2011.05.010 (cit. on pp. 24, 208).

Theofanous, TG; Mitkin, V and Chang, CH (2016): "The dynamics of dense particle clouds subjected to shock waves. Part 1. Experiments and scaling laws". In: *Journal of Fluid Mechanics* 792, pp. 658–681. doi: https://doi.org/10.1017/jfm.2016.97 (cit. on pp. 17, 18).

Theofanous, TG; Mitkin, V and Chang, CH (2018): "Shock dispersal of dilute particle clouds". In: *Journal of fluid mechanics* 841, pp. 732–745. doi: https://doi.org/10.1017/jfm.2018.110 (cit. on p. 18).

Thompson, KW (1987): "Time dependent boundary conditions for hyperbolic systems". In: *Journal of Computational Physics* 68.1, pp. 1–24. doi: https://doi.org/10.1016/0021-9991(87)90041-6 (cit. on pp. 38, 39).

Titarev, VA and Toro, EF (2004): "Finite-volume WENO schemes for three-dimensional conservation laws". In: *Journal of Computational Physics* 201.1, pp. 238–260. doi: https://doi.org/10.1016/j.jcp.2004.05.015 (cit. on p. 35).

Toro, EF (2013): Riemann solvers and numerical methods for fluid dynamics: a practical introduction. Springer Berlin, Heidelberg. doi: https://doi.org/10.1007/b79761 (cit. on pp. 9, 59, 80).

Uhlmann, M (2005): "An immersed boundary method with direct forcing for the simulation of particulate flows". In: *Journal of Computational Physics* 209.2, pp. 448–476. doi: https://doi.org/10.1016/j.jcp.2005.03.017 (cit. on pp. 42, 43, 265, 266).

Vartdal, M and Osnes, AN (2018): "Using particle-resolved LES to improve Eulerian-Lagrangian modeling of shock wave particle cloud interaction". In: *Proceedings of the Summer Program*, pp. 25–34 (cit. on pp. 19, 42, 118, 221).

Verzicco, R and Orlandi, P (1996): "A Finite-Difference Scheme for Three-Dimensional Incompressible Flows in Cylindrical Coordinates". In: *Journal of Computational Physics* 123.2, pp. 402–414. doi: https://doi.org/10.1006/jcph.1996.0033 (cit. on p. 34).

VonNeumann, J and Richtmyer, RD (Mar. 1950): "A Method for the Numerical Calculation of Hydrodynamic Shocks". In: *Journal of Applied Physics* 21.3, pp. 232–237. doi: https://doi.org/10.1063/1.1699639 (cit. on p. 35).

Wagner, JL; Beresh, SJ; Kearney, SP; Pruett, BOM and Wright, EK (Dec. 2012a): "Shock tube investigation of quasi-steady drag in shock-particle interactions". In: *Physics of Fluids* 24.12, p. 123301. doi: 10.1063/1.4768816 (cit. on pp. 16, 82).

Wagner, JL; Beresh, SJ; Kearney, SP; Trott, WM; Castaneda, JN; Pruett, BO and Baer, MR (2012b): "A multiphase shock tube for shock wave interactions with dense particle fields". In: *Experiments in Fluids* 52.6, pp. 1507–1517. doi: https://doi.org/10.1007/s00348-012-1272-x (cit. on p. 17).

Whitaker, S (1972): "Forced convection heat transfer correlations for flow in pipes, past flat plates, single cylinders, single spheres, and for flow in packed beds and tube bundles". In: *AIChE Journal* 18.2, pp. 361–371. doi: https://doi.org/10.1002/aic.690180219 (cit. on p. 94).

Wikimedia (2022): File:Photography of bow shock waves around a brass bullet, 1888.jpg — Wikimedia Commons, the free media repository (cit. on p. 2).

Willis, AP and Kerswell, RR (Mar. 2008): "Coherent Structures in Localized and Global Pipe Turbulence". In: *Phys. Rev. Lett.* 100 (12), p. 124501. doi: 10.1103/PhysRevLett.100.124501 (cit. on p. 72).

Wohletz, KH; McGetchin, TR; Sandford II, MT and Jones, EM (1984): "Hydrodynamic aspects of caldera-forming eruptions: Numerical models". In: *Journal of Geophysical Research: Solid Earth* 89.B10, pp. 8269–8285. doi: https://doi.org/10.1029/JB089iB10p08269 (cit. on pp. 1, 3).

Xu, T; Lien, FS; Ji, H and Zhang, F (2013): "Formation of particle jetting in a cylindrical shock tube". In: *Shock Waves* 23.6, pp. 619–634. doi: https://doi.org/10.1007/s00193-013-0472-5 (cit. on p. 42).

Yamaleev, NK and Carpenter, MH (2009): "A systematic methodology for constructing high-order energy stable WENO schemes". In: *Journal of Computational*

Physics 228.11, pp. 4248–4272. DOI: https://doi.org/10.1016/j.jcp.2009.03.002 (cit. on p. 51).

Yamanaka, A; Yuki, T and Mitsuishi, N (1976): "Combined forced and natural convective heat transfer from spheres at small Reynolds number". In: *Journal of Chemical Engineering of Japan* 9.6, pp. 445–449. DOI: https://doi.org/10.1252/jcej.9.445 (cit. on p. 94).

Yao, J and Hussain, F (2020): "Turbulence statistics and coherent structures in compressible channel flow". In: *Physical Review Fluids* 5.8, p. 084603. DOI: https://doi.org/10.1103/PhysRevFluids.5.084603 (cit. on p. 12).

Yee, HC (1981): Numerical approximation of boundary conditions with applications to inviscid equations of gas dynamics. Tech. rep. (cit. on pp. 38, 39).

Yee, HC; Sandham, ND and Djomehri, MJ (1999): "Low-Dissipative High-Order Shock-Capturing Methods Using Characteristic-Based Filters". In: *Journal of Computational Physics* 150.1, pp. 199–238. DOI: https://doi.org/10.1006/jcph.1998.6177 (cit. on p. 52).

Yin, S; Meyer, M; Li, W; Liao, H and Lupoi, R (2016): "Gas Flow, Particle Acceleration, and Heat Transfer in Cold Spray: A review". In: *Journal of Thermal Spray Technology* 25.5, pp. 874–896. DOI: https://doi.org/10.1007/s11666-016-0406-8 (cit. on p. 1).

Yu, M; Xu, CX and Pirozzoli, S (2019): "Genuine compressibility effects in wall-bounded turbulence". In: *Physical Review Fluids* 4.12, p. 123402. DOI: https://doi.org/10.1103/PhysRevFluids.4.123402 (cit. on p. 12).

Zhang, R; Zhang, M and Shu, CW (2011): "On the Order of Accuracy and Numerical Performance of Two Classes of Finite Volume WENO Schemes". In: *Communications in Computational Physics* 9.3, pp. 807–827. DOI: https://doi.org/10.4208/cicp.291109.080410s (cit. on pp. 49, 52).

Zhao, S; Lardjane, N and Fedioun, I (2014): "Comparison of improved finite-difference WENO schemes for the implicit large eddy simulation of turbulent non-reacting and reacting high-speed shear flows". In: *Computers Fluids* 95, pp. 74–87. DOI: https://doi.org/10.1016/j.compfluid.2014.02.017 (cit. on p. 35).

Zuber, N. (1964): "On the dispersed two-phase flow in the laminar flow regime". In: *Chemical Engineering Science* 19.11, pp. 897–917. DOI: https://doi.org/10.1016/0009-2509(64)85067-3 (cit. on p. 206).

Zwart, PJ; Budwig, R and Tavoularis, S (1997): "Grid turbulence in compressible flow". In: *Experiments in Fluids* 23.6, pp. 520–522. doi: https://doi.org/10.1007/s003480050143 (cit. on pp. 12, 13).

A Definitions of averaging operators and flow field decomposition

Details of the volume-averaging procedures and the volume-averaged governing equations have been provided by Gray and Lee (1977), Michaelides et al. (2022), and Schwarzkopf and Horwitz (2015). The reader is suggested to follow the references for mathematical details. Detailed definitions of the averaging operators used in the current work are provided.

A.1 Averaging operators

Following the nomenclature of Mehta et al. (2020), first an indicator function I_g is defined, which demarcates the solid and fluid phases. The definition of the indicator function is given in eq. (A.1).

$$\mathrm{I}_g = \begin{cases} 1\,, & \text{Inside the fluid phase} \\ 0\,, & \text{Inside the solid phase} \end{cases} \tag{A.1}$$

Let L_x, L_y and L_z represent the domain lengths in the cartesian domain along the x, y and z directions respectively. If N_x, N_y and N_z represent the number of gridpoints, then the grid-spacing along the three directions are given by $\mathrm{d}x = L_x/(N_x - 1)$, $\mathrm{d}y = L_y/(N_y - 1)$, and $\mathrm{d}z = L_z/(N_z - 1)$ respectively. Let the total volume occupied by the solid and fluid phase be V, such that $V = L_x L_y L_z = V_g + V_s$. The volume occupied by the fluid phase is V_g and V_s is the volume occupied by the solid phase. Let $F(x, y, z, t)$ be any variable defined

on the cartesian grid. Then the volume average of F is given by eq. (A.2).

$$\overline{F} = \overline{F}_{x,y,z} = \frac{1}{V} \int_V I_g(x,y,z,t) F(x,y,z,t) \, \mathrm{d}x \, \mathrm{d}y \, \mathrm{d}z \tag{A.2}$$

In addition to the volume average, an analogous area average can also be defined at a plane inside the three-dimensional volume. The area average in the $x-y$ plane at $z = z_o$ is defined as eq. (A.3). The area average along the $y-z$ and $x-z$ planes can be defined in a similar way.

$$\overline{F}_{x,y} = \frac{1}{A_{xy}} \int_{A_{xy}} I_g(x,y,z_o,t) F(x,y,z_o,t) \, \mathrm{d}x \, \mathrm{d}y \tag{A.3}$$

In eq. (A.3), A_{xy} is the total number of grid points in the $x-y$ plane given by $A_{xy} = L_x L_y$. The intersecting area occupied by the solid phase in the chosen plane is then given by $A_{s,xy}$.

$$V_g = \int_V I_g(x,y,z,t) \, \mathrm{d}x \, \mathrm{d}y \, \mathrm{d}z \tag{A.4}$$

The total volume occupied by the fluid phase, V_g is defined in eq. (A.4). Analogously, the area occupied by the pure fluid in the $x-y$ plane at $z = z_o$ is given in eq. (A.5). Similar definitions for the area occupied by the fluid phase can be obtained for the $y-z$ and $x-z$ planes.

$$A_{g,xy} = \int_{A_{xy}} I_g(x,y,z_o,t) \, \mathrm{d}x \, \mathrm{d}y \tag{A.5}$$

The phase average is defined as the average of a flow quantity over the volume occupied by the pure fluid. The phase average of a fluid occupying a volume V_g is defined in eq. (A.6) and the corresponding counterpart for the phase

average in the $x-y$ plane is given in eq. (A.7).

$$\langle F \rangle = \langle F \rangle_{x,y,z} = \frac{1}{V_g} \int_V I_g(x,y,z,t)\, F(x,y,z,t)\ \mathrm{d}x\, \mathrm{d}y\, \mathrm{d}z \tag{A.6}$$

$$\langle F \rangle_{x,y} = \frac{1}{A_{g,xy}} \int_{A_{xy}} I_g(x,y,z_o,t)\, F(x,y,z_o,t)\ \mathrm{d}x\, \mathrm{d}y \tag{A.7}$$

The phase average defined in a volume V and the area A_{xy} is related to the corresponding volume and area average through the solid volume fraction as shown in eq. (A.8). In the eq. (A.8), ϕ_p is the solid volume fraction in the volume V and $\phi_{p,xy}$ is the corresponding definition in the $x-y$ plane at $z = z_o$.

$$\phi_p = \frac{V_s}{V}, \quad \phi_{p,xy} = \frac{A_{s,xy}}{A_{xy}} \tag{A.8}$$

$$\overline{F}_{x,y,z} = (1-\phi_p)\langle F \rangle_{x,y,z}, \quad \overline{F}_{x,y} = (1-\phi_{p,xy})\langle F \rangle_{x,y} \tag{A.9}$$

For non-conservative flow variables like velocity, a Favre average is defined as in eq. (A.10) over the volume V and the $x-y$ plane. Extension to the other planes is straightforward.

$$\widetilde{F} = \widetilde{F}_{x,y,z} = \frac{\overline{\rho F}_{x,y,z}}{\overline{\rho}} = \frac{\langle \rho F \rangle_{x,y,z}}{\langle \rho \rangle} \tag{A.10}$$

$$\widetilde{F}_{x,y} = \frac{\overline{\rho F}_{x,y,z}}{\overline{\rho}} = \frac{\langle \rho F \rangle_{x,y}}{\langle \rho \rangle} \tag{A.11}$$

A.1.1 Slab averaging

In addition, slab averaging can be defined as the phase or Favre averaging of a flow quantity in a slab whose volume (V_{slab}) is a subset of the total volume V of the cartesian domain. Consider a slab of width B_x along the streamwise direction and lengths L_y and L_z along the transverse directions as shown in fig. A.1. The slab volume is then given by $V_{slab} = B_x \times L_y \times L_z$.

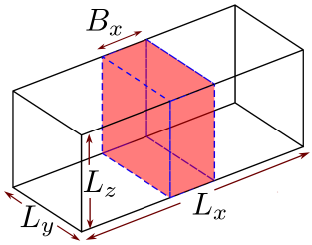

Figure A.1: Visualization of the slab volume of width B_x in a cartesian domain with $x \in [0, L_x]$, $y \in [0, L_y]$, and $z \in [0, L_z]$. The slab is represented in red.

Slab averaging for a fluid property

Analogous to eq. (A.4), the volume occupied by the pure-fluid inside the slab can be represented in eq. (A.12). For the flow quantity $F(x,y,z,t)$, the slab average for a fluid property in the context of the current work will only consider the phase average and the Favre average over the volume occupied by the pure fluid as given in eq. (A.13) and eq. (A.14) respectively.

$$V_{g,slab} = \int_{V_{slab}} I_g(x,y,z,t)\,\mathrm{d}x\,\mathrm{d}y\,\mathrm{d}z \tag{A.12}$$

$$\langle F \rangle_{slab} = \frac{1}{V_{g,slab}} \int_{V_{slab}} I_g(x,y,z,t)\,F(x,y,z,t)\;\mathrm{d}x\,\mathrm{d}y\,\mathrm{d}z \tag{A.13}$$

$$\widetilde{F}_{slab} = \frac{\langle \rho F \rangle_{slab}}{\langle \rho \rangle_{slab}} \tag{A.14}$$

Slab averaging for a general quantity

For a general quantity, not defined for the fluid, the slab-averaging can simply be defined as the mean of the quantity over the considered slab. Let N_s represent the total number of samples of a quantity $Q(n)$ located inside the slab given by fig. A.1. Then, the slab average for the quantity over the slab is given by eq. (A.15)

$$\langle Q \rangle_{slab} = \frac{1}{N_s} \sum_{n=1}^{N_s} Q(n) \tag{A.15}$$

A.1.2 Hemispherical Shell averaging

In order to perform the shell-averaging procedure, N_s discrete Lagrangian markers are distributed uniformly in a hemispherical region with inner radius R_i and outer radius R_o upstream of the reference particle n having a radius $R = R_i$. The hemispherical shell is such that the normal to the plane surface of the hemispherical shell aligns with the streamwise direction (in the present work, along x-axis) and its center coincides with the center of the reference particle n. Let the common center be located at $\mathbf{X}_c$ and the coordinate of the m^{th} lagrangian marker be denoted by $\mathbf{X}_s^{(m)}$. The discrete Lagrangian markers satisfy eq. (A.16).

$$\forall m \in \{1, 2, \ldots, N_s\},\ R < |\, \mathbf{X}_s^{(m)} - \mathbf{X}_c \,| \leq R_o \text{ and } \mathbf{X}_s^{(m)} \cdot \hat{\imath} < \mathbf{X}_c \cdot \hat{\imath} \tag{A.16}$$

In the eq. (A.16), $\hat{\imath}$ is the unit vector along the streamwise direction. If the coordinate system on the cartesian grid is denoted by $\mathbf{X} = [x, y, z]$, then the interpolated value of $F(x,y,z,t)$ (defined on the cartesian grid) on the m^{th} lagrangian marker point is given as $F_s^{(m)}$. The value of $F_s^{(m)}$ is obtained by trilinear interpolation from the cartesian coordinate system $\mathbf{X}$ to $\mathbf{X}_s^{(m)}$. The volume occupied by the hemispherical shell is denoted as in eq. (A.17).

$$V_s = \frac{2}{3}\pi(R_o - R)^3 \tag{A.17}$$

In addition, analogous to eq. (A.1), an indicator function can be defined to differentiate the lagrangian markers that lie in the solid phase (Ω_s) and the

fluid phase (Ω_f) and is given in eq. (A.18).

$$\mathrm{I}_{g,s}\,(\mathrm{m}) = \begin{cases} 1\,, & \mathbf{X}_s^{(m)} \in \Omega_f \\ 0\,, & \mathbf{X}_s^{(m)} \in \Omega_s \end{cases} \tag{A.18}$$

Let the volume occupied by the pure fluid inside the hemispherical shell be given by $V_{g,s}$. Then, the expression for phase average and Favre average for the quantity $F_s^{(m)}$ defined on the discrete lagrangian markers inside the volume occupied by the hemispherical shell is given by eq. (A.19) and eq. (A.19) respectively. In eq. (A.19), $\mathrm{d}V_s^{(m)}$ is the differential volume associated with the lagrangian marker m.

$$\langle F \rangle_{shell} \;=\; \frac{1}{V_{g,s}} \int_{V_s} I_{g,s}(m)\, F_s^{(m)}\; \mathrm{d}V_s^{(m)} \tag{A.19}$$

$$\widetilde{F}_{shell} \;=\; \frac{\langle \rho F \rangle_{shell}}{\langle \rho \rangle_{shell}} \tag{A.20}$$

A.1.3 Particle averaging

Let N_p represent the total number of particles in a volume V under consideration and $Q(n)$ represent a quantity defined for the particle n such that $n \in \{1, 2, \ldots N_p\}$. Then the particle average $\langle Q \rangle_p$ represents the average of $Q(n)$ over all the particles inside the volume V and is represented in eq. (A.21).

$$\langle Q \rangle_p \;=\; \frac{1}{N_p} \sum_{n=1}^{N_p} Q(n) \tag{A.21}$$

A.1.4 Particle Conditioned Averaging

The details for the procedure for particle-conditioned averaging are given in Garcia-Villalba et al. (2012). The procedure is briefly discussed in the context of the current work. It should be noted that the particles are considered to be fixed and the flow is assumed to be steady. Consider a slab of volume

$V = V_{slab}$ as shown in fig. A.1. Let $N_{p,slab}$ represent the number of particles out of N_p which lie inside V_{slab}. Let $x_{slab,l}$ and $x_{slab,r}$ represent the limits of the slab along the streamwise direction (x-axis in the current work). Then $N_{p,slab}$ is represented in eq. (A.22).

$$N_{p,slab} = \left|\left\{m \in \{1, \dots, N_p\} \mid x_{slab,l} \leq X_c^{(m)} \leq x_{slab,r}\right\}\right| \tag{A.22}$$

Consider now a flow quantity $S(\mathbf{X})$ on the cartesian domain $\mathbf{X} = [x, y, z]$. The instantaneous coordinate relative to the $m^{(th)}$ particle located at $\mathbf{X}_c^{(m)} = [x_c, y_c, z_c]$ is given by eq. (A.23).

$$\mathbf{X}^{(m)} = \mathbf{X} - \mathbf{X}_c^{(m)} \tag{A.23}$$

The flow quantity S defined on the coordinate system relative to the m^{th} particle is then defined as in eq. (A.24).

$$S(\mathbf{X}^{(m)}) = S(\mathbf{X}) - S(\mathbf{X}_c^{(m)}) \tag{A.24}$$

Consider an indicator function given in eq. (A.25) defined on the coordinate-system $\mathbf{X}^{(m)}$ which demarcates the grid points in the solid (Ω_s) or fluid (Ω_f) phase.

$$\psi_f(\mathbf{X}^{(m)}) = \begin{cases} 1, & \mathbf{X}^{(m)} \in \Omega_f \\ 0, & \mathbf{X}^{(m)} \in \Omega_s \end{cases} \tag{A.25}$$

Let the number of samples associated with a gridpoint on the cartesian grid ($\mathbf{X}$) used for the averaging procedure be defined as $N^{(s)}$ defined in eq. (A.26).

$$N^{(s)} = \sum_{m=1}^{N_{p,slab}} \psi_f(\mathbf{X}^{(m)}) \tag{A.26}$$

The particle-conditioned average of S in the slab between $x_{slab,l}$ and $x_{slab,l}$ can then be computed from eq. (A.27)

$$\langle S_{x=x_{slab,l},\, x_{slab,r}} \rangle_{pc} \;=\; \frac{1}{N^{(s)}} \sum_{m=1}^{N_{p,slab}} \psi_f(\mathbf{X}^{(m)})\, S(\mathbf{X}^{(m)}) \tag{A.27}$$

It should be noted that the value of $S(\mathbf{X}^{(m)})$ is not directly available, since the gridpoints in $\mathbf{X}^{(m)}$ do not coincide with $\mathbf{X}$. Hence, $S(\mathbf{X}^{(m)})$ is obtained by trilinear interpolation from the values defined in $\mathbf{X}$ onto $\mathbf{X}^{(m)}$. This concludes the discussion on the procedure for particle-conditioned averaging in a x-slab between $x_{slab,l}$ and $x_{slab,r}$ for a flow quantity $S(\mathbf{X})$.

A.1.5 Temporal averaging

The time average of a flow quantity $F(x,y,z,t)$ defined on the cartesian grid average over time between the time $t = t_1$ to $t = t_2$ is given in eq. (A.28)

$$\langle F \rangle_t \;=\; \frac{1}{t_2 - t_1} \int_{t=t_1}^{t_2} F(x,y,z,t)\; \mathrm{d}t \tag{A.28}$$

A.1.6 Flow field fluctuations

The fluctuations with respect to the phase average quantities are represented by the superscript $(\cdot)'$ as in eq. (A.29) and the fluctuations with respect to the Favre average quantities are represented by $(\cdot)''$ as shown in eq. (A.30). In the current work, the symbols to represent spatial flow field fluctuations will depend on the type of averaging performed and will be represented by the corresponding subscripts used in the averaging procedure. The fluctuations with respect to the phase, favre, or time average can be defined in eqs. (A.29)

to (A.31) respectively.

$$F' = F - \langle F \rangle \tag{A.29}$$

$$F'' = F - \widetilde{F} \tag{A.30}$$

$$F''' = F - \langle F \rangle_t \tag{A.31}$$

A.2 Common nomenclature

$\langle F \rangle = \langle F \rangle_{x,y,z}$	Phase average over the entire volume.
$\langle F \rangle_t = \langle F \rangle_{x,y,z,t}$	Time and phase average over the entire volume.
$\widetilde{F} = \widetilde{F}_{x,y,z}$	Favre average over the entire volume.
$\widetilde{F}_t = \widetilde{F}_{x,y,z,t}$	Time and Favre average over the entire volume
$\langle F \rangle_{y,z}$	Phase average in the $y-z$ plane at a given x plane.
$\langle F \rangle_{y,z,t}$	Time and phase average in the $y-z$ plane at a given x plane.
$\widetilde{F}_{y,z}$	Favre average in the $y-z$ plane at a given x plane.
$\widetilde{F}_{y,z}$	Time and Favre average in the y,z plane at a given x plane
$\langle F \rangle_{shell}$	Phase average over hemispherical shell upstream of a given particle
$\langle F \rangle_{shell,t}$	Time and Phase average over hemispherical shell upstream of a given particle
$\widetilde{F}_{shell}$	Favre average over hemispherical shell upstream of a given particle
$\widetilde{F}_{shell,t}$	Time and Favre average over hemispherical shell upstream of a given particle
$\langle F \rangle_{slab}$	Phase average of F in a chosen slab
$\langle F \rangle_{slab,t}$	Time and phase average of F in a chosen slab
$\widetilde{F}_{slab}$	Favre average of F in a chosen slab
$\widetilde{F}_{slab,t}$	Time and Favre average F in a chosen slab

$\langle F \rangle_p$	Particle average of F over a given number of particles in a volume
$\langle F \rangle_{p,t}$	Particle and time average of F over a given number of particles in a volume
$\langle F_{x=x_1,x_2} \rangle_{pc}$	Particle conditioned average of F over a given number of particles in a slab between $x = x_1$ and $x = x_2$
$\langle F_{x=x_1,x_2} \rangle_{pc,t}$	Time and Particle conditioned average of F over a given number of particles in a slab between $x = x_1$ and $x = x_2$

B Discretization of viscous terms

This section describes the discretization of the viscous terms for the compressible Navier-Stokes equations on a 2D collocated grid. For simplicity and conciseness, the additional source terms are neglected. Extension to the discretization on a 3D grid is straightforward. The compressible Navier-Stokes equations in 2D reduce to

$$\frac{\partial}{\partial t}(\rho u) + \frac{\partial}{\partial x_j}(\rho u u_j) + \frac{\partial p}{\partial x} = \frac{\partial \sigma_{xx}}{\partial x} + \frac{\partial \sigma_{xy}}{\partial y} \tag{B.1}$$

$$\frac{\partial}{\partial t}(\rho v) + \frac{\partial}{\partial x_j}(\rho v u_j) + \frac{\partial p}{\partial y} = \frac{\partial \sigma_{yx}}{\partial x} + \frac{\partial \sigma_{yy}}{\partial y} \tag{B.2}$$

$$\begin{aligned}\frac{\partial E}{\partial t} + \frac{\partial}{\partial x_j}(u_j(E+p)) = \frac{\partial}{\partial x}\left(\kappa\frac{\partial T}{\partial x} + u\sigma_{xx} + v\sigma_{yx}\right) + \\ \frac{\partial}{\partial y}\left(\kappa\frac{\partial T}{\partial y} + u\sigma_{xy} + v\sigma_{yy}\right)\end{aligned} \tag{B.3}$$

$$\sigma_{xx} = \frac{4}{3}\mu\frac{\partial u}{\partial x} - \frac{2}{3}\mu\frac{\partial v}{\partial y} \tag{B.4}$$

$$\sigma_{xy} = \mu\left(\frac{\partial u}{\partial y} + \frac{\partial v}{\partial x}\right) \tag{B.5}$$

$$\sigma_{yx} = \sigma_{xy} \tag{B.6}$$

$$\sigma_{yy} = \frac{4}{3}\mu\frac{\partial v}{\partial y} - \frac{2}{3}\mu\frac{\partial u}{\partial x} \tag{B.7}$$

The collocated grid is shown below. It is important to note that the conservative variables are stored at the integral grid points, i.e., (i, j), where i, j are integers.

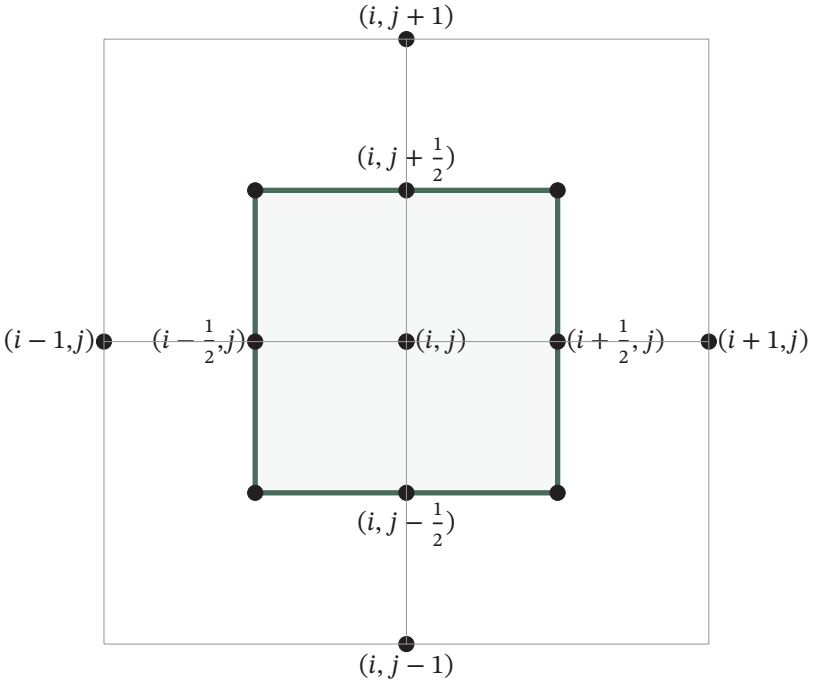

Figure B.1: The 2D collocated grid

Consider the right-hand side of the equations B.1, B.2 and B.3. The viscous terms are discretized as follows.

$$\left(\frac{\partial \sigma_{xx}}{\partial x} + \frac{\partial \sigma_{xy}}{\partial y}\right)_{i,j} \approx \frac{(\sigma_{xx})_{i+1/2,j} - (\sigma_{xx})_{i-1/2,j}}{\Delta x} + \frac{(\sigma_{xy})_{i,j+1/2} - (\sigma_{xy})_{i,j-1/2}}{\Delta y} \tag{B.8}$$

$$\left(\frac{\partial \sigma_{yx}}{\partial x}+\frac{\partial \sigma_{yy}}{\partial y}\right)_{i,j} \approx \frac{(\sigma_{yx})_{i+1/2,j}-(\sigma_{yx})_{i-1/2,j}}{\Delta x}+\frac{(\sigma_{yy})_{i,j+1/2}-(\sigma_{yy})_{i,j-1/2}}{\Delta y} \tag{B.9}$$

$$\begin{aligned}&\left(\frac{\partial}{\partial x}\left(\kappa\frac{\partial T}{\partial x}+u\sigma_{xx}+v\sigma_{yx}\right)+\frac{\partial}{\partial y}\left(\kappa\frac{\partial T}{\partial y}+u\sigma_{xy}+v\sigma_{yy}\right)\right)_{i,j} \approx \\ &\frac{(\kappa\frac{\partial T}{\partial x}+u\sigma_{xx}+v\sigma_{yx})_{i+1/2,j}-(\kappa\frac{\partial T}{\partial x}+u\sigma_{xx}+v\sigma_{yx})_{i-1/2,j}}{\Delta x}+ \\ &\frac{(\kappa\frac{\partial T}{\partial y}+u\sigma_{xy}+v\sigma_{yy})_{i,j+1/2}-(\kappa\frac{\partial T}{\partial y}+u\sigma_{xy}+v\sigma_{yy})_{i,j-1/2}}{\Delta y}\end{aligned} \tag{B.10}$$

where the terms σ_{xx}, σ_{xy}, σ_{yx}, σ_{yy}, $\kappa\frac{\partial T}{\partial x}$, $u\sigma_{xx}$, $v\sigma_{yx}$, $u\sigma_{xy}$, $v\sigma_{yy}$ and $\kappa\frac{\partial T}{\partial y}$ are evaluated at the cell interfaces. Some of the terms can be calculated as follows. The rest of the terms can be evaluated using the manipulation of indices.

$$\begin{aligned}(\sigma_{xx})_{i-1/2,j} \approx &\frac{4}{3}\mu_{i-1/2,j}\left(\frac{u_{i,j}-u_{i-1,j}}{\Delta x}\right) \\ &-\frac{2}{3}\mu_{i-1/2,j}\left(\frac{v_{i-1,j+1}-v_{i-1,j-1}+v_{i,j+1}-v_{i,j-1}}{4\Delta y}\right)\end{aligned} \tag{B.11}$$

$$\begin{aligned}(\sigma_{xy})_{i,j-1/2} \approx &\mu_{i,j-1/2}\left(\frac{u_{i,j}-u_{i,j-1}}{\Delta y}\right) \\ &+\mu_{i,j-1/2}\left(\frac{v_{i+1,j}-v_{i-1,j}+v_{i+1,j-1}-v_{i-1,j-1}}{4\Delta x}\right)\end{aligned} \tag{B.12}$$

$$(\sigma_{yx})_{i-1/2,j} \approx \mu_{i-1/2,j}\left(\frac{v_{i,j}-v_{i-1,j}}{\Delta x}\right) + \mu_{i-1/2,j}\left(\frac{u_{i,j+1}-u_{i,j-1}+u_{i-1,j+1}-u_{i-1,j-1}}{4\Delta y}\right) \tag{B.13}$$

(B.14)

$$(\sigma_{yy})_{i,j-1/2} \approx \frac{4}{3}\mu_{i,j-1/2}\left(\frac{v_{i,j}-v_{i,j-1}}{\Delta y}\right) - \frac{2}{3}\mu_{i,j-1/2}\left(\frac{u_{i+1,j}-u_{i-1,j}+u_{i+1,j-1}-u_{i-1,j-1}}{4\Delta x}\right) \tag{B.15}$$

$$(u\sigma_{xx})_{i-1/2,j} \approx \left(\frac{u_{i,j}+u_{i-1,j}}{2}\right)(\sigma_{xx})_{i-1/2,j} \tag{B.16}$$

(B.17)

$$(v\sigma_{yx})_{i-1/2,j} \approx \left(\frac{v_{i,j}+v_{i-1,j}}{2}\right)(\sigma_{yx})_{i-1/2,j} \tag{B.18}$$

(B.19)

$$(u\sigma_{xy})_{i,j-1/2} \approx \left(\frac{u_{i,j}+u_{i,j-1}}{2}\right)(\sigma_{xy})_{i,j-1/2} \tag{B.20}$$

(B.21)

$$(v\sigma_{yy})_{i,j-1/2} \approx \left(\frac{v_{i,j}+v_{i,j-1}}{2}\right)(\sigma_{yy})_{i,j-1/2} \tag{B.22}$$

$\mu_{i-1/2,j}$, $\mu_{i,j-1/2}$ and other terms can be calculated as the average of adjacent grid points. For example, $\mu_{i-1/2,j} \approx (\mu_{i,j}+\mu_{i-1,j})/2$.

$$\left(\kappa\frac{\partial T}{\partial x}\right)_{i-1/2,j} \approx \left(\frac{\kappa_{i,j}+\kappa_{i-1,j}}{2\,cv}\right)\frac{e_{i,j}-e_{i-1,j}}{\Delta x} \tag{B.23}$$

$$\left(\kappa\frac{\partial T}{\partial y}\right)_{i,j-1/2} \approx \left(\frac{\kappa_{i,j}+\kappa_{i,j-1}}{2\,C_v}\right)\frac{e_{i,j}-e_{i,j-1}}{\Delta y} \tag{B.24}$$

κ is the material's thermal conductivity, e is the specific internal energy, and C_v is the heat capacity at constant volume.

C Non-dimensionalisation

Let the governing differential equations for compressible flow without additional source terms be written as follows

$$\mathbf{U}_t + \nabla \cdot \mathbf{F} = 0 \tag{C.1}$$

In the eq. (C.1), $\mathbf{U}$ is the vector of conservative variables, and $\mathbf{F}$ is the tensor of surface fluxes.

$$\mathbf{U} = (\rho, \rho u, \rho v, \rho w, E) \tag{C.2}$$

ρ is the density of fluid and u, v, w are the fluid velocities along the x, y and z directions respectively. Let E_m be the total energy per unit mass defined as

$$E_m = \frac{1}{2}(u^2 + v^2 + w^2) + e \tag{C.3}$$

where e is the internal energy per unit mass given by $e = c_v T$. c_v is the specific heat at constant volume. The ideal gas equation of state is assumed

$$e = \frac{p}{(\gamma - 1)\rho} \tag{C.4}$$

The local speed of sound is a function of the local pressure (p), density (ρ), and the ratio of specific heat capacities (γ) and is given in eq. (C.5)

$$a = \sqrt{\frac{\gamma p}{\rho}} \tag{C.5}$$

The governing equations in the index notation can be written as

$$\begin{aligned} \partial_t(\rho) + (\rho u_j)_{,j} &= 0 \\ \partial_t(\rho u_i) + (\rho u_i u_j + \delta_{i,j} p)_{,j} &= (\tau_{i,j})_{,j} \\ \partial_t(\rho E_m) + (\rho u_j E_m + u_j p)_{,j} &= (u_i \tau_{i,j} - q_j)_{,j} \end{aligned} \tag{C.6}$$

The viscous stresses for a Newtonian fluid are expressed as follows

$$\tau_{i,j} = \mu \left(u_{i,j} + u_{j,i} - \frac{2}{3} u_{k,k} \delta_{i,j} \right) \tag{C.7}$$

Where μ is the fluid's dynamic viscosity, expressed as a temperature-dependent viscous law. Sutherland's law for viscosity is considered in the current chapter. Extension to other viscous laws is relatively straightforward.

$$\mu(T) = \mu_o \left(\frac{T}{T_o} \right)^{3/2} \left(\frac{T_o + S}{T + S} \right) \tag{C.8}$$

μ_o is the reference dynamic viscosity of the fluid evaluated at the temperature T_o, and S is the Sutherland constant. For air, the Sutherland constant takes the value of $S = 110.4K$. The heat flux is given by

$$q_i = -\kappa T_{,i} \tag{C.9}$$

κ is the thermal conductivity of the fluid, which can be expressed in terms of the Prandtl number (Pr) as

$$\kappa = \frac{\mu C_p}{Pr} \tag{C.10}$$

In the current work, the Prandtl number (Pr) is assumed to be constant and takes the value of $Pr = 0.7$ for air. Expanding the eq. (C.10), the heat flux can be rewritten as

$$q_j = -\frac{\mu \gamma}{Pr} e_{,j} \tag{C.11}$$

Non-dimensional form

The following reference scales are used for non-dimensionalization.

$$l_{ref} = l_o \tag{C.12}$$
$$u_{ref} = a_o \tag{C.13}$$
$$t_{ref} = t_o = l_o/a_o \tag{C.14}$$
$$\rho_{ref} = \rho_o \tag{C.15}$$
$$p_{ref} = \rho_o a_o^2 \tag{C.16}$$
$$E_{m,ref} = a_o^2 \tag{C.17}$$
$$\mu_{ref} = \mu_o \tag{C.18}$$
$$T_{ref} = T_o \tag{C.19}$$
$$e_{ref} = a_o^2 \tag{C.20}$$

The subscript "o" refers to the reference fluid state (In this case, the state at free-stream), and the corresponding speed of sound relates to other free-stream quantities as follows

$$a_o^2 \;=\; \gamma p_o/\rho_o \;=\; \gamma(\gamma-1)\,C_v T_o \tag{C.21}$$

Here, C_v is the specific heat at constant volume, and T_o is the reference temperature, assumed to be 293.7 K for the present studies. Let the superscript "*" represent the non-dimensional form of the variables. Replacing the dimensional variables in equations eq. (C.6) with the product of non-dimensional quantities times the respective reference scales, the following equations are obtained

$$\begin{aligned}
\partial_t^*(\rho^*) \;+\; (\rho^* u_j^*)_{,j} \;&=\; 0 \\
\partial_t^*(\rho^* u_i^*) \;+\; (\rho^* u_i^* u_j^* \;+\; \delta_{i,j} p^*)_{,j} \;&=\; (\tau_{i,j}^*)_{,j} \\
\partial_t^*(\rho^* E_m^*) \;+\; (\rho^* E_m^* u_j^* \;+\; u_j^* p^*)_{,j} \;&=\; (u_i^* \tau_{i,j}^* \;-\; q_j^*)_{,j}
\end{aligned} \tag{C.22}$$

The transformation leads to a change in the form of the terms in the RHS of the equations C.22 as follows

$$\tau^*_{i,j} = \frac{\mu^*}{Re_o}\left(u^*_{i,j} + u^*_{j,i} - \frac{2}{3}u^*_{k,k}\delta_{i,j} \right) \tag{C.23}$$

Where the Reynolds number (Re) at the reference state reads

$$Re_o = \frac{\rho_o l_o a_o}{\mu_o} \tag{C.24}$$

In the eq. (C.23), the non-dimensional dynamic viscosity (μ^*) is computed from the non-dimensional form of Sutherland's law

$$\mu^* = T^{*\,(3/2)}\left(\frac{1+\tilde{S}}{T^*+\tilde{S}}\right) \tag{C.25}$$

The non-dimensional temperature (T^*) can be represented in terms of the non-dimensional internal energy (e^*) as follows

$$T^* = \gamma(\gamma-1)e^* \tag{C.26}$$

Note that the equation C.26 can be used to compute the non-dimensional temperature (T^*) from the non-dimensional internal energy (e^*), which can be further used in the non-dimensional viscous law in eq. (C.25). The transformed Sutherland constant, $\tilde{S}$ is given as

$$\tilde{S} = \frac{S}{T_o} \tag{C.27}$$

and T_o is the reference temperature given as $T_o = 293.7$ K. The non-dimensional form of the heat flux is given by

$$q^*_i = -\mu^* T^*_{,i}\left(\frac{1}{Pr\, Re_o(\gamma-1)}\right) = -\mu^* e^*_{,i}\frac{\gamma}{Pr\, Re_o} \tag{C.28}$$

Furthermore, the equation of the state in non-dimensional form can be represented as follows

$$\gamma p^* = \rho^* T^* \tag{C.29}$$

In addition, several other relations are modified in the non-dimensional form as follows

$$E_m^* = \frac{1}{2}(u^{*2} + v^{*2} + w^{*2}) + e^* = \frac{1}{2}(u^{*2} + v^{*2} + w^{*2}) + \frac{T^*}{\gamma(\gamma - 1)} \tag{C.30}$$

$$p^* = \rho^* \left(E_m^* - \frac{1}{2}(u^{*2} + v^{*2} + w^{*2})\right)(\gamma - 1) \tag{C.31}$$

D Sphere volume discretization

In the context of the immersed boundary method for compressible flows explained in section 4.3, the particles must be resolved using Lagrangian marker points distributed uniformly throughout the particle volume. These lagrangian force point locations are further used to implement appropriate boundary conditions on the particle surfaces. This chapter explains the distribution of lagrangian markers and the geometrical construction used for the immersed boundary procedure, a direct extension from Uhlmann (2005). The geometrical description is shown in fig. D.1.

Distribution of lagrangian markers

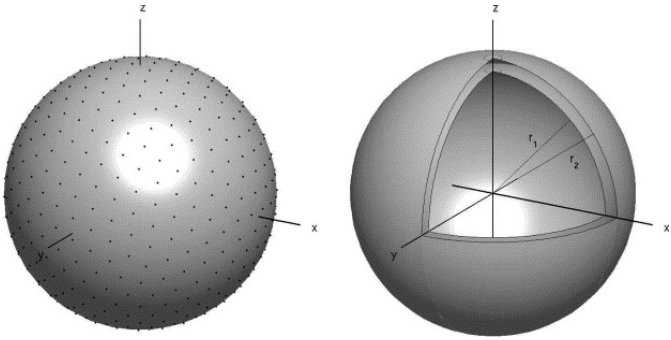

Figure D.1: Geometric description of spherical particle and distribution of lagrangian markers in the outer shell. The left figure shows the geometric distribution of 515 Lagrangian markers on the outermost shell. The figure on the right shows a cut-view for the outermost shell between radius r_1 and r_2. Figure reproduced from Uhlmann (2005)

Following Uhlmann (2005) and based on the choice of particle resolution ($D/\,\mathrm{d}x$), a fixed number of lagrangian markers are first distributed uniformly across the outer shell of the sphere located between $r_1 = r_c - h/2$ and $r_2 = r_c + h/2$. Where, r_c is the particle radius, and h is the uniform grid spacing on the cartesian grid. The distribution of lagrangian markers on a shell is repeated successively until only a tiny sphere with outer-radius $r_2 < h$ remains, after which a final lagrangian marker is added to the center.

Definition of forcing volumes

Consider a shell with radius r_{shell} such that the inner and outer radius are $r_{shell}-h/2$ and $r_{shell}+h/2$ respectively. Consequently, the immersed boundary forcing volume ΔV_l used in eq. (4.30) can be defined as

$$\Delta V_l = \frac{\pi h}{3N_{shell}} (12r_{shell}^2 + h^2) \tag{D.1}$$

Based on the requirement that $\Delta V_l \approx h^3$, the number of lagrangian markers for the shell reads

$$N_{shell} \approx \frac{\pi}{3} \left(12\frac{r_{shell}^2}{h^2} + 1 \right) \tag{D.2}$$

E Derivation of the ODEs for the Couette flow with variable dynamic viscosity

The non-dimensionalization of the governing differential equations for the compressible Couette flow test from section 5.2.3 with variable dynamic viscosity (μ) is given in the current section. With the assumptions specified in section 5.2.3, the governing differential equations reduce to a set of ordinary differential equations that can be solved numerically.

E.0.0.1 Non-dimensionalization

A non-dimensional length η is introduced such that $\eta = y/H$, $u = u_o\, u^*(\eta)$, $\mu = \mu_o \mu^*(\eta)$ and $i = i_o i^*(\eta)$. The quantities with the superscript '$*$' represent the non-dimensional quantities, and the ones with the subscript 'o' represent the quantities evaluated at the bottom wall, which is the reference plate for this test. The non-dimensional quantities at the bottom reference wall can be represented by eq. (E.1).

$$\mu^*(0) = u^*(0) = e^*(0) = i^*(0) = 1 \tag{E.1}$$

Substituting the non-dimensional variables multiplied with the respective reference quantities into the compressible Couette flow equations, we obtain

$$\mu^*\, u^{*\,\prime} = \text{constant} = u^{*\,\prime}(0) = \mu^*(1)\, u^{*\,\prime}(1) \tag{E.2}$$

$$\frac{d}{d\eta}(\mu^* i^{*\,\prime}) + \frac{u_o^2\, Pr}{i_o}\mu^* (u^{*\,\prime})^2 = 0 \tag{E.3}$$

Let $b = u_o^2/i_o$. Then, the energy equation in eq. (E.3) can be written as eq. (E.4).

$$\frac{d}{d\eta}(\mu^* i^{*\prime}) + b\,Pr\mu^*\,(u^{*\prime})^2 = 0 \tag{E.4}$$

Substituting the eq. (E.2) in eq. (E.4) and simplifying, we obtain

$$\frac{d}{d\eta}\,(\mu^*\, i^{*\prime} + b\,Pr\,u^{*\prime}(0)\,u^*) = 0 \tag{E.5}$$

The eq. (E.5) can then be integrated with respect to η. After a re-substitution back from eq. (E.2) and substituting $u^*(1) = 0$, we get

$$\mu^*\, i^{*\prime} + b\,Pr\,\mu^*\,u^{*\prime}\,u^* = \text{const} = i^{*\prime}(0) + Pr\,b\,u^{*\prime}(0) = \mu^*(1)\,i^{*\prime}(1) \tag{E.6}$$

Next, after dividing eq. (E.6) by eq. (E.2) and integrating w.r.t. u^*, we obtain

$$i^* + \frac{Pr\,b\,(u^{*\prime})^2}{2} = \left[\frac{i^{*\prime}(1)}{u^{*\prime}(1)}\right] u^* + C \tag{E.7}$$

C is the constant of integration whose value can be obtained with the fact that at $\eta = 1 : u^* = 0,\ i^* = i^*(1)$. Substituting the value of C, we get

$$i^* = i^*(1) + \left[\frac{i^{*\prime}(1)}{u^{*\prime}(1)}\right] u^* - \frac{Pr\,b\,(u^{*\prime})^2}{2} \tag{E.8}$$

At $\eta = 0$, we have $u^*(0) = 1,\ i^*(0) = 1$. Hence, we obtain eq. (E.9). By integrating eq. (E.2) with respect to η, we get eqs. (E.10) and (E.11).

$$1 = i^*(1) + \frac{i^{*\prime}(1)}{u^{*\prime}(1)} - \frac{Pr\,b}{2} \tag{E.9}$$

$$\int_0^{u^*} \mu^*\,du^* = -u^{*\prime}(0)(1-\eta) \tag{E.10}$$

$$\int_0^1 \mu^*\,du^* = -u^{*\prime}(0) \tag{E.11}$$

For the current Couette flow problem, the velocity u_o of the lower wall and the specific enthalpy i at the lower wall are specified. However, in order to solve the equations, a viscous law is needed. A simple viscous law is assumed where the dynamic viscosity is proportional to the specific enthalpy such that

$$\mu^* = i^* \tag{E.12}$$

Using the viscous law along with the eq. (E.8) and eq. (E.10) gives us:

$$\int_0^{u^*} i^* du^* = -u^{*\prime}(0)(1-\eta) \tag{E.13}$$

Finally, by substituting the expression for specific enthalpy in eq. (E.8) and integrating, we get

$$i^*(1)\, u^* + \frac{1}{2}\left[\frac{i^{*\prime}(1)}{u^{*\prime}(1)}\right] u^{*2} - \frac{Pr\, b\, (u^{*\prime})^3}{6} = -u^{*\prime}(0)(1-\eta) \tag{E.14}$$

$$i^*(1) + \frac{1}{2}\left[\frac{i^{*\prime}(1)}{u^{*\prime}(1)}\right] - \frac{Pr\, b}{6} = -u^{*\prime}(0) \tag{E.15}$$

$i^*(0)$ and $i^*(1)$ are specified at the boundary conditions. Also, the eqs. (E.2), (E.6), (E.9) and (E.15) can be solved simultaneously with the help of the viscosity law eq. (E.12) to obtain the values of $i^{*\prime}(0)$, $i^{*\prime}(1)$, $u^{*\prime}(0)$ and $u^{*\prime}(1)$. These values can then be substituted in the ordinary differential eqs. (E.8) and (E.14) and solved numerically to obtain the solutions of specific enthalpy and velocity.

For the current test case, the ordinary differential equations are numerically solved on a Chebychev-Gauss-Lobato grid using a Newton-Raphson method and then spectrally interpolated to a uniform grid with an arbitrary number of grid points to obtain the reference solution.

The term b in the differential equations directly influences the Mach number of the flow at the steady state. By choosing u_o and b, we indirectly specify the specific internal energy (e_o) or the specific enthalpy (i_o) of the lower plate,

consequently determining the Mach number of the flow near the lower plate. It can be shown as follows:

$$b = \frac{u_o^2}{i^o} = \frac{\rho_o\, u_o^2(\gamma - 1)}{\gamma\, p_o} = \frac{u_o^2}{c_o^2}(\gamma - 1) = Ma^2(\gamma - 1) \tag{E.16}$$

In eq. (E.16), c_o is the speed of sound of the flow near the lower plate. In the validation tests, specifying the value of i_o or e_o at the boundary will determine the value of b, which should be used to determine the reference solution for a given test.

F Drag and Nusselt number formulation

Evaluation of Drag and Lift coefficients

Consider a single isolated sphere for conciseness. Let F_x be the axial component of the hydrodynamic force acting upon the particle evaluated from the immersed boundary procedure explained in section 4.3. Then, the Drag coefficient (C_d) on the particle can be evaluated as follows

$$C_d = \frac{F_x}{\rho\, u_\infty^2\, A_{frontal}/2} \tag{F.1}$$

Let the non-axial components of hydrodynamic force be given by F_y and F_z. Then, the magnitude of the lift force can be computed as the $F_l = \sqrt{F_y^2 + F_z^2}$. Then the lift coefficient (C_l) can be evaluated as

$$C_l = \frac{F_l}{\rho\, u_\infty^2\, A_{frontal}/2} \tag{F.2}$$

For a sphere, the frontal area $A_{frontal}$ is given as $A_{frontal} = \pi D^2/4$, and D is the sphere's diameter.

Evaluation of Nusselt number

Consider a viscous flow around an isolated rigid sphere such that the velocity components $u, v,$ and w are zero inside the sphere. In that case, using the

first law for the sphere as a closed system, the total heat added to the sphere can be represented as

$$\delta Q = C_v \, dT \tag{F.3}$$

In the eq. (F.3), δQ is the heat added, C_v is the specific heat capacity at constant volume, and dT is the differential change in the internal energy. In the integral form, this leads to the energy conservation equation for the sphere as follows

$$\int_V \rho C_v \frac{\partial T}{\partial t} \, dV \; = \; \int_S q_{local} \, dS \tag{F.4}$$

Consider a sphere with T_{surf} being the constant temperature on the surface of the sphere and T_∞ be the temperature at the free stream such that the wall internal energy can be represented as

$$e_{surf} \; = \; C_v \, T_{surf} \tag{F.5}$$

From Newton's law of cooling and Fourier's law of heat conduction, we obtain

$$q_{local} = -\kappa \left(\frac{\partial T}{\partial n} \right)_{wall} = \hbar (T_{surf} - T_\infty) \tag{F.6}$$

q_{local} = Local heat flux at the surface of the sphere
$\hbar$ = Heat transfer coefficient
T_∞ = Free-stream temperature
κ = Thermal conductivity
n = Normal vector to the sphere surface

The surface averaged Nusselt number ($\overline{Nu}$) can be evaluated from the local Nusselt number as in eq. (F.7).

$$\overline{Nu} = \frac{1}{S} \int_S Nu_{local}\, dS \tag{F.7}$$

$$= \frac{D}{\kappa(T_{surf} - T_\infty)}\, \bar{q} \tag{F.8}$$

Where S is the surface area of the sphere and $\bar{q}$ is the average heat flux. It should be noted that we directly obtain the value of $\int_V \rho\ (\partial e_i/\partial t)\, dV$ from the immersed boundary procedure as in section 4.3. Finally by using eqs. (F.4) and (F.7), the average Nusselt number, $\overline{Nu}$ in terms of the dimensional quantities can be written as

$$\overline{Nu} = \frac{Pr}{\mu_{surf}\, \gamma\, \pi\, D\, (e_{surf} - e_\infty)} \int_V \rho\, \frac{\partial e}{\partial t}\, dV \tag{F.9}$$

μ_{surf} is the dynamic viscosity of the fluid near the sphere surface, γ is the ratio of heat capacities, D is the diameter of the sphere, e_{surf} is the internal energy of the fluid near the sphere surface and e_∞ is the internal energy of the fluid at the free-stream.

Using the reference quantities in appendix C, the average Nusselt number can be represented in terms of the non-dimensional quantities as follows

$$\overline{Nu} = \frac{Pr\, Re_D}{Ma_\infty\, \mu^*_{surf}\, \gamma\, \pi\, D^*\, (e^*_{surf} - e^*_\infty)} \int_V^* \rho^*\, \frac{\partial e^*}{\partial t^*}\, dV^* \tag{F.10}$$

The integral in eq. (F.10) is directly obtained from the immersed boundary procedure.

G Particle arrangement dependence

The effect of different arrangements for compressible flow through a fixed particle array as discussed in chapter 6 is studied. Two different fixed-particle arrangements for flow through a finite-sized array are considered, and the effects on mean flow fields, particle forces, and heat transfer are discussed. For the two cases, the particle resolution given by $D_p/\mathrm{d}x = 20$ is chosen, while the other parameters are the same as the base case $M166_{30}$ given in table 6.1. The two cases will be referred to as $M166_{20a}$ and $M166_{20b}$. The parameters are summarized again in table G.1.

Table G.1: Parameters for the simulations of shock interaction with an array of fixed particles with finite thickness: Shock Mach number Ma_s, Reynolds number Re_{ps}, volume fraction ϕ, Temperature ratio T_p/T_{ps}, Wake region length L_w, Tranverse region length L_y, L_z, resolution $D_p/\mathrm{d}x$, and Prandtl number Pr.

Type	Ma_s	Re_{ps}	ϕ	T_p/T_{ps}	L_p	$L_y = L_z$	$D_p/\mathrm{d}x$	Pr
$M166_{20a}$	1.66	100	0.05	0.70	$30D_p$	$20D_p$	20	0.7
$M166_{20b}$	1.66	100	0.05	0.70	$30D_p$	$20D_p$	20	0.7

G.1 Mean flow fields

fig. G.1 shows the comparison of slab-averaged mean density, velocity, pressure, and temperature profiles for the cases $M166_{20a}$ and $M166_{20b}$ at late times. Neglecting, the local flow variations, it is observed that the normalized mean flow profiles look statistically similar for the two different arrangements along the particle curtain.

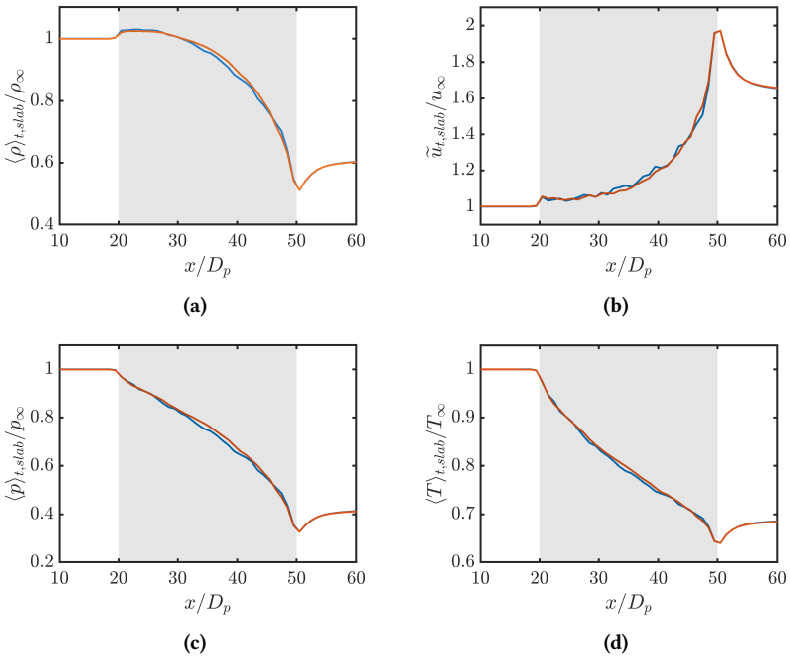

Figure G.1: Time and slab averaged flow-field profiles for (a) Density (b) velocity (c) Pressure (d) Temperature normalized with inflow conditions at late times as a function of normalized streamwise distance for the cases (——) $M166_{20a}$ (——) $M166_{20b}$.

G.2 Reynolds and Mach number variations

fig. G.2a and fig. G.2b show the slab averaged based Reynolds ($\langle Re \rangle_{t,slab}$) and Mach number ($\langle Ma \rangle_{t,slab}$) profiles defined in eq. (6.11). The Reynolds and Mach number profiles show an increasing trend along the streamwise position inside the curtain. In addition, the Mach number shows a sharp increase near the downstream edge of the curtain as observed previously for $M166_{30}$ in fig. 6.23b. The observed trend is because of the sharp flow acceleration in the region as explained previously in section 6.4.1. Similar to the mean flow profiles, the Reynolds and Mach profiles also appear statistically similar for both the particle-arrangements.

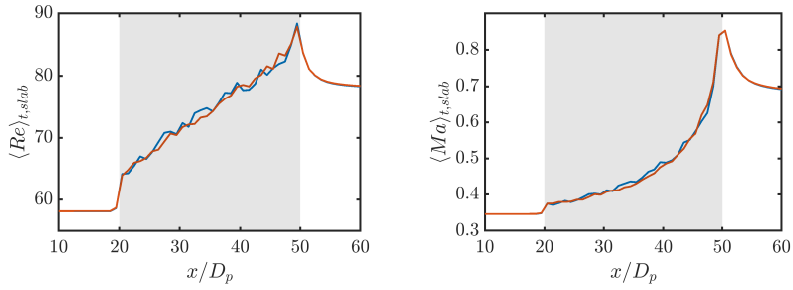

Figure G.2: Time and slab averaged (a) Reynolds number (b) Mach number for the cases (——) $M166_{20a}$ (——) $M166_{20b}$.

G.3 Velocity fluctuations

The profiles for normalized slab-averaged pseudo-turbulent kinetic energy (PTKE) and corresponding turbulent Reynolds number (Re_t) profiles are shown in figs. G.3a and G.3b respectively. The general trend along the streamwise direction is statistically similar in both the cases.

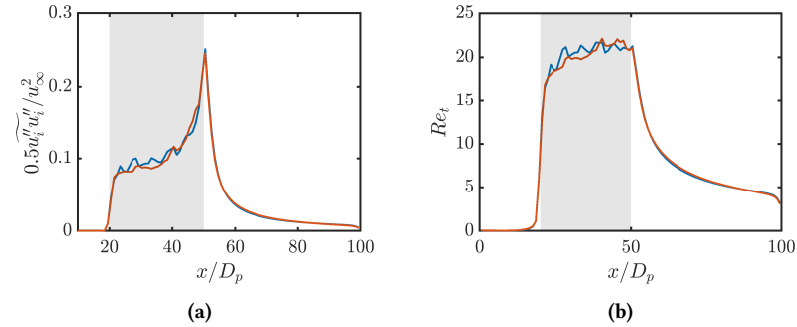

Figure G.3: (a)Comparison of time and slab averaged based Normalized pseudo-turbulent kinetic energy (PTKE) ($0.5\widetilde{u_i'' u_i''}/u_\infty^2$) and (b) turbulent Reynolds number, $Re_t = \left(\langle \rho \rangle_{t,slab} D_p \sqrt{0.5\widetilde{u_i'' u_i''}}\right)/\langle \mu \rangle_{t,slab}$. The two arrangements are represented by (——) $M166_{20a}$ (——) $M166_{20b}$.

G.4 Particle force and heat transfer

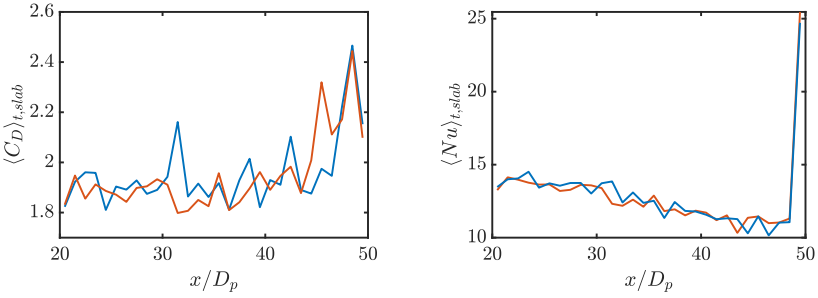

Figure G.4: Comparison of time and slab averaged based (a) Drag coefficient ($\langle C_D \rangle_{t,slab}$) and (b) Nusselt number ($\langle Nu \rangle_{t,slab}$). The two arrangements are represented by (——) $M166_{20a}$ (——) $M166_{20b}$.

fig. G.4 show the slab-average based Drag coefficient ($\langle C_D \rangle_{t,slab}$) and Nusselt number ($\langle Nu \rangle_{t,slab}$) for the cases $M166_{20a}$ and $M166_{20b}$. The definitions of the drag and Nusselt numbers are given in eq. (6.14). In both the particle arrangements, the general trend including peaking of the drag coefficient near the downstream edge of the curtain, and the general decrease of Nusselt number along the streamwise position inside the curtain are captured. In addition, the sharp increase of the Nusselt number at the downstream edge of the curtain, as the particle-to-fluid temperature ratio approaches unity is also captured by both the arrangements.

H Force coefficient based on Stokes drag

In this chapter, the total force on the particles inside a finite-sized curtain as given in chapter 6 is compared to the Stokes drag as defined in eq. (H.1). In the equation, D_p is the diameter of the spherical particles inside the curtain, μ is the fluid dynamic viscosity, and $\widetilde{u}$ is the density weighted streamwise velocity field. $\langle\cdot\rangle_{slab}$ represents the phase average of a fluid quantity in a streamwise x-slab of width D_p (shown in appendix A.1.1) inside the curtain.

$$F_{Stokes} = 3\pi D_p \langle\mu\rangle_{slab} \widetilde{u}_{slab} \tag{H.1}$$

Based on the definition of the Stokes drag, a force coefficient is defined as shown in eq. (H.2) and used to compare the streamwise variation of the drag forces on the particles inside the curtain for the cases $M122_{30}$, $M166_{30}$, and $M260_{30,ps}$ at late times, where the flow has negligible temporal fluctuations.

$$C_{F,St} = \frac{\langle F_x\rangle_{slab}}{F_{Stokes}} \tag{H.2}$$

In eq. (H.2), $\langle F_x\rangle_{slab}$ represents the slab-averaged drag force on the particles at a given x-slab location. $C_{F,St}$ qualitatively measures the total force on the particles compared to the force experienced by the particles in the Stokes flow regime. Hence, regions where $C_{F,St}$ is low, represent the flow to be governed

by viscous effects. Conversely, high values of $C_{F,St}$ would represent additional effects which may contribute to the drag force on the particles. $C_{F,St}$ is compared for the three cases as shown in fig. H.1.

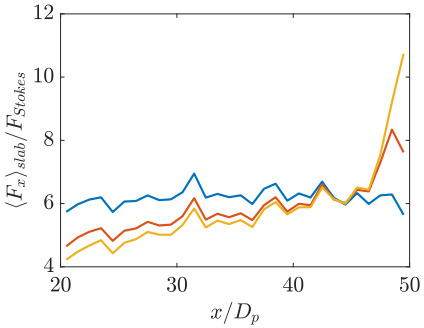

Figure H.1: Comparison of the force coefficient ($C_{F,St}$) along the particle curtain from the DNS for the cases (——) $M122_{30}$, (——) $M166_{30}$, and (——) $M260_{30,ps}$. The cases are the same as in chapter 6.

It is observed that $C_{F,St}$ is lowest for the case $M260_{30,ps}$ and highest for $M122_{30}$ at the upstream edge of the particle curtain. However the trend reverses at the downstream edge of the particle curtain. In addition, $C_{F,St}$ is observed to be approximately equal for the three cases at $x/D_p = 44$. This is explained by the comparison of the temperature profiles as shown in fig. 6.21d.

Since the fluid is hottest for the case $M260_{30,ps}$ at the upstream edge of the curtain, from the Sutherland's law, it is also more viscous compared to the other two cases. Hence, it is expected that the total forces on the particles near the upstream edge of the curtain will be closer to the Stokes flow regime. However, moving along the curtain, the flow becomes cooled (at a higher rate for the case $M260_{30,ps}$ compared to $M122_{30}$ and $M166_{30}$), resulting in the fluid viscosity to decrease, and a departure from the Stokes flow regime. This is more apparent for the cases $M166_{30}$ and $M260_{30,ps}$, which have higher streamwise temperature gradients in the flow. Near the downstream edge of the particle curtain, strong flow acceleration occurs (refer to fig. 6.23b) for the case $M166_{30}$ and $M260_{30,ps}$, which is reflected as a peak in the $C_{F,St}$ shown in fig. H.1.

I Description of one dimensional two-phase model

A one dimensional physics-based model for shock-wave interaction with a particle curtain was provided by Ling et al. (2012). Their one-dimensional model is simplified in the current work for study of shock-wave interaction with a fixed particle array with the setup shown in fig. 6.2. The assumptions used for the model in the current work are stated below.

- The continuous phase follows an ideal gas law.
- The continuous phase is treated as inviscid, except for interphase energy and momentum exchange.
- The particles are assumed to be fixed and homogeneously distributed inside the curtain.
- The three dimensional effects inside the curtain are neglected.
- The temperature on the particles is assumed to be constant and uniform.

The continuous phase is treated in the Eulerian framework and the corresponding governing differential equations are shown in eqs. (6.32) to (6.34). The geometrical length scales L_p and L_x for the one-dimensional simulations are the same as the three dimensional DNS. In addition, the global volume fraction (ϕ), the location of the incident shock, the particle-to-fluid temperature ratio (T_p/T_{ps}), the pre/post-shock conditions for the initial flow conditions are the same as the three-dimensional DNS runs given in section 6.1. However, a simple zero-flux boundary conditions were used,

different from the three-dimensional DNS, which used the non-reflecting inflow-outflow boundary conditions.

I.1 Numerical Framework

Let N_{DNS} represent the total number of particles with diameter (D_p) homogeneously distributed in a domain with a volume fraction of ϕ inside the curtain for the three dimensional DNS. If the length of the transverse domain are given by $L_y = L_z$, the streamwise domain by L_x, and the width of the curtain is L_p in the DNS simulations, then N_{DNS} will be represented by eq. (I.1).

$$N_{DNS} = \frac{6\phi L_p L_y L_z}{\pi D_p^3} \qquad \phi = \frac{N\pi D_p^3}{6L_p L_y L_z} \tag{I.1}$$

If $nx_{p,1d}$ represents the total number of grid points used to discretize the curtain width in the one-dimensional model, then the effective number of computational particles N_{cp} that represent the number of true particles present inside each of the two adjacent grid-points inside the curtain can be obtained by $N_{cp} = N_{DNS}/(nx_{p,1d}-1)$. If the grid spacing inside the curtain is represented by Δx_{1d}, then $\Delta x_{1d} = L_p/(nx_{p,1d} - 1)$ and the effective volume of the grid cell is given by $V_{cell} = \Delta x_{1d} L_y L_z$. Consequently, the equations in eqs. (6.32) to (6.34) can be written in the form given by Ling et al. (2012) as follows

$$\frac{\partial(\rho^g \phi^g)}{\partial t} + \frac{\partial(\rho^g \phi^g u_g)}{\partial x} = 0 \tag{I.2}$$

$$\frac{\partial(\rho^g \phi^g u^g)}{\partial t} + \frac{\partial(\rho^g \phi^g u^g u^g)}{\partial x} = -\frac{\partial p^g}{\partial x} - \frac{1}{V_{cell}} \sum_i N_{cp} F_i^{cp} \tag{I.3}$$

$$\frac{\partial(\rho^g \phi^g E^g)}{\partial t} + \frac{\partial(\rho^g \phi^g u^g E^g)}{\partial x} = -\frac{\partial(u^g p^g)}{\partial x} - \frac{1}{V_{cell}} \sum_i N_{cp}(G_i^{cp} + Q_i^{cp}) \tag{I.4}$$

Where, F_i^{cp} and Q_i^{cp} represent the overall hydrodynamic force and heat exchange between the two phases. In addition, G_i^{cp} is the internal energy and kinetic energy transferred to the continuous media due to F_i^{cp}. Their expressions represented by F_i^{gp}, Q_i^{gp}, and G_i^{gp} in the original literature was used in the present work. Consistent with the *a priori* modeling efforts given in section 6.5.1, the viscous unsteady contributions for momentum and heat exchange were neglected to model the flow at late times.

The Eulerian model is solved using a third-order Runge-Kutta method for time-stepping (Rai and Moin 1991) and a TENO scheme given by Fu et al. (2016) for the advection. The solution is advanced in time until the flow is established for comparisons with the late time mean flow fields obtained from the DNS section 6.4.

List of Figures

List of Tables